EXPERIMENTAL STUDY AND ANALYTICAL MODELING OF TRANSLAYER FRACTURE IN PULTRUDED FRP COMPOSITES

A Dissertation
Presented to
The Academic Faculty

By

Rani Fayez El-Hajjar

In Partial Fulfillment
Of the Requirements for the Degree
Doctor of Philosophy in the
School of Civil and Environmental Engineering

Georgia Institute of Technology

May 2004

EXPERIMENTAL STUDY AND ANALYTICAL MODELING OF TRANSLAYER FRACTURE IN PULTRUDED FRP COMPOSITES

Approved by:

Dr. Rami Haj-Ali, Advisor

Dr. Ashok Saxena

Dr. Erian Armanios

Dr. Donald White

Dr. Laurence Jacobs

Dr. Abdul-Hamid Zureick

March 9, 2004

Dedicated to the memory of
Naji Al-Ali, Rachel Corrie and Edward Said

ACKNOWLEDGEMENTS

My thanks and appreciation go to Dr. Rami Haj-Ali, my advisor, for his guidance, encouragement, persistence, patience and expert advice. Interaction with him has inspired my love of research and has allowed me to seek new and exciting challenges. I will always remember the time we spent on research and publications. This final manuscript has also been greatly affected by the expert advice of my defense reading committee comprised of Dr. Erian Armanios, Dr. Laurence Jacobs, Dr. Ashok Saxena, Dr. Donald White, and Dr. Abdul-Hamid Zureick. My gratitude also goes to my colleagues Anastasia Muliana, Shane Johnson, Ahmet Citipitioglu and Hakan Kilic for all the scientific discussions. Thanks are also in order to Bradley Boyce of Stress Photonics Inc. for his expert advise and valuable technical assistance in the field of Infrared Thermographic Stress Analysis. I would also like to acknowledge the support of the National Science Foundation, through the Civil and Mechanical Systems Division under grant number 9876080.

My admiration and respect go to my friends and comrades in Atlanta who have all been an amazing source of hope and inspiration: Marcia Mihdawi, Mohammed Brewish, Manal Milhem, Thomas MacMaster, Sara Totonchi, Barry Flanagan, Elizabeth Corrie, Jason Shultz, Nadia Ali, Reema Ali, Samir Moukaddam, Hazem Ziade, Deborah Middleton, Sameh Dardona, Bissan Salhi, Carole Montarou, Sobukweku Kuumba, Yosef Abuneaj, Adam Levenstein, Frank Salerno and Dianne Mathiowetz. I would also like to thank Marcia Mihdawi for her support and help in rehearsing my defense presentation. Finally, my deepest thanks go to my wonderful family especially my sisters, Dana and Rana (the mothers of my beautiful nieces, Aya, Sara and Hannah) and most importantly to my parents Fayez and Ferial for their endless love and continuous encouragement during this endeavor.

TABLE OF CONTENTS

LIST OF FIGURES

LIST OF TABLES

SUMMARY

A new nonlinear fracture analysis framework is developed for the mode-I and II fracture response of thick-section fiber reinforced polymeric (FRP) composites. This framework employs 3D micromechanical constitutive models for the nonlinear material behavior along with cohesive elements for crack growth. Fracture tests on various cracked geometries are used to verify the prediction of the failure loads and the crack growth behavior. A commercially available pultruded E-glass/polyester and vinylester thick-section FRP composite material was used to demonstrate the proposed fracture approach along with the nonlinear constitutive modeling. A new Infra-red thermography technique is derived to measure the surface strain field near the crack tip in the linear response range. Mode I and II fracture toughness tests for pultruded composites are also examined using the eccentrically loaded, single-edge-notch tension, ESE(T), single-edge-notch tension, SEN(T), and a butterfly specimen with an Arcan-type fixture. Material nonlinearity and crack growth effects were observed during the tests and investigated using the proposed analysis framework. The effect of material orthotropy on the stress intensity factor solutions was addressed using the virtual crack closure technique. The analytic and experimental results support the use of the ESE(T) specimen for the measuring the mode-I fracture toughness and the butterfly shaped specimen for measuring the mode-II toughness. The calibrated cohesive models were able to predict the measured crack growth in both modes I and II for various crack geometries. A mixed mode failure criterion is proposed and verified with test results. Examples are presented for using this criterion and crack growth analyses. The experimental and analytical results of this study can form a foundation for using fracture-based methods for the design of structures using these materials.

CHAPTER 1

INTRODUCTION

Fracture mechanics employs energy based theories to determine sudden or propagating failures in structures. These theories can be used to define certain material properties and to analytically quantify the stresses near various crack configurations. For example, the fracture toughness under different modes can be directly linked to the stress fields ahead of a crack tip. Fracture mechanics theories have been widely accepted for failure analysis in metallic structures but their use in the field of FRP composite structures is relatively new. The application of fracture mechanics theories in fiber reinforced polymeric (FRP) laminated composite systems has been complicated by crack branching or the lack of self-similar crack growth. This is also because the emergence and development of fracture mechanics was largely driven by the unexplained failures of large metallic structures around the turn of the last century (e.g. the failure of 'Liberty' ships in the United States Navy of World War II). More recently, fracture mechanics has been used to explain damage development in composite materials at different levels of magnification such as fiber-matrix interface cracks, fiber bridging, microcracks in the matrix and delamination amongst many others.

Thick-section composites are a class of FRP composites that are widely used in many structural applications. One method of manufacturing thick-section composites is the "pultrusion" process whereby different types of fiber reinforcements are guided from a creel, impregnated with resin and then drawn through a preform block through a heated die for curing. Thick-section composites offer important advantages over traditional engineering materials such as high strength and stiffness, high strength/weight ratio, resistance to certain corrosive environments, superior absorption of energy and shielding of electrical and magnetic fields. Pultruded composite prismatic structural members can be manufactured in

large lengths having a general constant cross-sectional profile similar to standard profiles found in metallic frames, e.g. I-shapes, tubes, and angles.

Traditional design techniques in these orthotropic composites have relied upon the use of high design safety factors and linear analysis techniques. Fracture analyses techniques of pultruded FRP having mode-I and II translayer (interlaminar) macro-cracks has been largely missing. These cracks can form during service or from the manufacturing process that may result in a number of defects such as matrix microcracks and voids in the finished product. The voids and microcracks can grow and coalesce to form a crack on the macroscopic level and may cause catastrophic failure. Service conditions or overloads of the structure may also cause crack propagation and structural failure. Crack initiation is also believed to occur these composites in areas of high stress concentrations such as the flange/web interface of pultruded I-beams. Application of fracture mechanics techniques also becomes more important when the size of the structure increases. Compared to traditional laminated structures the size of structures made with FRP pultrusions is large. For example, pultruded FRP members can be found in various FRP bridges, transmission towers, and structural frame components. Additionally, pultruded materials and structures may exhibit nonlinear material behavior when subjected to multi-axial loading. These nonlinear effects can interact with geometric and material discontinuities such as cracks at the structural level.

This chapter presents a literature review of the significant studies characterizing the mechanical response of thick-section pultruded composites and the applications of interlaminar fracture mechanics on composite materials. In addition, a review of prior work on infrared thermography techniques is presented especially when used to study the full-field stress state of materials with crack systems. The final section of this chapter will outline the objectives and research approach of the present study.

1.1 Pultruded FRP Composite Materials

Pultrusion is a manufacturing process whereby different types of fiber reinforcements are guided (or pulled) from a creel, impregnated with resin and then drawn through a preform block through a heated die for curing. Pultruded composites are thick heterogeneous materials that can combine various forms of reinforcement systems repeated through the thickness of the member, such as roving, continuous filament mats (CFM), woven fabrics, and braided preforms. Currently CFM and roving reinforcements are widely used. The CFM layer consists of relatively long and swirled filaments that are randomly oriented in the plane of the layer. The CFM is usually used for multi-directional secondary reinforcement and to provide material continuity in transition regions of the cross-section, e.g. near the web-flange junction in an I-shape pultruded member. The fibers can be made of carbon or glass. Matrix materials are commonly made of polyester, vinylester, epoxy or urethane and can include additives such as glass microspheres and clay particles. The fiber volume fraction (FVF) is relatively low in pultruded composites when compared to 'thin' laminated composites. Herakovich and Mirzadeh (1991) studied the effects of fiber spacing and fiber volume content on the effective properties of a pultruded graphite/epoxy composite. Fiber waviness was found to reduce the stiffness and strength of the pultruded composite. Binshan et al. (1995) performed a series of FVF tests on E-glass/polyester and E-glass/vinylester pultruded specimens and found that grating and reinforcement bar specimens had the highest FVF and the lowest amount of added fillers, while standard profile specimens had a relatively low FVF and high filler content. The voids were also found to range from 3-5%, with the addition of fillers reducing the void content and mechanical properties and significantly increasing the mass of the pultruded composite. Wang and Zureick (1994) characterized the tensile behavior of coupon specimens cut from different locations of a pultruded I-shape beam. A significant number of voids were found in these coupons and the roving reinforcements were distributed unevenly.

Bank (1990) noted the nonlinear shear response in pultruded composites by using the Iosipescu fixture to test specimens cut from pultruded beams. Several methods have been proposed for the measurement of the in-plane shear properties in pultruded composites. These include off-axis test methods, such as the $\pm$ 45^o degree tension/compression test, the cylinder-torsion method, and variations to the Iosipescu specimen. Chamis and Sinclair (1977) proposed using a 10^o off-axis tensile test to the obtain the in-plane shear properties of composites but had the limitation of the results being largely affected by orientation misalignment and gripping effects. Turvey (1998) used 6.4 mm glass/polymer pultrusions in torsion tests to determine the in-plane and through thickness shear moduli. Haj-Ali and Kilic (2002) proposed the use of the $\pm$ 45^o compression test for thick pultruded composites. Note that the application of this method to laminated composite systems was limited by the inability to preclude buckling before a shear induced failure. In the cylinder-torsion method, a torque is applied to a thin cylindrical specimen at the ends to induce a state of shear. A major disadvantage is the likelihood of failure at the ends (grips). Barbero et al. (1999) used torsion tests on pultruded rods made of only roving layers to determine the shear stiffness and strength. Davalos et al. (2002), used torsion tests on rectangular bars to determine the shear moduli in E-glass/vinylester pultruded composites. The linear elasticity shear solutions of Lekhnitskii and Whitney were used for data reduction purposes. Therefore, the method was applicable when the stress-strain response is close to linear, early in the loading stages. Zureick(1999) proposed the use of a modified Iosipescu specimen for shear property measurement in pultruded composites. A major advantage of this method compared to the off-axis test was the low levels of the longitudinal strain and the large gage section. Arcan et al. (1978) proposed a biaxial fixture, commonly known as the Arcan fixture, to produce biaxial states of stress. The compact nature of the Arcan fixture enables obtaining the shear properties in all in-plane directions in a relatively simple manner. The Arcan fixture can be used to apply both shear and axial forces to the test specimen. Voloshin and Arcan (1980) used this method to determine the longitudinal and through-thickness shear modulus in a

unidirectional laminated FRP composite. Their results compared favorably to those obtained from cylinder–torsion tests. Hung and Lechti (1997, 1999) performed extensive finite element analysis on the Arcan specimen for pure shear and biaxial loading conditions. Compared to the Iosipescu specimen, it was found that proper specimen alignment was easier to achieve thereby eliminating the bending and twisting effects noted in the Iosipescu specimen. In Hung and Lechti (1997), they used Moirè interferometry to examine the strain fields and their uniformity in unidirectional laminated specimens of AS4/PEEK tested in an Arcan fixture. Their sample was 2.5 mm (0.098 in) in thickness. They found that aligning the fibers with the loading direction and using a 90^o notch produced a uniform 'pure shear' state in the gage section. Different fiber orientations resulted in different optimum notch angles.

The overall effective mechanical properties and response of a composite material can be characterized from its fiber and matrix constituents. More refined models can include the fiber coating and the interphase (or interface) between the constituents. Several micromodels have been proposed to characterize the effective properties of FRP pultruded composites. Barbero (1991) and Sonti and Barbero (1996) proposed a linear micromechanical modeling approach to generate the overall effective stiffness of pultruded composite material systems. The micromodel, which employed the periodic microstructure formulae of Luciano and Barbero (1994), was combined with the classical lamination theory and mechanics of laminated beams to determine the overall effective stiffness of pultruded beams. The in–plane stiffness for the CFM layers was modeled using approximate models proposed by Tsai and Pagano (1968). The predicted effective stiffness matched well with their experimental results. A 3D micromechanical and structural modeling framework for the nonlinear analysis of pultruded composite materials and structures has been proposed (Haj–Ali et al., 2001, Haj–Ali and Kilic 2002, 2003). Multi–scale micromodels were used to model the roving and CFM layers. A sublaminate model was used to generate the through–thickness 3D effective behavior of the material. Kilic and Haj–Ali (2003a, 2003b)

coupled the nonlinear micromechanical formulation along with different failure models to perform progressive failure analysis of pultruded components. Finite element (FE) models have been used to analyze pultruded composite structures. Most of these studies consider the material to be linear orthotropic and homogeneous. Bank and Yin (1999) studied the separation between the compression flange and web of an I shape pultruded beam in postbuckling regime. A FE analysis was generated using a node separation technique in order to simulate the progressive failure of flange-web junction following a local buckling of the flange. Smith et al. (1998) performed experimental tests and FE analyses using shell elements for connections in FRP pultruded members. The strength and stiffness of the box-beam were found to be higher than the examined I-beam.

1.2 Fracture in FRP Composite Materials

While limited attention has been paid to modeling the fracture of crack-like flaws in pultruded composite systems, fracture mechanics has previously been advocated and applied to thin-section laminated composites. Sih et al. (1965) used a complex variable approach to derive the general equations of crack-tip stress fields in anisotropic bodies. Finite element analysis using the virtual crack closure technique (Raju, 1987 and Krueger, 2002) have been used to determine the strain energy release rate and relate it to the SIF. In an attempt to use existing stress intensity factor (SIF) solutions derived for isotropic conditions, Mandell et al. (1974) used hybrid FE analysis to show that the SIF can be dependent on the degree of material anisotropy for various specimen geometries. The SIF change between isotropic and anisotropic cases was relatively constant for varying crack lengths in a given geometry. The material constants were found to have an effect on the crack-tip stresses. Boa et al. (1992a, b) used an orthotropy rescaling technique to fit formulae into numerical calibrations to quantify the effect of material orthotropy on notched bars, delaminated beams, and hybrid sandwiches.

Stress based failure criteria were proposed to determine the strength of notched composites. Some of these criteria were evaluated pointwise while others were determined using average variables or characteristic lengths. Whitney and Nussimer (1974) proposed a failure criterion using the average stress distribution calculated from the edge of the hole to a given characteristic distance. The distance from the edge was considered as a material property since it did not depend on the size of the notch. A second related criterion was proposed where failure is assumed to occur when the stress, at a distance away from the notch, reaches the strength of the unnotched material. The proposed criteria were applied to graphite/epoxy and glass/epoxy laminated composites with straight cracks and were used to explain the reduction in strength of composites with larger hole sizes. Sih et al. (1975) proposed a strain energy density failure criterion to predict fracture in unidirectional composites subject to off-axis loading. Despite limitations, such as the violation of self-similar crack growth in various laminates, Linear Fracture Mechanics (LFM) has been applied to study failure in different composite systems (Konish et al., 1972, Saxena, 1979, Parhizgar et al., 1982). Waddoups et al. (1971) used a stress intensity factor (SIF) calculated based on a modified crack size. The larger effective crack length was determined by equating the intense energy region ahead of the crack to a material dependent characteristic length. Holdsworth et al. (1974) used LFM to predict the fracture of notched plates and box-section beams made from chopped strand mat with glass fibers and polyester resin using an effective crack size approach similar to Waddoups et al. (1971). The effective crack length was determined based on modifying the initial diameter of the notched holes. Kanninen et al. (1977a, 1977b) reviewed the applicability of fracture mechanics in composite materials and advocated the integration of micromechanical failure methods within a global structural analysis. In their approach, the material can be considered heterogeneous when microstructural effects are predominant and as homogenous anisotropic continuum otherwise. Fracture toughness tests have primarily focused on unidirectional FRP composites with the interlaminar fracture as the primary mode of fracture. Brunner (2000)

reviewed the various standards available for this mode of fracture. The Double Cantilever Beam (DCB) specimen, the End Notch Flexure (ENF), and the Mixed Mode Bending (MMB) specimen were addressed. Armanios (1989) proposed using a cracked-lap-shear configuration to investigate the interlaminar fracture of a graphite/epoxy composite. An analytical model of damage growth was used to predict the fracture behavior that followed a resistance curve during tensile loading. For materials that display the R-curve behavior, Bower and Ortiz (1991) analyzed the individual contributions of the constituents to the fracture toughness of a reinforced brittle material where crack trapping and bridging occurred. Toll and Aronsson (1992) have investigated the use of the damage zone criterion and the damage zone models amongst other criteria for determining the notched strength of various injection-moulded plates having different fiber systems. In the damage zone criterion, the stress in the damaged zone was assumed equal to the material's unnotched strength, and failure occurred when the damage zone reached a critical length. They found better predictions when using the damage zone model, where the damaged zone was propagated when the stresses reached the unnotched strength ahead of an equivalent crack (damaged zone). A linear relationship between the cohesive stresses and the crack opening was used within the damaged zone. Underwood et al (1995) studied the fracture behavior using the three-point bend, compact tension and the eccentrically loaded, single-edge-notch, tension, ESE(T) specimen. The specimens were used to determine the translayer fracture toughness of two types of carbon/polymer laminates. It was found that the largest translayer toughness was obtained using the ESE(T) specimen. Some of the results from this work were used in the original ASTM E1922 (1997) fracture test standard. Cowley and Beaumont (1997) used a compact tension specimen configuration to determine the effect of temperature on the mode-I fracture toughness of a carbon/polymer composite. From their tests, they found limited fiber bridging that resulted in similar values for the initiation and propagation fracture toughness. Since the temperature resulted in a reduction of the elastic modulus of the composite, the critical strain energy release rate was found to

increase with increase in temperature. Reber et al. (2000) successfully determined the interlaminar fracture toughness in knitted fabric reinforced composites based on a compliance technique to determine the energy release rate for crack extension.

Jurf and Pipes (1982), investigated the mixed mode translaminar fracture of a graphite/epoxy laminated composite using single-edge notched specimen adhesively bonded to the Arcan fixture. They proposed a quadratic mixed mode failure criterion based on the mode-I and II stress-intensity factors. Banks-Sills et al. (1984a) initially proposed the use of a mode-II fracture specimen for the mode-II toughness testing of brittle steels. Finite element analysis was performed to obtain the K_{II} calibrations and a test was conducted on a brittle steel specimen to measure the mode-II toughness. From the finite element results, it was found that the mode-II SIF was very sensitive to the specimen geometry. Limited amount of K_I was present during the mode-II tests. Banks-Sills et al. (1984b) used photoelasticity analysis to study an Arcan type mixed mode fracture specimen found that the optimum uniformity in the biaxial stress field occurred for angles less than 20 degrees from the specimen's vertical line of symmetry. Finite element analysis were also conducted to obtain the calibration formulas for the K_I and K_{II} SIFs. A further development of this specimen was presented by Banks-Sills and Arcan (1986) to determine the mode-II toughness of Plexiglass. Yuan et al. (1994) found favorable results using the J-integral method to study the mode-II fracture toughness specimen proposed by Banks-Sills (1984a). When compared to the other specimens considered, it yielded the smallest ratio of K_I/K_{II}. Applications of this specimen were seen in Pang and Seetoh (1997) who used a specimen similar to the Arcan specimen made of two aluminum segments joined by an adhesive to investigate the mixed mode fracture of bonded joints using a stress-intensity based failure criterion. The aluminum specimen was attached to the loading fixture using a bolted type connection. Rikards (2000) used a specimen similar to the Arcan specimen to determine mode-I, II and mixed mode I/II critical strain energy release rates in a glass/epoxy FRP using the modified virtual crack closure integral method and the measured critical loads.

1.3 Infrared Thermography in Composites

Thermoelastic stress analysis (TSA) is an infrared thermography non-contact stress analysis technique whereby a system with infrared (IR) digital sensors is used to detect small changes of temperature from a stressed body. Under adiabatic and reversible conditions in isotropic materials, the application of a small cyclic load will induce small and repeated variations in temperature that are proportional to the sum of principal stresses. Kelvin (1878) first derived the linear relationship between the temperature change and the first invariant of stress. TSA has been applied in composite materials to measure stresses in thin laminated composites with and without damage. Potter and Greaves (1987) used Wong's (1987) formulation with the classical lamination theory to derive a form of the thermoelastic equations for thin laminates and to relate the adiabatic change of temperature to a given change in the strain. Their attempt to relate individual strain components to the TSA signal was not always successful in the general case of multi-axial deformations and different material systems. Several difficulties may arise in TSA applied to laminated composites such as the effects of mean stress and test frequency. Temperature diffusion and non-adiabatic approaches have been proposed to model the thermoelastic effect in laminated composites. Dunn (1992, 1993) used a mathematical model to account for the thermal conduction in the top epoxy layer of a graphite/epoxy composite. Kyriakopoulos et al. (1992) used heat conduction finite element analysis to quantify the TSA signal in the absence of adiabatic conditions. In the case of complex laminates, the IR camera detected temperature changes on the surface ply alone. It is well known that dissipative and damage effects can render the TSA method as qualitative. This is especially true in the case of damping in FRP composites, e.g. Adams and Short (1973) and Chandra et al. (1999). The thermoelastic relations may not be valid and used to extract the surface stress field. In these cases, coupled mechanical and thermal conduction with advanced constitutive description of the material are needed.

Bakis and Reifsnider (1991) examined TSA measurements for different graphite/epoxy laminated composites and found that the non-adiabatic conditions made quantitative measurements difficult. A simplified micromechanical model was used with linear anisotropic thermoelasticity to investigate the changes in the temperature at the micro-level during an assumed adiabatic deformation. Van Hemelrijck et al. (1992) showed that using adiabatic theory to correlate the TSA measurements at a single point on the surface of thin carbon/epoxy laminates led to poor results and higher frequencies were required for better correlation. Lin and Rowlands (1995) used anisotropic elasticity solutions with complex variables to correlate individual stresses from measured TSA data adjacent to traction free boundaries in orthotropic composite plates. Mackin and Vernon (2001) proposed an IR method to detect and quantify the extent of damage caused by sub-surface cracks in a 3-layer laminated polymer membrane utilizing the distinct thermal signature associated with the sub-surface cracks. Zhang et al. (1990) showed that the TSA signal across the two phases in a carbon/epoxy system results in opposite signs during the same mode of loading. This was attributed to the negative axial coefficient of thermal expansion of the carbon fibers. This effect was more pronounced under higher frequencies and made quantitative TSA difficult for these composite material systems. Adding a thick resin surface layer was found to stabilize the TSA signal and attenuate the heat transfer from the carbon/epoxy inner layers. Mackenzie (1989) and Welch and Zickel (1993) investigated the characteristics of the thermal radiation signal emitted from different surface coatings. The solution of Mackenzie for the thermal wave problem characterized the IR flux amplitude from the surface as a function of IR reflection and thermal material properties of the considered substrate-coat-air system. Using material properties of a typical paint coating, a range of thicknesses and applied thermal frequencies was identified to allow the coat to act as a strain witness layer. Barone and Patterson (1998) proposed using a polymeric coating to extract the strain field from TSA measurements. Their method was applied for isotropic substrates.

Good correlation between analytical solutions and measured TSA responses was obtained for aluminum plates with circular holes.

1.4 Present Study

The application of both linear and nonlinear fracture mechanics to thick-section FRP pultruded composites has been limited. This study is concerned with the development of mode-I and II models for translayer fracture in pultruded composites. Tests methods are proposed for determining the mode-I and II translayer fracture toughness of these composites. This is performed by proposing and using American Society for Testing and Materials (ASTM) testing standards. A new nonlinear 3D micromechanical constitutive material modeling approach is combined with cohesive fracture models for the failure and crack growth analysis. The proposed computational fracture analysis is carried out to predict the mechanical response beyond the peak load. In addition, a new full-field stress-imaging technique based on IR thermography is developed to verify the proposed fracture mechanics methods.

The chapters in this manuscript are organized as follows, Chapter 2 describes the material characterization studies and the micromechanical constitutive models. The 3D-micromechanical constitutive models for pultruded composites are formulated and used to generate the effective nonlinear response based on in situ matrix and fiber properties. The proposed micromodels are applied for a pultruded composite system having E-glass fibers and a polyester resin based matrix. The prediction for the nonlinear material response under multi-axial stress states is then verified by testing a series of off-axis coupons cut from a monolithic pultruded plate. In Chapter 3, a new IR thermography, TSA technique is developed for thick-section orthotropic composites coated with in-plane isotropic layers. In this method, the material is idealized as a layered composite and lamination theory considerations are applied to derive expressions that can relate the TSA signal to the sum of the surface strains. Quantitative strain measurements using TSA are verified for multi-axial

stress states by comparing the in-plane strain invariant from experimental TSA results in woven and pultruded plates with circular cut-outs to the strain fields obtained from FE simulations.

In Chapter 4, experimental and numerical analyses are performed to determine the fracture toughness and the crack growth behavior in the pultruded composite using the eccentrically loaded, single-edge-notch tension, ESE(T) specimen. Finite element analyses using the virtual crack closure technique were performed to assess the effect of material orthotropy on the mode-I SIF in the ESE(T) specimen. The FE SIF, for the proposed ESE(T) geometry, are calculated as a function of the material orthotropic parameters. Crack growth measurements were performed to determine the amount of stable crack growth before reaching critical load. Test procedures and methods for mode-I translayer fracture toughness are examined. Two data reduction methods based on the modification of existing ASTM testing standards are proposed for the calculation and interpretation of fracture test results. The validity of using the critical load in calculating the fracture toughness is also discussed.

In Chapter 5, the nonlinear micromechanical constitutive models are used with cohesive fracture layers in FE models to predict the crack growth and failure response. A generalized method is proposed for analyzing pultruded composite structures with mode-I cracks. The micromechanical constitutive models account for the nonlinear material behavior while the cohesive models are used to model the propagating crack. Test results in the form of load versus notch mouth opening displacement (NMOD) from ESE(T) and single-edge-notch tension SEN(T) specimen were used to calibrate and verify the predictions of the proposed fracture modeling approach. The developed TSA method is employed to verify the FE predictions for the surface strains in the linear range before the onset of crack growth.

Mode-II (shear dominated) translayer fracture toughness is examined in Chapter 6. A modified Arcan test fixture and butterfly specimen geometry are proposed for determining the mode-II fracture toughness. The modified-Arcan fixture and its butterfly specimen are

first investigated without an induced notch to determine the shear moduli, nonlinear stress–strain response, and strength under 'pure' shear and different biaxial stress conditions. The presence of direct stresses in a pure shear mode configuration is also examined. FE analyses are used to investigate the effect of notch radius and material orthotropy on the uniformity and distribution of stresses in the significant section of the butterfly specimen. The nonlinear shear stress–strain response is examined against shear test results from off–axis compression tests. The proposed combined micromechanical/cohesive modeling approach is also used to predict the Mode–II behavior for notched butterfly specimen. A simple optical grid imaging technique is developed to measure the apparent sliding strain from tracking the displacement of pre–marked dots near the notch mouth. A mixed mode failure criterion for translaminar fracture is presented in Chapter 7. Several applications are also presented illustrating the possible utility of fracture mechanics in the design of composite structures. Finally, conclusions from the current research and recommendations for future research are presented in Chapter 8.

CHAPTER 2

MATERIAL CHARACTERIZATION AND CONSTITUTIVE MODELING

In this chapter, the mechanical properties of a thick-section pultruded E-glass/polyester FRP composite system are presented. Three-dimensional micromechanical models are proposed to generate the nonlinear constitutive material response. The applied micromechanical models used for the roving and CFM layers recognize the material response at the fiber and matrix constituents. The proposed constitutive framework is implemented as a nested set of nonlinear micromodels in a displacement-based FE code. The micromechanical models are then calibrated for the E-glass/polyester pultruded composite using results from axial and transverse coupon tests. The nonlinear axial shear response is used to calibrate the in-situ matrix nonlinear parameters. The nonlinear constitutive framework is verified by examining the overall nonlinear axial responses from off-axis coupons under tension and compression.

2.1 Material Description

Glass/polymer pultrusions represent an important class of thick-section FRP composites. The pultruded composite material system used in this study consists of layers of polyester resin reinforced with E-glass unidirectional roving and continuous filament mats (CFM). This thick heterogeneous material can be idealized as a perfectly bonded layered system with its alternating roving and CFM layers. The roving unidirectional fiber layer is considered the primary reinforcement layer. The CFM layer consists of relatively long and swirled filaments that are randomly oriented in the plane of the layer. The CFM is usually used for multi-directional secondary reinforcement and to provide material continuity in transition regions of the cross-section, e.g. near the web-flange junction in an I-shape pultruded member. The thickness reduction due to the pultruded manufacturing

process results in CFM fibers appearing close to the surface. In addition to roving and CFM reinforcements, pultruded composites can combine other forms of reinforcement systems repeated through the thickness such as woven fabrics and braided preforms. Currently CFM and roving reinforcements are widely used. Layers of A-glass/polyester or pure polyester resin surface veils are usually added to form a smooth surface and for environmental protection (Creative Pultrusions, 2000). Pultruded FRP composites can also be manufactured into relatively thick-section (larger than 6.4 mm (0.25in)) structural members such as I-sections, tubes, plates and angles. Matrix burn-out tests to determine the fiber volume fractions in the layers of this and other pultruded composite material systems were previously conducted (Haj-Ali et al., 2002a,b). The volume fraction within the roving layer was 0.407 and was found to be 0.305 for the CFM. The overall average fiber volume fraction in the material was 0.34. Production of pultruded composites may result in a number of manufacturing defects such as matrix microcracks and voids. The nonlinearity in the pultruded composite is primarily due to the soft response of the matrix and the existence of manufacturing defects. These voids and microcracks can grow and coalesce to form a crack on the macroscopic level and may cause structural failure. Figure 2.1 shows a side view cross-section illustrating the layered nature of this composite. Some voids are clearly visible between the alternating CFM and roving layers. Figure 2.2 shows a top view of a sectioned coupon exposing the CFM and roving layers. The CFM and roving layers can have different thicknesses throughout the cross-section. Figure 2.3 shows an SEM micrograph of E-glass fibers in a pultruded composite surrounded by the polyester matrix.

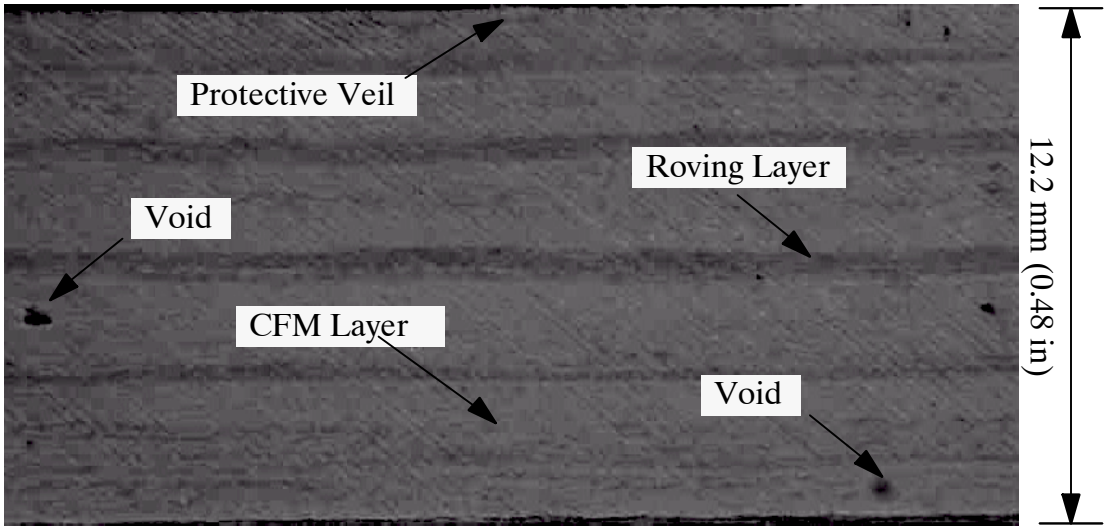

Figure 2.1 Cross-section of E-glass/polyester pultruded composite showing the layered medium with scattered voids

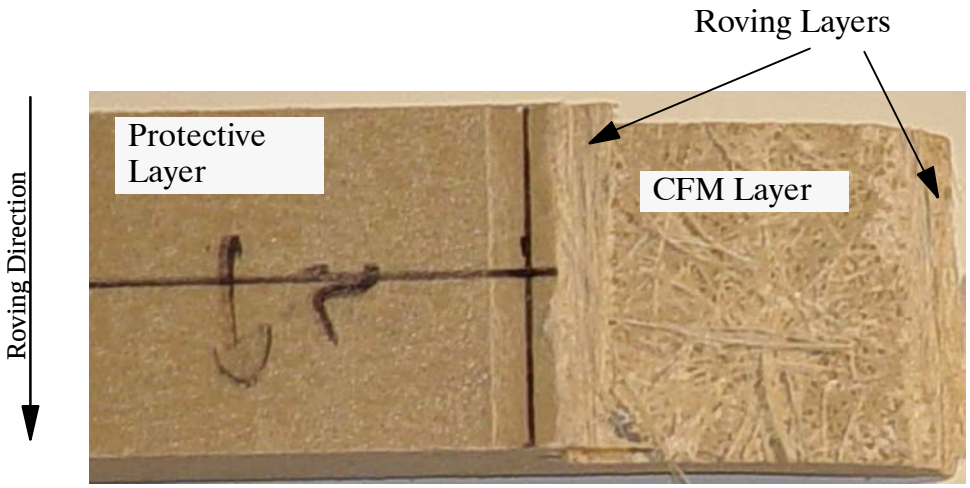

Figure 2.2 Sectioned coupon cut across the thickness of a pultruded composite showing swirled CFM fibers and the unidirectional roving bundles

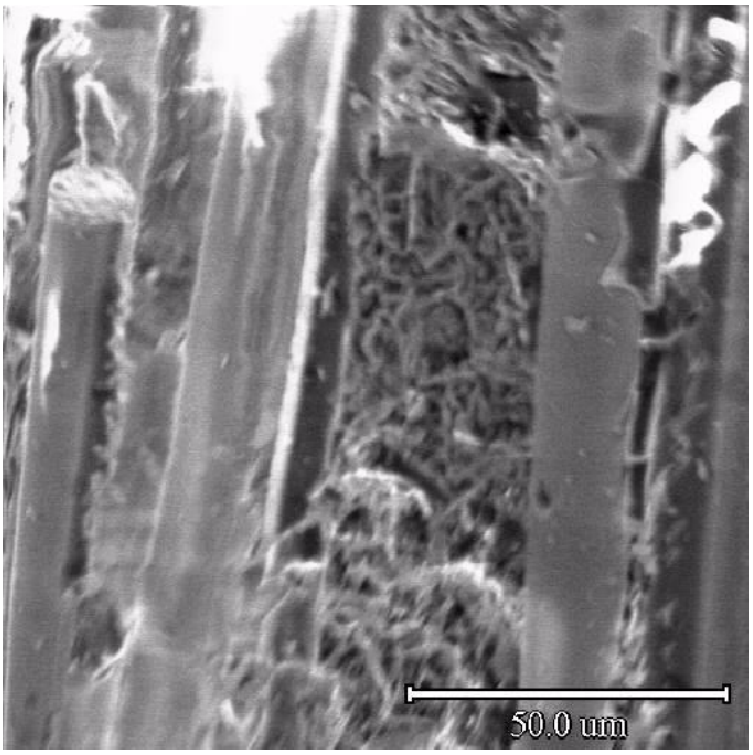

Figure 2.3 SEM micrograph of a pultruded composite showing E-glass fibers surrounded by polyester resin

2.2 Formulation of Applied Micromechanical Models

Nonlinear 3D micromechanical models are used to generate the effective response for the roving and CFM layers. The micromechanical constitutive models for the roving and CFM layers were first derived for pultruded composites by Haj-Ali et al. (2001, 2002c). The two micromodels explicitly recognize the response of the fiber and matrix constituents. These models are incorporated through a nested structure representing the composite systems that exist within the thickness of the cross-section. The homogenized equivalent continuum is generated for a periodic sequence of two alternating layers through the thickness of each section. This level of the model is referred to as the sublaminate model. It employs the 3D lamination theory to generate a nonlinear continuum response for the CFM and the roving layers. The micromechanical models are integrated with plane-strain or plane-stress 2D continuum finite element models by adding the appropriate constraints to the overall formulation. The homogenization is performed at each material point (Gaussian

integration points) in the thickness direction which is the third axis in the local material orientation system attached with each finite element. In the case where a plane stress state exists, the CFM and roving 3D micromodels are constrained to have zero out-of-plane overall average stress. Figure 2.4 shows a schematic of a pultruded cross-section with the idealized roving and CFM layers. The two micromodels are formulated using state variables in the form of average stresses and strains in their unit cells. The micromechanical equations that involve the state variables represent crude approximation of the traction and displacement continuity of the fiber and matrix phases in each layer. The material subroutine 'UMAT' of the finite element code ABAQUS (2002) is used for this purpose. The sublaminate model is used to generate an equivalent continuum response for the roving and CFM layers in a thick-section pultruded composite. This is done using in-plane and out-of-plane applied patterns of stress and strain where the stress and strain vectors for each layer are partitioned into *in-plane* and *out-of-plane* components.

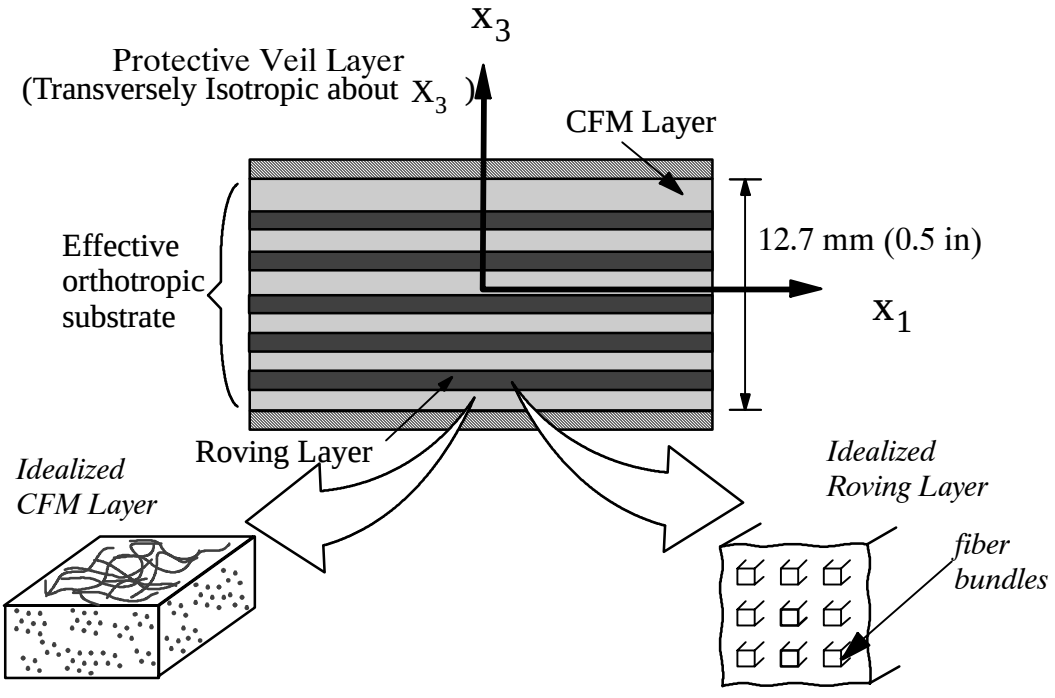

Figure 2.4 Schematic of a pultruded cross-section with idealized CFM and roving layers

The assumption of a perfect bond between adjacent layers requires displacement continuity which results in continuous in-plane strains (ϵ_{11}, ϵ_{22}, γ_{12}) across the interface between the layers. The traction continuity across the interface requires that the out-of-plane stresses (σ_{33}, τ_{13}, τ_{23}) also be continuous. As a result, the in-plane strains and out-of-plane stresses are the same throughout the sublaminate for an applied in-plane strain and out-of-plane stress. The complementary stress and strain components may differ in the roving and CFM layers. The homogenized in-plane stresses and out-of-plane strains are taken as the weighted averages, using the relative CFM and roving thicknesses. The roving and CFM sequence information is not preserved in the sublaminate model. In the case where this sequence is important, the sublaminate model is not used. Instead, the response of each layer is sampled several times through its cross section and the total response is generated by numerical integration in a ply-by-ply approach. The homogenized equivalent continuum is generated from the average response of the roving and CFM micromodels.

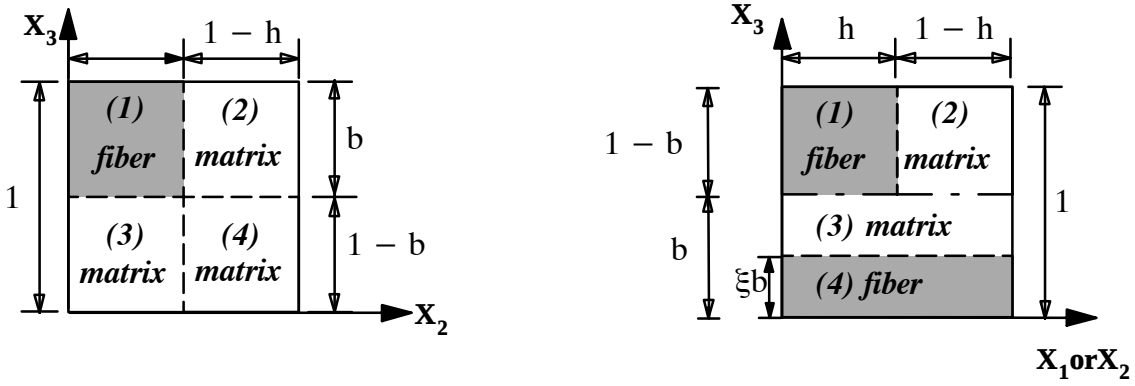

Figure 2.5 Unit-cells for the roving and CFM layers in a pultruded composite

Roving Micromodel

The unidirectional roving layer is idealized as a doubly periodic array of fibers with a rectangular cross-section embedded in the matrix. The long fibers are aligned in the x_1 direction. The traction and displacement continuity between the subcells are approximated by using the average stress and strain components of the four subcells. Figure 2.5 shows the unit cell for the roving layer in the pultruded composite. This approach is similar to Aboudi's Method of Cells (Aboudi, 1991), however, it makes the average stress and strain vectors in the subcells as the only state variables. The notation for the stress and strain vectors, defined for each of the subcells are:

$$\begin{aligned} \sigma_i^{(\alpha)} &= \left\{ \sigma_{11},\ \sigma_{22},\ \sigma_{33},\ \tau_{12},\ \tau_{13},\ \tau_{23} \right\}^T \\ \epsilon_i^{(\alpha)} &= \left\{ \epsilon_{11},\ \epsilon_{22},\ \epsilon_{33},\ \gamma_{12},\ \gamma_{13},\ \gamma_{23} \right\}^T \quad i = 1,..,6 \qquad \alpha = 1,..,4 \end{aligned} \tag{2.1}$$

where (α) denotes a subcell number and (i) denotes a stress or strain component.

Compatibility in the axial direction dictates that the average axial strains be the same in all subcells. Therefore, the longitudinal (mode-1) micromechanical relations are:

$$\begin{aligned} \epsilon_1^{(1)} &= \epsilon_1^{(2)} = \epsilon_1^{(3)} = \epsilon_1^{(4)} = \bar{\epsilon}_1^{(R)} \\ v_1\,\sigma_1^{(1)} &+ v_2\,\sigma_1^{(2)} + v_3\,\sigma_1^{(3)} + v_4\,\sigma_1^{(4)} = \bar{\sigma}_1^{(R)} \end{aligned} \tag{2.2}$$

Where $v_{(\alpha)}$ denotes the relative volume of subcell (α). Traction continuity along interfaces with normals in the x_2 direction, yields the following relations in terms of the stress components:

$$\begin{aligned} \sigma_2^{(1)} &= \sigma_2^{(2)} \qquad \sigma_4^{(1)} = \sigma_4^{(2)} \qquad \sigma_6^{(1)} = \sigma_6^{(2)} \\ \sigma_2^{(3)} &= \sigma_2^{(4)} \qquad \sigma_4^{(3)} = \sigma_4^{(4)} \qquad \sigma_6^{(3)} = \sigma_6^{(4)} \end{aligned} \tag{2.3}$$

The corresponding strain compatibility relations are:

$$\begin{aligned}
&\frac{v_1}{v_1+v_2}\,\epsilon_2^{(1)} + \frac{v_2}{v_1+v_2}\,\epsilon_2^{(2)} = \bar{\epsilon}_2^{(R)} \\
&\frac{v_3}{v_3+v_4}\,\epsilon_2^{(3)} + \frac{v_4}{v_3+v_4}\,\epsilon_2^{(4)} = \bar{\epsilon}_2^{(R)}
\end{aligned} \qquad \text{(a)}$$

$$\begin{aligned}
&\frac{v_1}{v_1+v_2}\,\epsilon_4^{(1)} + \frac{v_2}{v_1+v_2}\,\epsilon_4^{(2)} = \bar{\epsilon}_4^{(R)} \\
&\frac{v_3}{v_3+v_4}\,\epsilon_4^{(3)} + \frac{v_4}{v_3+v_4}\,\epsilon_4^{(4)} = \bar{\epsilon}_4^{(R)}
\end{aligned} \qquad \text{(b)} \qquad (2.4)$$

Traction continuity consideration for interfaces with normals in the x_3 direction, yields the following conditions for out-of-plane stress components:

$$\begin{aligned}
&\sigma_3^{(1)} = \sigma_3^{(3)} \qquad \sigma_5^{(1)} = \sigma_5^{(3)} \qquad \sigma_6^{(1)} = \sigma_6^{(3)} \\
&\sigma_3^{(2)} = \sigma_3^{(4)} \qquad \sigma_5^{(2)} = \sigma_5^{(4)} \qquad \sigma_6^{(2)} = \sigma_6^{(4)}
\end{aligned} \qquad (2.5)$$

The corresponding strain compatibility relations are:

$$\begin{aligned}
&\frac{v_1}{v_1+v_3}\,\epsilon_3^{(1)} + \frac{v_3}{v_1+v_3}\,\epsilon_3^{(3)} = \bar{\epsilon}_3^{(R)} \\
&\frac{v_2}{v_2+v_4}\,\epsilon_3^{(2)} + \frac{v_4}{v_2+v_4}\,\epsilon_3^{(4)} = \bar{\epsilon}_3^{(R)}
\end{aligned} \qquad \text{(a)}$$

$$\begin{aligned}
&\frac{v_1}{v_1+v_3}\,\epsilon_5^{(1)} + \frac{v_3}{v_1+v_3}\,\epsilon_5^{(3)} = \bar{\epsilon}_5^{(R)} \\
&\frac{v_2}{v_2+v_4}\,\epsilon_5^{(2)} + \frac{v_4}{v_2+v_4}\,\epsilon_5^{(4)} = \bar{\epsilon}_5^{(R)}
\end{aligned} \qquad \text{(b)} \qquad (2.6)$$

Finally, the transverse strain compatibility relation cannot be exactly satisfied for all components. Instead, the average overall relation is used in the form:

$$v_1\,\epsilon_6^{(1)} + v_2\,\epsilon_6^{(2)} + v_3\,\epsilon_6^{(3)} + v_4\,\epsilon_6^{(4)} = \bar{\epsilon}_6^{(R)} \qquad (2.7)$$

CFM Micromodel

The CFM phenomenological model generates the 3D equivalent response from a weighted average of two simplified unidirectional models consisting of matrix and fiber dominated modes. The two parts of the CFM model can be combined to form a one 4-subcell model. Figure 2.5 shows the unit cell for the CFM layer in the pultruded composite. The matrix-mode layer (part-A) is composed of subcells (1) and (2), while the fiber-mode layer (part-B) is composed of subcells (3) and (4). The out-of-plane thickness direction is taken in the x_3 axis. The formulation is presented in terms of average stress and strains of subcells A and B for convenience. The fiber volume fractions within these parts is the same as the CFM. This introduces the following relations:

$$\frac{v_1}{v_1 + v_2} = h = v_{f_C} \qquad \frac{v_4}{v_3 + v_4} = \xi = v_{f_C} \tag{2.8}$$

The out-of-plane traction and displacement continuity between the two parts are:

$$\sigma_o^{(A)} = \sigma_o^{(B)} = \overline{\sigma}_o^{(C)} \qquad \varepsilon_i^{(A)} = \varepsilon_i^{(B)} = \overline{\varepsilon}_i^{(C)} \tag{2.9}$$

The weighted averages of the in-plane stresses and out-of-plane strains are:

$$\overline{\sigma}_i^{(C)} = \frac{1}{v}\left(v_A\, \sigma_i^{(A)} + v_B\, \sigma_i^{(B)} \right) \qquad \overline{\varepsilon}_o^{(C)} = \frac{1}{v}\left(v_A\, \varepsilon_o^{(A)} + v_B\, \varepsilon_o^{(B)} \right) \tag{2.10}$$

In the matrix-mode (part-A), the average stresses in the fiber and matrix are the same, while the average strain is taken as the volume average of the two:

$$\overline{\sigma}^{(A)} = \sigma^{(1)} = \sigma^{(2)} \qquad \overline{\varepsilon}^{(A)} = \frac{1}{v_A}\left(v_1\, \varepsilon^{(1)} + v_2\, \varepsilon^{(2)} \right) \tag{2.11}$$

The analogous relations for the fiber-mode in part-B are:

$$\begin{aligned} \sigma_o^{(3)} &= \sigma_o^{(4)} = \overline{\sigma}_o^{(B)} & \overline{\sigma}_i^{(B)} &= \frac{1}{v_B}\left(v_3\, \sigma_i^{(3)} + v_4\, \sigma_i^{(4)} \right) \\ \varepsilon_i^{(3)} &= \varepsilon_i^{(4)} = \overline{\varepsilon}_i^{(B)} & \overline{\varepsilon}_o^{(B)} &= \frac{1}{v_B}\left(v_3\, \varepsilon_o^{(3)} + v_4\, \varepsilon_o^{(4)} \right) \end{aligned} \tag{2.12}$$

Numerical Implementation

The proposed micromodels are implemented as a nested set of nonlinear constitutive models in a displacement-based FE code (Abaqus, 2000). A plane-strain constraint is imposed on the top level sublaminate model to force a zero out-of-plane strain for the effective continuum when the constitutive models are used for 2D FE fracture simulations. The fiber subcells are linear while the matrix is considered as nonlinear. J2 deformation plasticity is used for the matrix with the Ramberg-Osgood uniaxial stress-strain representation:

$$\gamma = \frac{\tau}{G} + \beta\left(\frac{\tau}{\tau_o}\right)^n. \tag{2.13}$$

Where γ and τ are the shear strain and stress respectively. G is the matrix initial shear modulus and β, τ_o, n are the three nonlinear parameters. The micromechanical relations are implemented in an incremental form. Initially, linearized (tangential) relations are used to predict the incremental strains at all fiber and matrix subcells in both roving and CFM micromodels. For a given finite strain increment, the tangential stresses and strains are likely to violate the nonlinear constitutive relations in the matrix subcells. In order to satisfy the actual stress-strain relationships as well as the approximate traction and compatibility constraints, a stress update algorithm is used (Haj-Ali and Pecknold, 1996). Both stiffness-based and compliance-based correction schemes are incorporated for the different levels of the micromodels. The stress update algorithm at a given level usually consists of two steps: a predictor step, which may be a tangential or a trial elastic predictor, followed by a correction step, in which the trial elastic state is adjusted in order to arrive at accurate stress values. Using a predictor step alone, without subsequent corrections, may lead to unacceptable accumulation of error.

2.3 Material Coupon Tests

Material tests were performed to establish the calibration and confirm the predictions of the applied micromechanical models. The off-axis coupon tests conducted were used to generate the initial effective elastic properties and the nonlinear stress-strain response. The coupon tests were conducted according to ASTM D 3039 (2000) and ASTM D3410 (1995). The coupons were made from a 1525 Pultex series FRP flat sheet manufactured by Creative Pultrusions Inc. (2000). Different geometries were used for the tension and compression coupons in order to prevent buckling during the compression tests. The tension coupons were 305 x 32 x 12 mm (12 x 1.25 x 0.48 in) and the compression coupons were 190 x 32 x 12 mm (7.5 x 1.25 x 0.48 in). The load was applied using an MTS 810 servo-hydraulic test system with a 22.2 kN (50 kip) capacity. The tests were conducted in a displacement control mode with a rate of 0.5 mm/min. The accuracy of the acquired strains is within $\pm$ 50 microstrains and the load is within $\pm$ 0.22 kN (50 lb). To reduce torsional stresses from misalignment of the grips, a steel plate with a high torsional stiffness was used to align the grips. Foil strain gages were used to record the strains on both sides of the specimen. The shear forces and bending couples at the grips result in a limited error at the location of strain measurement of less than 1%, (Kilic, 2001). The coupons were gripped along a length of 64 mm (2.5 in) from the ends. The coupons were gripped along a length of 64 mm (2.5 in) from the ends. The grip pressure was controlled at 14 MPa (2 ksi) to prevent the coupons from slipping and from high stresses developing at the grips. Most of the tested coupons failed at the center indicating that the grips did not significantly affect the failure mode. The grip pressure was controlled at 14 MPa (2 ksi) to prevent the coupons from slipping and from high stresses developing at the grips. Most of the tested coupons failed at the center indicating that the grips did not significantly affect the failure mode.

2.4 Calibration of Micromechanical Models

The CFM and roving micromodels are calibrated by assuming the same linear and nonlinear in-situ properties for the fiber and matrix subcells (Table 2.1). These are taken from known or assumed values. In addition the fiber volume fractions and the thicknesses of the CFM and roving layers are needed to complete the linear calibration. Results from the coupon tests were used to calibrate the nonlinear stress-strain behavior of the pultruded composite. In the off-axis coupon tests, the nonlinear responses begin at a very low strain. The test responses from the transverse coupons ($\theta = 90^0$) were used to calibrate the nonlinear matrix behavior. The Ramberg-Osgood in-situ parameters for the matrix constituents in Equation (2.13) are calibrated from the overall nonlinear behavior of these transverse coupons. The matrix Ramberg-Osgood stress-strain relationship is calibrated by varying its parameters until the overall effective response is matched. A lower bound biased calibration was performed on the experimental results from the tension tests. Table 2.1 shows the typical mechanical properties of the E-glass fiber and the polyester matrix used to calibrate the models. Figure 2.6 shows the calibration curve of the micromodel in tension. The nonlinear model calibration (solid line) and the extension of the linear response (dashed line) illustrate the need for a nonlinear material model. Figure 2.7 shows the calibration of the compression response from compression tests on transverse coupons. The second calibration for compression may be required in some cases because of the different material response in this mode. Throughout this document only the tensile calibration is used because crack growth conditions occur primarily under tensile loads.

Table 2.1 Elastic properties and matrix nonlinear Ramberg–Osgood parameters, fiber volume fraction in: roving layers = 0.407 , CFM layers = 0.305

	E *(ksi)*	ν	β	n	τ_o *(ksi)*
Fiber (E–glass)	10500	0.25	–	–	–
Matrix (Tension) (Polyester + Fillers)	630	0.30	4.0	2.0	6.0
Matrix (Compression) (Polyester + Fillers)	630	0.30	3.0	4.0	4.0

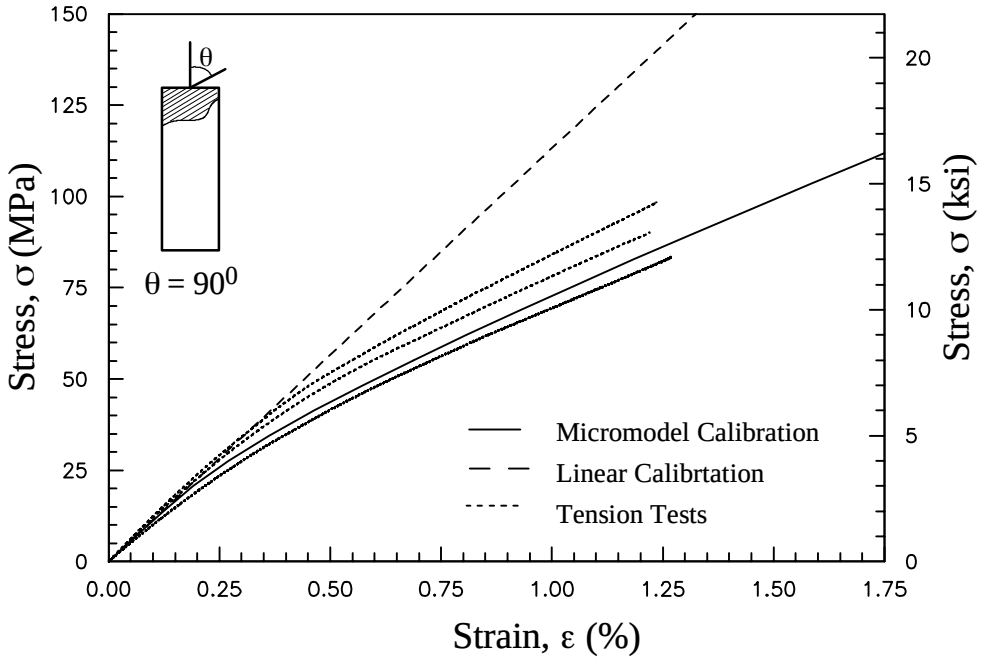

Figure 2.6 Calibration of nonlinear behavior from transverse coupons in tension

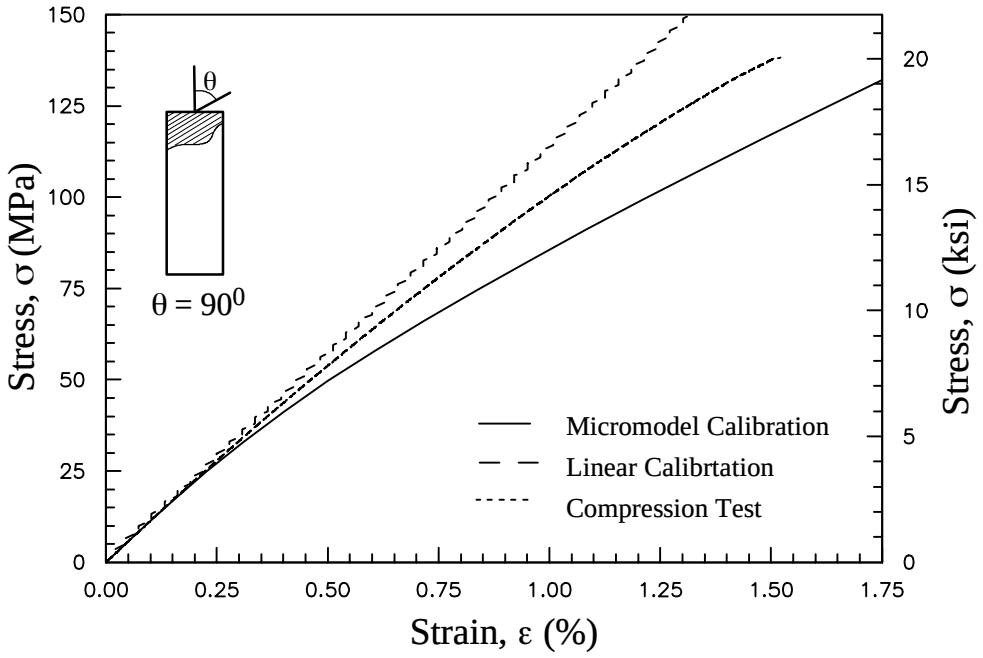

Figure 2.7 Calibration of nonlinear behavior from transverse coupons in compression

2.5 Prediction of Initial Stiffness and Nonlinear Response

Once the nonlinear response is calibrated, the model is ready to predict the pultruded material response under multi-axial stress states. The predicted effective moduli and Poisson's ratios of the pultruded material, from the roving/CFM sublaminate model, are reported in Table 2.2. The predicted values from the present analytical model compare favorably with those obtained experimentally. The lower experimental values of Young's modulus in tension are due to opening of existing voids and microcracks. Further, the fillers that are usually added to the matrix may be one of the reasons contributing to the different response in tension and compression.

Table 2.2 Predicted and experimental cross-section elastic properties

	E_1	E_2	E_3	G_{12}	G_{13}	G_{23}	ν_{12}	ν_{13}	ν_{23}
	GPa (Msi)								
Experimental (T)	17.1 (2.484)	9.96 (1.444)	- -	3.50 (0.507)	- -	- -	0.283	-	-
Experimental (C)	18.1 (2.627)	10.9 (1.582)	- -	3.58 (0.520)	- -	- -	0.291	-	-
Micromodel	18.8 (2.730)	11.3 (1.641)	7.79 (1.130)	4.20 (0.609)	2.60 (0.377)	2.46 (0.357)	0.273	0.295	0.319

The stress-strain results from coupon tests with roving off-axis angles ($\theta = 0^0, 15^0, 30^o, 45^0, 60^0$, and 90^0) were used to verify the micromodel predictions for both the initial stiffness and the complete stress-strain response. Figure 2.8 shows the results in the form of the initial Young's modulus from the off-axis coupons in tension and compression. The prediction of the model is plotted by the solid line. The elastic moduli are determined based on the slope of a linear regression line for the data between 1000-3000$\mu\varepsilon$. The model provides a good prediction of the initial modulus when compared with off-axis coupon tests. The results from off-axis tension tests are lower than those obtained from compressive tests. This decrease is more pronounced as the off-axis angle increases. The difference can be attributed to material imperfections such as existing voids and microcracks and the presence of fillers in the matrix. These imperfections are not accounted for in the current formulation. This explains the upper bound curve predicting the initial modulus for the different off-axis angles.

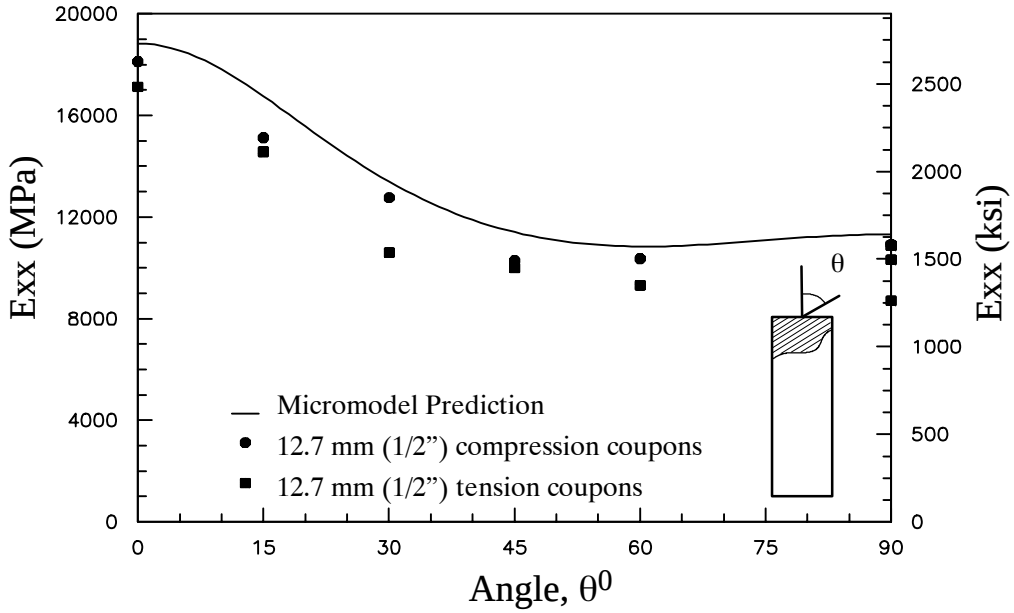

Figure 2.8 Prediction of initial Young's modulus of off-axis coupons tested in tension and compression.

Figure 2.9 shows the ability of the model to predict the complete nonlinear stress-strain response for general in-plane multi-axial states from the off-axis coupon tests. The last point in the plotted results is the ultimate failure point. Nonlinearity exists even in the 0^0 direction which corresponds to the stiffest response of the material. This is due to the relatively low overall fiber volume fraction in the tested material. The stress-strain curves for the 30^0, 45^0, 60^0, and 90^0 off-axis coupon tests are highly nonlinear. The larger nonlinearity in tension is expected because of the opening of existing voids and microcracks under tensile load. Figure 2.10 shows the prediction of the models on off-axis compression tests when using the compression test calibration parameters. The nonlinear prediction capability of the model compares very well with the test results. The results from the tension and compression tests confirm the validity of the proposed nonlinear micromechanical models for use in the E-glass/polyester thick-section FRP pultruded composite.

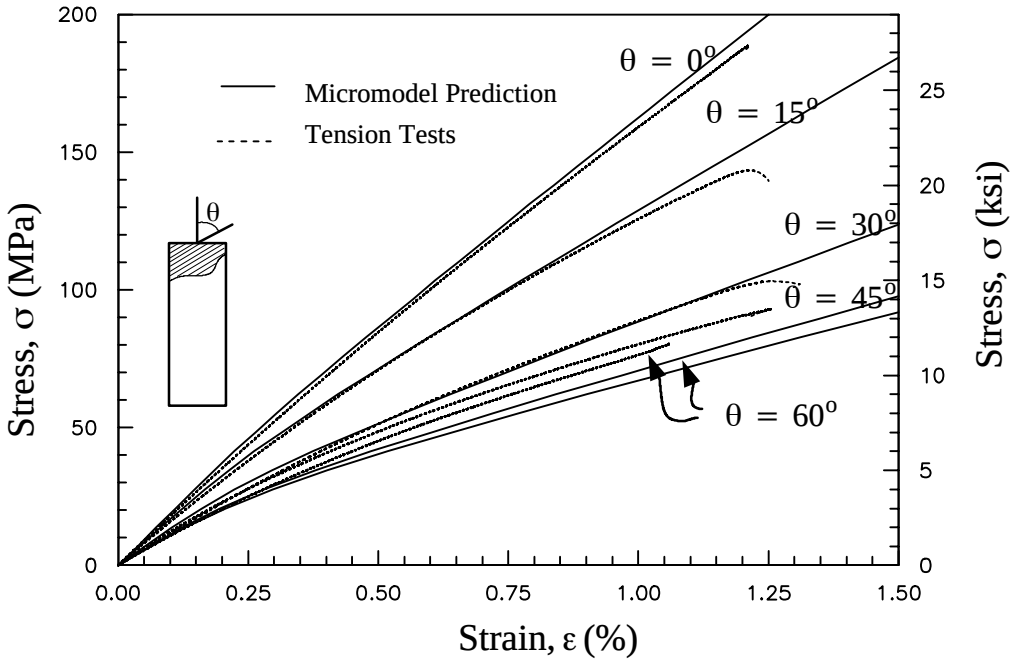

Figure 2.9 Prediction of the tensile axial stress–strain response for different E-glass/polyester off-axis tests

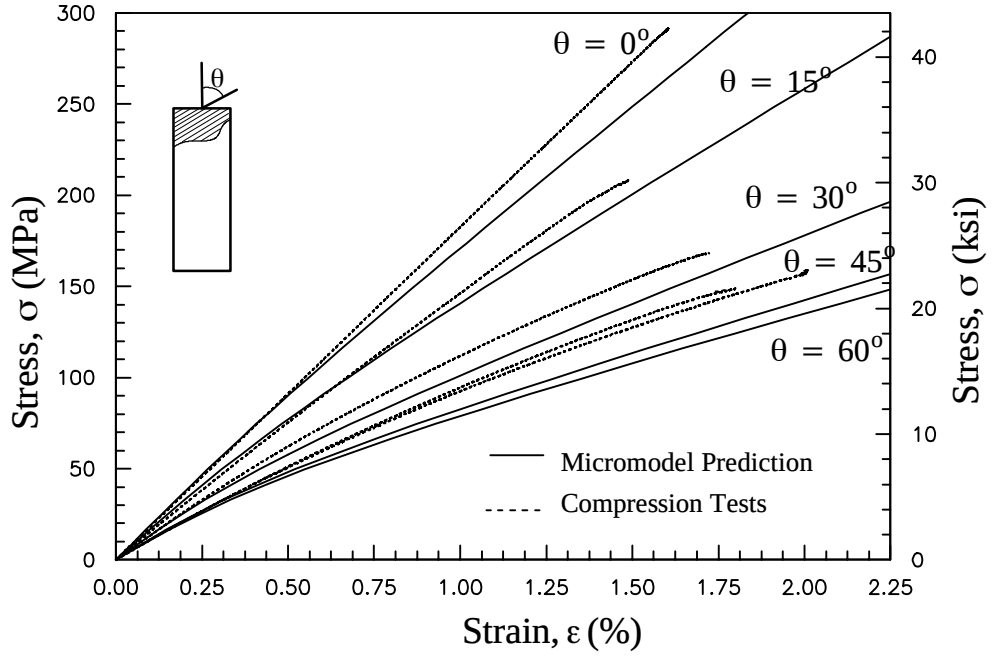

Figure 2.10 Prediction of the compressive axial stress–strain response for different E-glass/polyester off-axis tests

CHAPTER 3

A QUANTITATIVE THERMOELASTIC STRAIN ANALYSIS METHOD

A new experimental (quantitative) thermoelastic stress/strain analysis (TSA) technique is proposed to measure the sum of the direct surface strains in FRP pultruded and other thick-section composites. The new method can be used to verify computational models by providing a full-field measurement of the strain (or stress) invariant. The surface of the composite material tested is coated with an in-plane transversely isotropic (or fully isotropic) layer. The infrared (IR) signal from the coat is measured while the specimen is loaded and a combined material factor, comprised of mechanical and thermal properties, is calibrated such that the measured IR signal can be related to the sum of the in-plane direct strains. The theoretical derivation of this new method assumes adiabatic conditions and applies a thermomechanical theory to the case of multi-layered composite materials. The proposed method is validated by its application to thick-section pultruded E-glass/polyester, E-glass/vinylester, and woven carbon/epoxy composites. This method is also applied in subsequent chapters to examine the full-field deformation in the proposed fracture specimens.

3.1 Theoretical Derivation

The proposed formulation directly relates the TSA signal to the sum of the direct strains in a coated, layered composite medium. A perfect bond between all layers is assumed. The thermomechanical material response of the coat is considered linear elastic and independent of the mean applied stress and loading frequency. Figure 3.1 schematically illustrates a typical layered composite with surface coats and different orthotropic layers. If the elastic stiffness of the coat is small compared to the overall stiffness, the measured mechanical response is primarily due to the substrate. While assuming that the coat is responsible for the thermoelastic response, the TSA signal is interpreted to represent the change in the sum

of the direct in-plane strains of each layer. The new material constant that is derived relates the TSA signal to the change of the strains and can be calibrated experimentally from uniform TSA measurements when the strains are known.

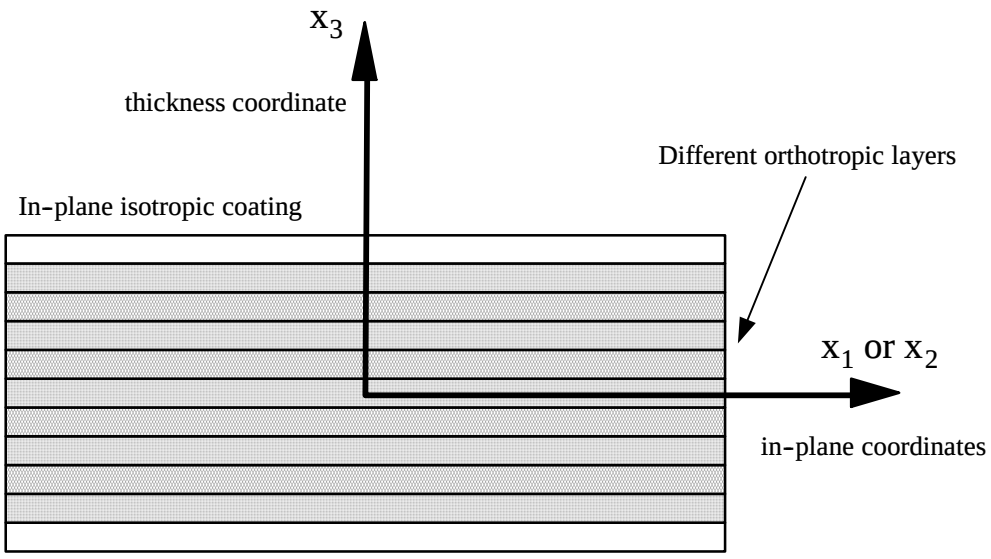

Figure 3.1 Schematic cross-sectional view of a layered orthotropic composite with coatings

Displacement continuity between the layers results in the same in-plane strains in all the layers when uniform in-plane loading is applied. The traction continuity will lead to the composite and surface layer having the same uniform out-of-plane stresses. The 3D lamination theory (Pagano, 1974), is used in this formulation to enforce traction and displacement continuity between the layers. This allows defining equivalent linear anisotropic stress-strain relations for the substrate. A basic equation governing the thermoelastic effect is given by (Wong, 1987):

$$Q_{i,i} = T \frac{\partial \sigma_{ij}}{\partial T} \dot{\varepsilon}_{ij} - \rho_o C_\varepsilon \dot{T} + \rho_o \dot{R} \qquad (3.1)$$

Where Q_i is the heat flux through the surface whose outward directed normal is n_i, T is temperature, σ_{ij} is the stress tensor, ε_{ij} is the strain tensor, ρ_o is the density, C_ε is the specific heat at constant deformation, and $\dot{R}$ is the heat production rate per unit mass of the internal

heat sources. The thermomechanical constitutive law for a linear anisotropic material is given by Hooke's law:

$$d\sigma_{ij} = C_{ijkl}d\varepsilon_{kl} - C_{ijmn}\alpha_{mn}dT \tag{3.2}$$

Where, C_{ijkl} is the fourth rank tensor of the material constants, α_{mn} are the coefficients of thermal expansion and dT is the change in temperature. If the material properties are assumed to remain constant with change in temperature, then the stress change in temperature is simply:

$$\frac{\partial \sigma_{ij}}{\partial T} = - C_{ijmn}\alpha_{mn} \tag{3.3}$$

Assuming adiabatic conditions and the absence of internal heat sources $Q_{i,i} = 0$, and $\dot{R} = 0$, Equations (3.3) and (3.1) are combined to give:

$$\rho_o C_\varepsilon \frac{\dot{T}}{T} = - C_{ijmn}\alpha_{mn}\dot{\varepsilon}_{ij} \tag{3.4}$$

Next, assuming small strain theory, and using the incremental form of Equation (3.2) to express for $C_{ijmn}d\varepsilon_{ij}$, Equation (3.4) is rewritten as:

$$\rho_o C_\varepsilon \frac{dT}{T} = - \alpha_{mn}[d\sigma_{mn} + C_{mnpq}\alpha_{pq}dT] \tag{3.5}$$

For the special case of an in-plane transversely isotropic coat under a state of plane stress, the in-plane material properties are equal, $\alpha_{11} = \alpha_{22} = \alpha$, $C_{11pq} = C_{22pq}$, $d\sigma_{33} = 0$. Placing theses conditions on Equation (3.5), it is then seen that the thermoelastic effect is dependent only on the in-plane properties:

$$\left[\frac{\rho_o C_\varepsilon}{T} + C_{mnpq}\alpha_{mn}\alpha_{pq}\right]dT = - (\alpha_{11}d\sigma_{11} + \alpha_{22}d\sigma_{22}) = - \alpha(d\sigma_{11} + d\sigma_{22}) \tag{3.6}$$

The general stress-strain relation for the in-plane isotropic coat is:

$$\begin{Bmatrix}\sigma_{11}\\ \sigma_{22}\\ \sigma_{33}\\ \tau_{23}\\ \tau_{13}\\ \tau_{12}\end{Bmatrix} = \begin{bmatrix} C_{11} & C_{12} & C_{13} & 0 & 0 & 0 \\ C_{12} & C_{11} & C_{13} & 0 & 0 & 0 \\ C_{13} & C_{13} & C_{33} & 0 & 0 & 0 \\ 0 & 0 & 0 & C_{44} & 0 & 0 \\ 0 & 0 & 0 & 0 & C_{44} & 0 \\ 0 & 0 & 0 & 0 & 0 & (C_{11}-C_{12})/2 \end{bmatrix} \begin{Bmatrix}\varepsilon_{11}\\ \varepsilon_{22}\\ \varepsilon_{33}\\ \gamma_{23}\\ \gamma_{13}\\ \gamma_{12}\end{Bmatrix} \tag{3.7}$$

The plane stress assumption in this layer enables expressing the out-of-plane strain ε_{33} in terms of the in-plane strain components:

$$\varepsilon_{33} = -\frac{C_{13}}{C_{33}}(\varepsilon_{11}+\varepsilon_{22}) = -\frac{C_{13}}{C_{33}}\varepsilon_{\alpha\alpha}\ ; \qquad \alpha = 1,2 \tag{3.8}$$

Therefore, the first stress invariant can be expressed as:

$$\Delta\sigma = \sigma_{\alpha\alpha} = \sigma_{11}+\sigma_{22} = \frac{\left(C_{11}C_{33}+C_{12}C_{33}-2C_{13}^{2}\right)}{C_{33}}(\varepsilon_{11}+\varepsilon_{22}) \tag{3.9}$$

From an experimental perspective, the infrared detector measures an un-calibrated TSA signal, S, that is linearly related to the radiant photons emitted due to a surface temperature change ($S \propto \Delta T/T \propto \Delta\sigma$). Equation (3.6) can be used to relate the TSA signal to the incremental change of the first stress invariant through a parameter k_σ:

$$\Delta\sigma = k_\sigma\ S \tag{3.10}$$

Substituting Equation (3.9) into (3.10) results in:

$$\frac{\left(C_{11}C_{33}+C_{12}C_{33}-2C_{13}^{2}\right)}{C_{33}}(\Delta\varepsilon_{11}+\Delta\varepsilon_{22}) = k_\sigma\ S \tag{3.11}$$

Next, the above elastic constants of the surface layer are used to relate the TSA signal to the direct in-plane strains instead of the stress invariant. This is important since all orthotropic layers have the same in-plane strains in a medium subjected to in-plane loading. A new constant k_ε can then be defined as:

$$k_\varepsilon = \frac{C_{33}}{\left(C_{11}C_{33} + C_{12}C_{33} - 2C_{13}^{2}\right)}\ k_\sigma \qquad (3.12)$$

This enables formulating a new thermoelastic equation, similar to Equation (3.10), in terms of the in-plane strains using the new relationship:

$$\Delta\varepsilon_{\alpha\alpha} = k_\varepsilon\ S \qquad \alpha = 1, 2 \qquad (3.13)$$

3.2 Experimental Setup

A DeltaTherm DT1500 thermoelasticity measurement system was used to acquire the thermal measurements. The camera's infrared array detector synchronized with the applied cyclic loading enables the detection of the transient thermoelastic effect. The infrared detector acts as a transducer, which converts the incident radiant energy into electrical signals. The IR camera has a thermal resolution of at least 1mK for image exposure times of one minute or less and can capture images at rates of more than 400 frames per second (DeltaTherm, 2001). A lock-in analyzer (a signal-processing unit) extracts the thermoelastic information from the detector's output signal by using the reference signal from the loading device (Figure 3.2). The reference signal is usually taken as the signal from the load cell of the testing machine. The lock-in analyzer uses the reference signal of the cyclic response to reject any non-stress thermal emissions. The loading frequency should also be high enough to prevent heat transfer due to stress gradients during the load cycle. Figure 3.3 shows an IR camera used to observe a test specimen during a typical TSA test. The tested specimen are usually coated with black paint (Krylon Ultra Flat) to improve the surface emissivity. With an emissivity of 94 percent, the paint maintains this emissivity from point to point within 2 percent out to a view angle of around 20 degrees from the surface (Oliver, 1988). The cyclic load is applied to the test specimen using an MTS 810 servo-hydraulic test system with a 22.2 kN (50 kip) capacity and an accuracy of $\pm$ 0.22 kN (50 lb). The applied load signal is used to integrate synchronized TSA images

that correspond to peak values of loading. The integration of the captured images is a temporal smoothing process performed over a specified period.

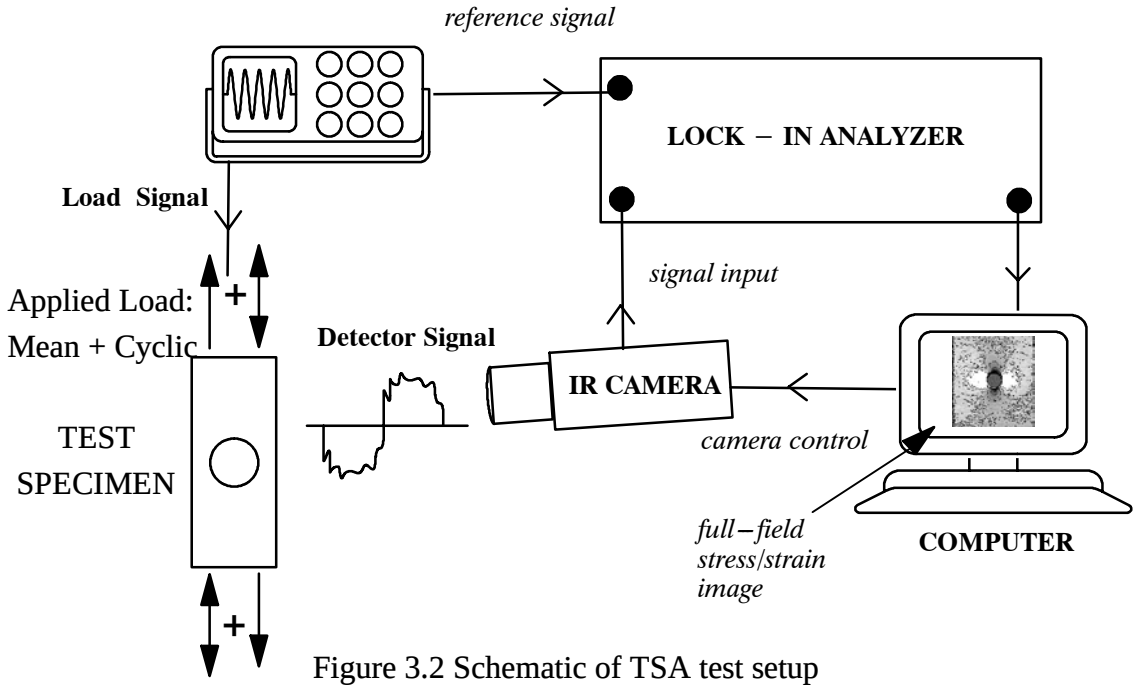

Figure 3.2 Schematic of TSA test setup

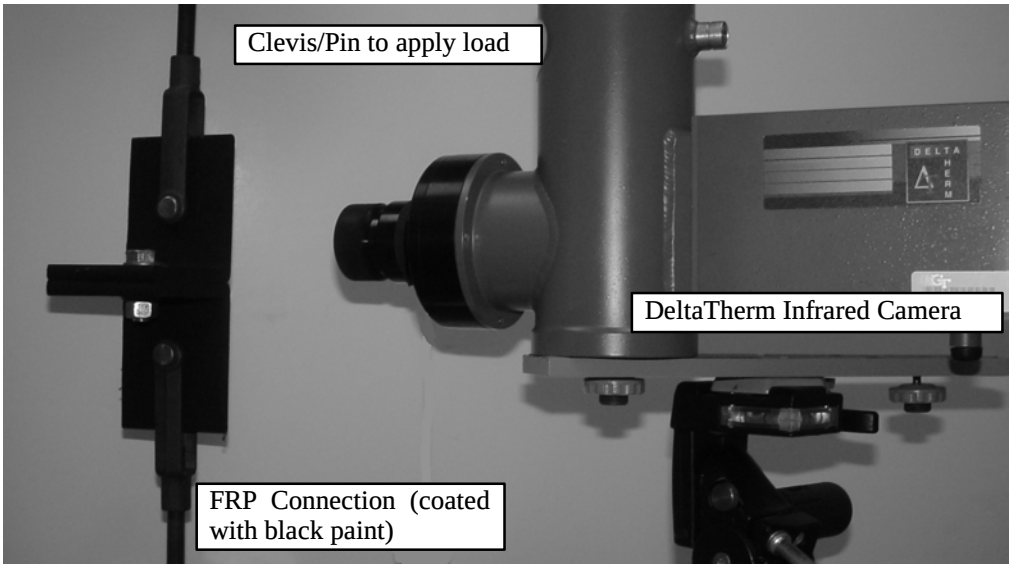

Figure 3.3 Infrared camera used to observe a specimen during a TSA test

3.3 Validation of TSA Technique on Pultruded Composites

The proposed TSA method was calibrated for E-glass/polyester and E-glass/vinylester pultruded FRP composite systems. The pultruded coupons were tested with the load applied parallel and transverse to the roving direction. The mechanical properties of the tested coupons are shown in Table 3.1. The tension coupons were 44.4 mm (1.75 in.) wide, had 152.4 mm (6 in.) ungripped length and a thickness of 12.2 mm (0.48 in.). Biaxial strain gages were oriented in the material directions to measure the surface strains. The TSA effect was calibrated for the linear elastic region of the stress-strain response curve (< 0.25 %) as shown in Figure 3.4. Time effects on the stress-strain response during each cyclic load application were not considered significant and the material was assumed to be under steady-state conditions.

Table 3.1 Elastic properties and tensile strength of E-glass/polyester and vinylester pultruded composites

	E_1	E_2	G_{12}	ν_{12}	σ_{ult} (axial)	σ_{ult} (transverse)
	GPa (Msi)				*MPa (ksi)*	
polyester	17.1 (2.484)	9.96 (1.444)	3.5 (0.507)	0.283	186.2 (27.0)	82.7 (12.0)
vinylester	18.2 (2.633)	10.25 (1.486)	4.45 (0.645)	0.330	244.8 (35.5)	75.85 (11.0)

Frequency and Mean Stress Effect

Coupons were also tested at different frequencies and mean stress levels to ensure that the TSA signal is uniform through these ranges. Figure 3.5 shows minor variation of the average TSA signal as a function of the applied mean stress. Axial and transverse coupons were also tested at different frequencies: 5, 10, 20, and 30 Hz. Changing the frequency did not affect the TSA signal for the tested range. Coupons with changing loading frequencies were tested by varying the stress amplitudes in order to extract the calibration relation between the TSA signal and the sum of direct strains in Equation (3.13). The test results for

the average TSA signal were taken along a horizontal line across the center of the specimen. Linear regression was used over all the test results to determine k_ε. Figures 3.6 and 3.7 show the calibration curves for the E-glass/polyester and E-glass/vinylester systems.

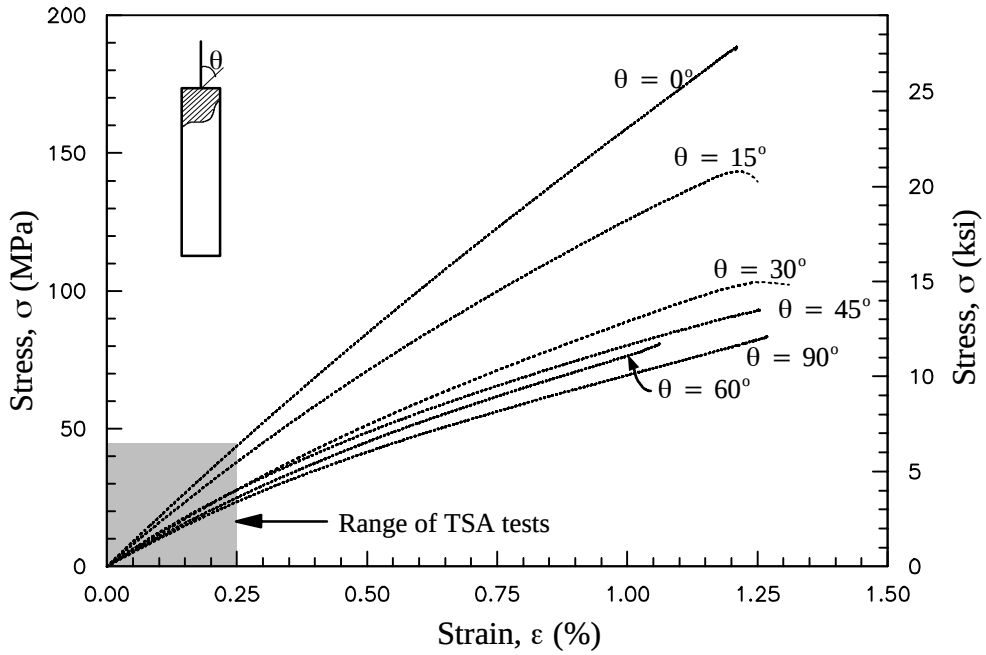

Figure 3.4 Range of calibration in relation to off-axis response from tension coupon tests on E-glass/polyester composite

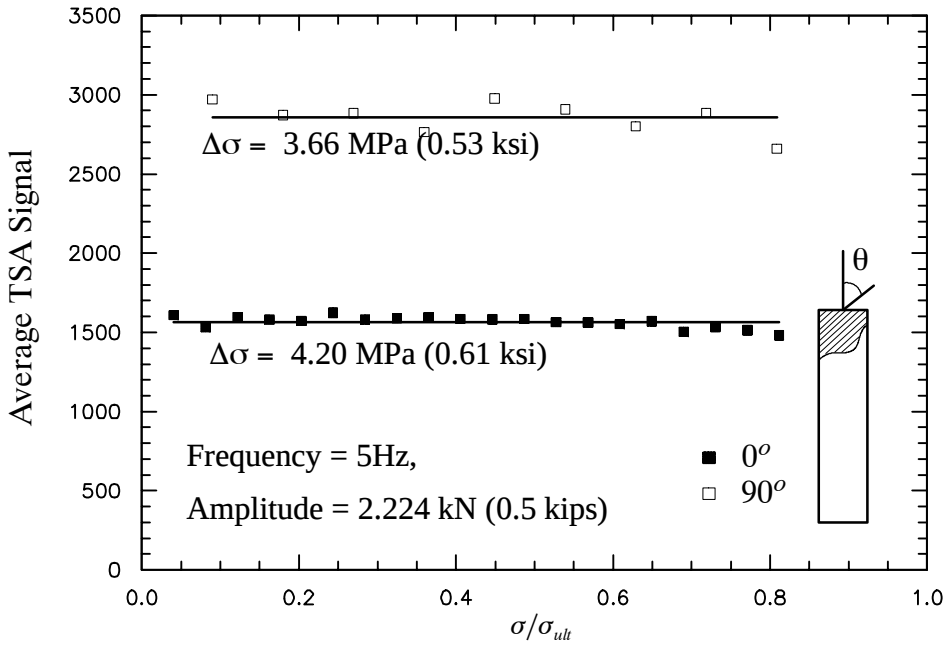

Figure 3.5 Effect of mean stress level on the TSA signal for constant amplitude tension loading for E-glass/polyester pultruded composite

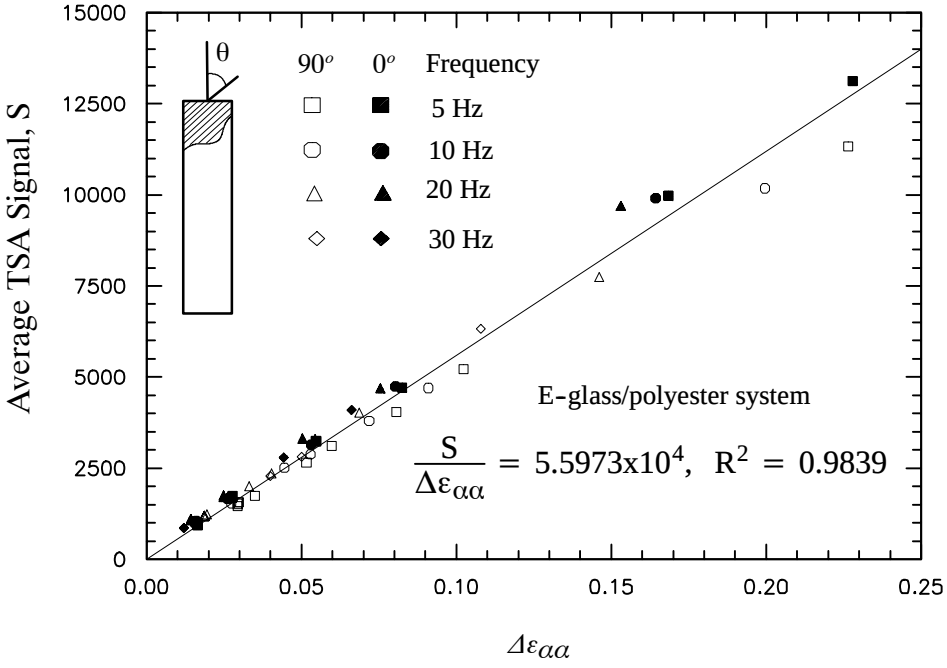

Figure 3.6 TSA calibration curve for E-glass/polyester pultruded FRP

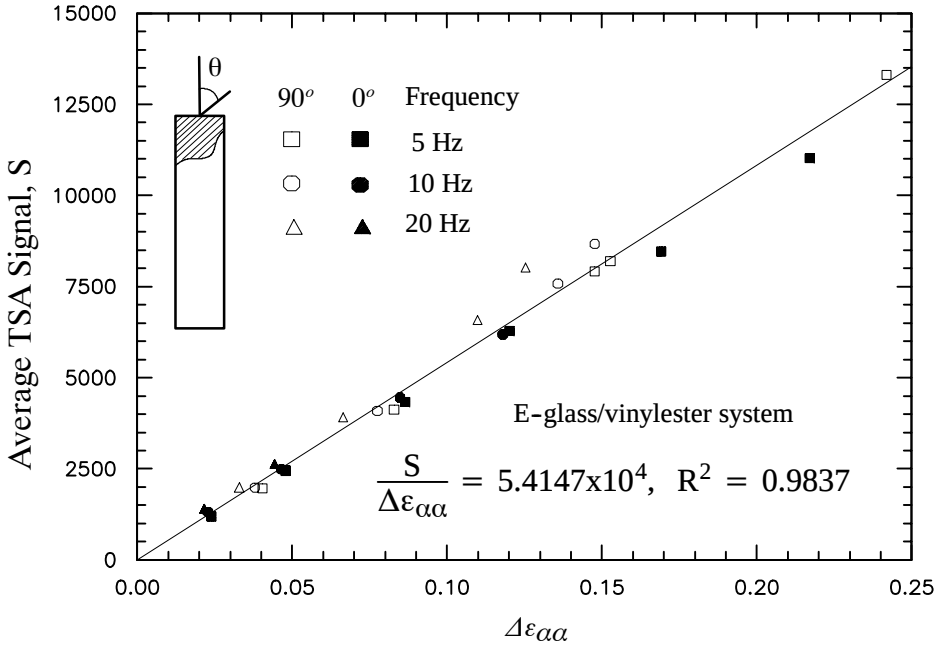

Figure 3.7 TSA calibration curve for E-glass/vinylester pultruded FRP

Validation under Multi-axial Stress States

Notched specimens with parallel and transverse roving orientations to the applied loads were tested to assess the ability of the proposed TSA method to quantitatively measure the strain fields under multi-axial stress states. The strains from the TSA method were compared to results obtained from FE simulations. The specimen geometry for the plates with a circular hole is shown in Figure 3.9. The thickness of the specimen was 12.2 mm (0.48 in) and the width was 63.5 mm (2.5 in) for the E-glass/polyester plates and 44.5 mm (1.75 in) for the E-glass/vinylester plates. The diameter of the drilled hole is 12.7 mm (0.5 in). The specimens were monotonically loaded to 4.45 kN (1 kip) and then a sinusoidal load was applied with amplitude of 2.22 kN (0.5 kips) and frequency of 5 Hz. The TSA images were integrated over a period of 3 minutes. The tests were conducted in the elastic response region. Figure 3.8 shows two TSA images of one of the specimens. The two plots are used to emphasize the predominant tension and compression responses around the circular cutout. The corresponding TSA signal in the out-of-phase range was similar in shape to Figure 3.8

but with magnitudes less than 5%. This indicates that energy dissipative effects, such as damping and damage, were small for the applied magnitudes of cyclic loading. The FE model utilized measured mechanical properties and those obtained from the overall effective linear orthotropic properties generated from the 3-D micromechanical models for pultruded composites. The formulation and calibration of the micromechanical models is discussed in Chapter 2. The FE analysis was performed using the ABAQUS (2002) FE-code on a half-model of the specimen. A mesh convergence study was performed and the converged mesh used had an average of 1500, 20-node brick elements with additional refinement around the circular hole as shown in Figure 3.9.

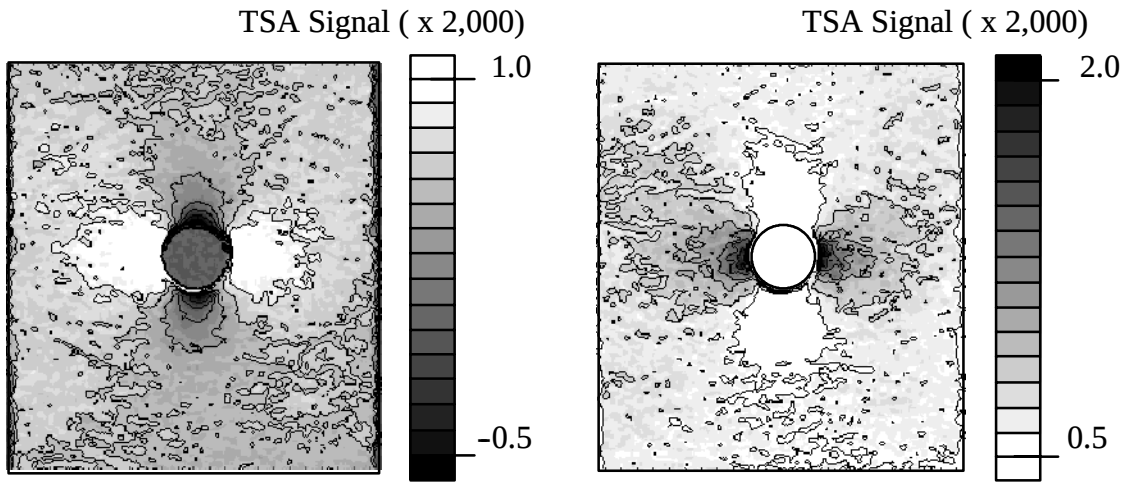

Figure 3.8 TSA images of thick-section E-glass/polyester pultruded composite

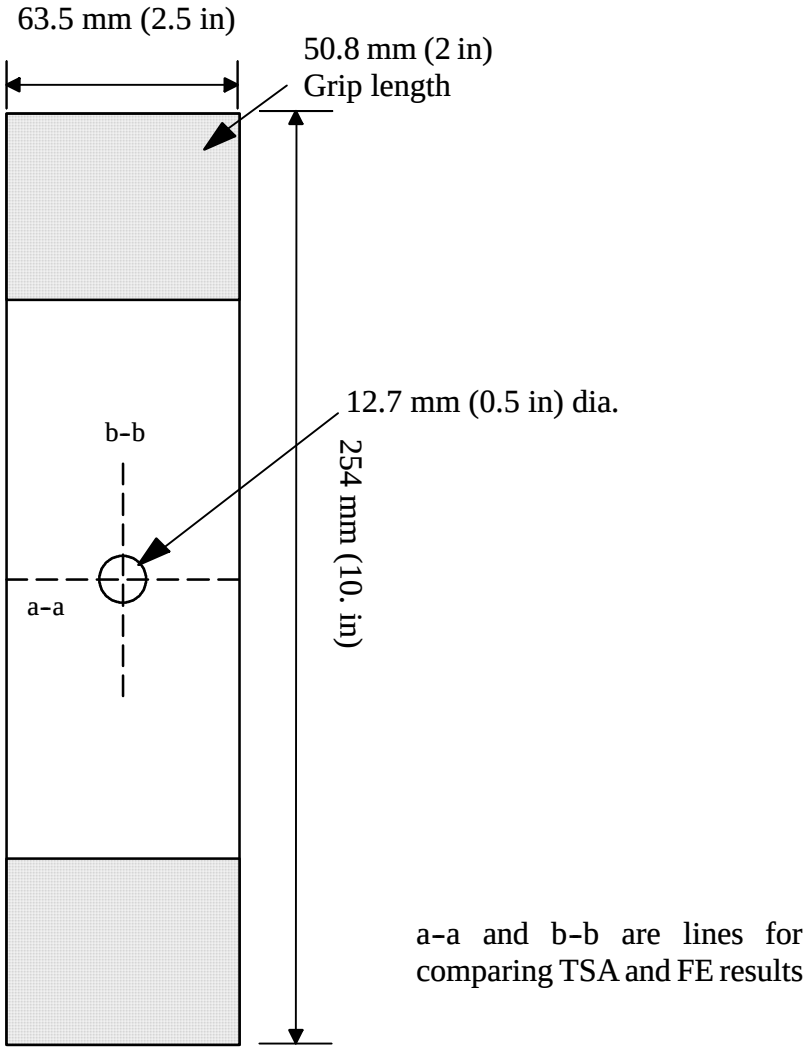

Figure 3.9 Geometry of notched test specimen used to verify the TSA technique

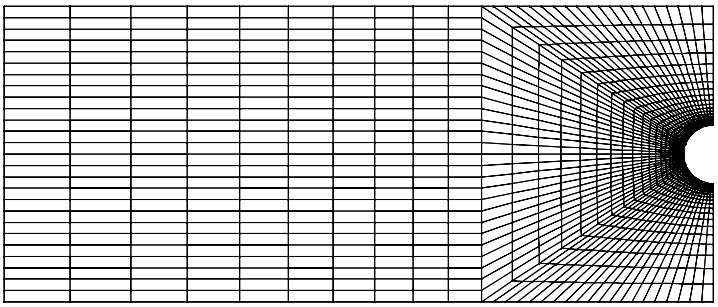

Figure 3.10 Half-model FE mesh used to model notched specimen

Figures 3.11 and 3.12 show the comparison between the predicted strains from the FE analysis and those obtained from the TSA experiments for 90^o and 0^o roving orientations for the E-glass/polyester specimen. The experimental strain quantity obtained using the TSA method are in good agreement with those from the FE results along the horizontal line a-a (Figure 3.9). Another comparison is also made along a vertical line b-b for a distance of $\pm$ W/2 from the center which includes a compressive zone near the top of the hole. Again, the TSA results are in good agreement with those obtained from the FE analysis as seen in Figures 3.13 and 3.14. Similarly, testing and FE analyses were also performed for the E-glass/vinylester material system. Figures 15 to 18 show good comparison between the measured TSA strains and the FE results.

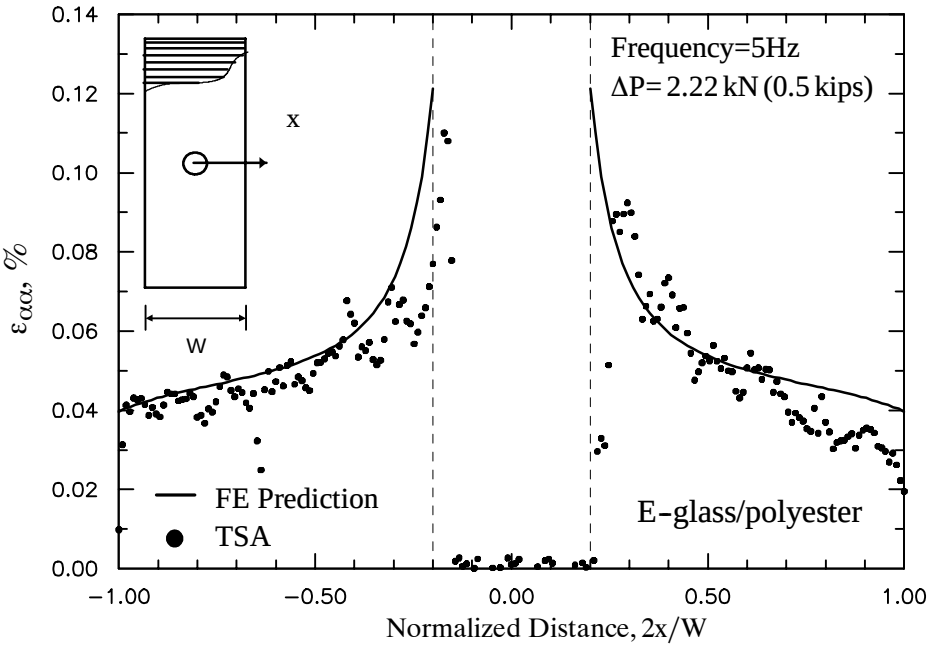

Figure 3.11 Comparison of TSA results with FE along a horizontal line from the center of a pultruded plate loaded transverse to the roving direction (E-glass/polyester)

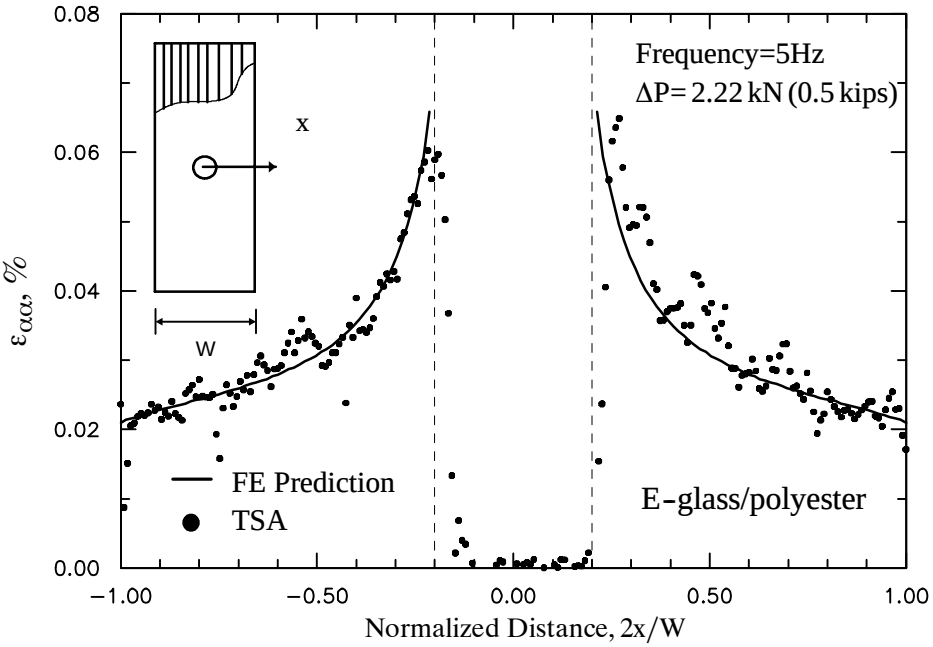

Figure 3.12 Comparison of TSA results with FE along a horizontal line from the center of a pultruded plate loaded in the roving direction (E-glass/polyester)

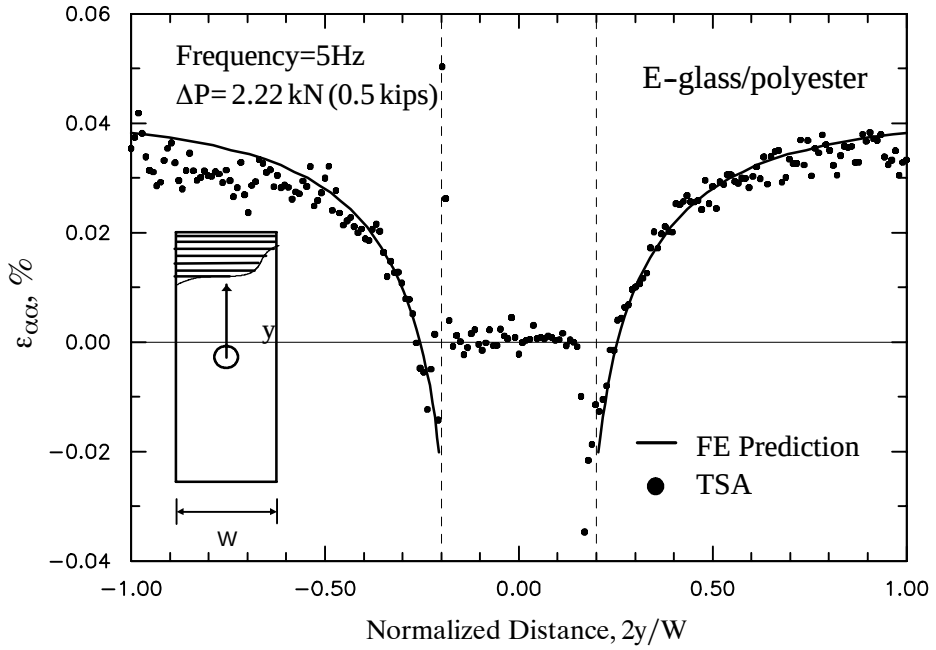

Figure 3.13 Comparison of TSA results with FE along a vertical line from the center for a pultruded plate loaded transverse to the roving direction (E-glass/polyester)

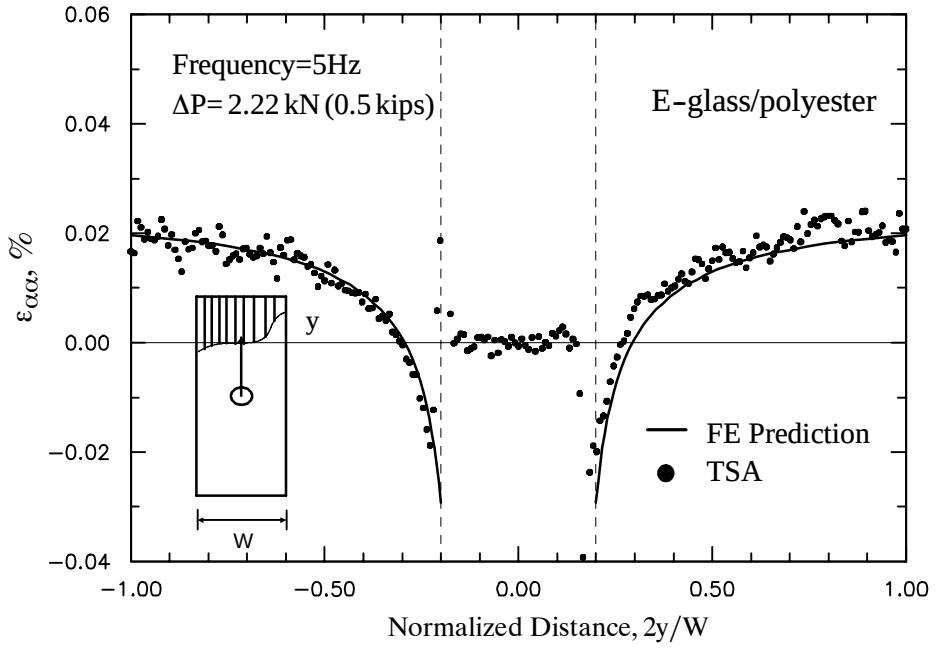

Figure 3.14 Comparison of TSA results with FE along a vertical line from the center for a pultruded plate loaded in the roving direction (E-glass/polyester)

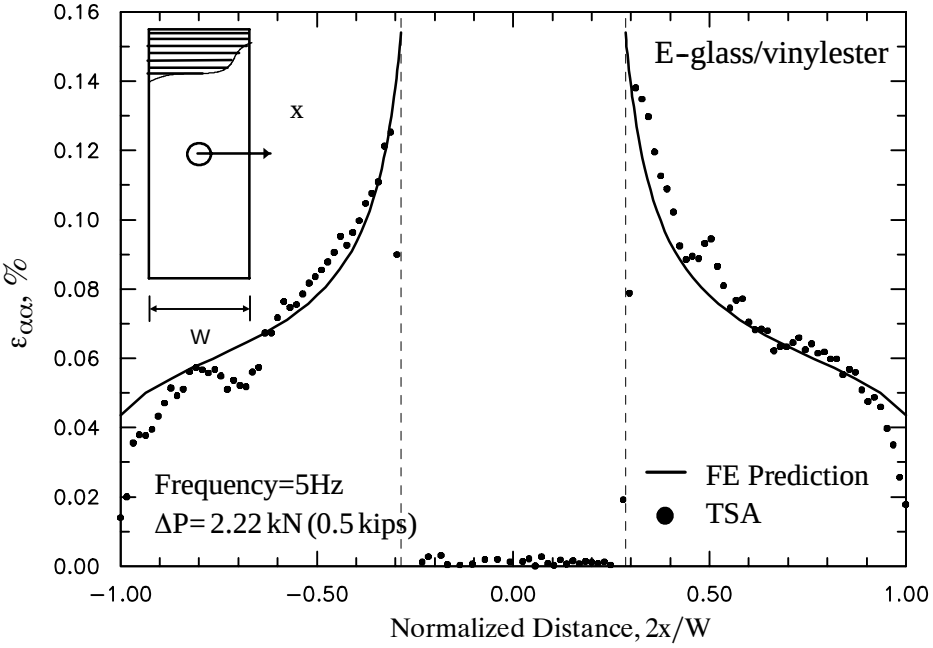

Figure 3.15 Comparison of TSA results with FE along a horizontal line from the center of a pultruded plate loaded transverse to the roving direction (E-glass/vinylester)

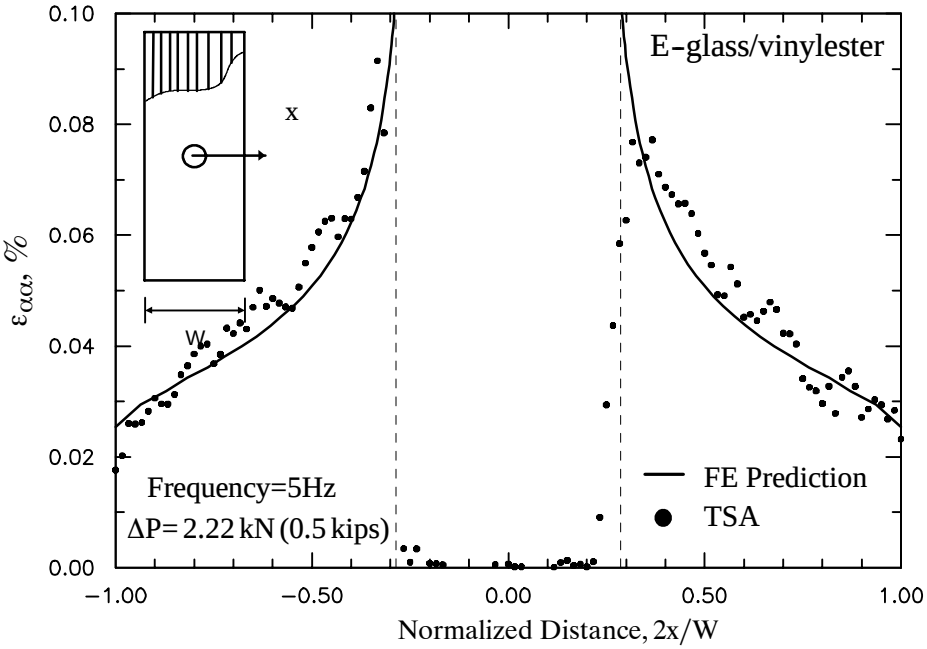

Figure 3.16 Comparison of TSA results with FE along a horizontal line from the center of a pultruded plate loaded in the roving direction (E-glass/vinylester)

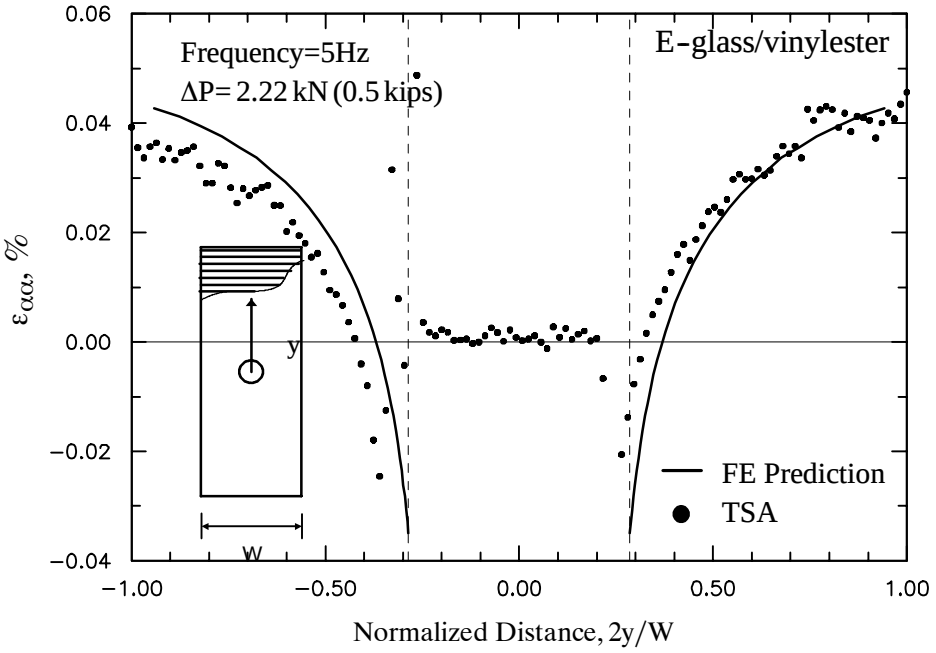

Figure 3.17 Comparison of TSA results with FE along a vertical line from the center for a pultruded plate loaded transverse to the roving direction (E-glass/vinylester)

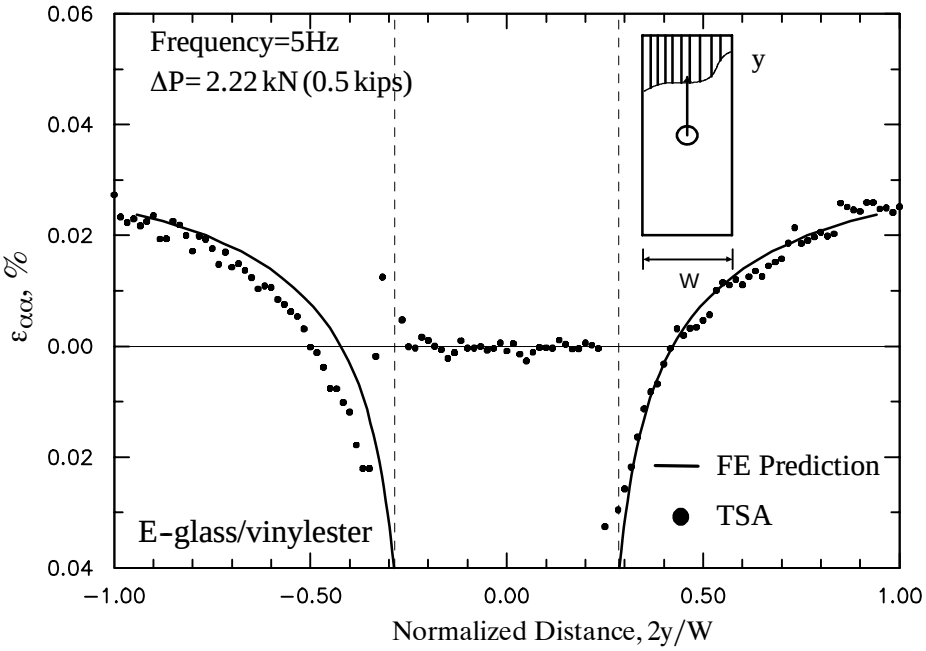

Figure 3.18 Comparison of TSA results with FE along a vertical line from the center for a pultruded plate loaded in the roving direction (E-glass/vinylester)

3.4 Validation of TSA Technique on Coated Woven Composites

A plain-weave carbon/epoxy woven composite was also used to validate the TSA method when using an applied coating to act as a 'strain witness'. Unlike the pultruded coupons, the coat on the woven composites was laminated after the composite was cured. The specimens tested were cut from a composite plate with a thickness of 2.5 mm (0.1 in). Tensile tests were conducted on woven composite coupons from this material to determine the mechanical properties. A shear test was also conducted using an Arcan-type fixture to determine the initial shear modulus. Table 3.2 shows a summary of the elastic material properties of this composite. A plastic layer of thickness 0.25 mm (0.01 in) with a reflective backing typically used for photoelastic measurements was bonded to the surface of the woven composite. The plastic coat had a Young's modulus of 2.5 GPa (360 ksi) and a Poisson's ratio of 0.38 (Vishay, 2003). Biaxial strain gages were oriented in the material directions to measure the surface strains and obtain the calibration parameter, k_ε from coupons under uniform conditions. To determine the effects on the measured signal, the TSA measurements were made at different levels of mean stress, amplitude and frequency (between 5 and 20 Hz). Figure 3.19 shows the calibration curve of the woven composite compared to that from the pultruded composite E-glass/polyester system. The calibrations are not affected by the orientation of the roving layers during the axial tests. The closeness of the calibrations between the two systems can be attributed to the similar thermomechanical properties of the two epoxy and polymer rich surfaces. The reported TSA signal represents an average of TSA measurements taken across the width of the coupon. The waviness of the plain weave pattern influences the quality and uniformity of the bond. Localized resin pockets can also degrade the observed TSA effect. However, the different responses shown in Figure 3.19 clearly indicate that the average TSA signal can be directly related to the sum of the surface strains for a wide range of frequencies.

Table 3.2 In–plane effective elastic properties of carbon/epoxy woven composite

E_1	E_2	G_{12}	ν_{12}
GPa (Msi)			
34.7 (5.033)	34.7 (5.033)	16.2 (2.352)	0.07

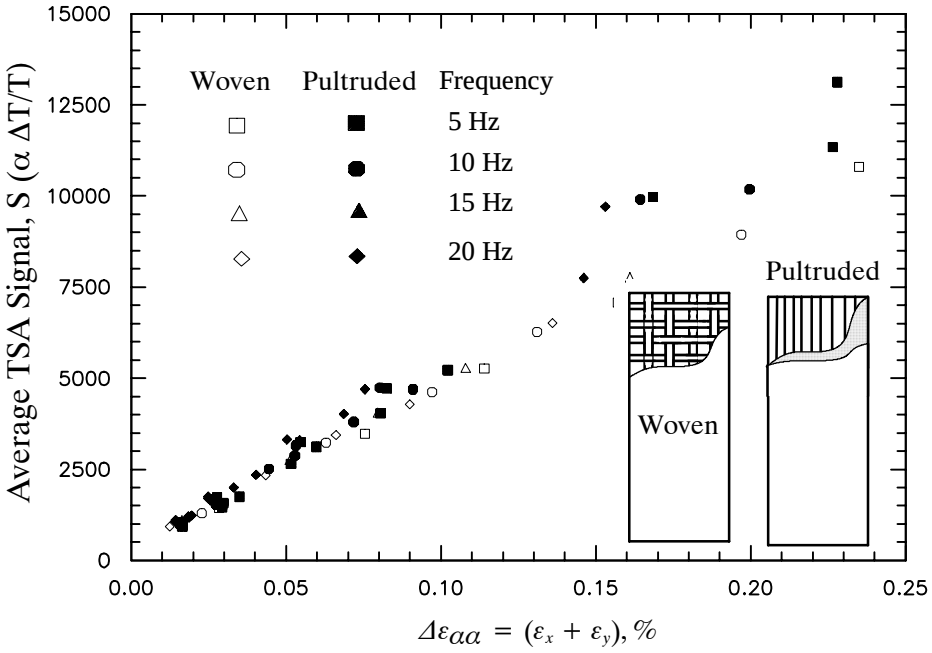

Figure 3.19 Averaged TSA versus strain response for woven and pultruded composite systems

Validation under Multi-axial Stress States

A carbon/epoxy specimen with a circular cutout is tested to assess the ability of the proposed TSA method to quantitatively measure the strains under non-uniform multi-axial stress states for other coated laminated composite systems. The strains from the TSA tests were then compared to results obtained from FE simulations. The thickness of the specimen was 2.5 mm (0.1 in) and the width was 50.8 mm (2.0 in). The diameter of the drilled hole was 12.7 mm (0.5 in.). The specimen was monotonically loaded to 6.67 kN (1.5 kip) and then a sinusoidal load was applied with amplitude of 3.0 kN (0.675 kips) and frequency of 5 Hz. The TSA images were integrated over a period of 5 minutes. The corresponding TSA signal in the out-of-phase range had magnitudes less than 5% of the in-phase response. This also indicates that energy dissipative effects, such as damping and damage, were small for the applied magnitudes of cyclic loading. However, the out-of-phase response appeared to oscillate between negative and positive values following the weave pattern indicating a small amount of heat transfer from the stresses in the carbon/epoxy phases. This effect was not observed in the pultruded specimens. Figure 3.20 shows two full-field TSA contours for the woven specimen. The two plots are used to emphasize the predominant tension and compression responses around the circular cutout. It is clear that more variability exists in the woven composite compared to the pultruded system.

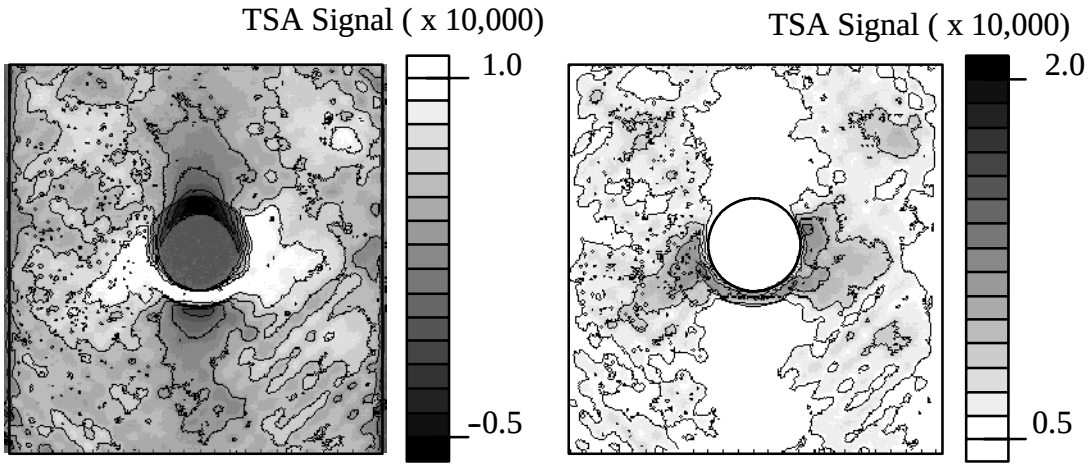

Figure 3.20 TSA images of a carbon/epoxy woven composite

For the finite element analysis a mesh convergence study was performed and the converged mesh used had an average of 7500 4-noded plane stress elements. The material properties reported in Table 3.2 were used to model the carbon/epoxy specimen. Figures 3.21 and 3.22 show the comparison between the analytical strains from the FE analysis and those obtained from the TSA method. The experimental strain invariant obtained is in good agreement with those from the FE results, along the horizontal line a-a and along a vertical line b-b for a total distance of the specimen's width (measured from the center). The bonded surface layer appeared to attenuate most of the IR emission that may have been generated inside the composite. Some variability of the TSA signal in woven composites is demonstrated in these curves and can be attributed to the variability in the bond layer. Overall, the results illustrate the accuracy of the proposed method in determining the full-field strain invariant in various classes of pultruded and thick-section composite systems.

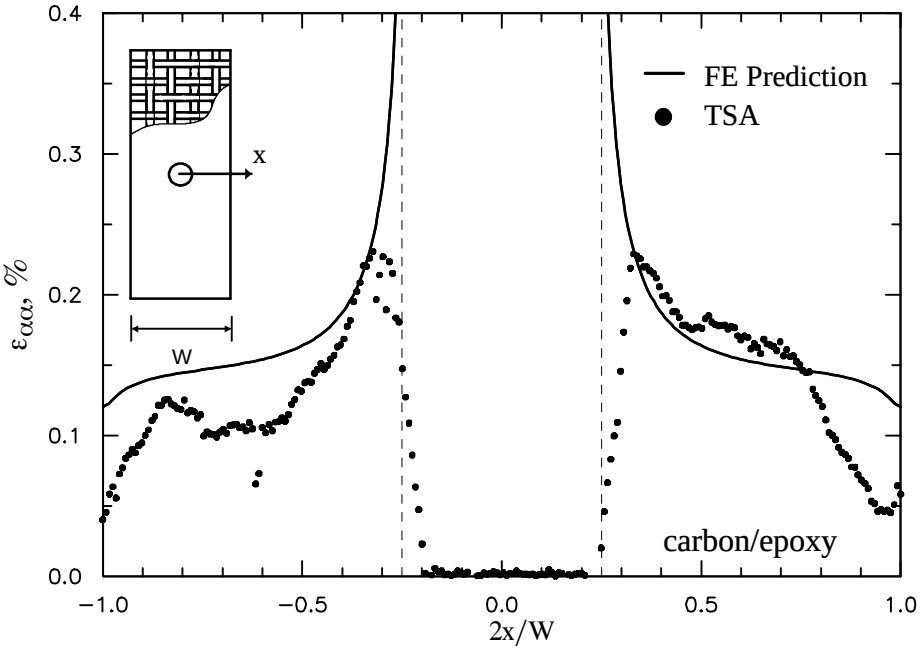

Figure 3.21 Comparison of TSA results with FE along a horizontal line from the center of woven carbon/epoxy plate

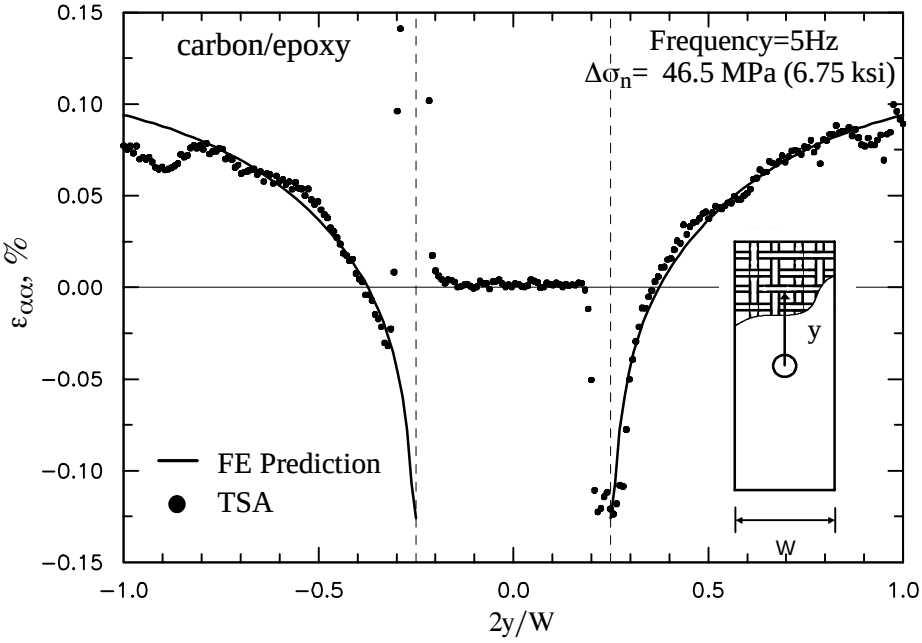

Figure 3.22 Comparison of TSA results with FE along a vertical line from the center of woven carbon/epoxy plate

CHAPTER 4

MODE-I FRACTURE TOUGHNESS

In this chapter results from experimental and numerical analyses are presented to investigate the mode-I fracture toughness of thick-section pultruded composites. The applicability of the eccentrically loaded, single-edge-notch tension, ESE(T) specimen from ASTM E1922 (1997) standard is examined for this purpose. Finite element analyses are conducted to assess the effect of material nonlinearity and orthotropy on the mode-I stress intensity factors (SIF) of the ESE(T) specimen. Crack growth measurements are also performed to determine the amount of stable crack growth before reaching critical load and to measure the post-critical growth. Two methods are presented for the calculation and interpretation of the fracture test results (data reduction). Criteria are proposed for assessing test validity and for determining the load used in calculating the fracture toughness.

4.1 Experimental Procedure based on ASTM E1922

The ESE(T) specimen geometry (also prescribed in ASTM E1922, 1997) used to determine the mode-I fracture toughness is shown in Figure 4.1. The fracture tests conducted followed to the largest degree possible the procedures outlined in ASTM E1922 (1997). However, as will be discussed in this chapter, this was not always possible due to various limitations in the existing procedure when applying it to polymeric/glass pultrusions. Compared to the standard compact tension specimen, the ESE(T) specimen moves the loading pins further away from the crack tip. The ESE(T) specimen was chosen because it has several advantages over other standard test specimen, such as the lower T-stresses ahead of the crack tip resulting in more self-similar crack growth and lower failure loads.

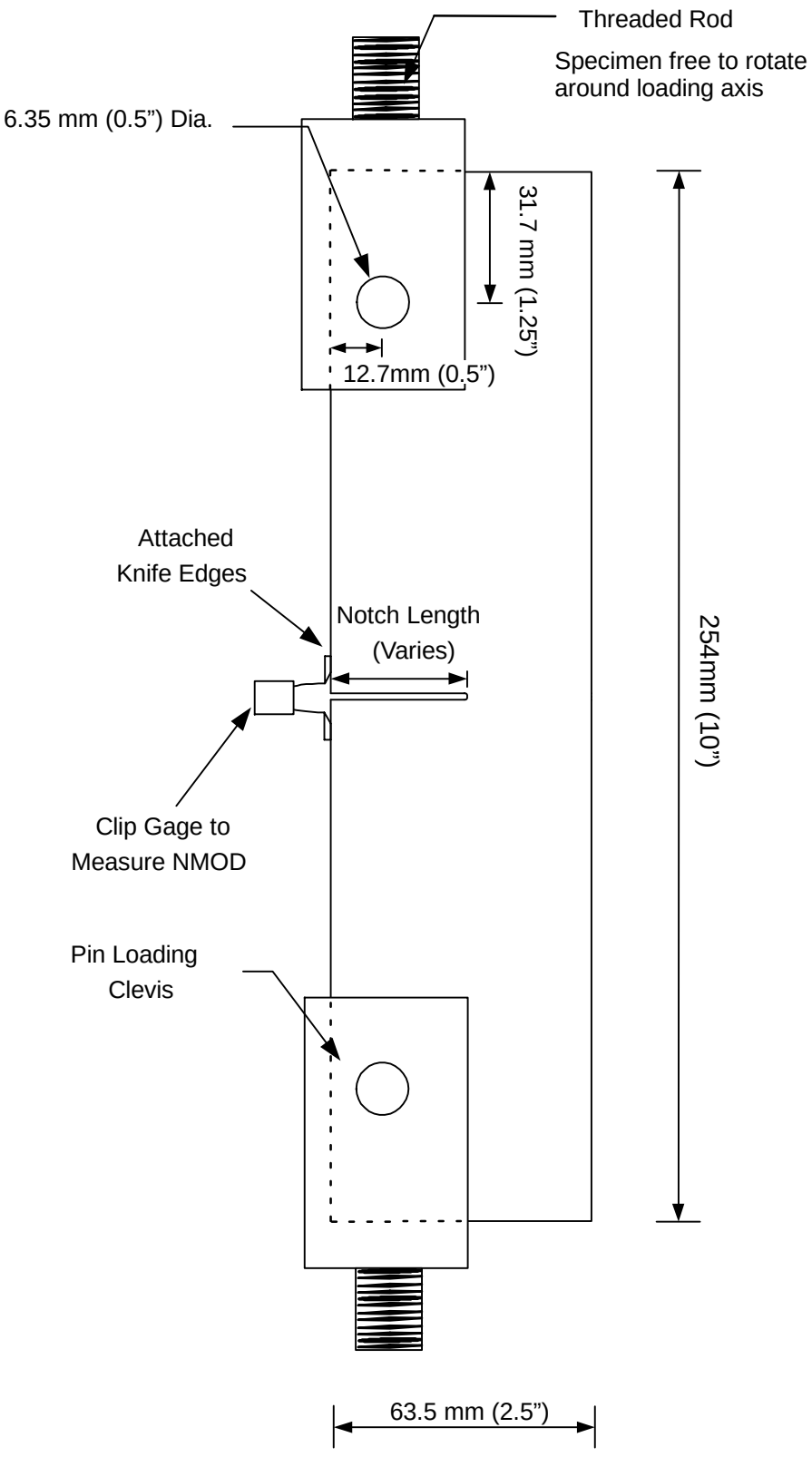

Figure 4.1 ESE(T) test specimen and experimental setup

The expression for the mode-I SIF for an isotropic ESE(T) specimen is (Piascik et al., 1997):

$$K_I = \frac{P}{BW^{1/2}} F(a/W) \tag{4.1}$$

$$K_I = [P/BW^{1/2}]\,\beta^{1/2}\,[1.4 + \beta]\,[3.97 - 10.88\beta + 26.25\beta^2 - 38.9\beta^3 + 30.15\beta^4 - 9.27\beta^5]/[1 - \beta]^{3/2} \tag{4.2}$$

Where P is the applied load at the pins, B is the specimen thickness, W is the width of the specimen, a is the original notch length, and, $\beta = a/W$.

Specimen Preparation and Test Setup

The ESE(T) fracture test specimens were machined from the center of a monolithic pultruded plate of 1.2 x 2.4 m (4 x 8 ft) with a thickness of 12.2 mm (0.48 in.). The notch was made using a diamond saw blade with a thickness of 0.15 mm (0.006 in.). Figure 4.1 illustrates the ESE(T) specimen dimensions. Figure 4.2 shows a special feature of the fixture design which allows the specimen to rotate around the loading axis thereby resulting in reduced torsional effects. The load is applied to the specimen by a pin clevis connected to the loading frame through a threaded rod. A clip gage attached to the specimen at the knife edges is used to measure the notch mouth opening displacement (NMOD). The fracture tests were performed in a displacement control mode at a rate of 1 mm/min using an MTS 810 servo-hydraulic test system with a 222.41 kN (50-kip) capacity. The accuracy of the recorded load is within $\pm$ 0.22 kN (50 lbf) and the NMOD data is within $\pm$ 3.3x10^{-2} mm (1.3x10^{-3} in).

A qualitative test and specimen integrity verification was also performed using the Thermoelastic Stress Analysis (TSA) technique discussed in Chapter 3. The TSA image of the thermoelastic effect was taken by applying a cyclic load during a separate test with an

ESE(T) specimen. Note that the thermoelastic effect in pultruded composite materials can be related to the sum of the in-plane direct strains on the surface and can provide a verification of the integrity of the test, such as the relative deformation in the loading pins and the extent of the far field deformations near the boundaries. Figure 4.3 is a an image of the TSA signals taken during the cyclic load. The image clearly shows the region ahead of the notch tip and the associated TSA cardoid contours that can be related to the first strain invariant on the surface. The TSA signal around the loading pins in the ESE(T) specimen indicate a smooth transfer of load.

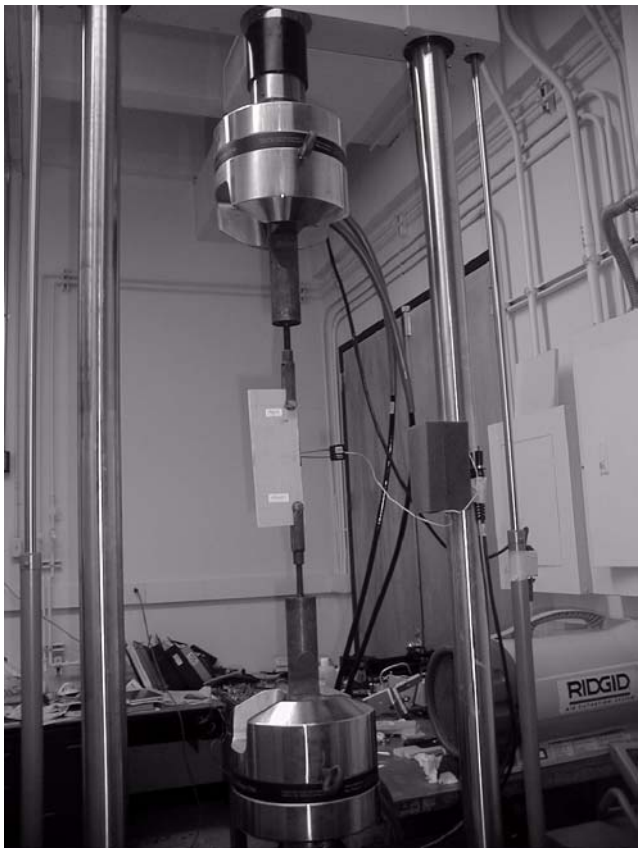

Figure 4.2 Servo-hydraulic test machine loading an ESE(T) specimen

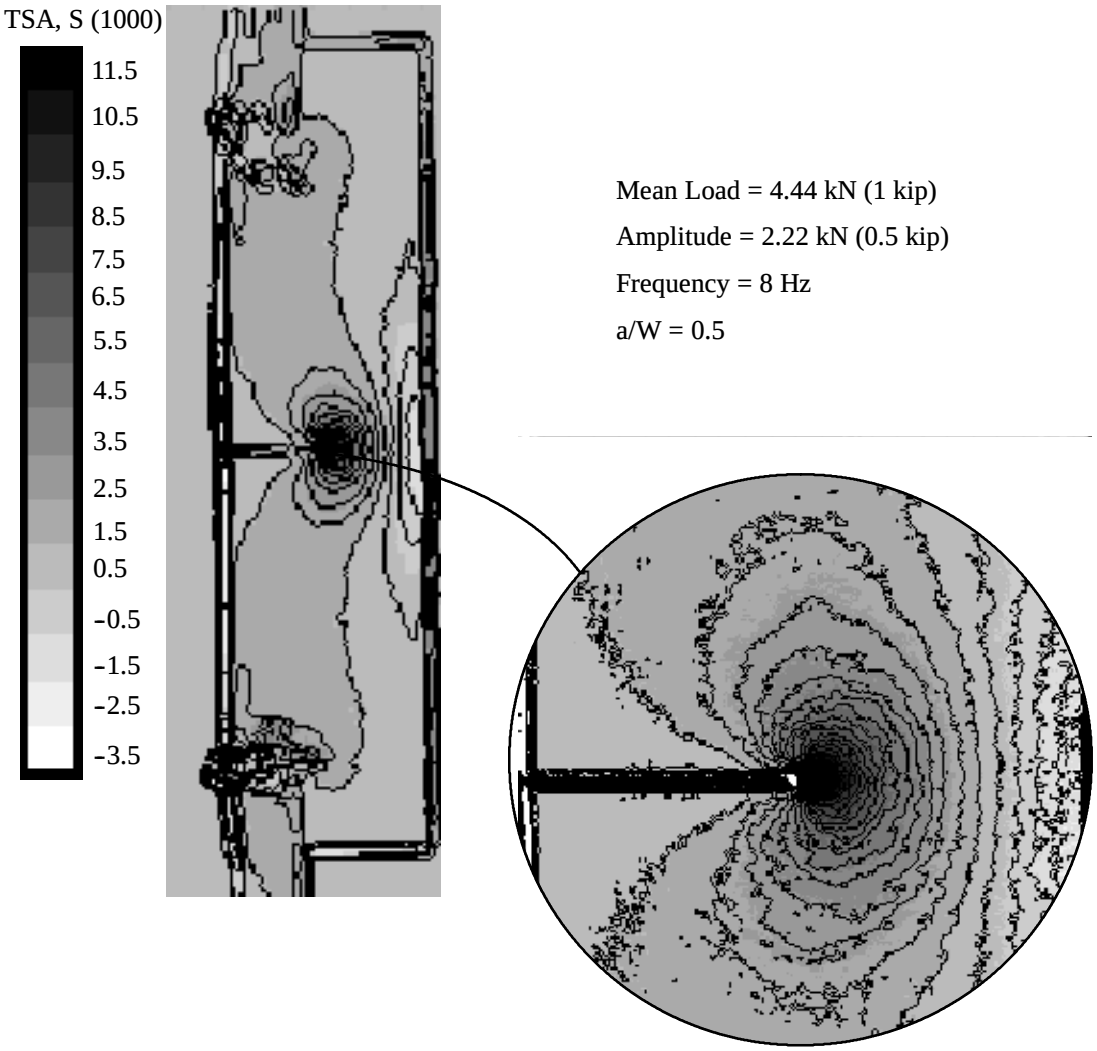

Figure 4.3 Qualitative test integrity assessment using TSA

4.2 Material Orthotropy Effect

A numerical study is conducted to assess the effect of material orthotropy on using the isotropic SIF solutions of the ESE(T) specimen to determine the fracture toughness. For the calculation of the strain energy release rates G_I, FE analyses using the virtual crack closure technique (VCCT) are used. Before the VCCT, the "crack closure method" as it is also sometimes called was used to calucate the energy release rates. In this method two separate FE analyses are required, where the global total energy release rate is obtained as global forces on a structural level are multiplied with global deformations to calculate the energy available to advance the crack. The forces required to close the crack are identical to the forces acting on the upper and lower surfaces of the closed crack. To obtain the strain energy release rate with one analysis, the VCCT method assumes that the crack extension does not significantly alter the displacements near the crack tip. A comprehensive discussion on the this technique can be found in Krueger (2002). Once G_I is calculated then it is possible to relate it to the SIF. For the FE calculations using the VCCT method, the ABAQUS (2002) finite element code is used with 8-node continuum plane stress elements (CPS8R). The average model contained 1700 elements and 5400 nodes. Figure 4.4 shows a schematic of the VCCT method with the 8 noded element. The springs 1 and 2 are modeled as soft springs in order to get the displacements at these two locations. The springs 3 and 4 are modeled as stiff springs to get the reactions at the crack tip. The material properties are embedded in the results obtained from the FE analysis. The mode-I strain energy release rate can then be calculated:

$$G_I = \frac{1}{2B\Delta}\left(F_3\delta_1 + F_4\delta_2\right) \tag{4.3}$$

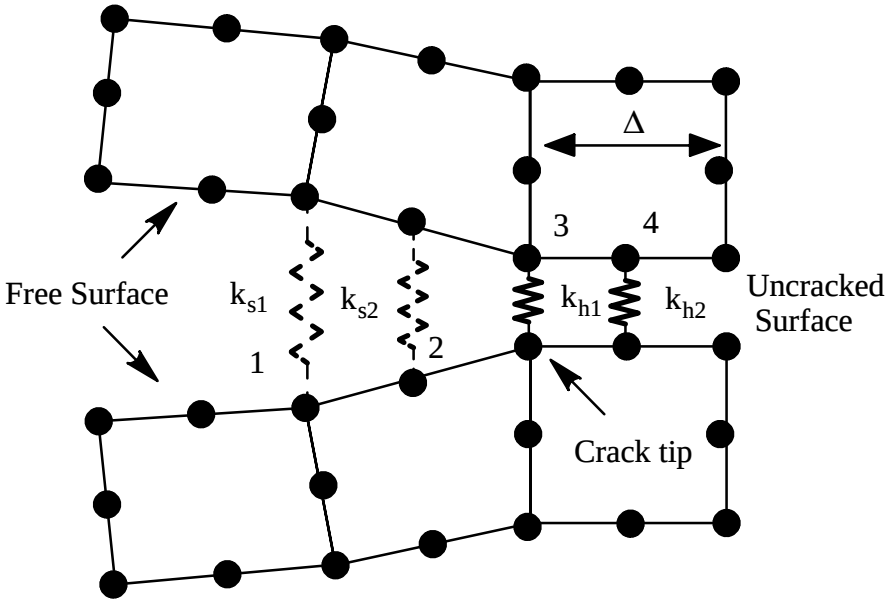

Figure 4.4 Mode-I VCCT for 8-noded elements

Where Δ is the element size and B is the thickness and δ_1 and δ_2 are the displacements in the soft springs. The element size was constant for all the elements along the crack path. The spring stiffnesses k_s and k_h used were $1x10^{-15}$ and $1x10^{+15}$ kip/in respectively. The soft springs are used for the purpose of determining the deformation on the free surface at the locations 1 and 2. The VCCT approach was verified by performing the analyses for the ESE(T) SIF under isotropic conditions. The results were found to be in agreement with those in Equations (4.1) and (4.2). For composites, a crack in the x_1-direction under a plane stress state allows the strain energy release rate, G_I, to be related to the mode-I SIF by (Suo et al., 1991):

$$G_I = \left(s_{11} s_{22} \frac{1 + \rho}{2} \right)^{\frac{1}{2}} \lambda^{-\frac{1}{4}} K_I^2 \qquad (4.4)$$

where s_{ij} are the compliances and the two parameters, ρ and λ, are measures of the in-plane material orthotropy:

$$\lambda = \frac{s_{11}}{s_{22}} = \frac{E_2}{E_1}, \qquad \rho = \frac{2s_{12} + s_{66}}{2\sqrt{s_{11}s_{22}}} = \frac{(E_1E_2)^{\frac{1}{2}}}{2G_{12}} - (\nu_{12}\nu_{21})^{\frac{1}{2}} \tag{4.5}$$

For thick-section composites such as the pultruded system used in this study, the expressions given for plane stress conditions can be modified to plain strain by replacing the corresponding elastic constants with:

$$\begin{aligned} E'_1 &= E_1/(1 - \nu_{13}\nu_{31}), & \nu'_{12} &= (\nu_{12} + \nu_{13}\nu_{32})/(1 - \nu_{13}\nu_{31}) \\ E'_2 &= E_2/(1 - \nu_{23}\nu_{32}), & \nu'_{21} &= (\nu_{21} + \nu_{23}\nu_{31})/(1 - \nu_{23}\nu_{32}) \end{aligned} \tag{4.6}$$

In Chapter 1, it was discussed how Boa et al. (1992a, b) used an orthotropy rescaling technique to fit formulae into numerical calibrations to quantify the effect of material orthotropy on notched bars, delaminated beams, and hybrid sandwiches. In this study a similar approach based on dimensionality, linearity, and orthotropic rescaling is used to rewrite the SIF for the ESE(T) specimen as:

$$K_I = \frac{P}{BW^{1/2}} F(a/W, \lambda^{1/4}L/b, \rho) \tag{4.7}$$

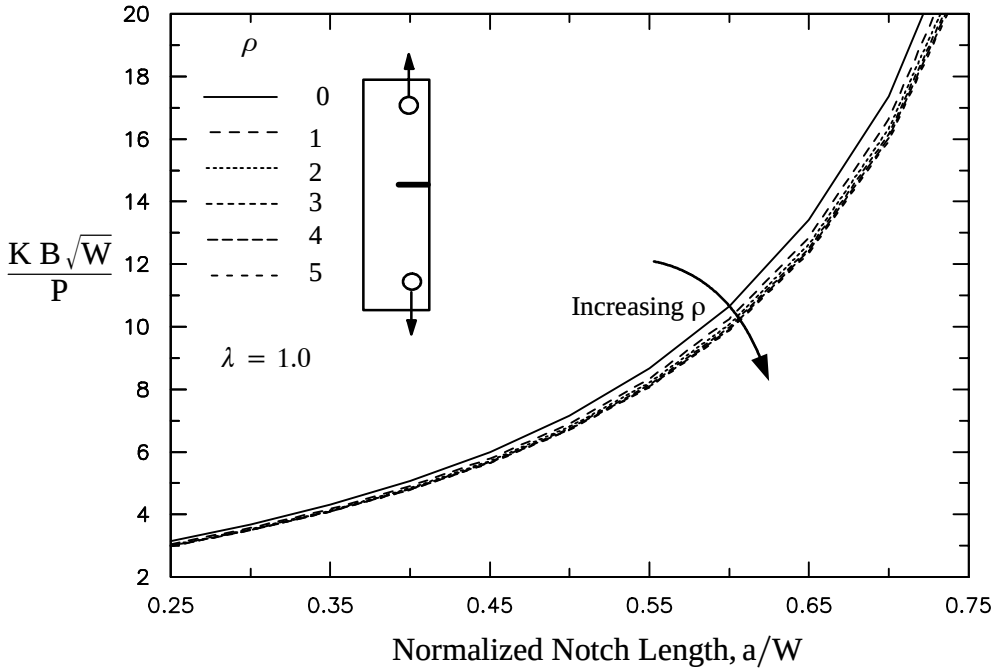

Figure 4.5 Effect of material orthotropy parameter, ρ , on the SIF in ESE(T) specimen

A FE parametric study on the ESE(T) specimen was performed to determine the effect of material orthotropy parameters, ρ and λ by incrementing ρ between, 0 and 5 and λ, between 0.5 and 10. Utilizing the VCCT method the analyses were performed for normalized crack ratios (a/W) between 0.25 and 0.75 to determine the effect on the function F in Equation (4.7). Figure 4.5 shows the effect of ρ on the F by plotting the function F while λ is kept constant ($\lambda = 1$). The material orthotropy parameter, ρ is varied between 0 to 5 to show the gradient in the response for the practical range of ρ analyzed for the ESE(T) specimen. As the parameter ρ increases the effect on the SIF diminishes. The curves are almost identical for $\rho \geq 3$ values. The analyses also showed a negligible effect of λ on the SIF. VCCT analyses were also performed for this pultruded composite material. The pultruded material tested in this study has a $\rho = 1.62$ and $\lambda = 0.623$ compared to the isotropic case ($\lambda = \rho = 1$). It is found that calculating the SIF with the 'isotropic' solution in Equation (4.1) will result in an error of less than 2 %. In the case when Equation (4.1)

is to be used for the above ranges of a/W, ρ and λ, the maximum error in the SIF was calculated to be about 5 %. For the pultruded system used in this study, the error drops to less than 1 % when using the approach proposed by Boa et al. (1992a, b):

$$K_I = \frac{P}{B\sqrt{W}} Y(\rho) F(a/W) \tag{4.8}$$

$$Y(\rho) = 1 + 0.1(\rho - 1) - 0.016(\rho - 1)^2 + 0.002(\rho - 1)^3/[(1 + \rho)/2]^{1/4} \tag{4.9}$$

4.3 Effect of Crack Growth on Mode-I Fracture Toughness

Crack growth behavior during additional fracture tests was monitored by bonding crack propagation gages (Krack-Gage) to the surfaces of the ESE(T) specimen. Figure 4.6 shows the crack propagation gage bonded to one of the surfaces of an ESE(T) specimen. The gages utilize the in-direct potential drop method for measuring the crack growth. The gage is excited using a constant current. The propagation of the crack causes a change in the voltage across the gage (Hartmann and Churchill, 1981). The crack length is determined by the pre-calibrated linear relationship between the change in voltage and the crack length. The gages used are able to measure up to 30 mm (1.18 in) of crack growth with an accuracy of 0.1 % of the gage length. The signal from the gage is measured simultaneously with the load, displacement and the NMOD. Two gages were attached to each test sample to measure the crack growth on both surfaces.

Figures 4.7 and 4.8 show the load versus the crack growth for specimen that were gaged on both surfaces. Self-similar crack growth on both surfaces is observed when the roving layers are oriented both axial and transverse to the loading direction. This can be explained by the fact that most of the crack growth occurs through the CFM layers. Some difference between growth in the two gages is seen for the case when the roving layers are oriented in the loading direction (Figure 4.8). The difference in the load-growth from the two gages maybe attributed to the material heterogeneous variability ahead of the crack in the roving

layers in this mode. A stable crack-growth of about 3 mm (0.12 in) occurs before reaching the critical load. Figure 4.9 shows two specimens showing the two typical fractures in the axial and transverse specimens. A scanning electron microscope was also used to take micrographs after the fracture of an ESE(T) specimen with $a/W = 0.5$. Figure 4.10 shows the fracture surface ahead of the notch tip in a region with a roving bundle. The fiber in the roving bundle appear to be clear of the adhering matrix. Further a uniform fracture is seen in the CFM layer ahead of the notch. Figure 4.11 shows a micrograph of a manufacturing defect (void) in the notch region area.

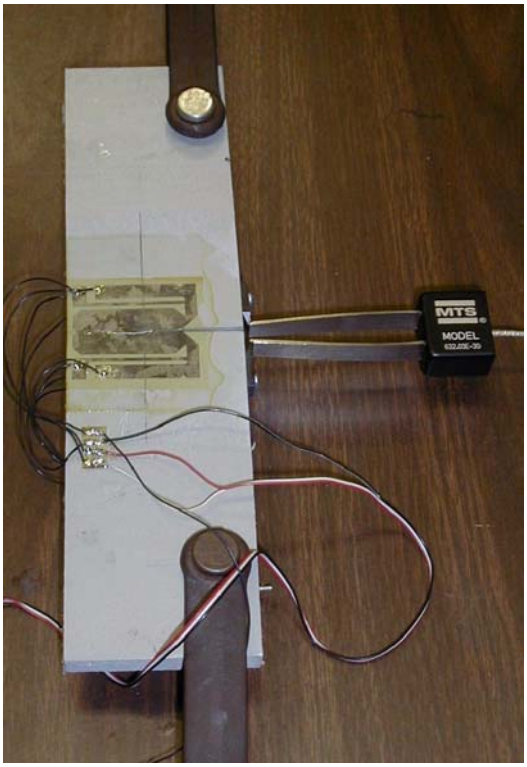

Figure 4.6 ESE(T) specimen of pultruded composite with crack gage

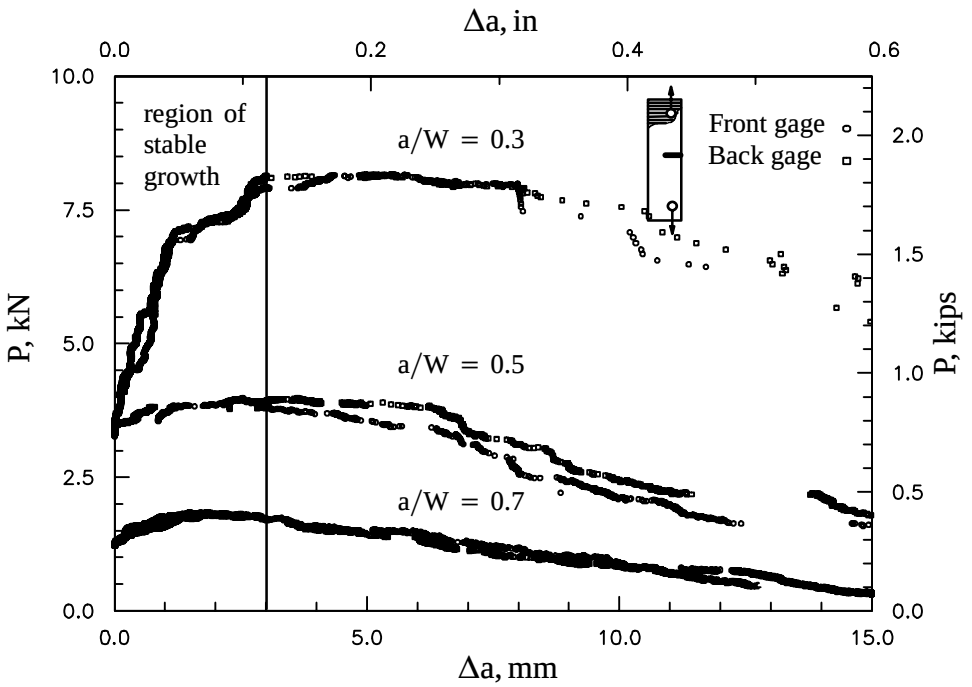

Figure 4.7 Load versus crack growth curves for ESE(T) specimen with θ= 90 degrees

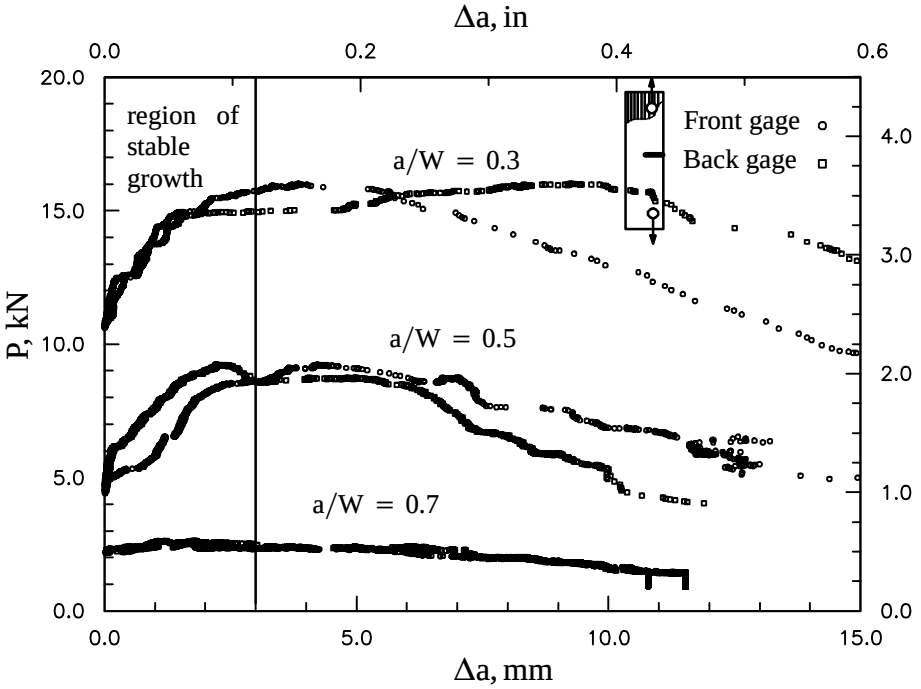

Figure 4.8 Load versus crack growth curves for ESE(T) specimen, θ= 0 degrees

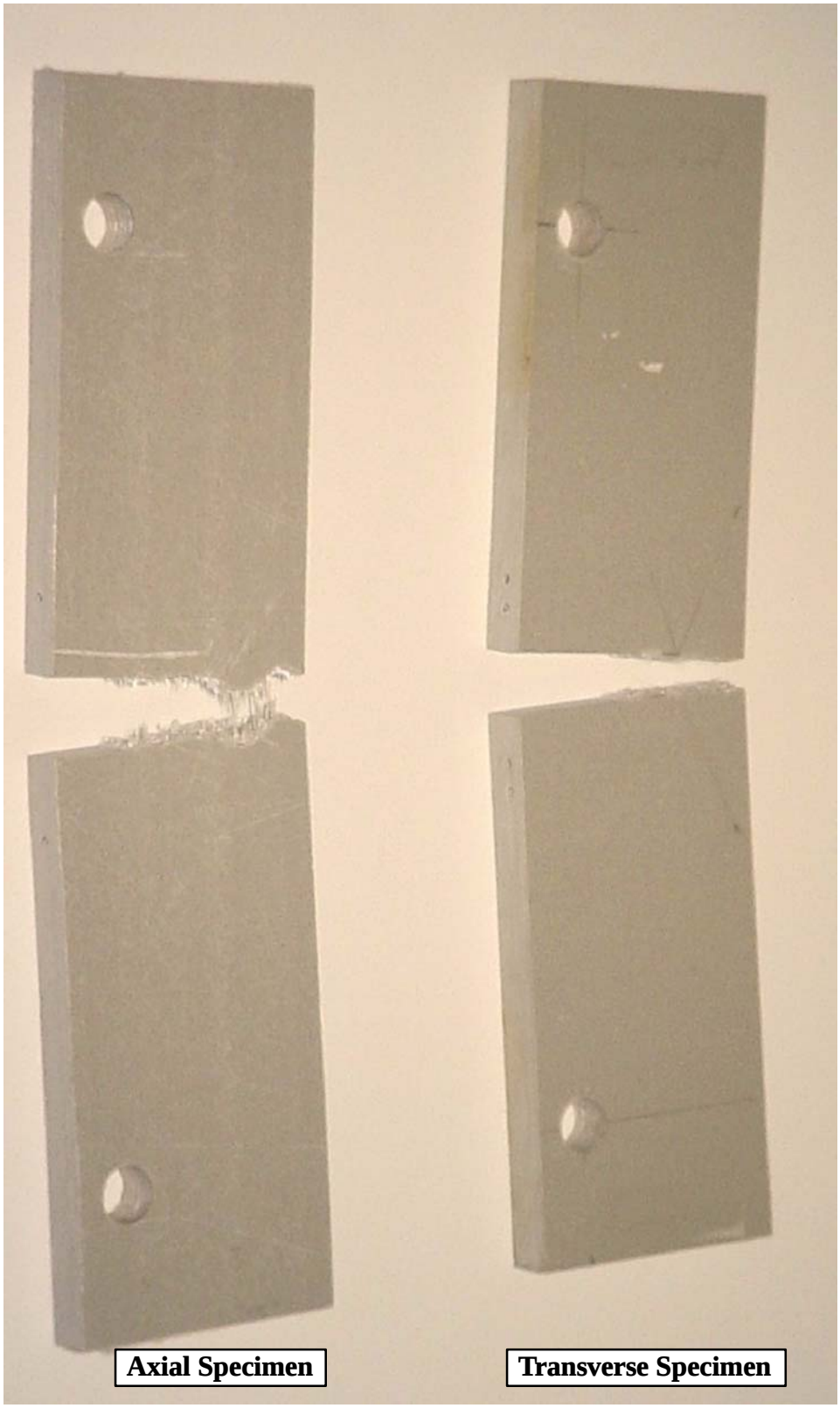

Figure 4.9 Typical fractures of ESE(T) specimens

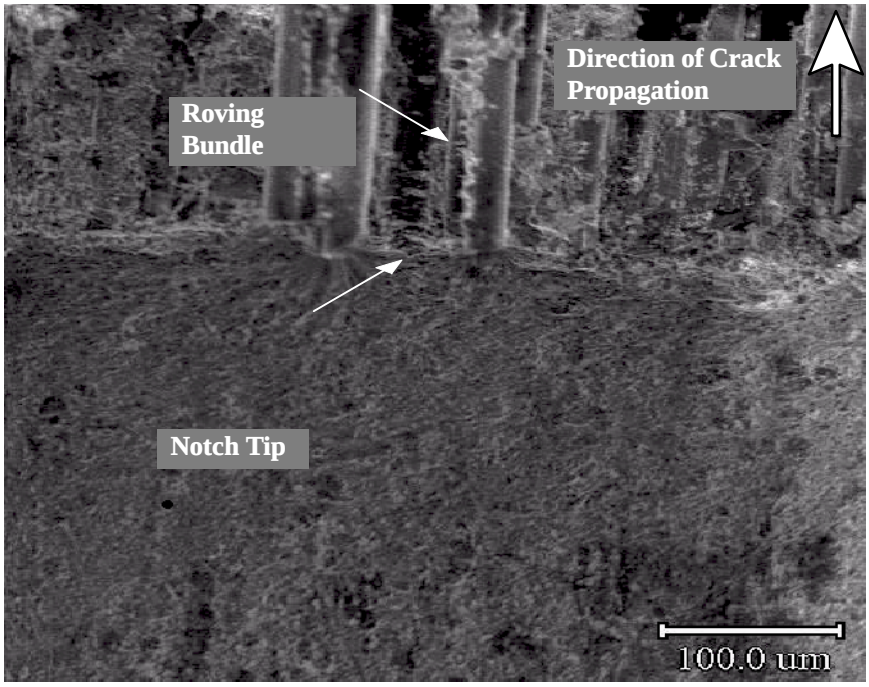

Figure 4.10 SEM micrograph of roving area ahead of the notch tip

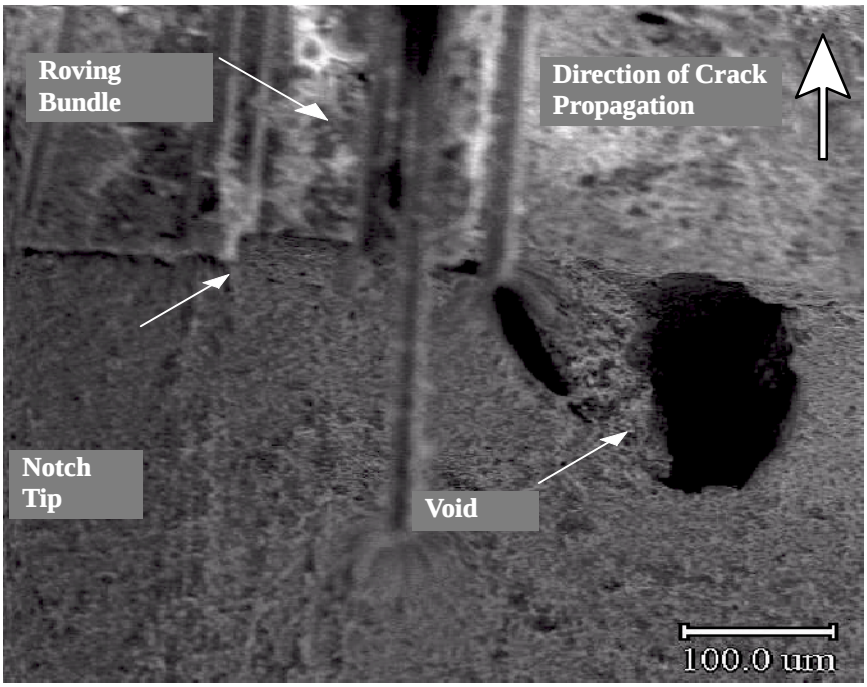

Figure 4.11 SEM micrograph of a manufacturing defect (void) in the notch region

4.4 Proposed Changes in ASTM E1922 Test Standard

The current study has resulted in several recommendations for modification of the existing ASTM standard for translaminar fracture in composite materials. The first recommendation is that it take into account the work performed on determining the mode-I fracture in FRP pultrusions. In this study it was found that ASTM Standard E 1922 (1997) can give satisfactory results when applied to thick section composites of thickness as high as 12 mm. Therefore, it is proposed that ASTM Standard E 1922 (1997) reflect on its applicability to moderately thick section composite materials (less than 12 mm). Currently, only composites of thickness less than 2 mm were considered. In reference to calculation and interpretation of results, it is recommended that specific changes be made to account for the different fracture response that results from different FRP material systems. For example, material nonlinearity that occurs in many composite systems is not currently addressed. The current criteria for test validity acceptance are very specific for a small number of composite systems. The standard could potentially be extremely useful, by attempting to address various composite systems separately. In the equation for calculation of the applied SIF, they do not currently take into account the role of material orthotropy. It is proposed that Equation (4.8) be used when accounting for material orthotropy is necessary. Material nonlinearity effects can also be addressed by supplementing the experimental approach with numerical analyses to account for the nonlinear response.

Calculation and Interpretation of Results

Two methods are proposed to determine the value of the measured mode-I translayer fracture toughness, K_{TL}. Both methods use the plots of the applied load, P, at the pins versus the NMOD, V_n. The toughness in method A is determined by using the maximum load from the $P-V_n$ curve in Equation (4.1). In method B, an offset to the original slope is used to determine the load from the intersection with the $P-V_n$ curve. Figures 4.13 and 4.14 show the data reduction of the two methods to determine the fracture toughness. The

criteria for test acceptability used currently in ASTM E-1922 (1997a) is used in method A (Figure 4.13). Similar to this standard, method A accepts tests with a limited amount of notch tip damage (or growth) as long as $\Delta V_n/V_{n-o} \leq 0.3$. Where, $V_{n-o} = V_n$ at $P = P_{max}$ on the extension of the linear portion of the load versus V_n plot as shown in Figure 4.13. Method B (Figure 4.14) uses a similar approach to the one in ASTM E 399 (1997b). A secant line with a reduced slope from the initial linear portion is used to obtain a candidate P_Q for calculating the fracture toughness. A fracture test record is likely to fall in one of the three general types of load-NMOD records. The slope of the secant line is determined by using the amount of crack growth observed before critical load in order to determine a modified a/W^*. A polynomial fit can be used to determine the slope of the P-V_n curve as a function of a/W and roving orientations as shown in Figure 4.12. Using the modified a/W^*, a new value is used to determine the slope of the offset line. The secant offset is used to allow a certain amount of damage and/or crack growth and will not always result in $P_Q = P_{max}$ in the calculation of K_{TL}. The load at which the secant line intersects the load-NMOD record is labelled, P_{of}. If the load-NMOD curve is monotonically increasing up to P_{of}, then, $P_Q = P_{of}$. If there is a maximum before P_{of}, then the maximum load is P_Q. A ratio of $P_{max}/P_Q < 1.1$ to ensure against erratic behavior is required as an additional constraint before accepting P_Q for determining K_{TL}. Using the two proposed methods, Table 4.1 summarizes the average mode-I fracture toughness values for both orientations. The axial and transverse fracture toughness values obtained from processing the results of method A and B are shown in Figures 4.15 and 4.16, respectively. The results indicate that the fracture toughness determined is largely independent of the normalized notch length and can thus can be considered a material property.

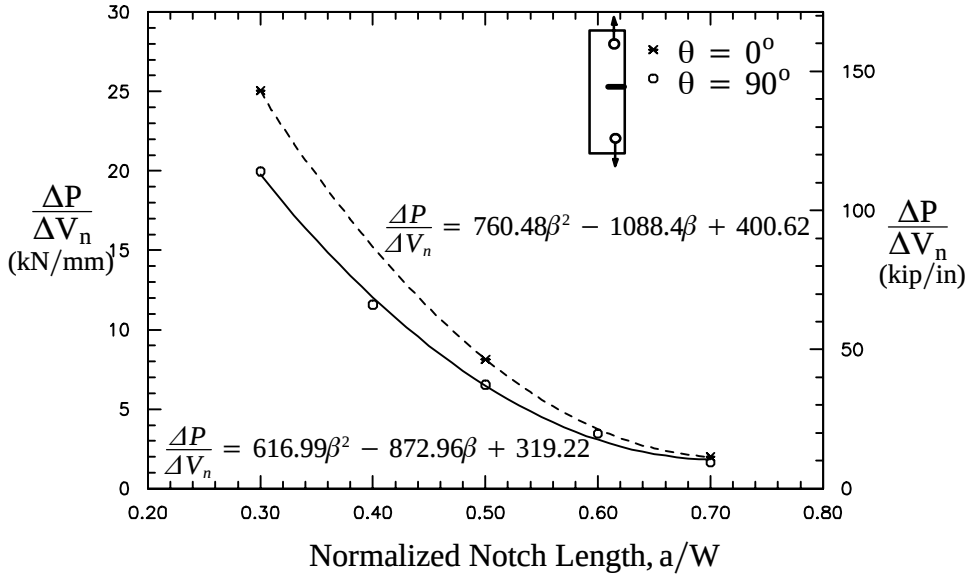

Figure 4.12 Inital slope of load-NMOD curve versus notch length with polynomial curve fits

In this study, current ASTM standards are applied to a specific thick-section pultruded composite known as the Pultex series 1525 (Creative Pultrusions, 2000). The overall objective of this study is to test the applicability of the current ASTM test method for a widely used class of pultruded composites. The effect of the normalized crack size, a/W, and the roving fiber orientation on the mode-I fracture toughness were investigated. Examining the nature of the variability of the fracture toughness across the myriad of pultruded systems possible is beyond the scope of this work. The size of the tested specimens were controlled by the specifications outlined in ASTM E1922 (1997). The mode-I fracture toughness was characterized using test results from 45 specimens. Of the 45 tested specimens, 28 were tested with the transverse (90 degree) roving orientation with targeted ratios of a/W=0.3, 0.4, 0.5, 0.6 and 0.7. More specimens were tested with the roving fibers in the transverse orientation because of the lower toughness in this mode. In addition, some of these specimens were also used to measure crack growth from two special crack gages mounted on their surfaces. All the tests met the acceptance criteria in method A for calculating and

interpreting the results. The arithmetic mean of the fracture toughness is found to be 9.40 MPa $\sqrt{m}$ (8.56 ksi$\sqrt{in}$), the median value is 9.31 MPa $\sqrt{m}$ (8.47 ksi$\sqrt{in}$), the standard deviation is 0.736 MPa $\sqrt{m}$ (0.67 ksi$\sqrt{in}$) and the coefficient of variation is 7.8 %. However 21 out of the 28 results met the acceptance criteria when method B is used. The mean of the fracture toughness is 9.24 MPa $\sqrt{m}$ (8.41 ksi$\sqrt{in}$), the median value is 9.27 MPa $\sqrt{m}$ (8.44 ksi$\sqrt{in}$), the standard deviation is 0.54 MPa $\sqrt{m}$ (0.50 ksi$\sqrt{in}$) and the coefficient of variation is 5.9 %. A total of 17 specimens were tested with the axial (0 degree) roving orientation with targeted ratios of a/W=0.3, 0.5 and 0.7. For method A, all the tests met the acceptance criteria. The mean of the fracture toughness is 17.8 MPa $\sqrt{m}$ (16.2 ksi$\sqrt{in}$), the median value is 17.36 MPa $\sqrt{m}$ (15.8 ksi$\sqrt{in}$), the standard deviation is 2.34 MPa $\sqrt{m}$ (2.13 ksi$\sqrt{in}$) and the coefficient of variation is 13.1 %. However, 14 out of the 17 tested specimens met the acceptance criteria of method B. The mean of the fracture toughness is 16.0 MPa $\sqrt{m}$ (14.6 ksi$\sqrt{in}$), the median value is 16.2 MPa $\sqrt{m}$ (14.7 ksi$\sqrt{in}$), the standard deviation is 3.21 MPa $\sqrt{m}$ (2.92 ksi$\sqrt{in}$) and the coefficient of variation is 20.0 %.

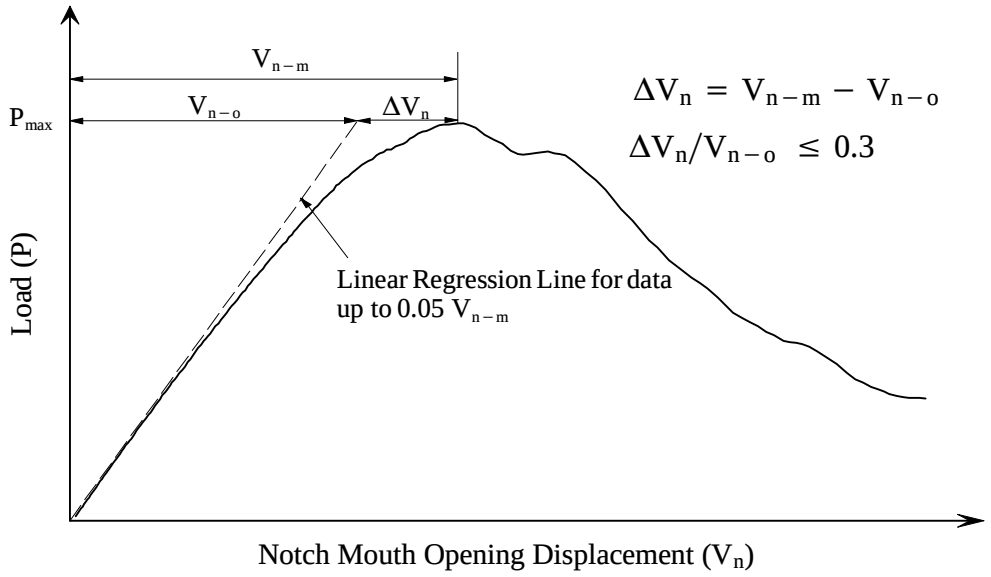

Figure 4.13 Data reduction from load-NMOD record for Method A

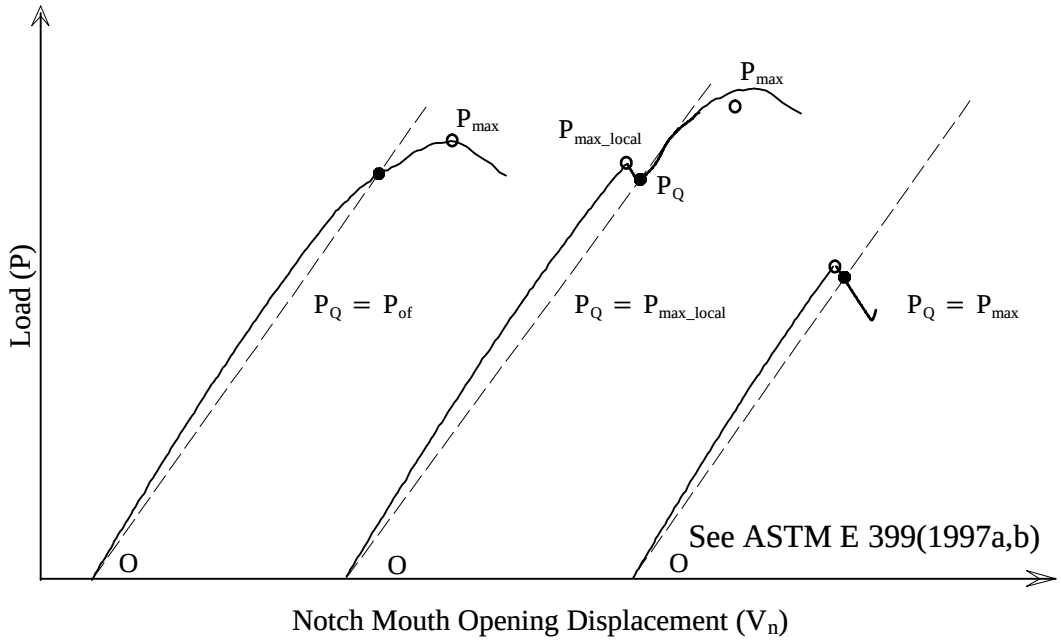

Figure 4.14 Data reduction from load–NMOD record for Method B

Table 4.1 Summary of Mode-I fracture toughness results

Roving Orientation, θ^o	K_{TL} MPa $\sqrt{m}$ (ksi $\sqrt{in}$) ± COV for Method A	K_{TL} MPa $\sqrt{m}$ (ksi $\sqrt{in}$) ± COV for Method B	P_{max}/P_Q Method B
90	9.40 (8.56) ± 7.8%	9.24 (8.41) ± 5.9%	1.03*
0	17.8 (16.2) ± 13.1%	16.0 (14.6) ± 20.0%	1.06†

*All results when a secant intersection was found where within $P_{max}/P_Q < 1.1$

†Excluding 3 results when $P_{max}/P_Q > 1.1$

Table 4.2 Material nonlinearity contribution from FE models at critical load, P_{max}

a/W	Roving Orientation, θ°	$\left(\frac{\Delta V_n}{\Delta V_{n-o}}\right)_{Nonlinear}$	$\left(\frac{\Delta V_n}{\Delta V_{n-o}}\right)_{Experiment}$
0.3	90	0.11	0.54
0.5	90	0.13	0.39
0.7	90	0.14	0.55
0.3	0	0.09	0.48
0.5	0	0.10	0.45
0.7	0	0.15	0.40

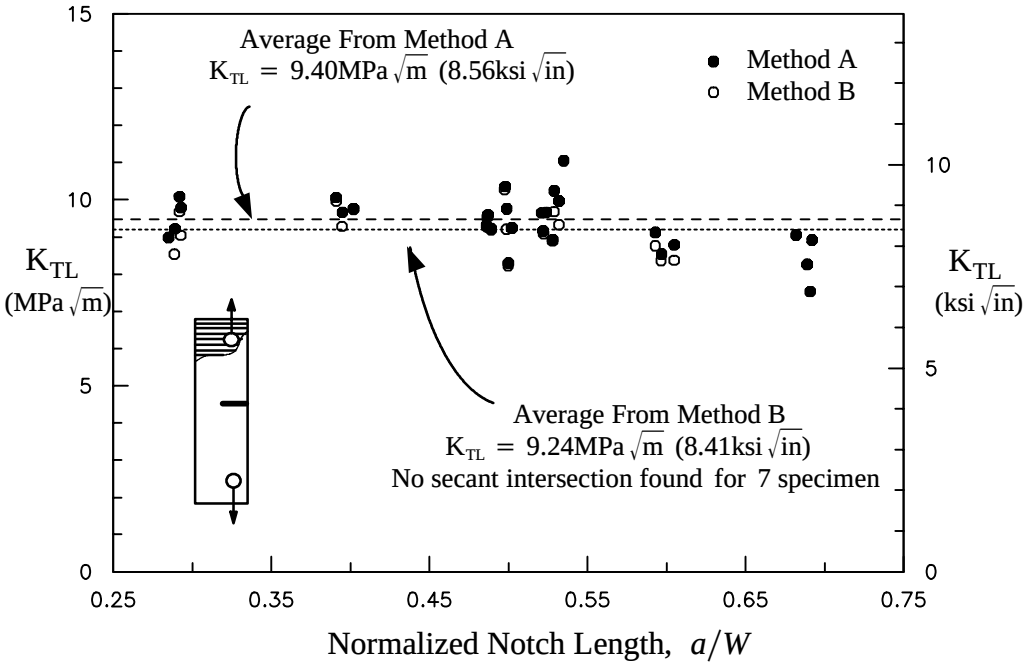

Figure 4.15 Mode-I fracture toughness versus normalized notch length for θ = 90 degrees

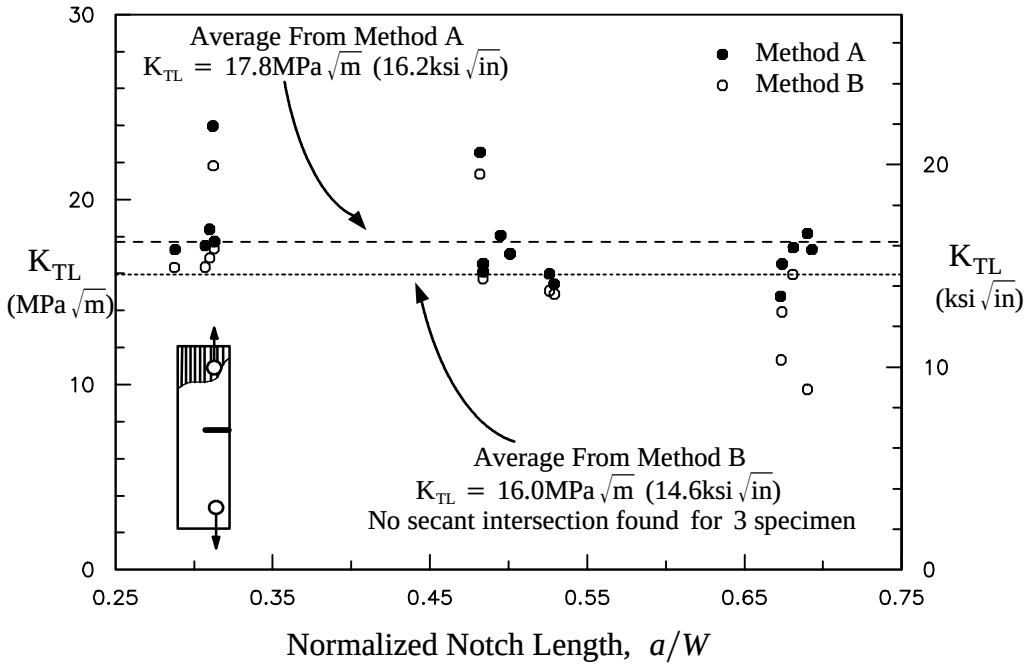

Figure 4.16 Mode-I fracture toughness versus normalized notch length for θ = 0 degrees

Material non-linearity and/or stable-crack growth explain the slight reduction of fracture toughness for larger a/W values. The material nonlinear contribution to $(\Delta V_n/\Delta V_{n-o})_{Nonlinear}$ was determined from FE analyses using the nonlinear micromechanical constitutive approach to account for the material behavior using the framework and the models proposed in Chapter 2. It is seen that even this nonlinear contribution (without damage) is within the acceptance criteria and can be neglected for toughness calculation. When processing the results with method A, the average $(\Delta V_n/V_{n-o})_{Experimental}$ was greater than 0.3 as shown in Table 4.2 and would constitute a violation of the acceptance criteria illustrated in Figure 4.13. The independence of the fracture toughness results on the normalized crack size illustrate the current limitation of $\Delta V_n/V_{n-o} \leq 0.3$ and the need to reconsider the value of 0.3 to account for the material nonlinearity contribution.

CHAPTER 5

NONLINEAR MODE-I COHESIVE CRACK-GROWTH ANALYSIS

In this chapter, a nonlinear micromechanical constitutive framework is combined with cohesive FE models for the analysis of crack propagation in thick-section FRP composites. Mode-I crack growth tests on pultruded eccentrically loaded, single-edge-notch, (tension), ESE(T) specimens with $a/W = 0.5$ are used to calibrate the cohesive parameters, which are used to predict the crack growth response for other a/W ratios. The nonlinear micromechanical constitutive models for the CFM and the roving layers (Chapter 2) are used to generate the effective material behavior from the in-situ fiber and matrix responses. The cohesive growth model consists of a traction-separation cohesive layer used to model the propagating crack. Models are used to simulate mode-I crack growth of ESE(T) specimens with unidirectional roving layers oriented in the axial and transverse directions respectively. The IR thermography technique of Chapter 3 is also used to verify the validity of the modeling approach in the linear region prior to crack growth. Crack growth predictions are presented for different ESE(T) geometries. Tests and models of single-edge-notch, tension, SEN(T), specimen were also conducted to verify the modeling approach.

5.1 Cohesive Layer Fracture Model

A cohesive growth model was used with a traction-separation cohesive layer combined with the nonlinear material modeling constitutive framework. The models for the geometries considered incorporate a fracture surface (cohesive layer) along the line of symmetry. The cohesive layer does not directly account for the softening associated with the fiber pullout ahead of the crack tip, but rather represents a homogenization of various failure mechanisms ahead of the crack tip. A displacement control mode is usually used to apply the loads. An opening-stress failure criterion was used to initiate the crack growth

process by following a linear traction-separation relation between the nodes on the crack surfaces. Other crack-growth parameters are needed to specify the manner in which the stresses across the failed interface were ramped to zero. The failure criterion used for the 2D fracture models is:

$$f = \sqrt{\left(\frac{\sigma_n}{\sigma_n^f}\right)^2 + \left(\frac{\tau_1}{\tau_1^f}\right)^2} \qquad (5.1)$$

where σ_n is the normal stress component, and τ_1 is the shear stress. The normal and shear failure stresses are σ_n^f and τ_1^f respectively. Only the normal stress contribution is considered for mode-I fracture because the shear stresses are absent in this mode. In addition to the failure stresses, other crack-growth parameters are needed. The parameters used in the calibration procedure for the crack growth parameters are illustrated in Figure 5.1. The failure criterion was evaluated at a distance L_c from the crack tip. The release-time and the distance L_c are calibrated from one set of experimental results. Specimen with other geometries are then used to examine the growth prediction ability of the proposed models. It should be noted that the release-time is a relative-time and it is a fraction of the total pseudo-time used in the static FE analyses. These parameters are used to specify the manner in which the traction across the failed interface is ramped to zero. The parameters of the traction separation curve are a function of continued opening displacement or pseudo time. This can be correlated to the apparent strain energy release rate. The traction is reduced to zero as a function of the time after debonding failure occurs. If the stresses are removed too rapidly, numerical convergence difficulties may arise.

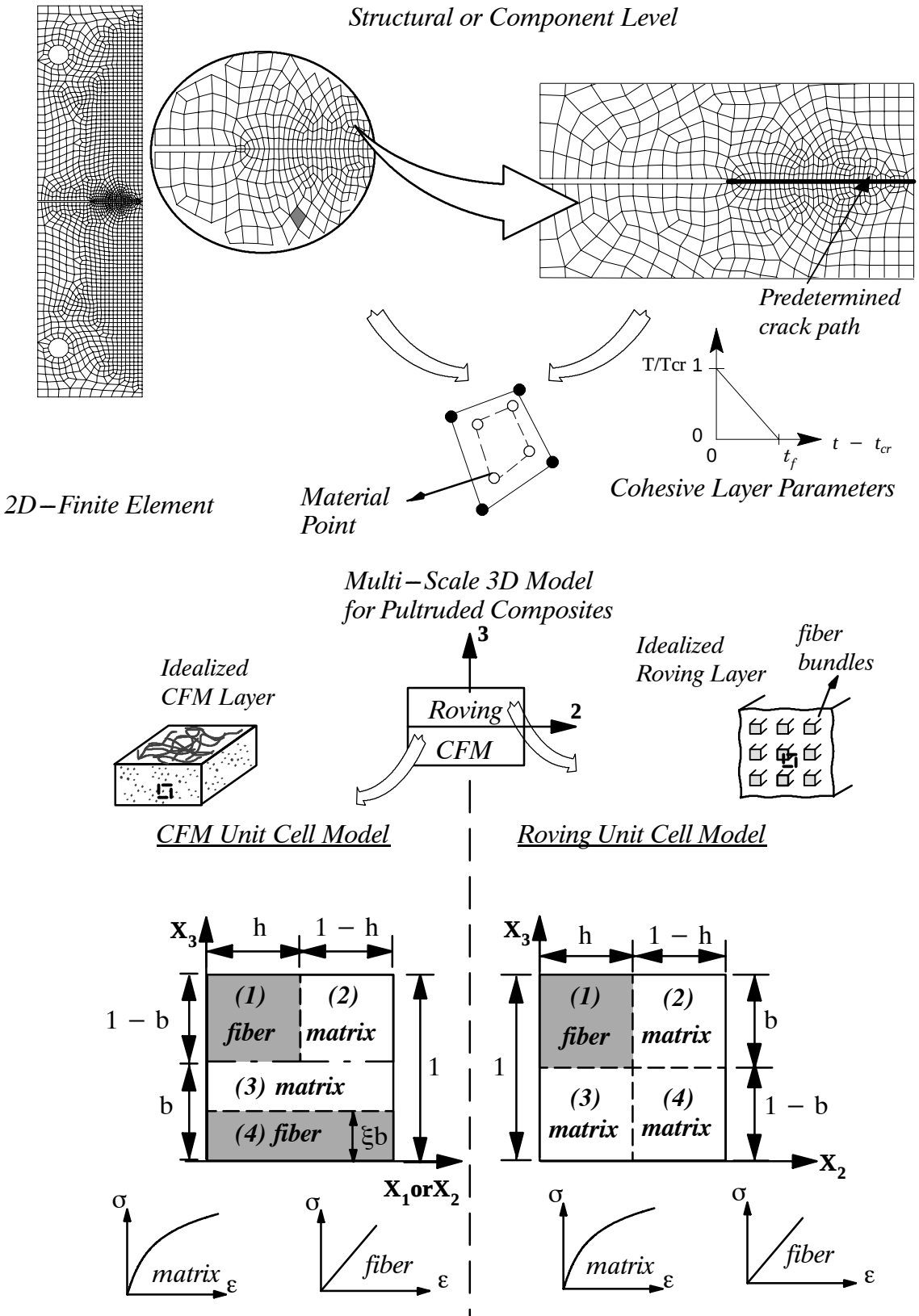

Figure 5.1 A framework for 3D nonlinear analysis of pultruded composite structures

5.2 Implementation of Integrated Micromechanical/Cohesive Models

The formulation, calibration and predictive capability of the nonlinear three-dimensional micromechanical constitutive models for the roving and CFM layers were presented in Chapter 2. The two micromodels were formulated using state variables in the form of average stresses and strains in their unit cells. The micromechanical equations that involve the state variables represent crude approximations for the traction and displacement continuity between the fiber and matrix phases in the two models. The proposed micromodels are implemented as a nested set of nonlinear constitutive models in a displacement-based FE code (Abaqus, 2002). To use the constitutive models with 2D FE fracture simulations, a plane-strain constraint is imposed on the top level sublaminate model to force a zero out-of-plane strain for the effective continuum. The fiber subcells are linear while the matrix is considered as nonlinear using the J2 plasticity with the Ramberg-Osgood nonlinear uniaxial representation. It was also shown how off-axis stress-strain responses of E-glass/polyester coupons were predicted by the proposed micromodels. The results demonstrate the ability of the proposed models to predict the nonlinear stress-strain response for general multi-axial stress states.

The cohesive layer fracture model is combined with the nonlinear constitutive material micromodels to study the behavior before and after the onset of crack propagation. The FE analysis was performed on different ESE(T) and SEN(T) specimen geometries. A fracture surface (cohesive layer) is introduced at the center and finely meshed with further refinement around the notch tip. Uniform displacements are applied at the remote node where the resultant force from the pin loading is assumed to act. The use of a specified crack path a priori is justified because of self-similar mode-I crack growth (See Figure 4.9). This is verified from repeated tests conducted in this study. A linear traction separation law is used to simulate the creation of traction free surfaces by ramping the nodal forces to zero with continued loading. The ABAQUS (2002) implicit finite element code is used with 4-node continuum plane strain elements (CPE4). A convergence study was initially performed to

determine an adequate mesh size. The ESE (T) average model size includes approximately 3000 elements and 3200 nodes. The SEN(T) average model size is 4500 elements and 5000 nodes. The use of micromechanical constitutive models allows plotting the average deformations at the CFM and roving layers while monitoring the crack growth. Axial and transverse stress contours are plotted for different loading levels for the roving and CFM layers. Figures 5.2 to 5.5 show the stresses in the homogenized roving and CFM layers for both ESE(T) and SEN(T) geometries, respectively. The stresses in these layers are plotted at the load that matches the maximum load from the experimental results. The stresses in the roving layers are not as close to their ultimate strength value. Damage is more wide-spread in the CFM layers.

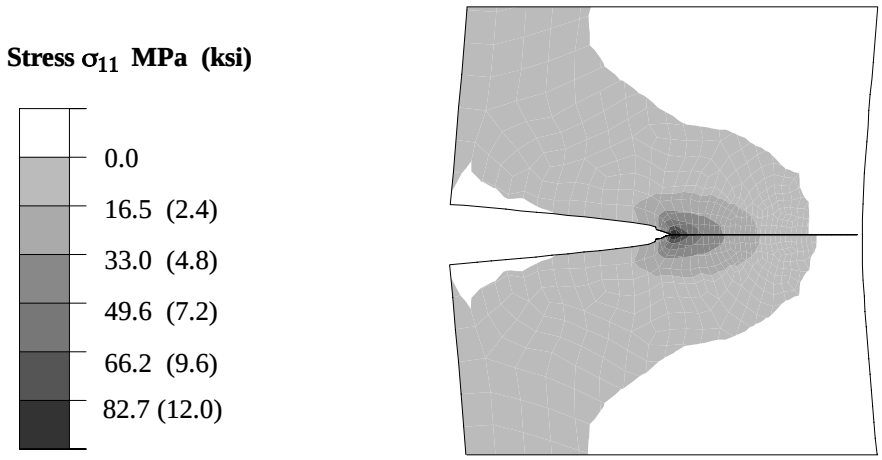

(a) Axial Stress (T-stress)

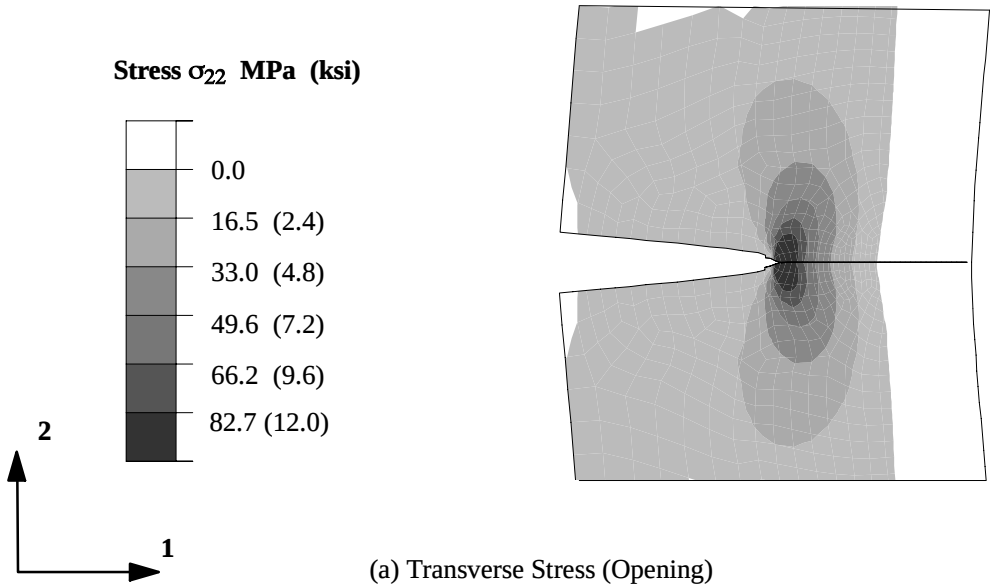

(a) Transverse Stress (Opening)

Figure 5.2 Axial and transverse stress contours in CFM layer from ESE(T) with a/W=0.5 at maximum load of 4.32 kN (0.971 kips)

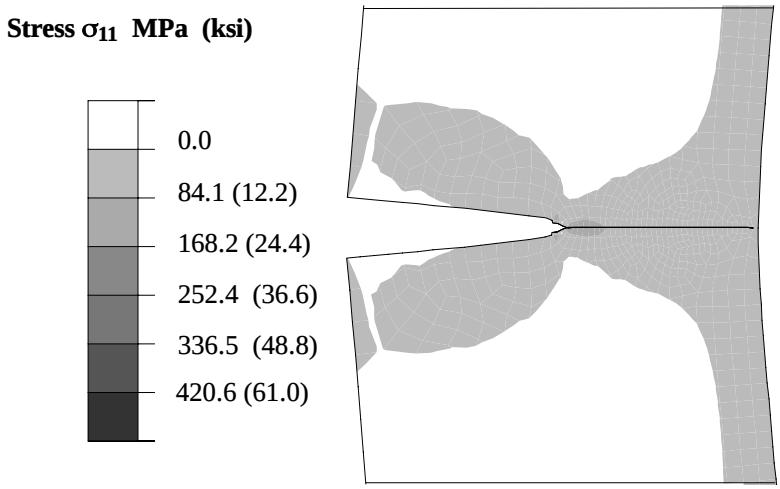

(a) Axial Stress (T-stress)

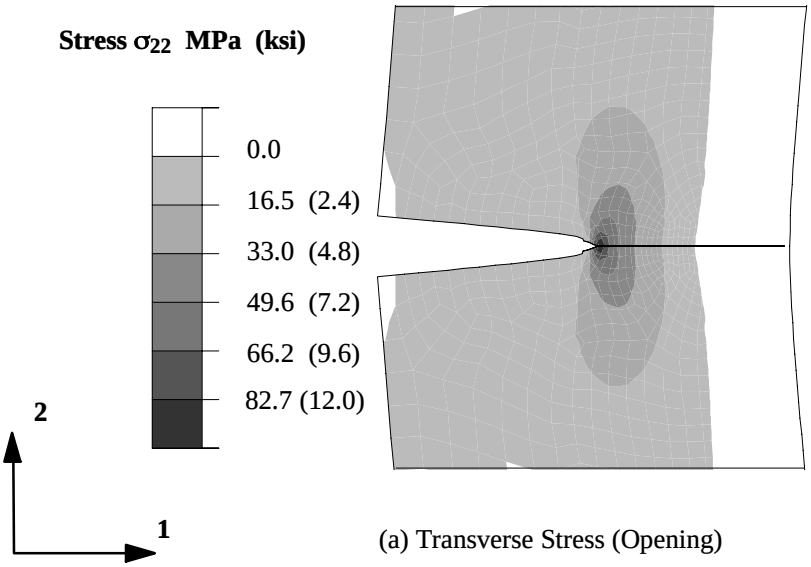

(a) Transverse Stress (Opening)

Figure 5.3 Axial and transverse stress contours in the roving layer from ESE(T) with a/W=0.5 at maximum load of 4.32 kN (0.971 kips)

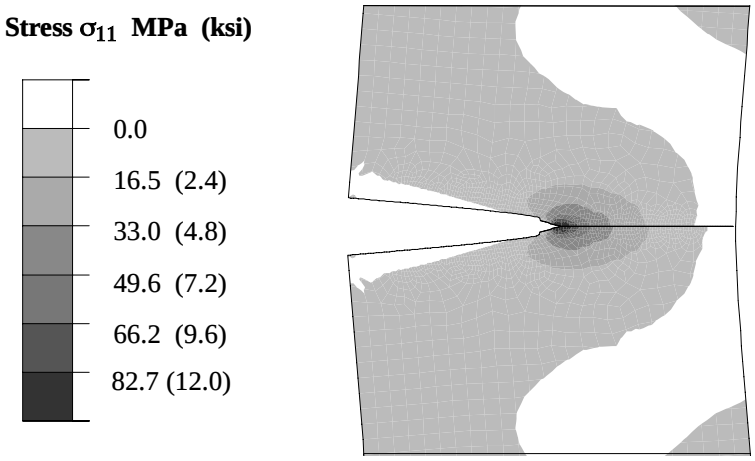

(a) Axial Stress (T-stress)

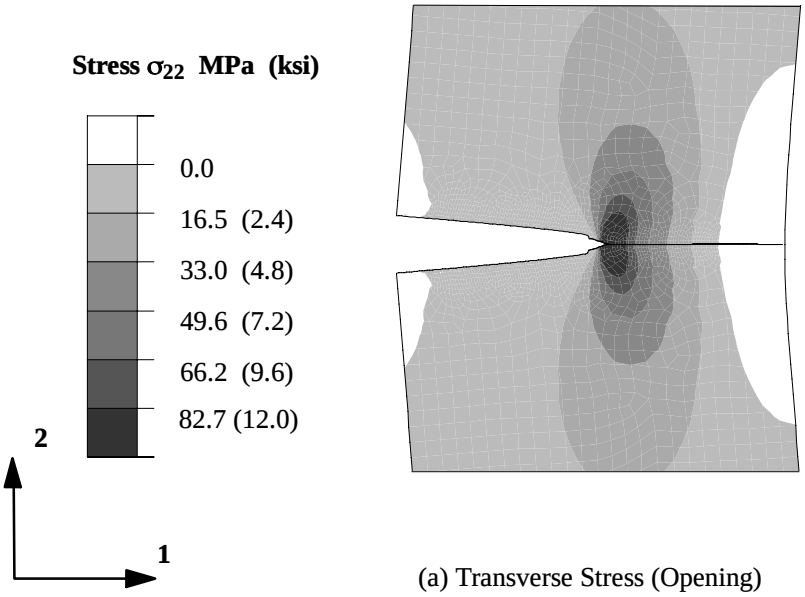

(a) Transverse Stress (Opening)

Figure 5.4 Stress contours in CFM layer from SEN(T) with a/W=0.5 at maximum load of 8.55 kN (1.923 kips)

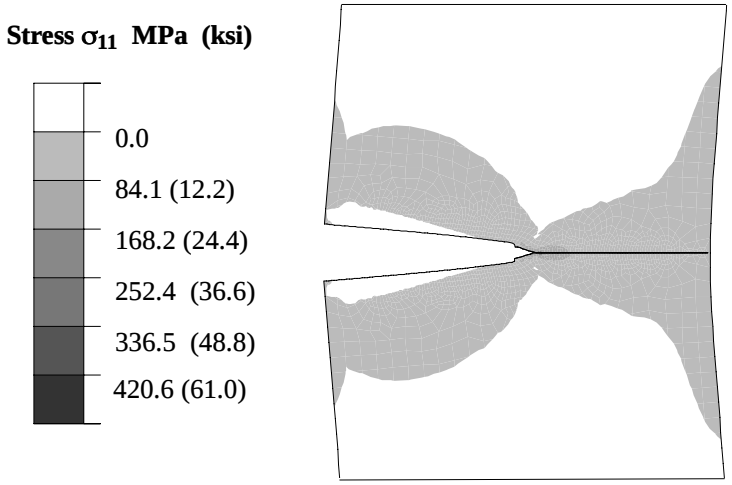

(a) Axial Stress (T-stress)

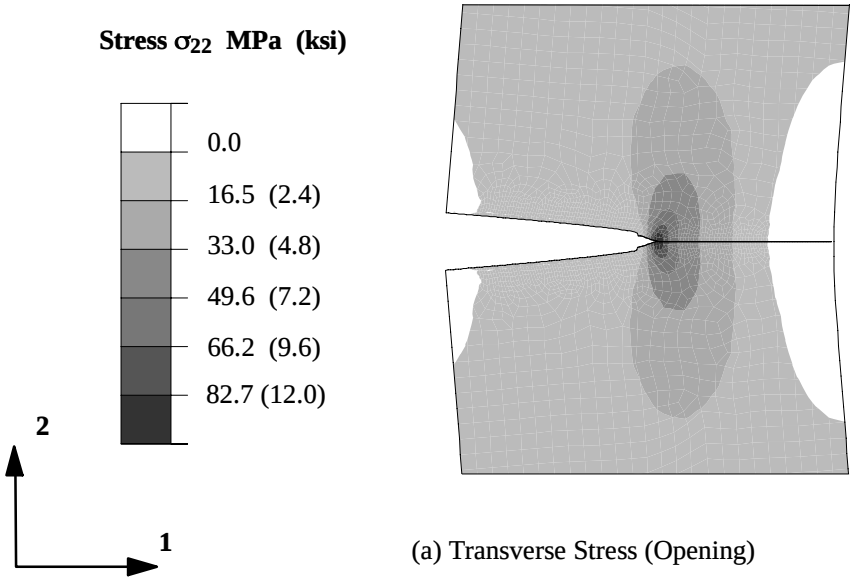

(a) Transverse Stress (Opening)

Figure 5.5 Stress contours from roving layer in SEN(T) with a/W=0.5 at maximum load of 8.55 kN (1.923 kips)

Calibration of Integrated Models

In Chapter 2, the calibration of the micromodels for the E-glass/polyester composite used in this study was presented. The CFM and roving micromodels were calibrated by assuming the same linear and nonlinear in-situ properties for their fiber and matrix subcells. These are taken from known or assumed values. In addition, the FVFs and thicknesses for the CFM and roving layers were used to complete the calibration. Coupon tests were performed to calibrate and correlate the off-axis stiffness and the nonlinear stress-strain response in tension and compression. The fracture tests on ESE(T) and SEN(T) specimen were conducted in accordance to the ASTM E1922 standard test method for translaminar fracture toughness of laminated polymer matrix composite materials. The geometry of the ESE(T) specimen is shown in Figure 5.6. Chapter 4 describes in detail the test procedures used to conduct these tests. Tests on SEN(T) specimen were also used to verify the modeling approach. The experimental load-NMOD for an ESE(T) specimen with a/W=0.5 was used to calibrate the parameters of the cohesive model. The cohesive normal failure stress, σ_n^f was set to 82.7 MPa (12 ksi) for the transverse fracture and to 151.6 MPa (22 ksi) for the axial fracture. These values are close to the unnotched uniaxial tensile strengths for both orientations. The release-time taken for the interface tractions to be ramped to zero was t_f = 0.03. The analysis was complete when the pseudo time reached t = 1.0. The distance from the crack tip at which the failure criterion was evaluated was taken as L_c = 1.78 mm (0.07 in) for both orientations. Figures 5.7 and 5.8 show the calibration curves for the ESE(T) specimen in the transverse and axial orientations respectively.

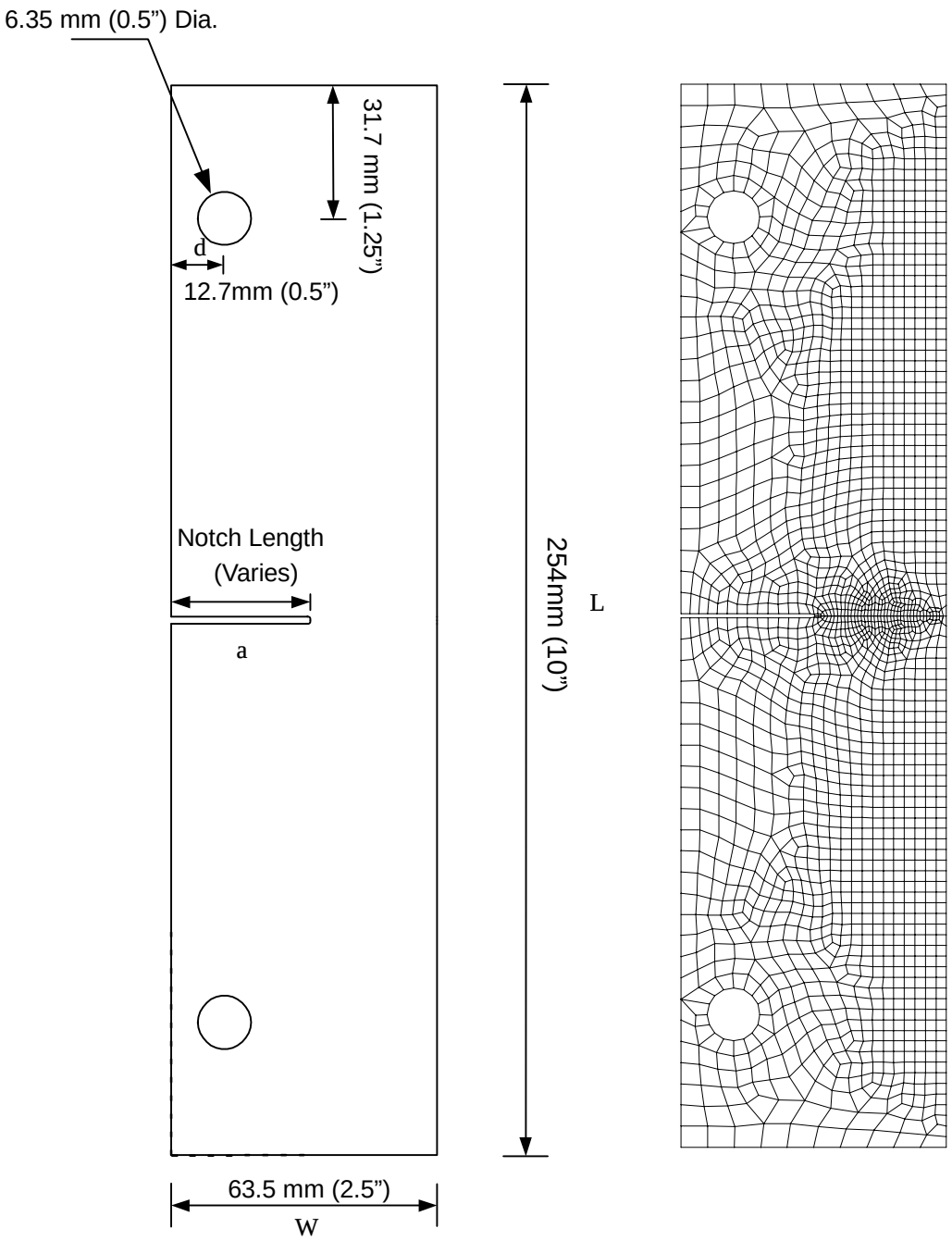

Figure 5.6 Typical ESE(T) test specimen with FE mesh

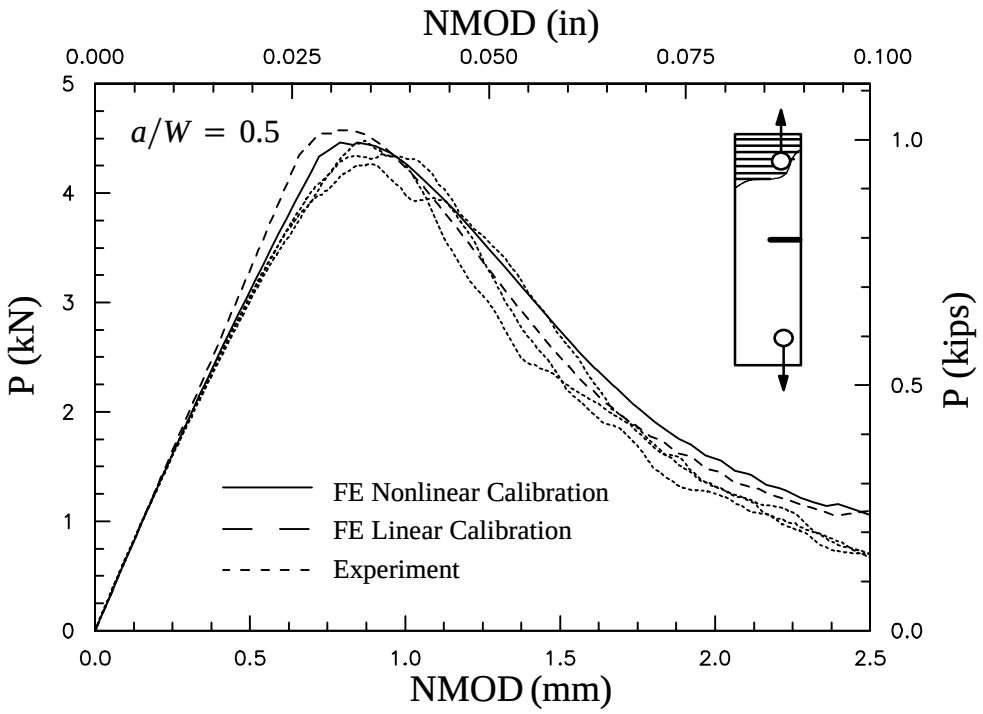

Figure 5.7 Load vs. NMOD response used for calibration of cohesive layer parameters from transverse ESE(T) specimens with a/W=0.5

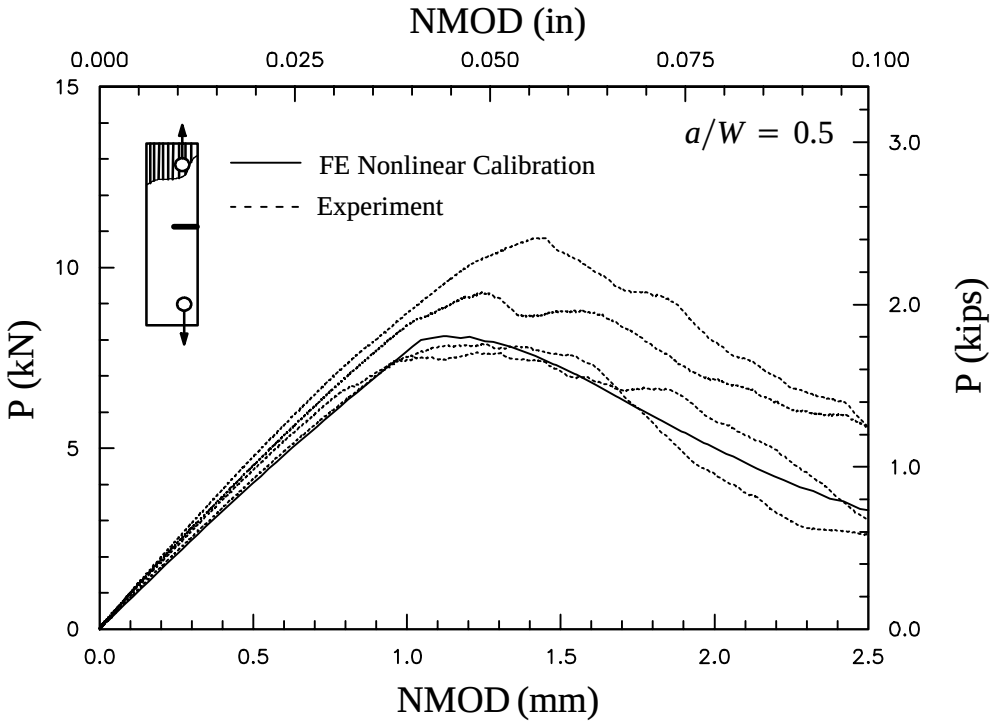

Figure 5.8 Load vs. NMOD response for calibration of cohesive layer parameters from axial ESE(T) specimens with a/W=0.5

5.3 Application of TSA to Verify Integrated Models

To verify the proposed integrated models, IR thermography tests using a new TSA method were performed on ESE(T) specimens. Chapter 3 presents a full discussion of this new method and its application on pultruded composites. The technique is used to measure the TSA signal and relate it to the sum of the in-plane direct strains on the surface. The TSA signal observed in pultruded composites is largely the result of the response in the polymer rich surface layer (CFM/veil). The tested specimens were coated with flat black paint to improve the surface emissivity. To acquire a TSA image, a sinusoidal load was applied with an amplitude of 1.22 kN (0.275 kips), frequency of 5Hz, and a mean value of 2.67 kN (0.6 kips). Data from the images were averaged by allowing an exposure time of 5 minutes during the applied loading. During the exposure time, TSA measurements were synchronized with the peaks of the applied cyclic loading (reference signal). A surface strain contour from a TSA test along with the corresponding FE results, for the case of a transverse specimen is shown in Figure 5.10. Good correlation was obtained between the cardoid shape of the strain field in both the FE and experimental contours. TSA results were compared with FE predictions along the crack line for ESE(T) specimen with both axial and transverse roving orientations, as shown in Figures 5.11 and 5.12, respectively. Localized damage and high strain levels near the crack tip may contribute to the deviation from the linear FE results near the crack tip. This nonlinearity or damage was manifested in the out-of-phase TSA response in this region. The TSA strain measurements compare favorably with FE results especially away from the notch tip.

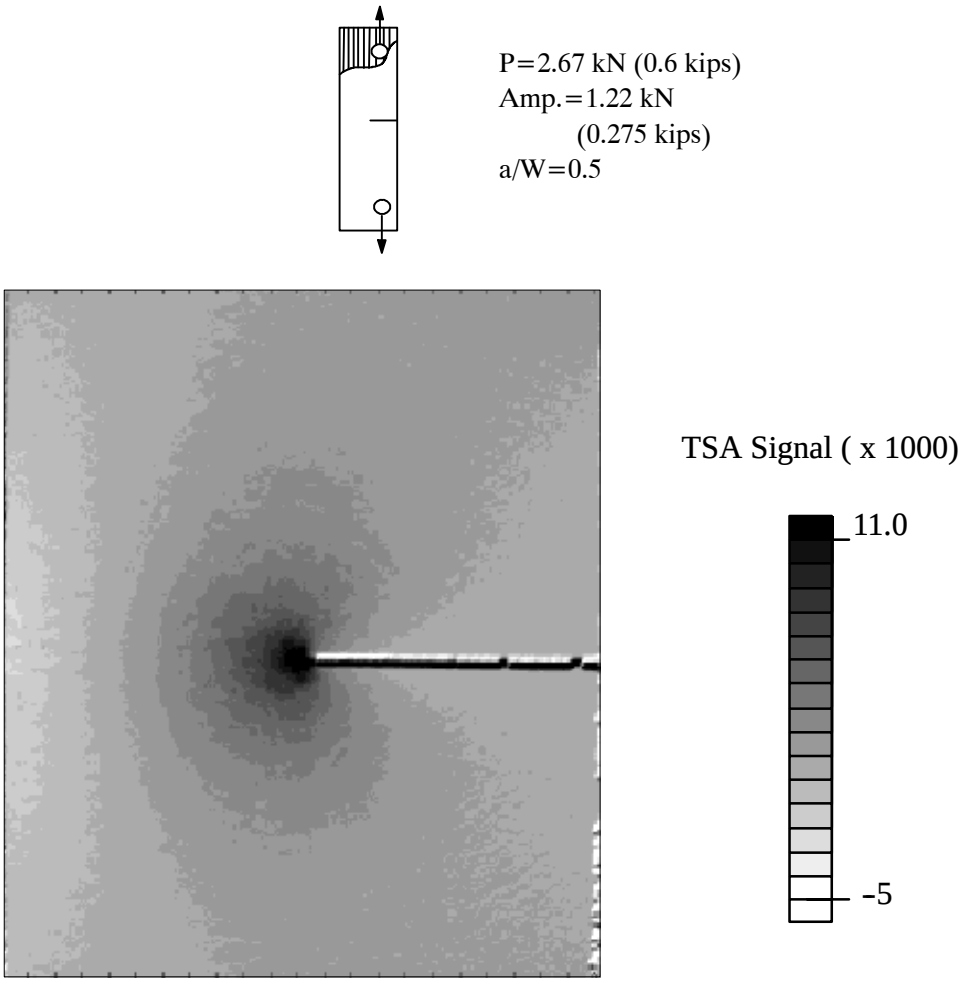

Figure 5.9 TSA image of axial ESE(T) specimen with a/W=0.5

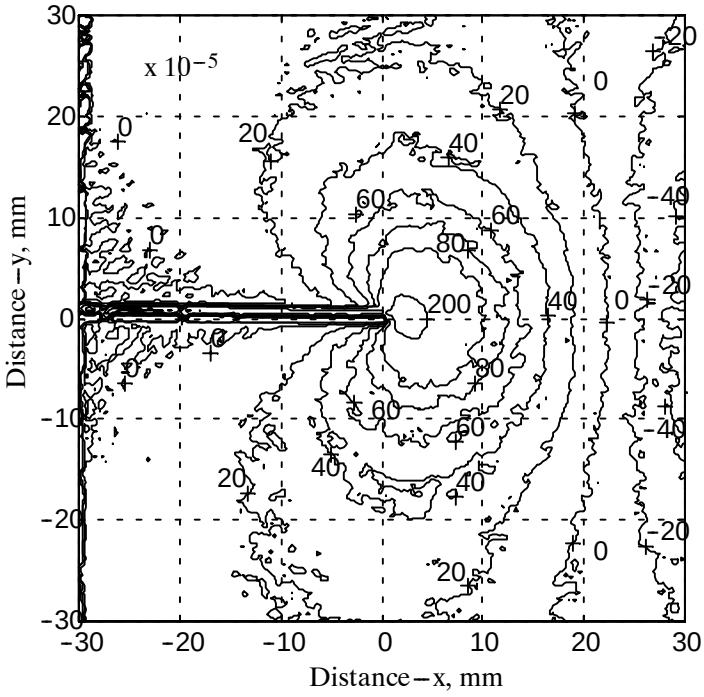

(a) TSA, Sum of direct in−plane strains around notch tip

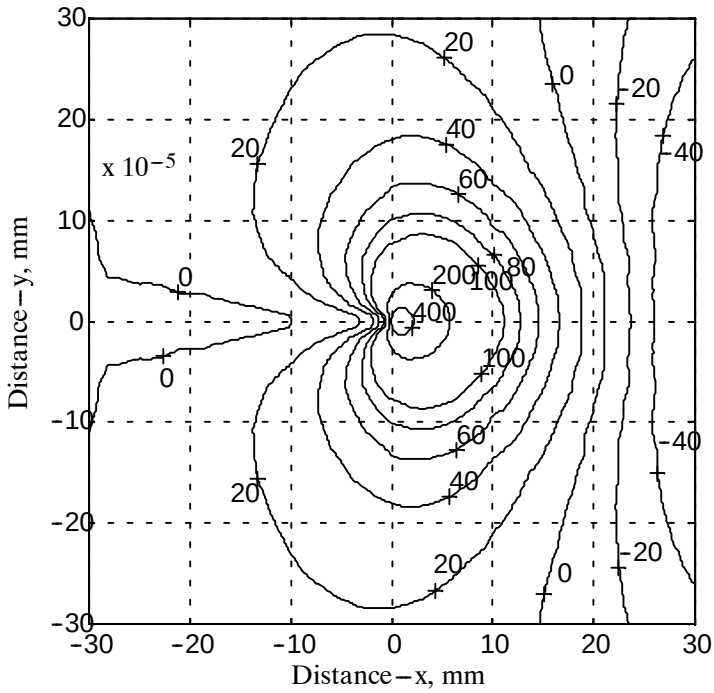

(a) FE, Sum of direct in−plane strains around notch tip

Figure 5.10 Strain contours of an ESE(T) specimen from TSA experiments and FE

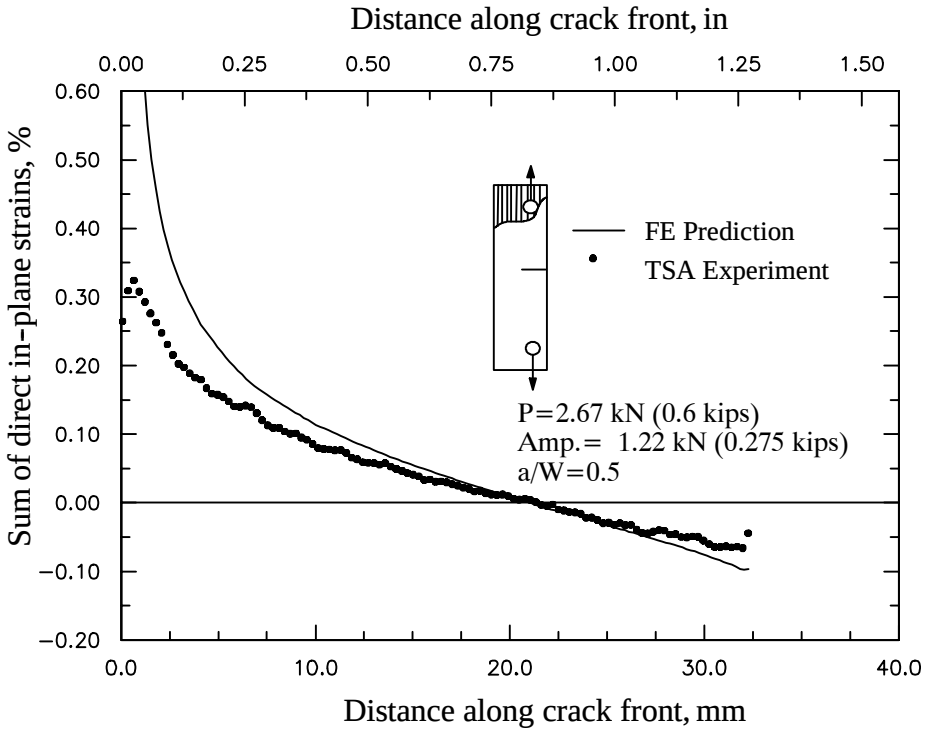

Figure 5.11 Experimental TSA and FE strains near crack tip in axial specimen

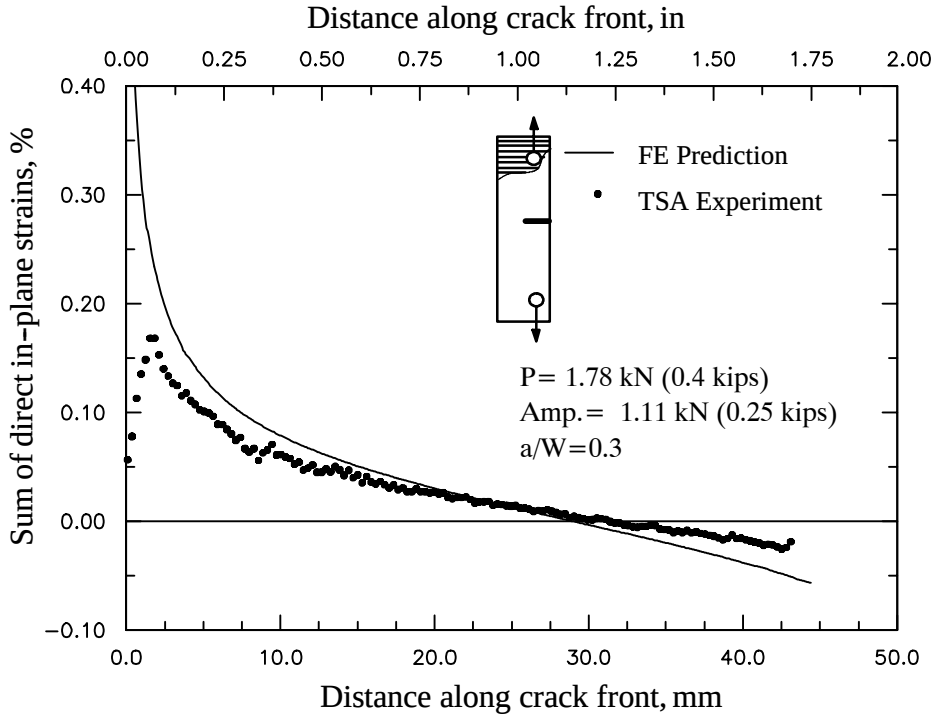

Figure 5.12 Experimental TSA and FE strains near crack tip in transverse specimen

5.4 Prediction of the Fracture Response

After the calibrations are performed, the proposed integrated models are used to predict the response and crack growth of other ESE(T) geometries. This modeling approach was also verified on a range of SEN(T) specimen. Good prediction is demonstrated by the combined fracture modeling approach for all ESE(T) coupons. The predicted load–NMOD results from the nonlinear micromodels with the cohesive FE are shown in Figures 5.13 – 5.16 for transverse ESE(T) specimen with a/W=0.3, 0.4, 0.6 and 0.7. The initial effective linear and some nonlinear responses are captured by these analyses. Figures 5.17 – 5.19 also shows the predicted response for the transverse SEN(T) fracture geometries. The same calibrated parameters, from transverse ESE(T) with $a/W = 0.5$ are used in the SEN(T) case. Good prediction is also shown for the SEN(T) fracture response. The predicted load–NMOD response when using the nonlinear micromodels better match the experimental data when compared with the FE models with homogenized linear properties. The predicted maximum loads from the nonlinear models are generally higher than the experimental results for the larger a/W values. This may be attributed to an added softening from a larger damaged zone. It is interesting to note that crack growth is predicted before the maximum applied load, e.g. for ESE(T) and SEN(T) with small $a/W = 0.3$. Good correlations are also seen in the predicted load–NMOD results, in the axial orientations as shown in Figures 5.20 and 5.21 for ESE(T) specimen with a/W=0.3 and 0.7.

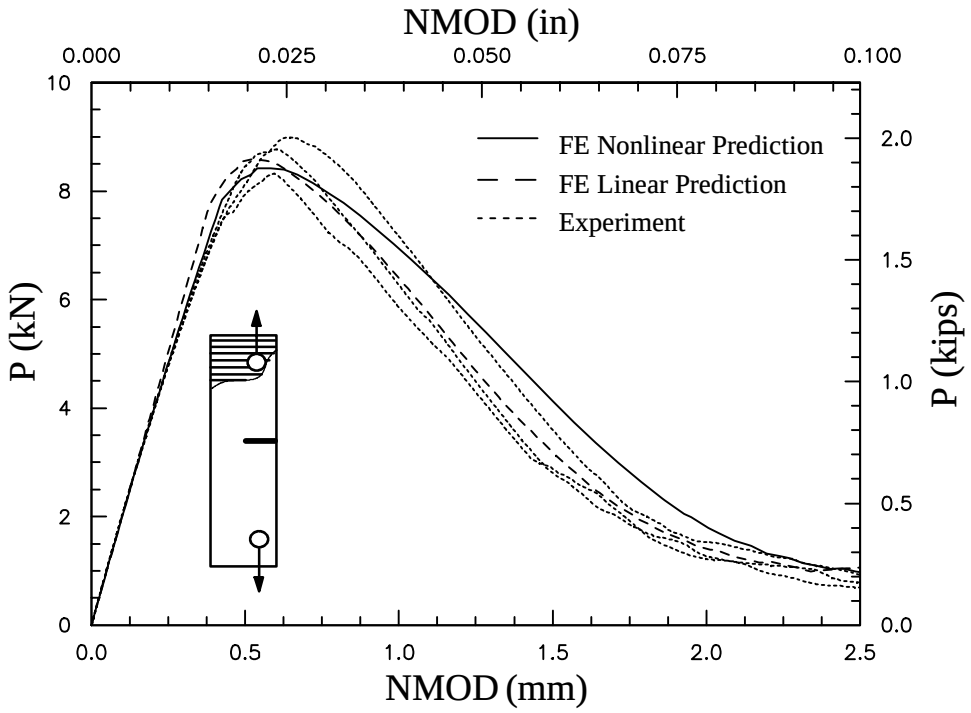

Figure 5.13 Prediction of load vs NMOD response in ESE(T) specimen for a/W=0.3

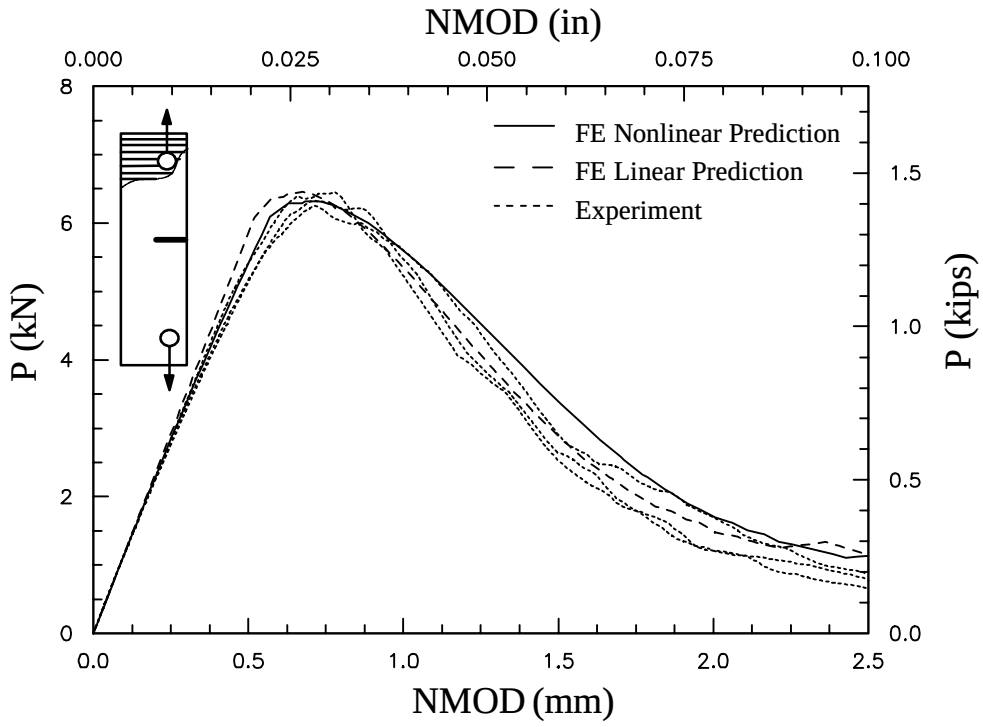

Figure 5.14 Prediction of load vs NMOD response in ESE(T) specimen for a/W=0.4

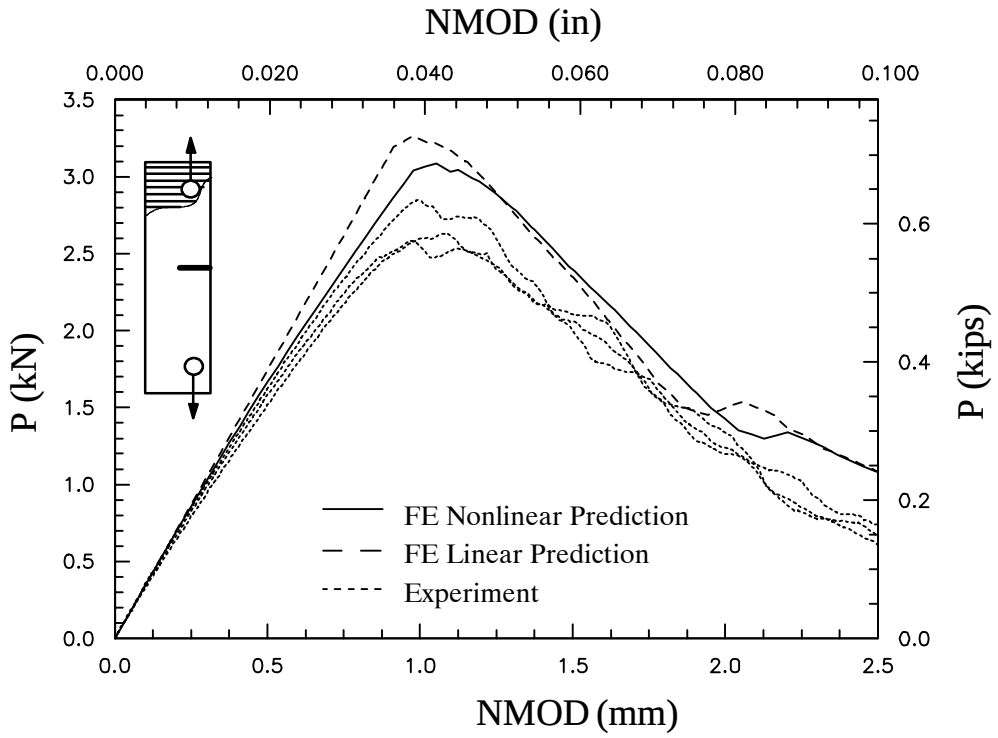

Figure 5.15 Prediction of load vs NMOD response in ESE(T) specimen for a/W=0.6

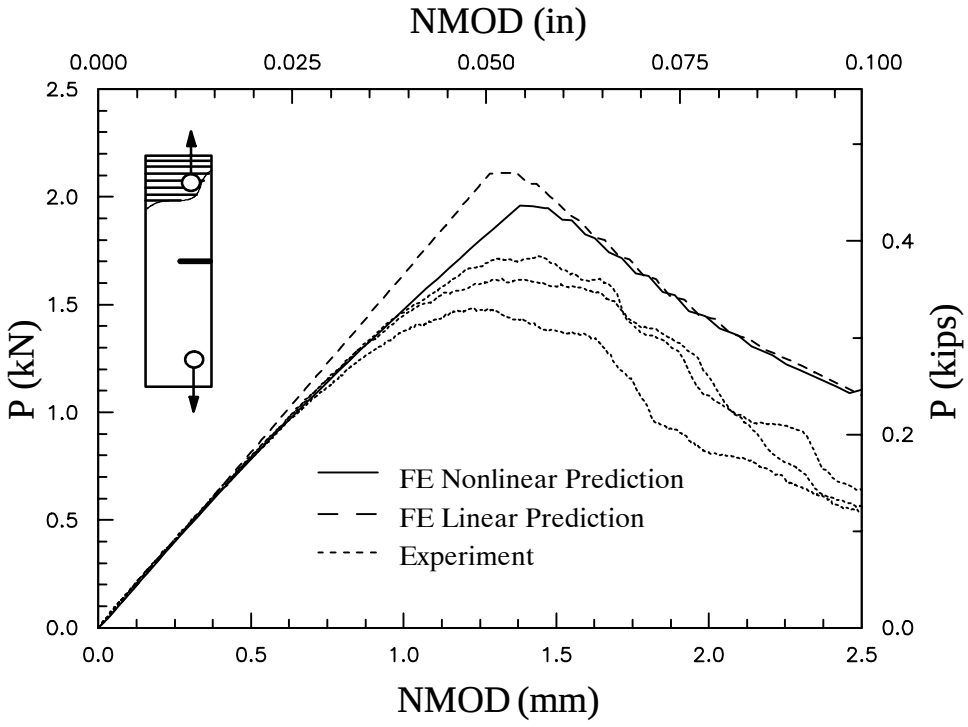

Figure 5.16 Prediction of load vs NMOD response in ESE(T) specimen for a/W=0.7

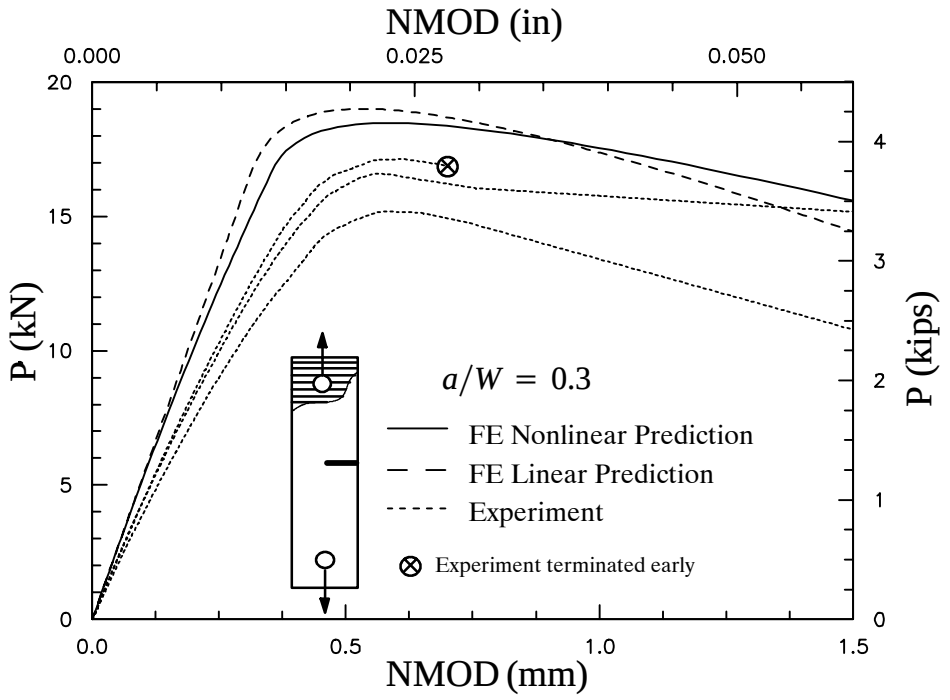

Figure 5.17 Prediction of load vs NMOD response in SEN (T) specimen for a/W=0.3

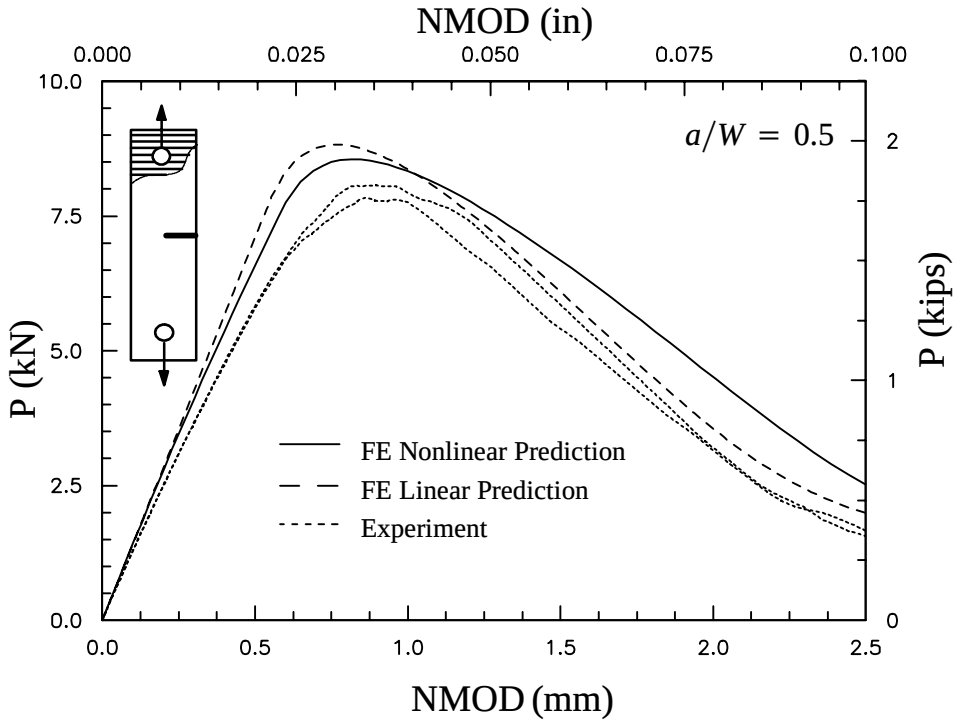

Figure 5.18 Prediction of load vs NMOD response in SEN (T) specimen for a/W=0.5

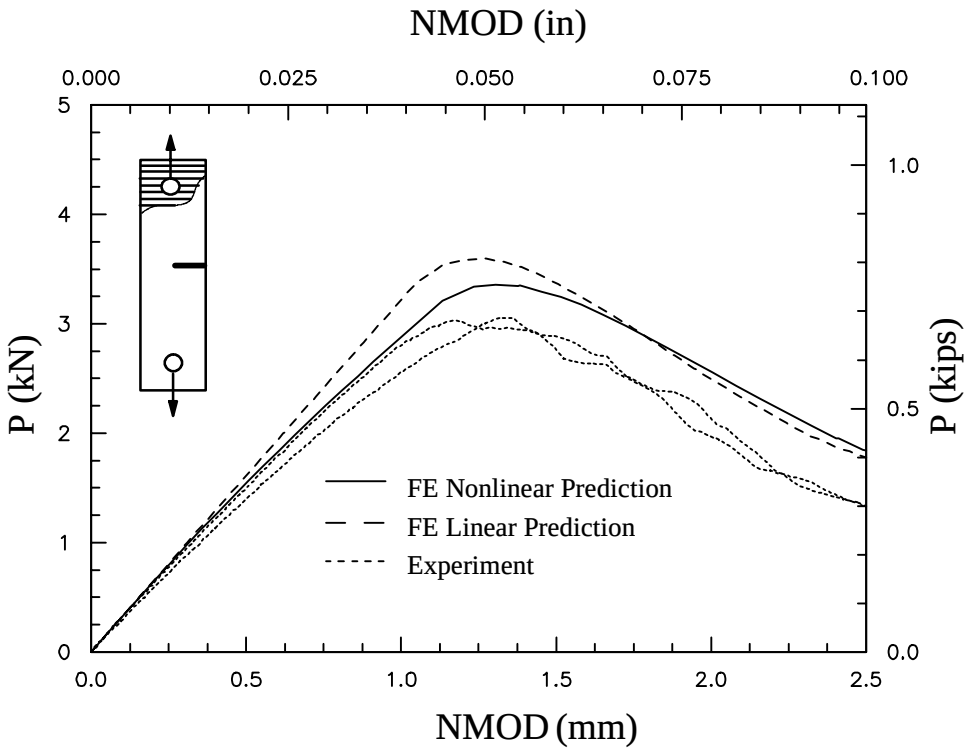

Figure 5.19 Prediction of load vs NMOD response in SEN (T) specimen for a/W=0.7

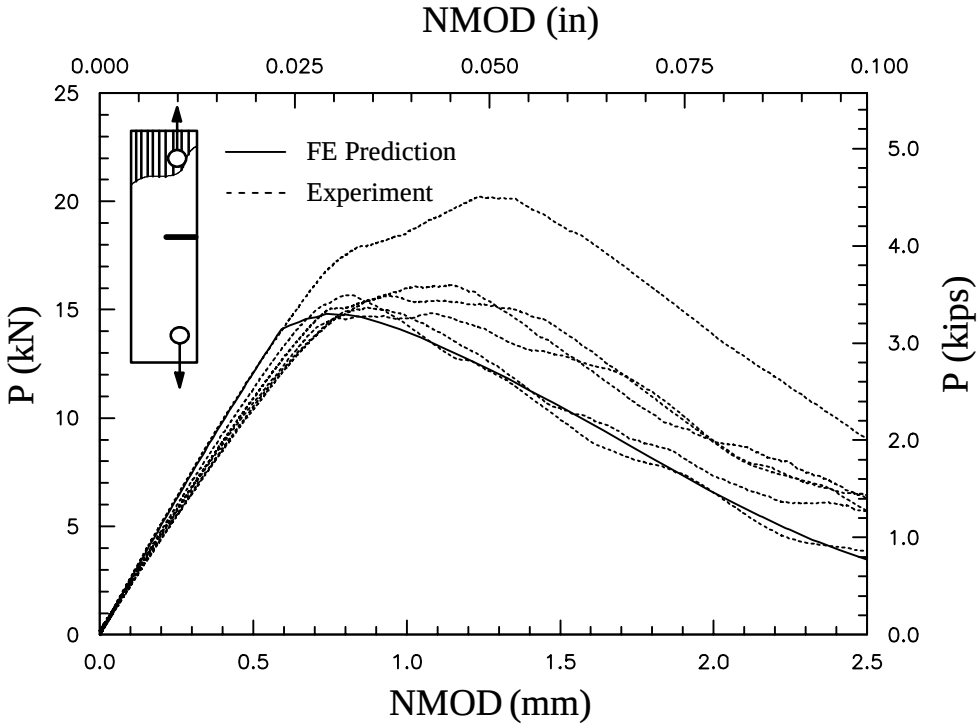

Figure 5.20 Prediction of load vs. NMOD response for axial ESE(T) specimen with a/W=0.3

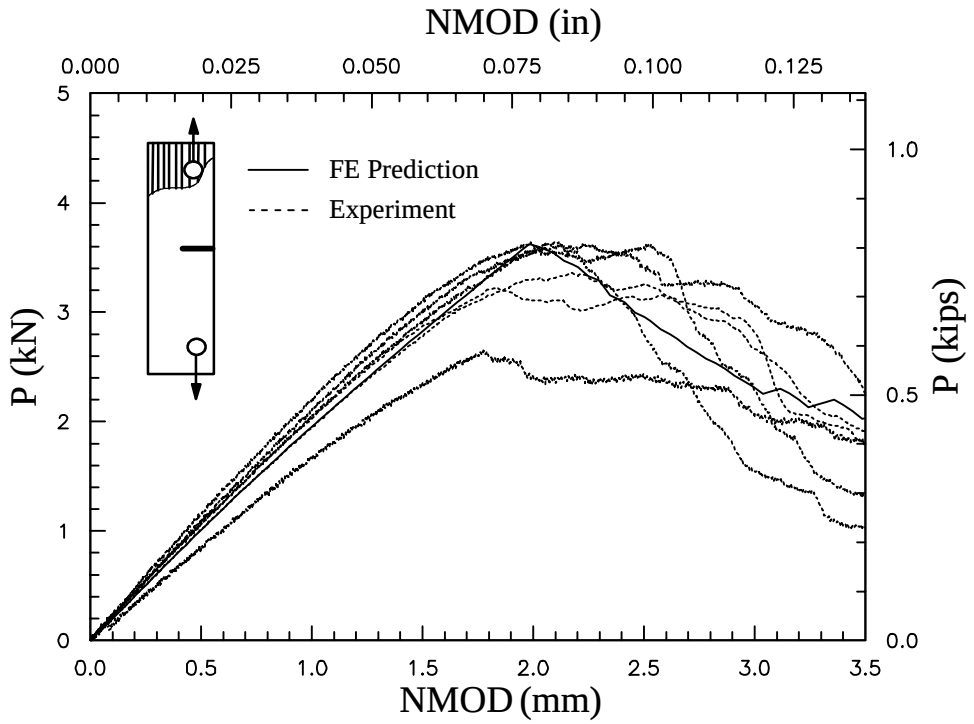

Figure 5.21 Prediction of load vs. NMOD response for axial ESE(T) specimen, a/W=0.7

5.5 Prediction of Crack Growth Response

Crack growth was monitored during the fracture tests using metallic foil crack propagation gages bonded to the surfaces of the ESE(T) specimen (See Chapter 4). The range of tested pultruded ESE(T) specimen included a/W ratios between 0.3 to 0.7 with both axial and transverse roving orientations. The crack propagation gage utilizes the in-direct potential drop method for measuring the crack growth (Hartmann and Churchill, 1981). The gage was bonded to the specimen in a similar way to the bonding of resistance strain gages, and was excited using a constant current. The propagation of the crack causes a proportional change in voltage across the gage. The crack length was determined from the linear relationship between the change in voltage and the crack length. The gages used were able to measure up to 30 mm (1.18 in) of crack growth and capture cracks growing away from the center line. This can be important in unidirectional ESE(T) specimen where the propagating crack is not always horizontal. The signal from the gage was measured

simultaneously with other test data, such as the load and NMOD. Two gages were attached to each specimen to measure the crack growth on both sides. Figure 4.6 shows a crack propagation gage bonded to an ESE(T) specimen. The accuracy of the acquired crack growth measurements were within 0.1% of the gage length. Crack growth results from the FE ESE(T) models are plotted in Figures 5.22 – 5.27 and compared with experimental results. The crack growth curves are plotted on the right y-axis and the load is plotted on the left y-axis. Both curves share the same NMOD x-axis. Experimental results show limited crack growth occurring before the peak load, e.g. for ESE(T) with small $a/W = 0.3$. Approximately 3 mm (0.12 in) of crack growth is observed in some cases. The cohesive models were able to account for the limited crack growth prior to attaining maximum load. The experimental results also show the crack growth to start earlier in the loading process. Crack growth was also found to be nearly identical on both sides of the transverse specimen. Figures 5.28 and 5.29 show the opening stress contours in ESE(T) and SEN(T) specimen after the onset of crack propagation from the integrated modeling approach. More variability in the load-NMOD response was observed in the axial orientations. Self-similar crack growth was evident in all axial specimen, probably due to the relatively low fiber volume fraction and the relatively smaller thickness of the roving layers. Self-similar crack growth was evident by examining the specimen after complete fracture occurred in both the transverse and axial specimen. This justifies the use of mode-I models with symmetric crack paths. Limited deviations from a straight (flat) crack were also observed, while the overall growth was self-similar in nature. This small disparity in the back-to-back crack growth can be attributed to a non-uniform through-thickness growth within the CFM and roving interior layers. In some of these test results (e.g. Figure 5.21 and 5.23), the deviation in the initial linear elastic response was due to a larger initial notch size.

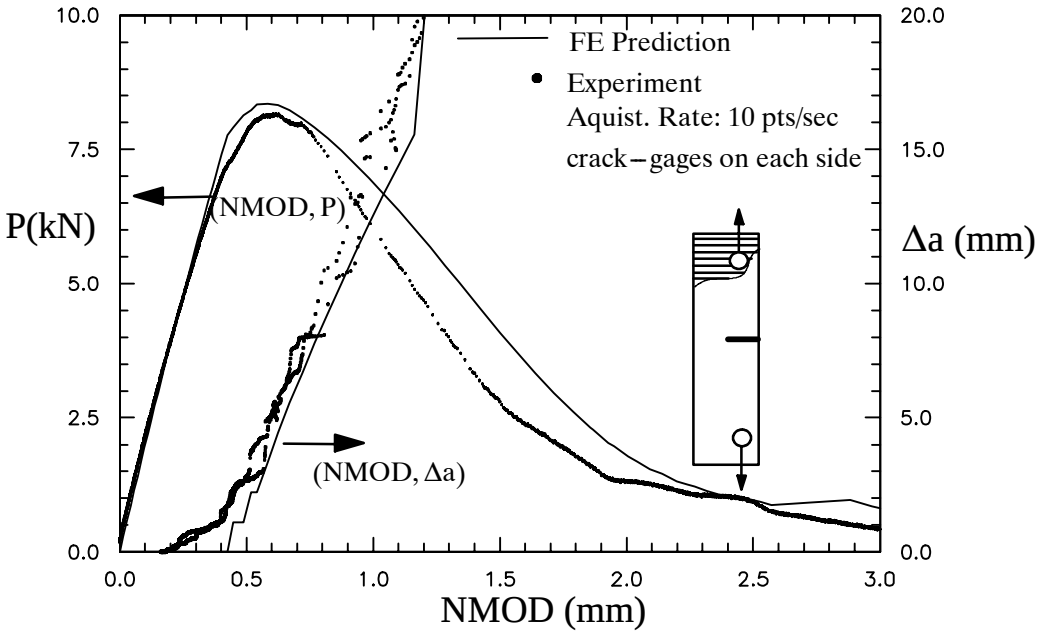

Figure 5.22 Predicted crack growth for transverse ESE(T) specimen with a/W=0.3

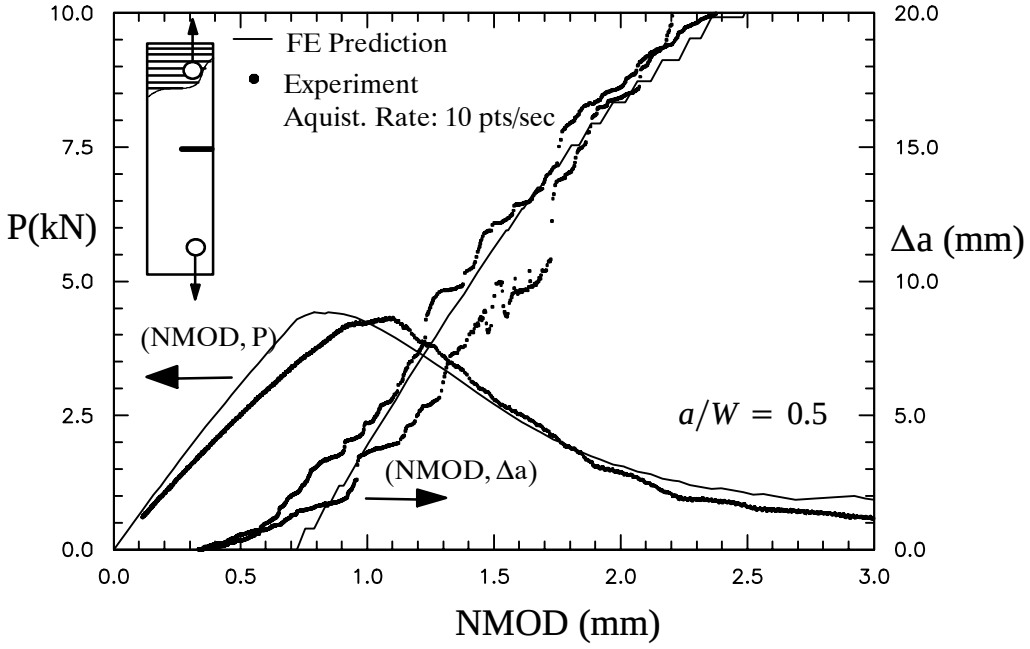

Figure 5.23 Predicted crack growth for transverse ESE(T) specimen with a/W=0.5

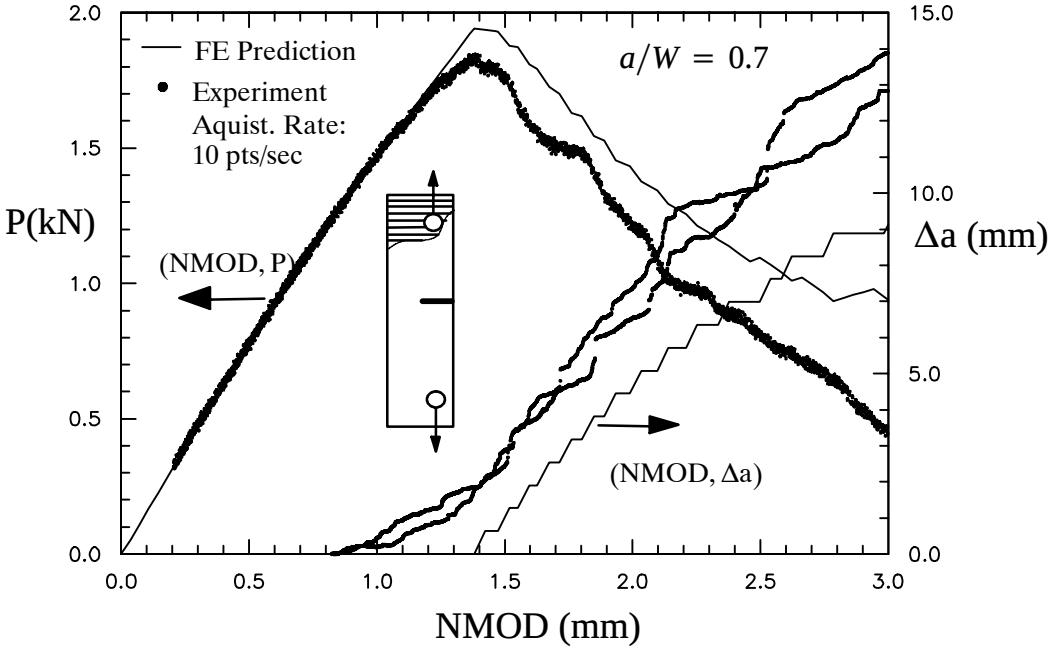

Figure 5.24 Predicted crack growth for transverse ESE(T) specimen with a/W=0.7

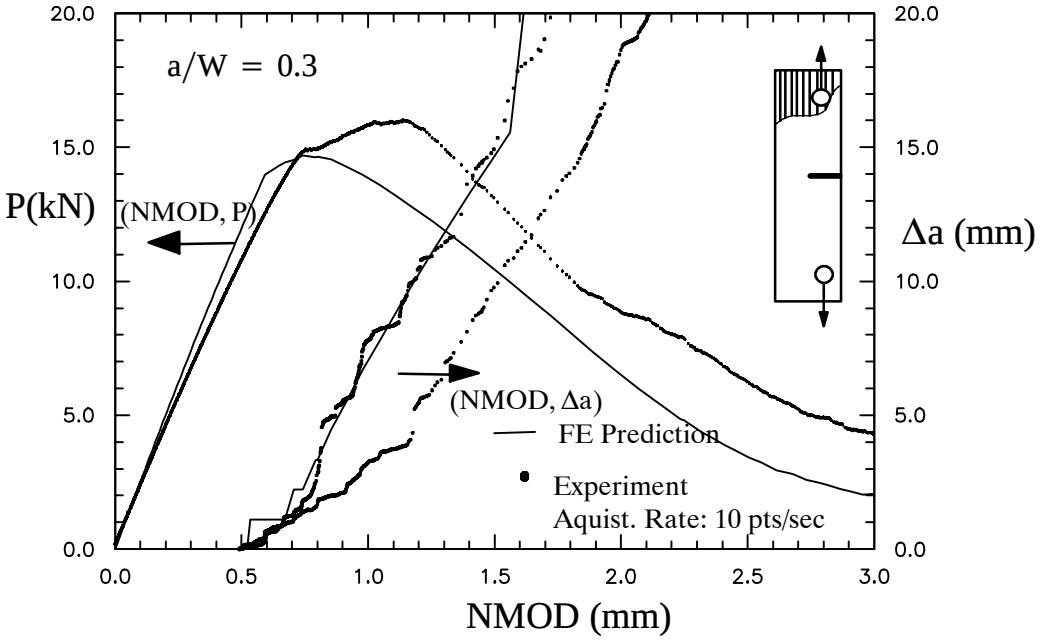

Figure 5.25 Predicted crack growth for axial ESE(T) specimen with a/W=0.3

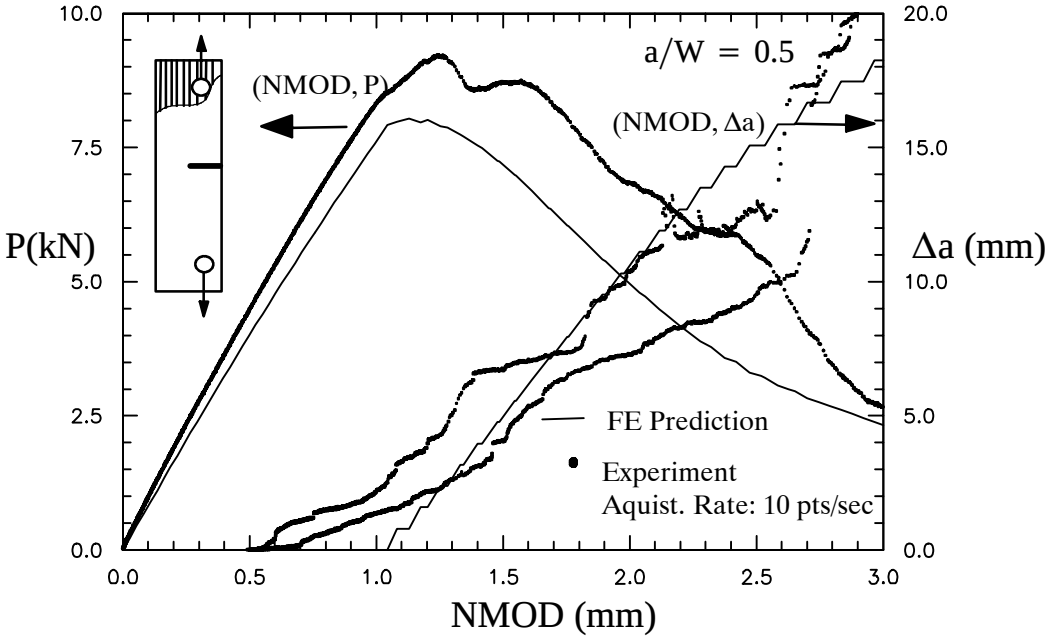

Figure 5.26 Predicted crack growth for axial ESE(T) specimen with a/W=0.5

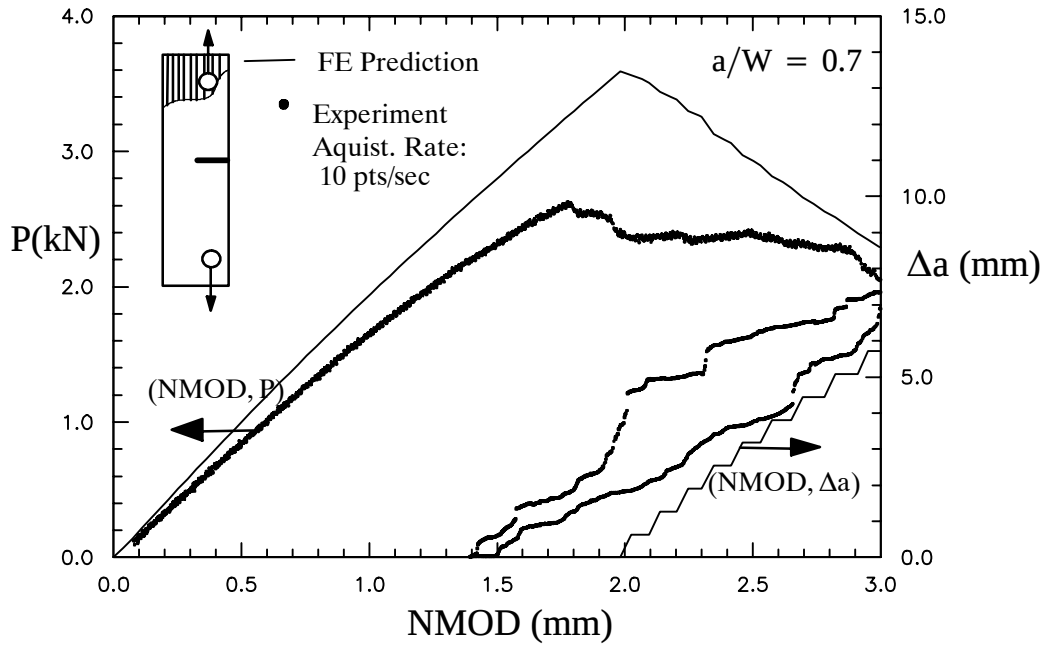

Figure 5.27 Predicted crack growth for axial ESE(T) specimen with a/W=0.7

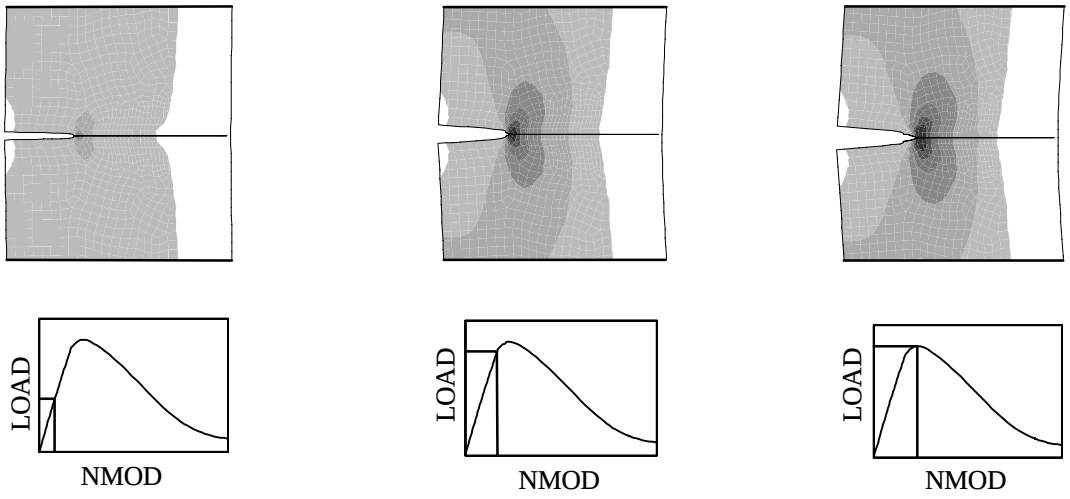

P	2.46 kN (0.554 kips)	7.78 kN (1.75 kips)	8.36 kN (1.88 kips)
Δ a	-	-	3.32 mm (0.131 in)

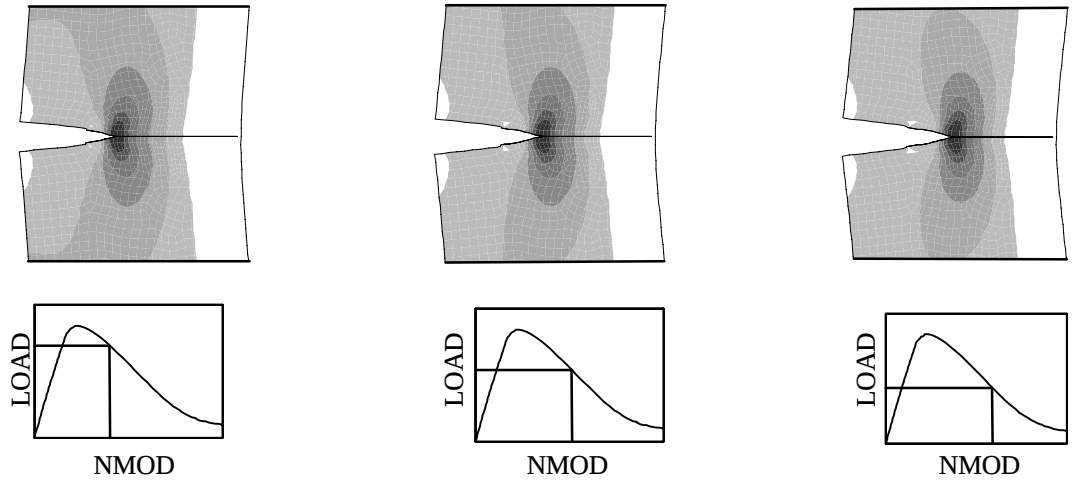

P	7.87 kN (1.772 kips)	7.23 kN (1.625 kips)	6.68 kN (1.501 kips)
Δ a	7.77 mm (0.306 in)	1.94 mm (0.437 in.)	13.5 mm (0.53 in)

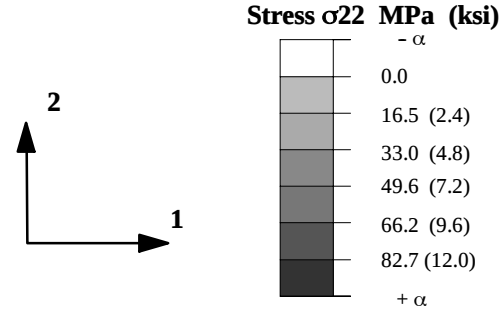

Figure 5.28 Stress contours from numerical simulation of crack propagation in ESE(T) specimen with a/W=0.3

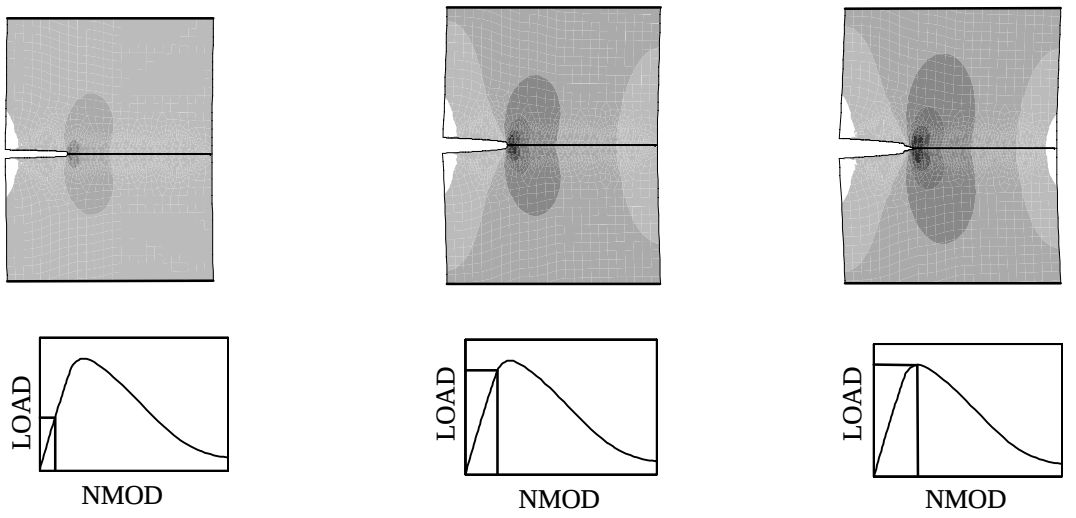

P	8.14 kN (1.83 kips)	16.9 kN (3.8 kips)	18.3 kN (4.12 kips)
Δ a	-	-	2.54 mm (0.1 in)

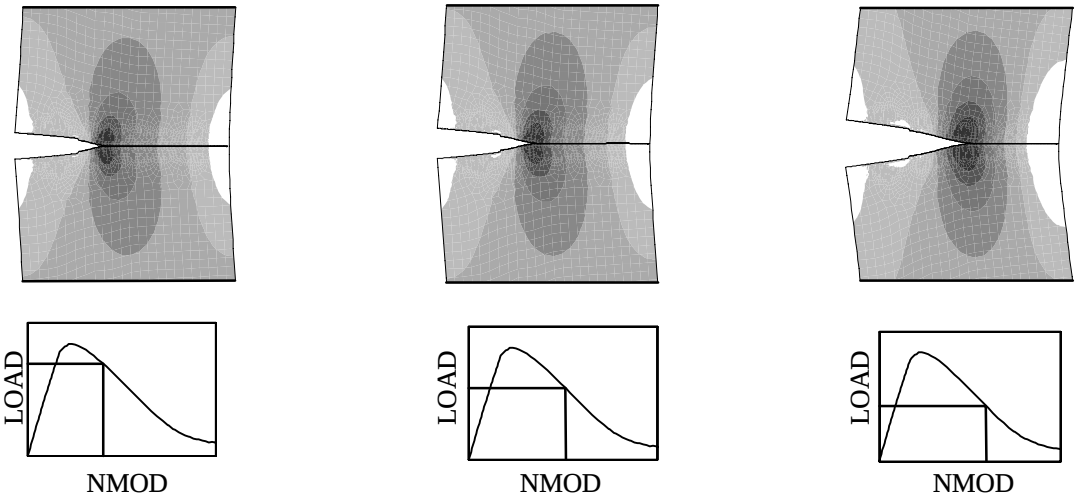

P	18.4 kN (4.13 kips)	18.1 kN (4.08 kips)	16.4 kN (3.68 kips)
Δ a	7.62 mm (0.3 in)	10.2 mm (0.4 in.)	17.8 mm (0.7 in)

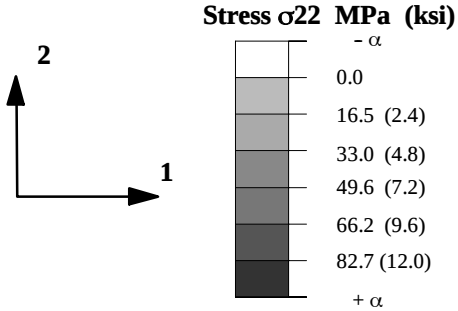

Figure 5.29 Stress contours from numerical simulation of crack propagation in SEN(T) specimen with a/W=0.3

CHAPTER 6

MODE-II FRACTURE TOUGHNESS AND CRACK GROWTH

In this chapter, a modified Arcan fixture with butterfly specimen geometry is designed to measure the translayer mode-II fracture response of thick-section pultruded FRP composites. Initially, the proposed fixture is examined in its ability to measure the shear moduli, nonlinear stress-strain response, and shear strength of pultruded composites under biaxial stress conditions. To optimize the design of the tested butterfly specimen, finite element (FE) models are generated to examine the effects of the notch radius and material orthotropy on the uniformity and distribution of stresses in the gage area. The axial-shear response is measured under different biaxial stress states by varying the angle of the applied load. The tested nonlinear shear stress-strain responses are compared to previous off-axis compression tests used to calibrate the multi-axial micromechanical constitutive model (Chapter 2). The presence of the direct stresses and their relative effect on the shear properties are also examined using strain gage rosettes. IR thermography testing is used in this case to examine the integrity of the butterfly specimen and the existence of a predominant region of 'pure shear' conditions at the center.

The butterfly geometry was modified for mode-II fracture toughness testing by an initiating an edge crack. The mode-II translayer fracture toughness was determined for different crack sizes for both the transverse and axial roving orientations. The VCCT method (Chapter 4) is also used to generate the stress intensity factors (SIF) of the tested material and geometries of the modified Arcan fixture. The cominbed micromechanical/cohesive modeling approach used for mode-I in Chapter 5 is also applied in this chapter to model the failure under mode-II conditions. To compare the experimental and numercial results, an apparent sliding strain metric is proposed. The apparent sliding strain from the FE models was compared with the mode-II tests using a simple optical grid analysis technique.

6.1 Modified Arcan Test Fixture and Butterfly Specimen

The test fixture used in this study is similar to the one originally proposed by Arcan et al. (1978) and modified by Yen et al. (1998). The modifications proposed by Yen et al. include bolting a butterfly-shaped specimen between two identical halves of the Arcan fixture. Using mechanical fastening and trapezoidal cutouts, specimens with different thicknesses can be accommodated without the use of adhesives. The fixture used in this study does not include a trapezoidal cutout. Instead, a larger number of bolts are used to connect the butterfly specimen to the steel fixture. The load is applied to the fixture using clevis pins to minimize out-of-plane forces and moments. Figure 6.1 shows a schematic of the modified Arcan fixture with the butterfly specimen. Biaxial stress states, can be obtained in a relatively simple manner by varying the angle (α) at which the load is applied. The fixture is made of four parts that are assembled using an alignment device. The entire fixture resembles a disk with a diameter of 229 mm (9 in) with the steel plates having a thickness of 6.4 mm (0.25 in). The fixture is flexible to accommodate pultruded specimens with various thicknesses. Six- 6.4 mm (0.25 in) diameter sleeve bolts are used to transfer the load from the steel fixture to each side of the specimen (Figure 6.9). The bolts are hand-tightened. Assuming a uniform stress distribution, both shear and axial forces are applied to the tested specimen by loading the sample as shown in Figure 6.1. A case of 'pure shear' is produced in section AB when $\alpha = 90^o$.

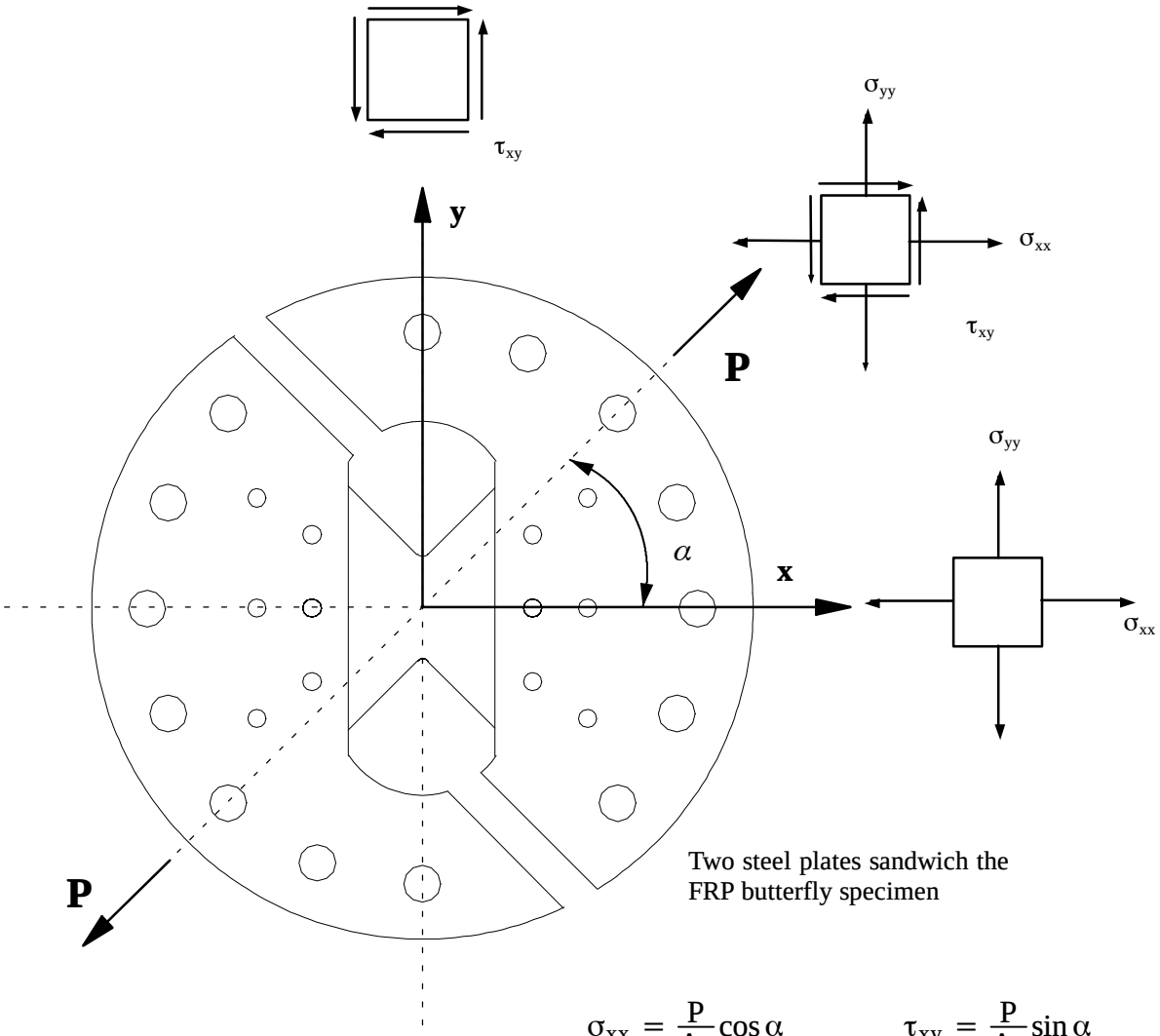

Figure 6.1 Modified Arcan fixture for shear testing of pultruded composites

Finite Element Models

Parametric analyses using linear finite element (FE) models were performed to determine the effect of notch radius and material orthotropy on the uniformity of stresses desired in section AB of the butterfly specimen,. The FE analyses were performed for the special case of 'pure shear' loading ($\alpha = 90^o$). The ABAQUS (2002) implicit finite element code was used with 4-node continuum plane-strain elements (CPE4) to model the specimen. The size of the models vary from 4000 to 9000 elements and 4200 to 10,000 nodes, depending on the refinement required around the notches. Figure 6.2 shows one of the FE meshes used in analyzing the butterfly specimen. Note the mesh refinement around the blunted notch tip. Figure 6.3 shows the effect of blunting the notch radius on the shear stresses in section AB. The shear stresses reported were normalized with respect to the nominal shear stress, $\bar{\tau}_{xy}$. Typical elastic properties were used for the isotropic case, with Young's modulus, E=206,820 MPa (E=30,000 ksi) and a Poisson's ratio of 0.3.

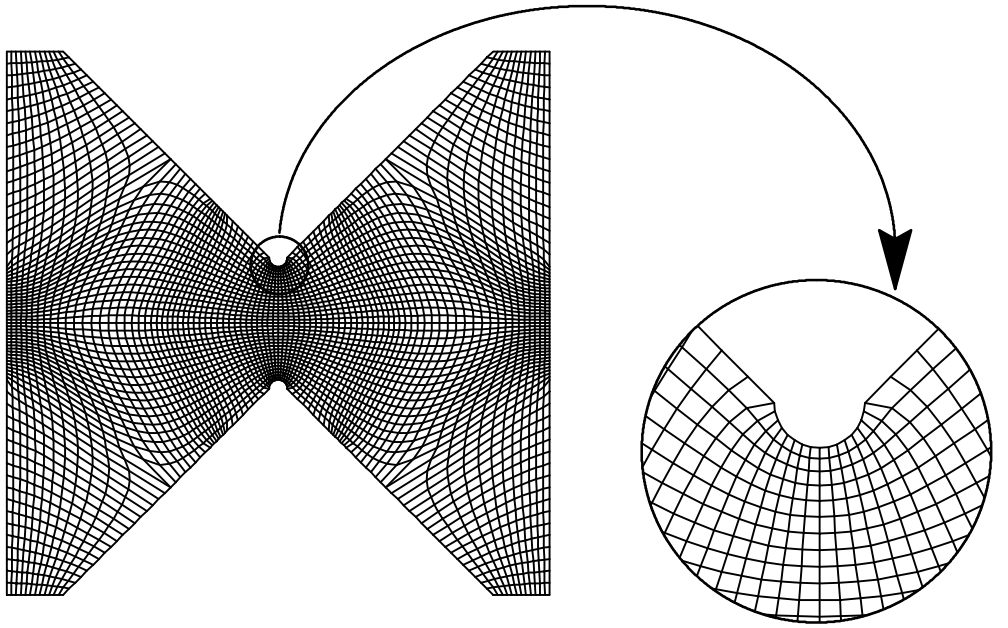

Figure 6.2 Example of an FE mesh used for the butterfly specimen

Compared to the sharp notch, the blunted notch (radius=2.54 mm (0.1in)) results in a lower stress concentration near the notch tip and a more gradual stress buildup. For the FE model with orthotropic properties, the stress profile is uniform near the blunted notch tip and results in a normalized shear stress closer to 1.0 at the center. Figure 6.4 shows the shear stress profile across the notch in the x-direction. The length of the gage section (W) was used to normalize the distance values on the x-axis. The shear stress values around the center line (x=0) were relatively constant for an approximate normalized distance of $\pm$ 0.05. This was considered an adequate length for a strain gage of about 2 mm (0.079 in) which also corresponds to a leg of a strain rosette gage selected for the experiments.

Three different notch radii were studied to determine an appropriate notch radius. FE analyses were performed for three notch radii, r= 1.27 (0.05), 2.54 (0.1), 5.08 (0.2) mm (in) with the principal material direction aligned in the loading direction (axial). Figure 6.5 shows the effect of the notch radius on the shear stress profile along the gage section. A normalized shear stress profile closer to 1.0 was found near the center for the specimen with a notch radius of 2.54 mm (0.1 in). Figure 6.6 shows the effects of varying the roving fiber orientation on the stress profile along the gage section of the notched specimen with radius 2.54 mm (0.1 in). The specimen, with roving fibers in the axial direction, resulted in a more uniform shear stress distribution. The specimen with the roving fibers in the transverse direction had a larger stress concentration around the notch area. The constraint provided by the roving layers may result in the larger stresses developing in the x-direction. Figure 6.7 shows the shear stress profile across the gage section for the two roving orientations. For 'pure shear' loading conditions, the specimen with the axial roving orientation had a relatively constant shear stress profile at the center of the gage section AB. The stresses were also closer to the nominal shear stress (within 1% of $\bar{\tau}_{xy}$). As a result of this study, a butterfly specimen with aa notch radius of 2.54 mm (0.1 in) with the roving fibers oriented in the loading direction was proposed. Figure 6.8 shows the geometry of the proposed butterfly specimen.

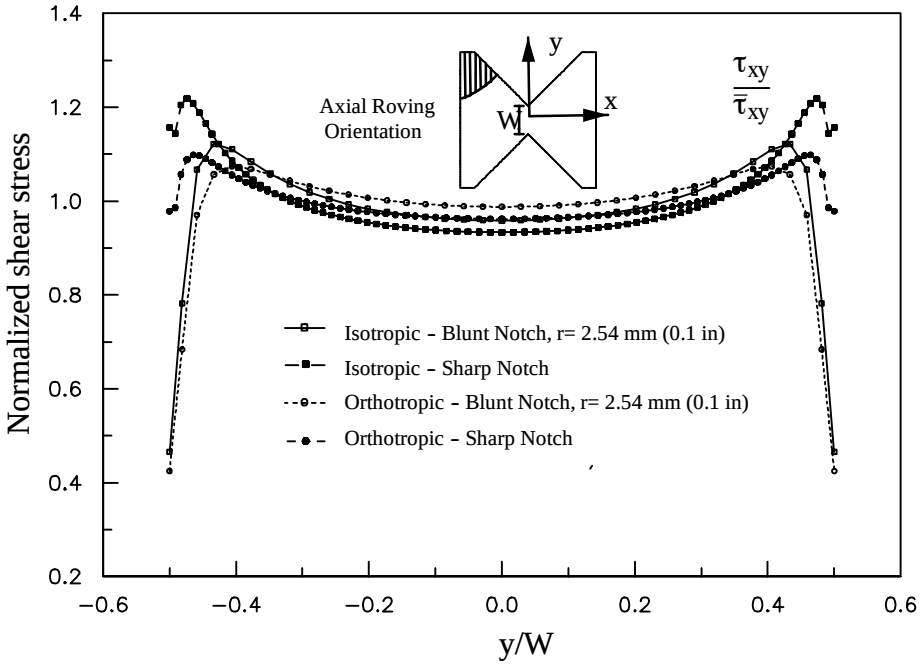

Figure 6.3 Effect of sharp notch on shear stress along the gage section

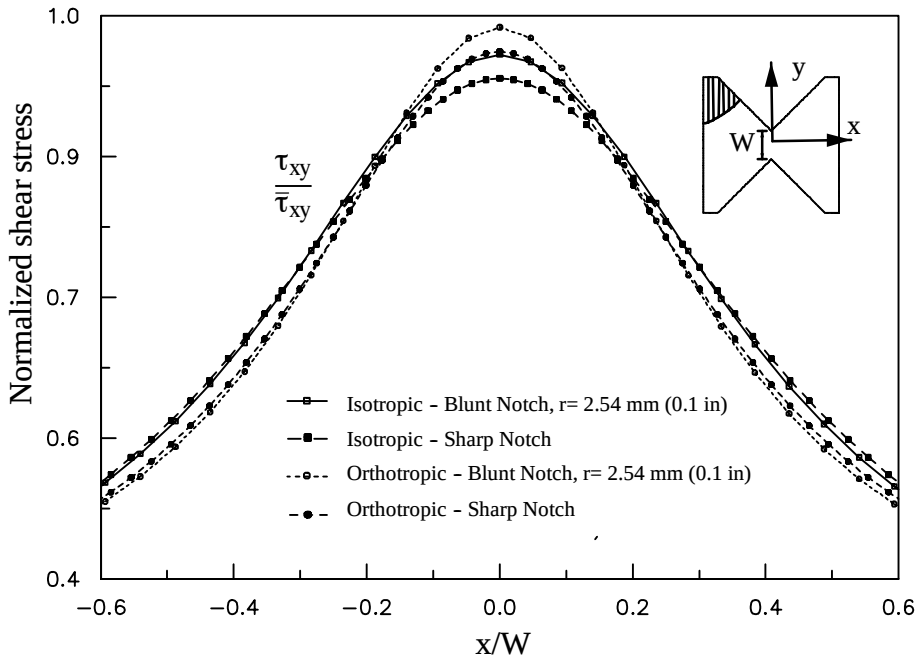

Figure 6.4 Effect of sharp notch on shear stress across the gage section

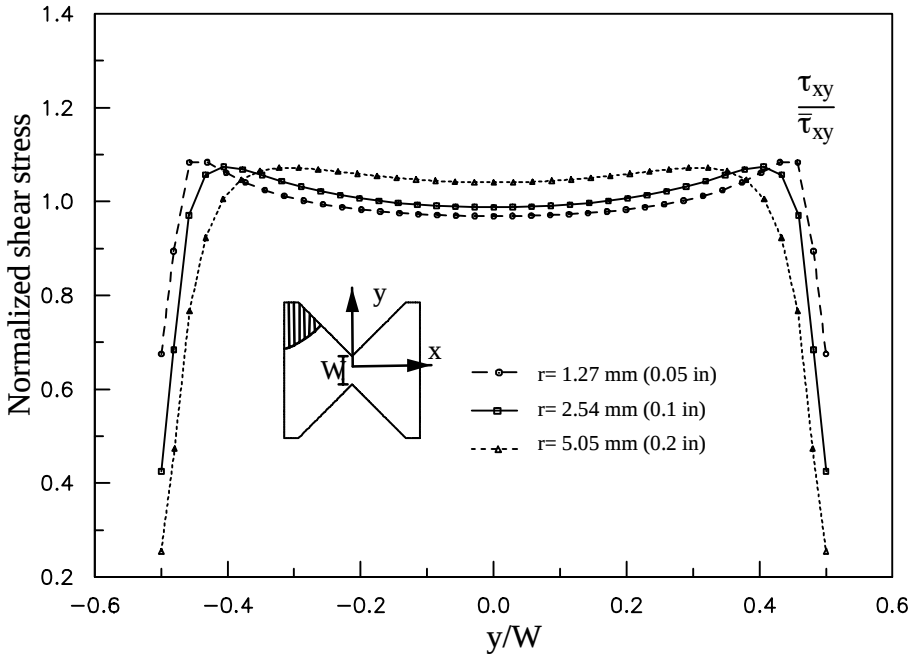

Figure 6.5 Effect of notch radius on shear stress profile along gage section

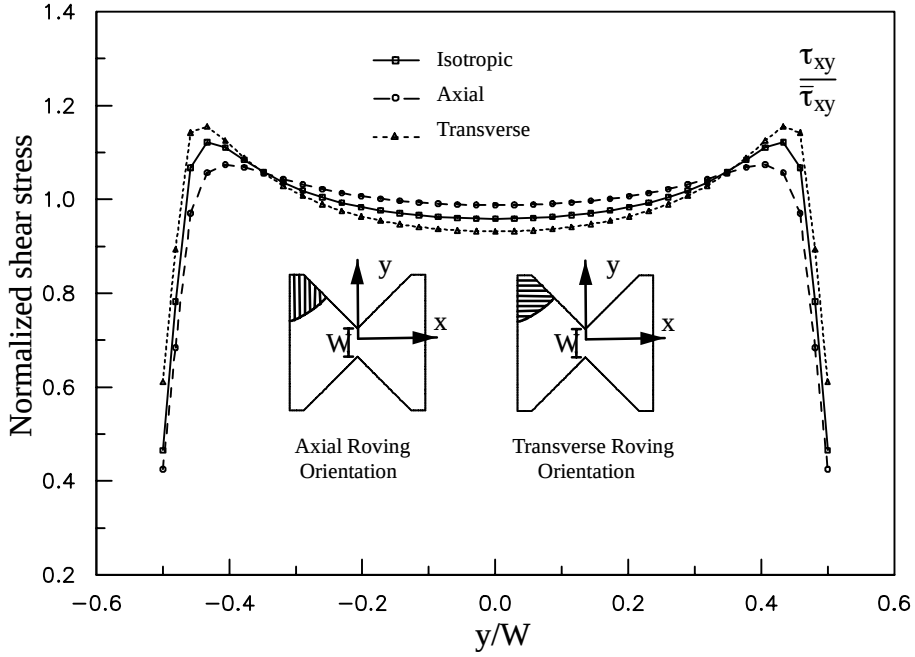

Figure 6.6 Effect of roving orientation on shear stress along the gage section

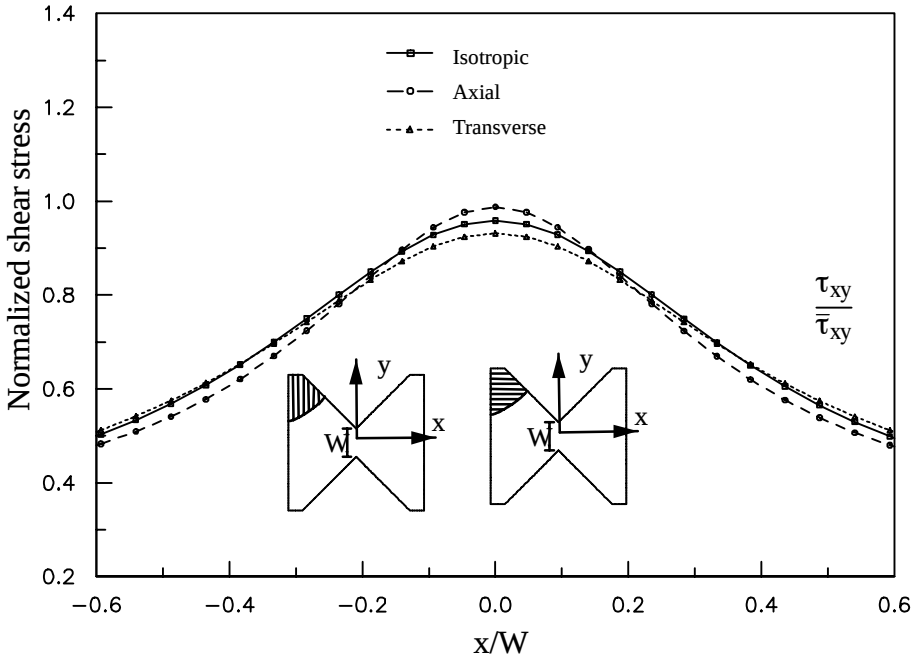

Figure 6.7 Effect of roving orientation on shear stress across the gage section

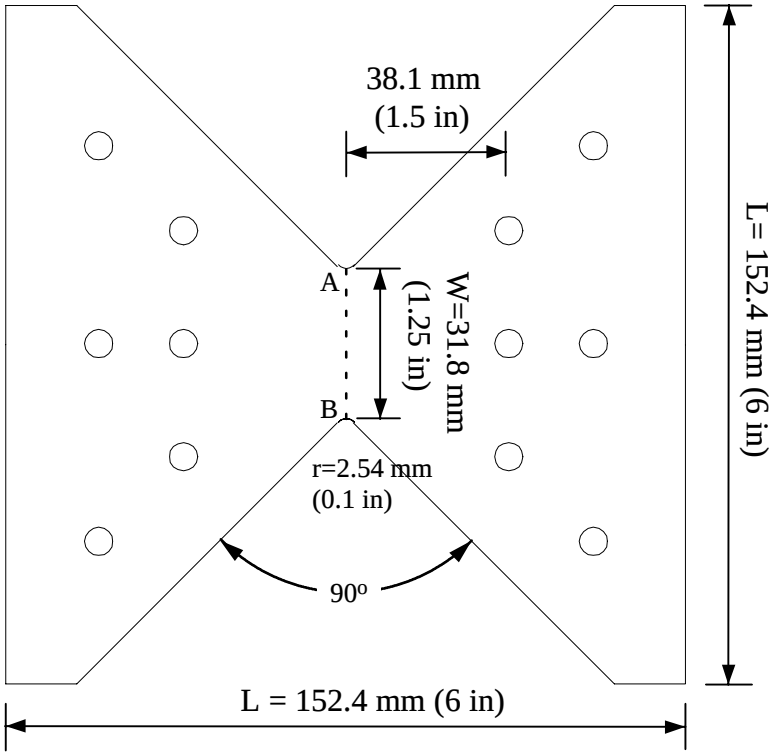

Figure 6.8 Proposed butterfly specimen

6.2 Experimental Procedures

The tested specimens were fabricated from one monolithic pultruded plate with 12.2 mm (0.48 in.) thickness. A water-jet machining system was used to manufacture the butterfly specimens with precise tolerances of $\pm$ 0.08 mm (0.003 in). Strain gage rosettes were used to measure the shear and normal strains at the center of section AB. The experiments were performed in a displacement control mode at a rate of 0.5 mm/min. The load was applied using an MTS 810 servo-hydraulic test system with a 220 kN (50-kip) capacity. The maximum error of the recorded strain was within $\pm$ 50 microstrains and the load was within $\pm$ 0.22 kN (50 lb). The experimental analysis of the specimens under 'pure shear' and with biaxial stress conditions was performed using strain-gage and infrared (IR) thermography. The biaxial testing was performed by varying the load angle, ($\alpha = 22.5^o, 45^o, 67.5^o$). Shear and normal strains were extracted from the rosettes at the center of each specimen during both 'pure shear' and biaxial tests.

Figure 6.9 Test-setup showing fixture and butterfly specimen

6.3 Nonlinear Shear Response

Figures 6.10 and 6.11 show the strains in the legs of the strain rosette versus nominal shear stress $\bar{\tau}_{xy}$ measured at the center of the specimen, during 'pure shear' ($\alpha = 90^o$) loading conditions, for both axial and transverse roving orientations. The symmetry in the ε^{+45} and ε^{-45} plots is an indication of the uniformity of the shear strain at the center of section AB. Slight variability in the normal strain, ε^0, values are observed between the various tested specimens. At around 50% of the ultimate shear stress, the ratio of the normal to shear strain is found to range from 0.3% to 9%. This can be attributed to initial misalignment of the specimen. Figure 6.12 shows the shear stress-strain response from the tested coupons ($\alpha = 90^o$). Good correlation is observed when comparing these results with off-axis compression tests used to calibrate a multi-axial nonlinear constitutive model as reported by Haj-Ali and Kilic (2002) and by Haj-Ali and El-Hajjar (2003). The results also confirm that the shear response from off-axis compression tests is close to the state of 'pure shear' because of the added normal compression stress, transverse to the roving direction (Haj-Ali and Kilic, 2002). The axial strain did not appear to affect the shear response observed throughout its nonlinear response. Small variation is observed in the ultimate shear stress values across the specimens tested, both axial and transverse. The full circles in figure 6.12 mark the ultimate stress values. The average ultimate shear stress is 73.0 ± 3.9 MPa (10.58 ± 0.56 ksi). The average ultimate shear strain is $2.71\% \pm 0.31\%$. Figure 6.13 shows two typical failed specimens when the loading angle, $\alpha = 90^o$. Examination of the two failed specimens after failure reveals that failure initiates at the notch radius and propagates through the section AB. Figure 6.14 shows the shear response under added biaxial conditions produced when varying the load angle α. All the biaxial test specimens failed at a lower ultimate load when compared to the case of $\alpha = 90^o$. This result may also explain the added nonlinear behavior in shear. The nonlinear shear stress-strain curves from the

biaxial tests are close to the 'pure shear' case until the ultimate stress values (especially for larger values of α).

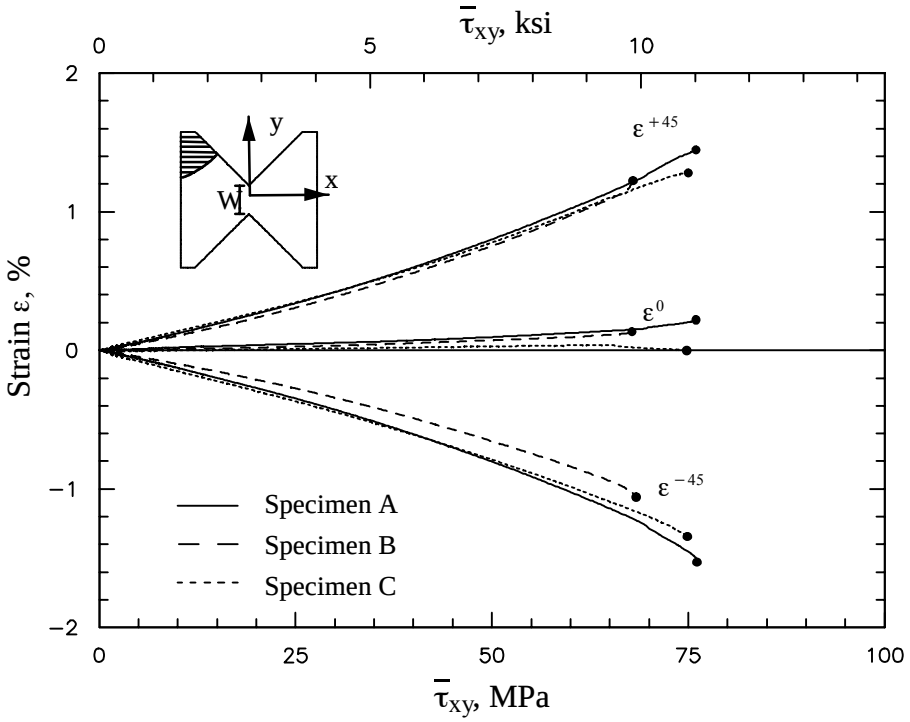

Figure 6.10 Measured strain profiles at center of transverse butterfly specimen during 'pure shear' tests

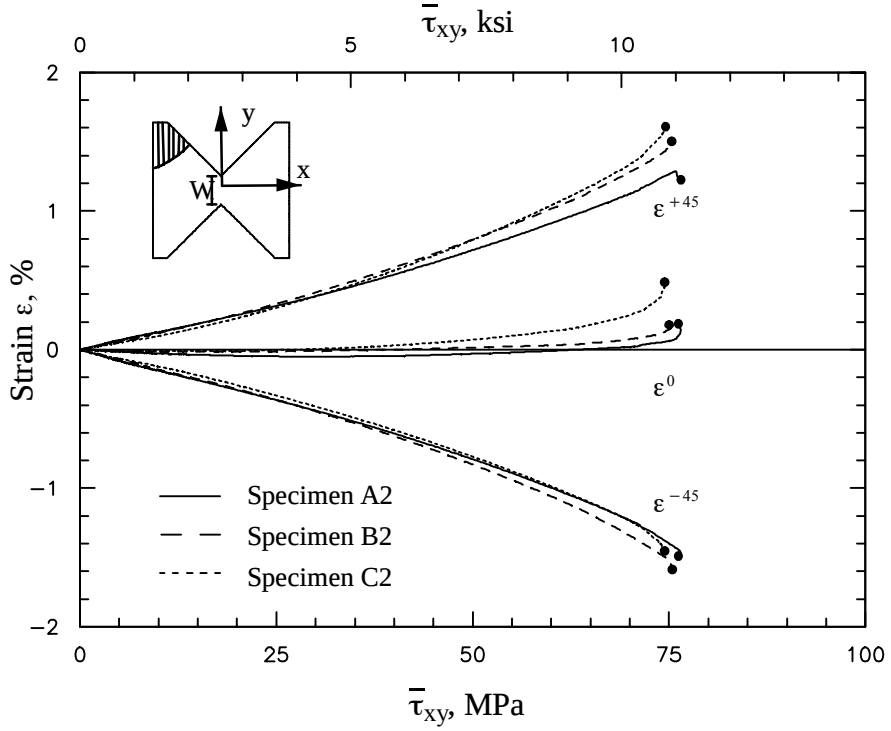

Figure 6.11 Measured strain profiles at center of axial butterfly specimen during 'pure shear' tests

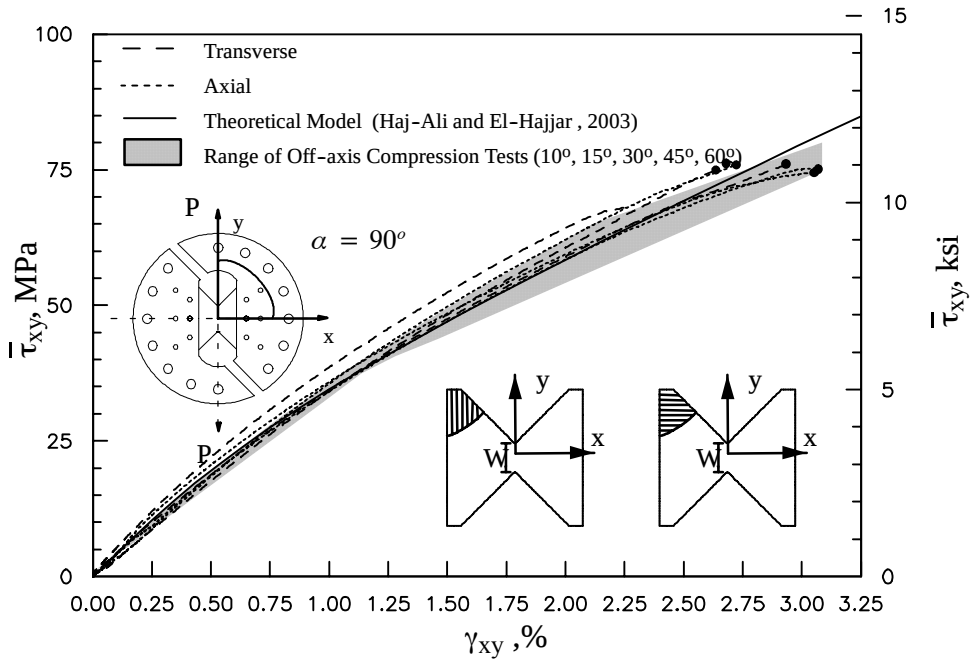

Figure 6.12 Shear stress strain response from 'pure shear' tests

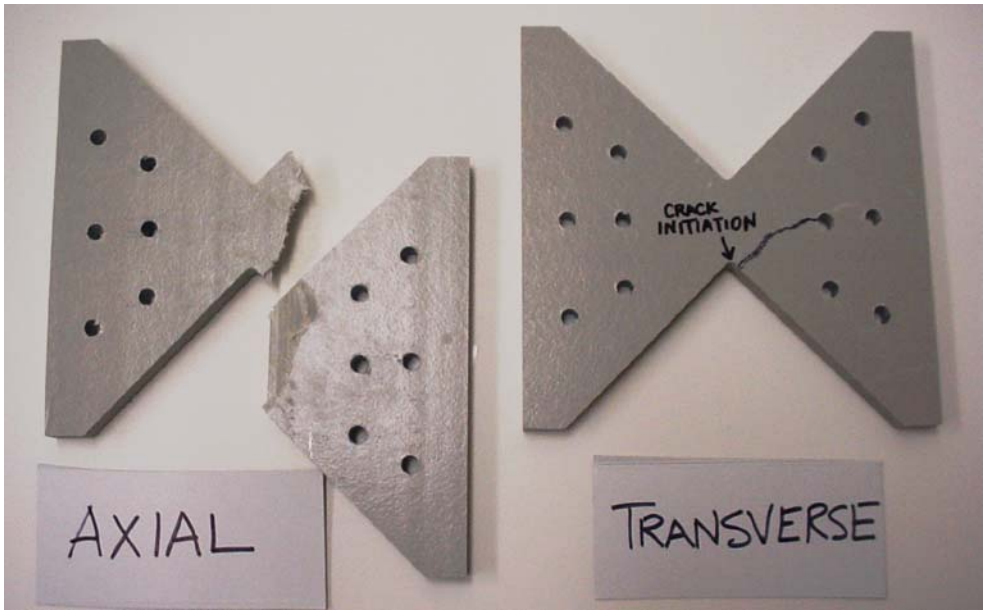

Figure 6.13 Failed axial and transverse specimen after reaching the ultimate stress

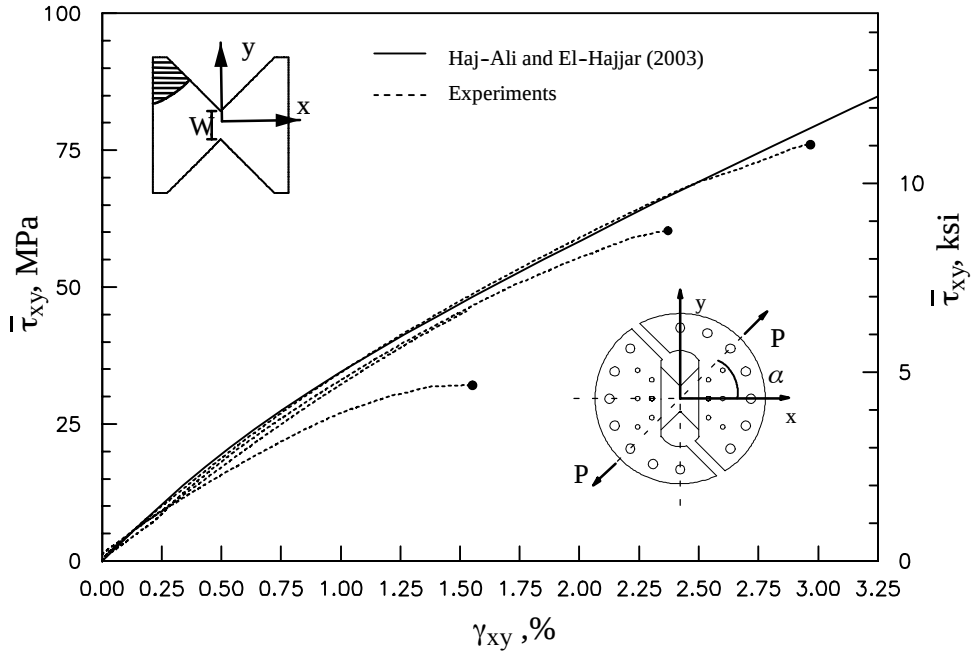

Figure 6.14 Shear stress strain response from biaxial testing

Verification of 'pure' shear conditions using TSA

IR thermography tests were performed on different butterfly specimens. The objective was to obtain a full-field stress measurement to assess the extent of 'pure shear' conditions from the entire specimen under loading. In the TSA method, the infrared detector measures an uncalibrated TSA signal, S, that is linearly related to the radiant photons emitted due to a surface temperature change ($S \propto \Delta T/T \propto \Delta\sigma_{\alpha\alpha} \propto \Delta\varepsilon_{\alpha\alpha}$). A case of 'pure shear' was expected to yield a zero (S) reading. The tested coupons were coated with flat black paint to improve the surface emissivity. To acquire a TSA image and achieve adiabatic conditions, a sinusoidal load was applied with an amplitude of 2.2 kN (0.5 kips), frequency of 5Hz, and a mean load value of 4.4 kN (1.0 kips). Data from the images were integrated (averaged) by allowing an exposure time of 5 minutes. Time effects during the exposure period were not considered significant. The TSA measurements were synchronized with the peaks of the applied cyclic loading (reference signal) in order to obtain the repeated elastic response. Figure 6.16 illustrates the TSA results from a 'pure shear' ($\alpha = 90^o$) and a biaxial test ($\alpha = 22.5^o$) when the same load is applied. The contour lines measure the relative TSA signal directly related to the sum of the surface in-plane strains. The first contour plot ($\alpha = 90^o$) clearly illustrates the near 'pure shear' conditions at the gage section where, $S \approx 0$. When the load was applied at an angle of $\alpha = 22.5^o$, more axial tension rather than shear was present at the gage section. IR thermography also shows large anti-symmetric stress concentrations for this angle of loading. Figure 6.15 shows the normalized TSA signal S for four loading angles, along the section AB. The value used for normalizing the curves was taken as the average of the TSA signal along AB when $\alpha = 0^o$. The fluctuation in the curves seem to be related to the loading angle, α, where a decrease in α increases the signal variation. Higher stress concentrations occur as the loading angle α decreases. This can be seen when comparing the magnitude of the signal near the edge to the one at the center (y=0). The signal from the 'pure shear' condition was uniform and closer to the theoretical value of zero. This deviation can be attributed to two sources. The first source can be the existence

of small biaxial stresses as seen from the strain measurements in Figure 6.11. The second reason maybe due to an error in the numerical algorithm used to process (integrate) the IR images.

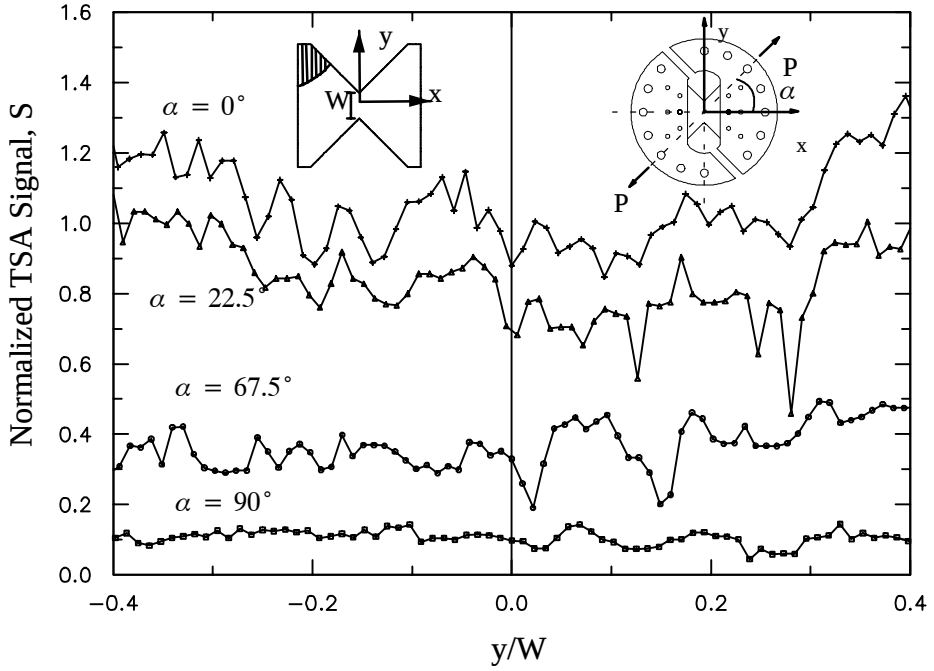

Figure 6.15 Normailized first stress invariant along gage section using TSA

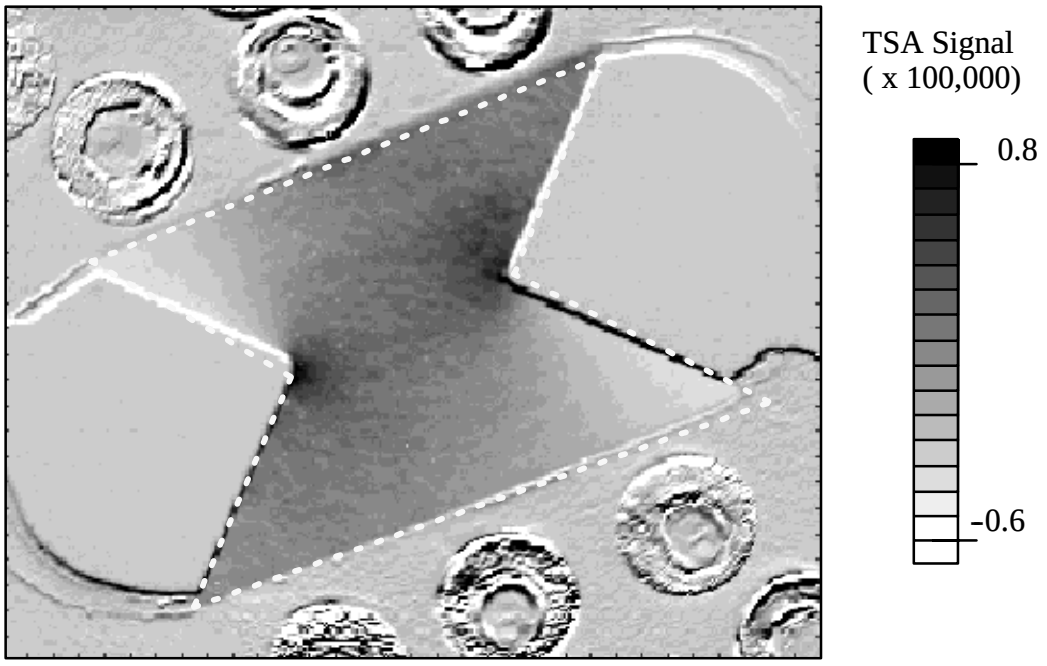

(b) $\alpha = 22.5^{\circ}$

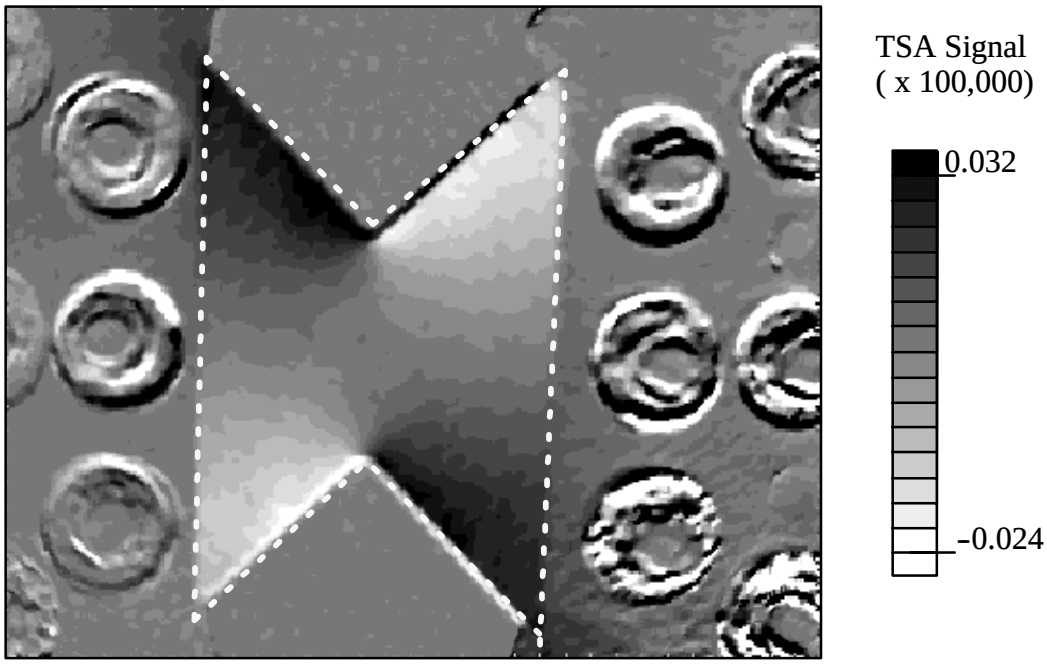

(b) $\alpha = 90^{\circ}$

Figure 6.16 Normalized first stress invariant in butterfly specimen using TSA

6.4 Modified Optical Grid Method for Mode-II Fracture

In this study, an optical, non-contact, non-interfereing means of measuring the sliding strain in mode-II fracture tests is proposed. The technique is automated with the applied load and displacement and provides a quantitative measurement of the deformation of the crack faces. Optical methods offer many advantages over traditional contact strain and displacement measurement techniques. One of the simplest methods of optical strain measurement involves placing a grid or reference points on the specimen and observing the movement of these points under stress. This is done by comparison to a reference image of the unloaded grid. Using a basic 2D grid, consisting of 3 dots, a 2D strain in-plance measurement or displacment can be made. Parks (1982) presented a comprehensive review of the grid method and the various techniques that are used to analyze the grids. Various aspects of this experimental technique such as the grid-pitch and line visibility were also examined. Examples of using the grid method include the work of Rand et al. (1996) that used an image by image analysis technique to determine the strains from uniaxial testing results of specimens made of 20-micron-thick polyethylene film. The specimens used had a large gage length with two marks on the specimen to obtain the desired resolution of strain. Towse et al. (2001), used the grid method with a video camera to measure the strain in uniaxial tesing of low and high modulus materials, for the shear strain measurement in adhesive joints and displacement measurement of long span bridges. A further advanced of the grid method is possible with advanced tracking of speckle schemes such as using the Digital Image Correlation method (Eg. Chu et al, 1985, and Sutton et al., 1991). Helm et al. (2001), applied a digital image analysis technique for measuring the crack growth in aluminum fracture specimens under tension and torsion loads.

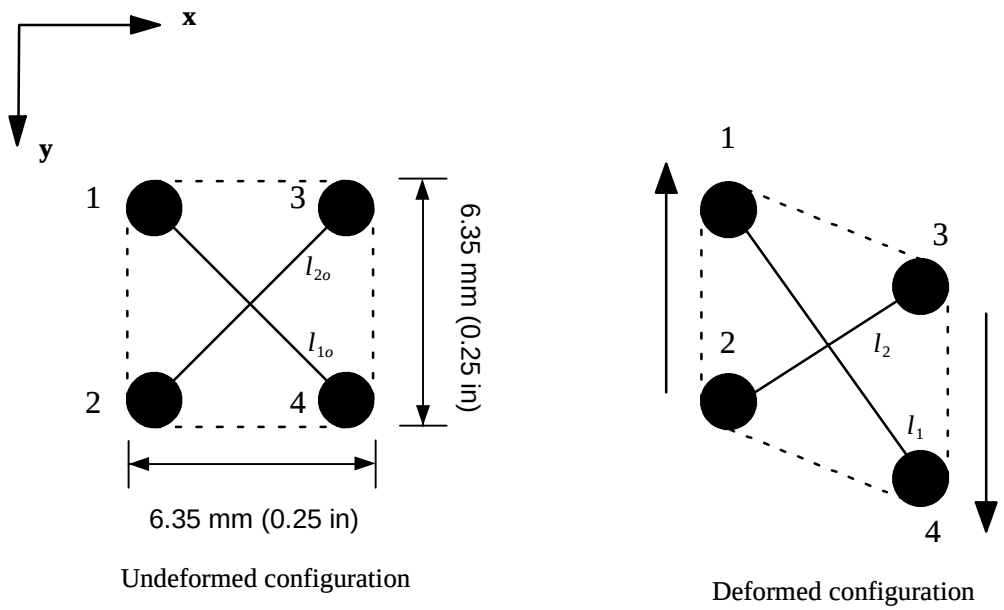

Figure 6.17 Pattern of nodes used in grid method for sliding strain measurement

In this study, an optical grid method is used to measure the crack sliding behavior during the mode-II fracture tests. In this method, the deformation of four dots pre-marked on the surface of the specimen are used to determine various strain quantities (Figure 6.17). During the test, white light is used to illuminate the background of the specimen and to increase the contrast of the dots on the surface. A charge coupled device or CCD camera is used to capture images of the dot pattern in the Tagged Image File Format (TIFF) with a resolution of 640x480 pixels. Figure 6.18 shows the Kodak MDS 100 CCD camera with a 10X macro lens together with the white light source. A triggering device is used to control the aquisition from the loading and imaging instruments and to record the exact time during the test at which each image is acquired. A software program developed in the MATLAB (2001) environment was used to process the captured images and the data from the load cell and actuator's displacement. The aquired image is first converted to a 'binary' file mode before

further processing. A binary version of the image is created by using the background threshold to distinguish between the black pixels (dots) and the white pixels (background). In a binary image, each image pixel assumes one of only two discrete value of either 0's (white) and 1's (dark). After converting the 'TIFF' image to a binary image, a special function is used to determine the number of objects in the image. Figure 6.19 shows the captured image before any processing is conducted. The conversion of the pixels to a binary format allows objects to be easily identified by the connectivity of pixel's having a value of '1' in the binary image. Pixels must touch along an edge to be considered connected. Each object is then labelled in relation to its distance from the origin. From the binary file it is then a simple task to determine the location and area of each node. In some circumstances, not all the dark areas or '1s' in the image correspond to an object, e.g. the area corresponding to the applied notch or dust particles on the specimen will also appear dark. For this reason, an algorith is used to reject objects which do not fit min/max elipticity and area criteria. Three coupons ($\theta = 0^o, 45^o, 90^o$) made from an E-glass/vinylester pultruded composite plate and a 'pure shear' butterfly specimen made from E-glass/polyester were used to verify the validity of using this technique on pultruded composites. The geometry of the tested coupons was previously reported in Chapter 2. The engineering axial and shear strains were measured by using an average of the relative displacement of the corresponding pre-marked dots. For the coupon tests, Figure 6.20 shows good correlation for the stress-strain responses from strain gage measurements and those obtained using the grid method. For the shear tests, Figure 6.21 shows good correlation between the proposed method and those previoulsy tested with strain gages. In general, the accuracy of this method increases with the number of pixels in the image. The size of the marked dots should be small enough to capture the local deformations and large enough to include the maximum number of pixels to obtain the desired resolution. The reason for the scatter using the grid method can be attributed to the accuracy of the instrumentation and image conversion errors. In addition some errors may arise because the gage areas are not identical for the strain gages and the pre-marked dots.

Figure 6.18 CCD camera and white light source used for strain measurement using the grid technique

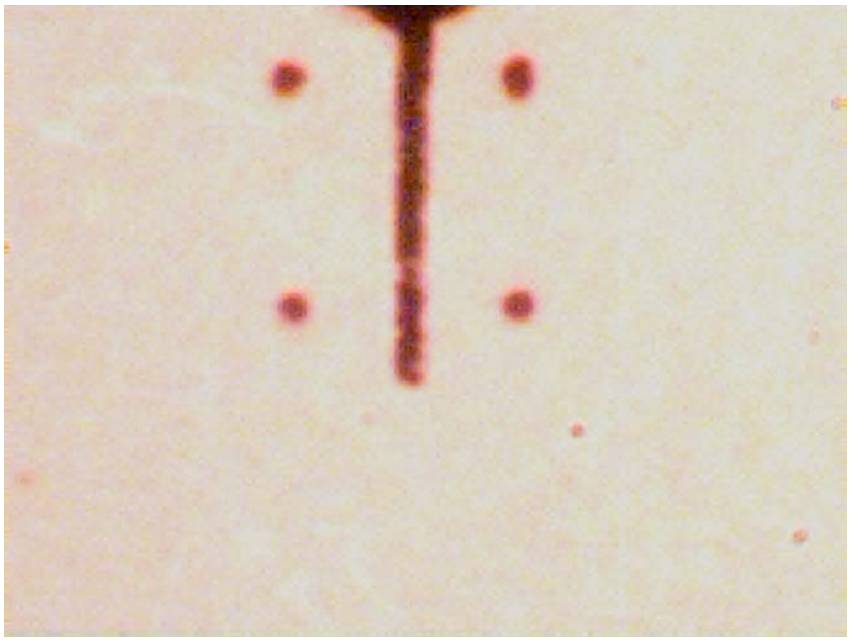

Figure 6.19 Image in ’TIFF’ format before any processing

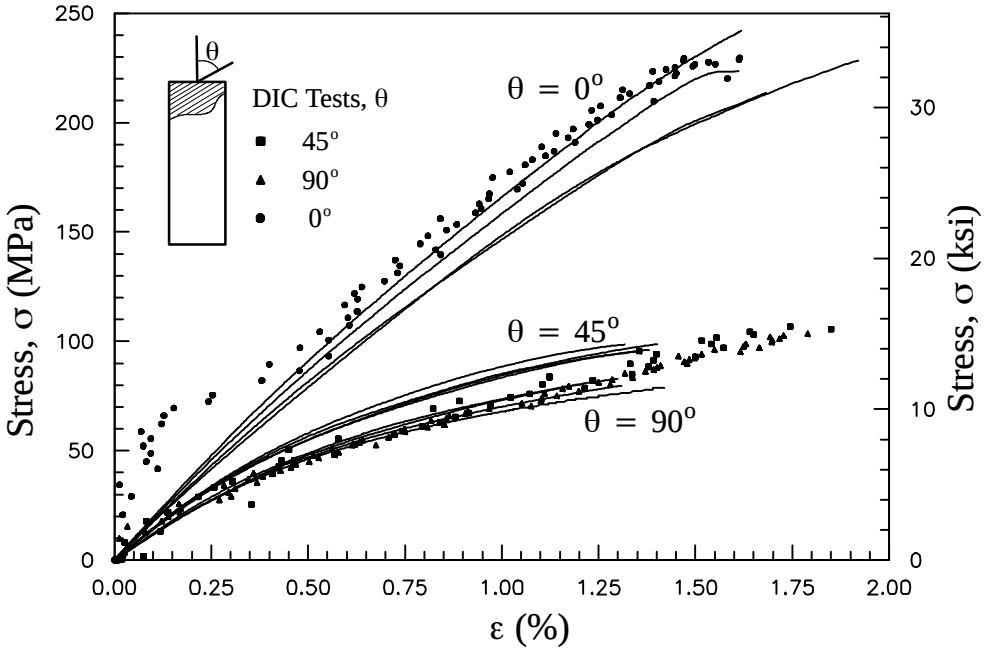

Figure 6.20 Stress strain response from off-axis E-glass/vinylester coupons using the grid technique and results from strain gage measurements

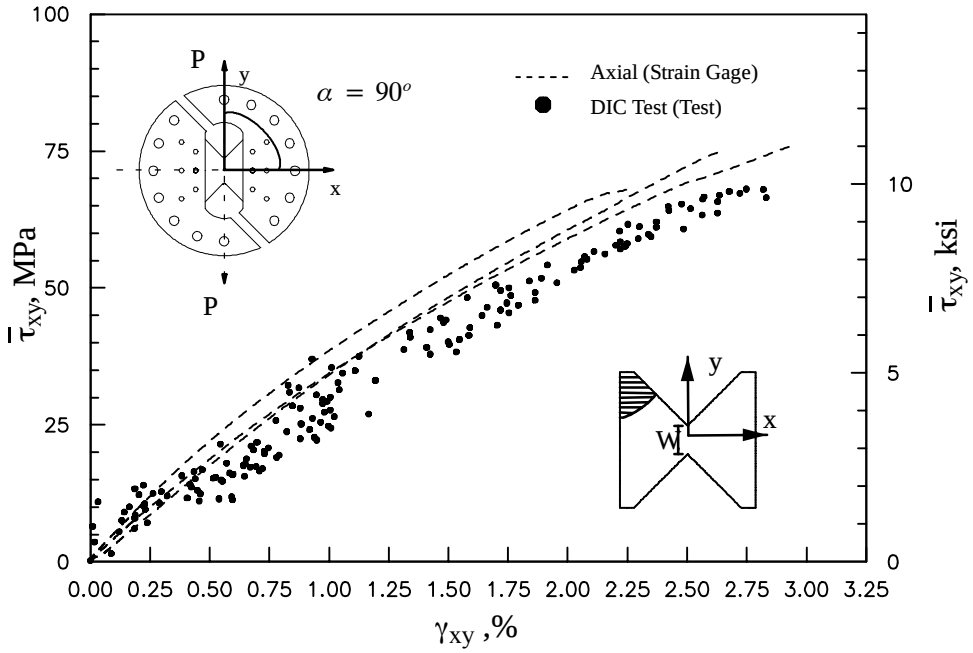

Figure 6.21 Shear stress-strain response using the grid technique

The grid technique is also applied during mode-II fracture tests to measure the crack sliding behavior. To the best knowledge of the author, there is no accurate and quantitative contact measurement technique for mode-II crack growth. This provided the motivation for using this method. A deformation metric called the 'apparent sliding strain' or γ_{SL} is proposed to provide information about the sliding deformation of the crack faces during mode-II tests. Axial strains are assumed to be minimal during the tests and their effect was on the sliding strain is considered negligible (<1%). To measure this quantity, an image of the undeformed pattern of dots on the test specimen is captured before any load is applied. The rectangular area around the notch tip that is imaged is around 12 mm wide and 9 mm in height. The top of the grid of premarked dots was placed at 1 mm (0.04 in) from the notch mouth. The CCD camera and the data aquisition are triggered using an external triggering device. This ensures that each acquired image is correlated with the exact load and actuator displacement. From each captured image, two diagonal chords l_1 and l_2 can be constructed between the dots as seen in Figure 6.17. The initial location of the 4 dots is given by $(x_o,y_o)_i$ where i is the node number. The undeformed lengths of the two chords l_{1o} and l_{2o} are calculated from the inital acquired image:

$$l_{1o} = \sqrt{(x_{4o} - x_{1o})^2 + (y_{4o} - y_{1o})^2} \quad , \quad l_{2o} = \sqrt{(x_{3o} - x_{2o})^2 + (y_{3o} - y_{2o})^2} \tag{6.1}$$

Figure 6.22 shows images of the pre-marked dots before and after deformation of the fracture specimen. As the specimen deforms, the locations of the 4 dots at any time during the test is given by the coordinates $(x, y)_i$. Similarly, the deformed lengths l_1 and l_2 can be determined:

$$\begin{aligned} l_1 &= \sqrt{(x_4 - x_1)^2 + (y_4 - y_1)^2} \\ l_2 &= \sqrt{(x_3 - x_2)^2 + (y_3 - y_2)^2} \end{aligned} \tag{6.2}$$

Using the deformed and undeformed chord lengths, the apparent sliding strain is:

$$\gamma_{sl} = \left| \frac{l_1 - l_{1o}}{l_{1o}} - \frac{l_2 - l_{2o}}{l_{2o}} \right| \tag{6.3}$$

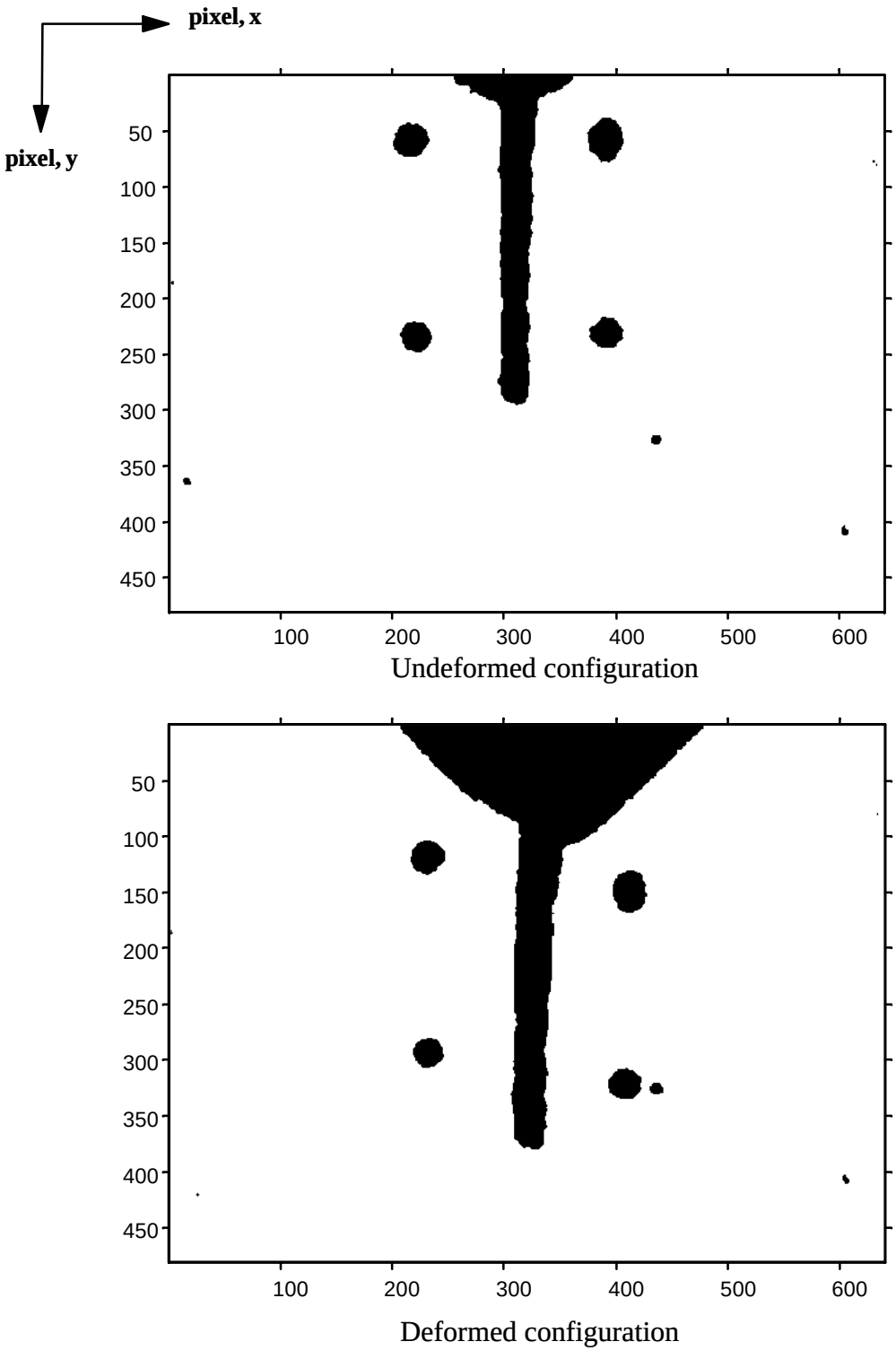

Figure 6.22 ’Binary’ images of pattern of dots during a mode–II fracture test

6.5 Mode-II Fracture Toughness

A numerical FE analysis using the VCCT method, described in Chapter 4, is used to determine the mode-II SIF solutions for the proposed butterfly specimen. Once G_{II} is calculated then it is possible to relate it to the SIF. The ABAQUS (2002) finite element code is used with 8-node continuum plane strain elements (CPE8R). A post-processing program was generated to read the FE results and apply the proper VCCT equation. A typical average FE model contained 5200 elements and 5700 nodes. The FE models were made for crack length ratios (a/W) between 0.3 and 0.5 with 0.05 increments. Figure 6.23 shows a schematic of the VCCT method with the 8 noded element. The springs 1 and 2 are modeled as soft and springs 3 and 4 are stiff springs. The analysis was repeated using isotropic and orthotropic proerties in the axial and transverse orientations respectively. The mode-II, strain energy release rate is given by:

$$G_{II} = \frac{1}{2B\Delta}\left(F_3\delta_1 + F_4\delta_2\right) \tag{6.4}$$

Where Δ is the element size and B is the thickness and δ's are the displacements in the soft springs and the F's are the reactions in the stiff springs. The spring stiffnesses k_s and k_h used were $1x10^{-15}$ and $1x10^{+15}$ kip/in respectively. Similar to the equation used to relate the mode-I strain energy release rate to the SIF (Equation 4.4), the mode-II strain energy release rate, G_{II} is related to the mode-II SIF, K_{II} by:

$$G_{II} = \left(s_{11}s_{22}\frac{1+\rho}{2}\right)^{\frac{1}{2}} \lambda^{\frac{1}{4}} K_{II}^{2} \tag{6.5}$$

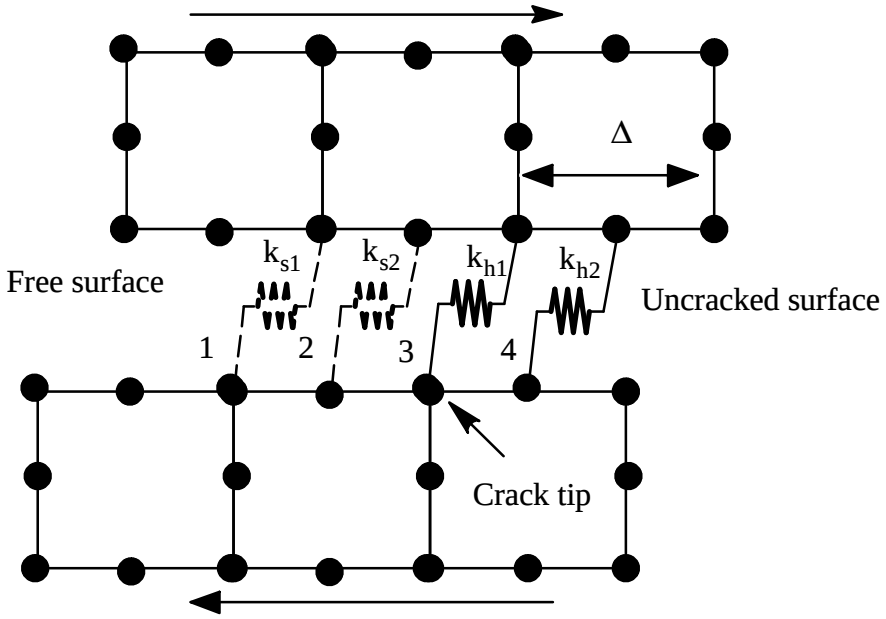

Figure 6.23 Mode-II VCCT for 8-noded elements in butterfly specimen

The FE analyses is performed with isotropic and orthotropic material properties. The pultruded material tested in this study has a $\rho = 1.62$ and $\lambda = 0.623$ compared to the isotropic case ($\lambda = \rho = 1$). It is found that calculating the SIF with the 'isotropic' solution will result in a maximum error of 2.71 % at the largest a/W ratio of 0.7. Using the FE results, a least squares polynomial fit is used to obtain the mode-II SIF calibration from the isotropic solution for the a/W ratio between 0.3 and 0.7. The mode-II SIF as a function of the loading angle can then be written as:

$$K_{II} = \frac{P \sin\alpha}{WB}\sqrt{(\pi a)}\ F_{II}(a/W) \tag{6.6}$$

$$F_{II}(a/W) = 1.0459 + 0.2528\beta - 1.5878\beta^2 + 2.4909\beta^3 \tag{6.7}$$

Where P is the applied load, B is the specimen thickness, W is the width of the specimen, a is the original notch length, and, β = a/W. For 'pure' mode-II loading α is 90 degrees. The Mode-I contribution of the SIF as a function of the loading angle can be similarly determined using the VCCT method described in Chapter 4:

$$K_I = \frac{P\cos\alpha}{WB}\sqrt{(\pi a)}\ F_{II}\,(a/W) \tag{6.8}$$

$$F_I\,(a/W) = -2.0841 + 27.296\beta - 66.859\beta^2 + 62.614\beta^3 \tag{6.9}$$

For 'pure' mode-I loading α is 0 degrees. Figure 6.24 and 6.25 show a comparison between the mode-I and II function F in the equations above. In addition, the SIF equations from the work of Banks-Sills and Arcan (1986) is shown for comparison of the trend knowing that their geometry is different. The differences in the results for mode-II can be attributed to the differences in their specimen which did not have a blunt notch and a taper angle. The significant dimensions of their specimen were W=30mm, r ≈3mm and L ≈90 mm.

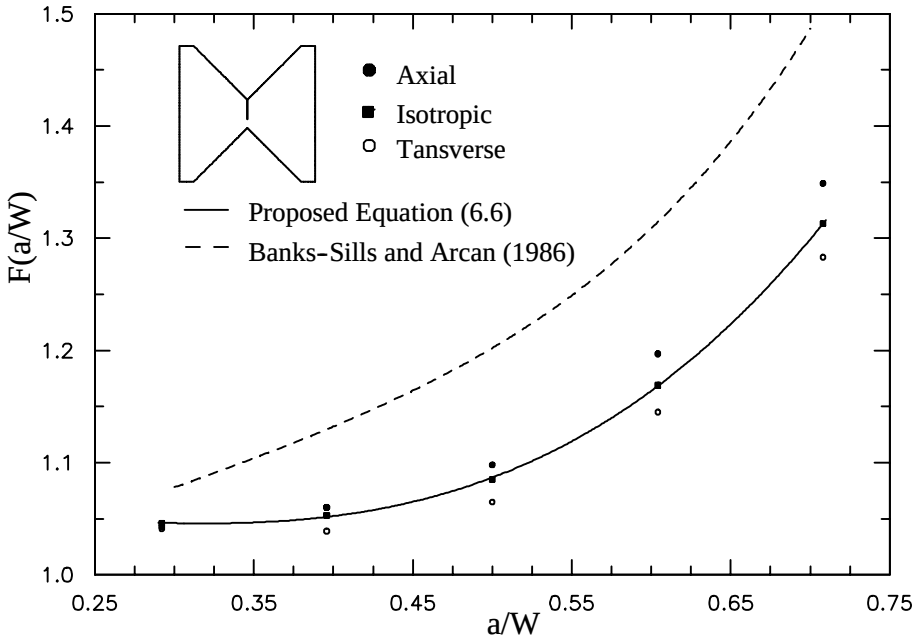

Figure 6.24 Normalized mode-II SIF for the butterfly specimen

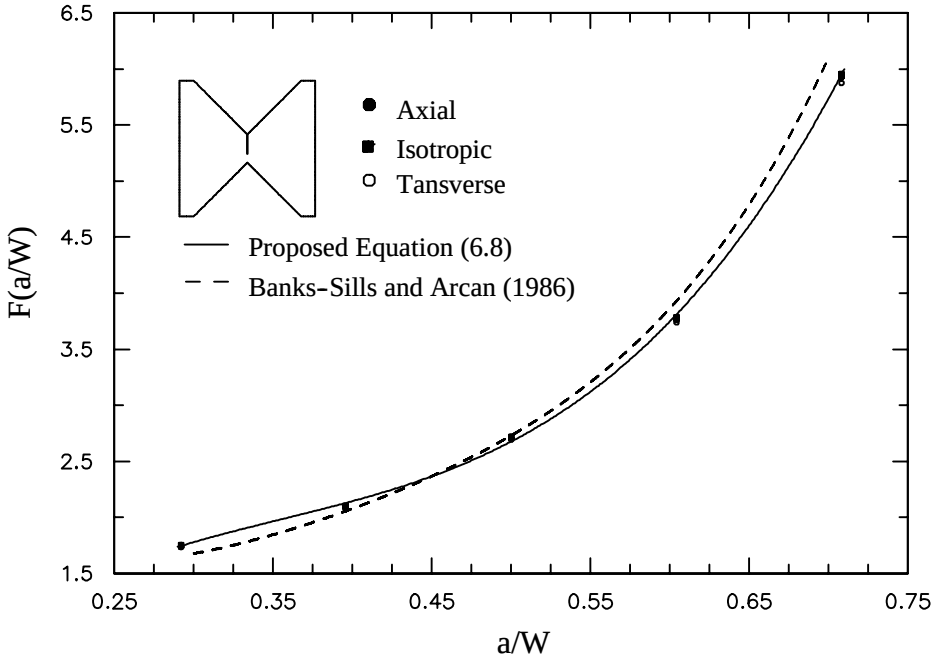

Figure 6.25 Normalized mode-I SIF for the butterfly specimen

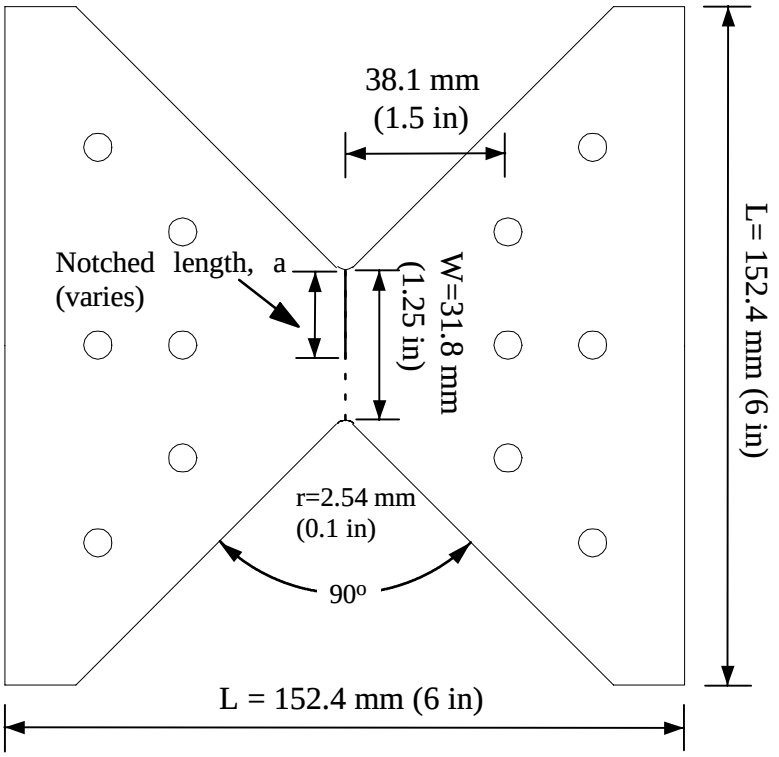

Figure 6.26 Geometry of notched butterfly specimen

Specimen Preparation and Testing

The tested specimens were first fabricated from one monolithic pultruded plate with 12.2 mm (0.48 in.) thickness. A water-jet machining system was used to manufacture the butterfly specimens with precise tolerances of ± 0.08 mm (0.003 in). The mode-II butterfly specimens were machined from the center of a monolithic pultruded plate of 1.2 x 2.4 m (4 x 8 ft) with a thickness of 12.2 mm (0.48 in). The notch was made using a diamond saw blade with a thickness of 0.38 mm (0.015 in). Figure 6.26 shows the schematic of the mode-II butterfly fracture specimen. The modified arcan fixture discussed in section 6.1 is used for the mode-II fracture tests. The load is applied to the fixture by the use of a pin clevis. Figure 6.27 shows the modified arcan fixture used for a mode-II fracture test. The mode-II fracture tests were performed in a displacement control mode at a rate of 0.5 mm/min using an MTS 810 servo-hydraulic test system. The maximum load and the nondimensonal crack size, a/W are the only values needed to determine the mode-II fracture toughness from Equations (6.6) and (6.7).

Figures 6.28 and 6.29 show the variation of the apparent sliding strain versus actuator displacement for transverse and axial mode-II fracture specimens with a/W=0.3 and 0.7. It is seen from these responses that each curve can be broken down into three regions. The first region corresponds to the bearing of the bolts on the specimen. The second is the steady range when full bearing of the pins has been reached and the last region with the largest slope corresponds to the region with rapid crack growth and ultimate failure. A similar response is observed in the load versus actuator displacement plots shown in Figures 6.30 and 6.31. Figure 6.32 and 6.33 show typical transverse and axial speciemens after failure during the mode-II fracture tests. The mode-II fracture toughness for the axial and transverse specimens is shown in Figure 6.34. In contrast to the mode-I results, the two roving fiber orientations are not found to affect the mode-II toughness. Of the 18 tested specimens, 9 were tested with the transverse roving orientation and 9 were tested in the axial roving orientation with 3 specimens in each mode for the targeted ratio of a/W=0.3, 0.5 and 0.7.

The arithmetic mean of the mode-II fracture toughness is found to be 7.87 MPa $\sqrt{m}$ (7.16 ksi$\sqrt{in}$), the median value is 7.91 MPa $\sqrt{m}$ (7.20 ksi$\sqrt{in}$), the standard deviation is 0.555 MPa $\sqrt{m}$ (0.505 ksi$\sqrt{in}$) and the coefficient of variation is 7.1%.

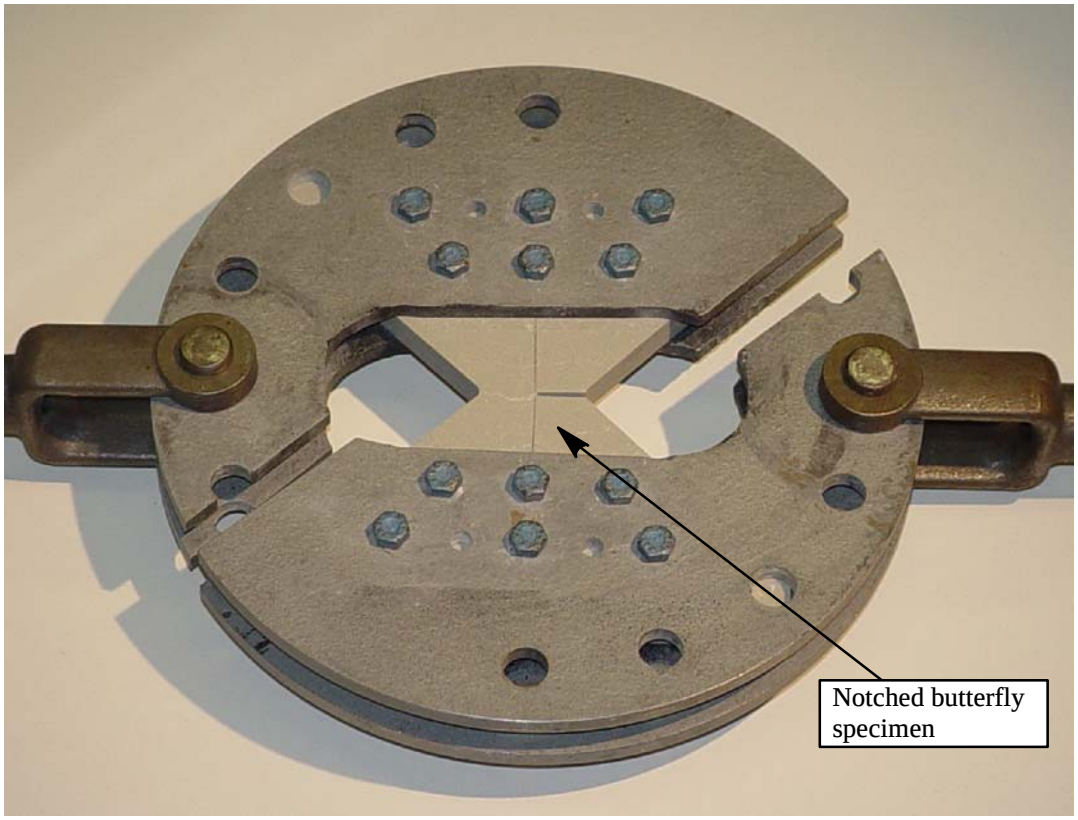

Figure 6.27 Modified Arcan fixture used for mode-II fracture testing

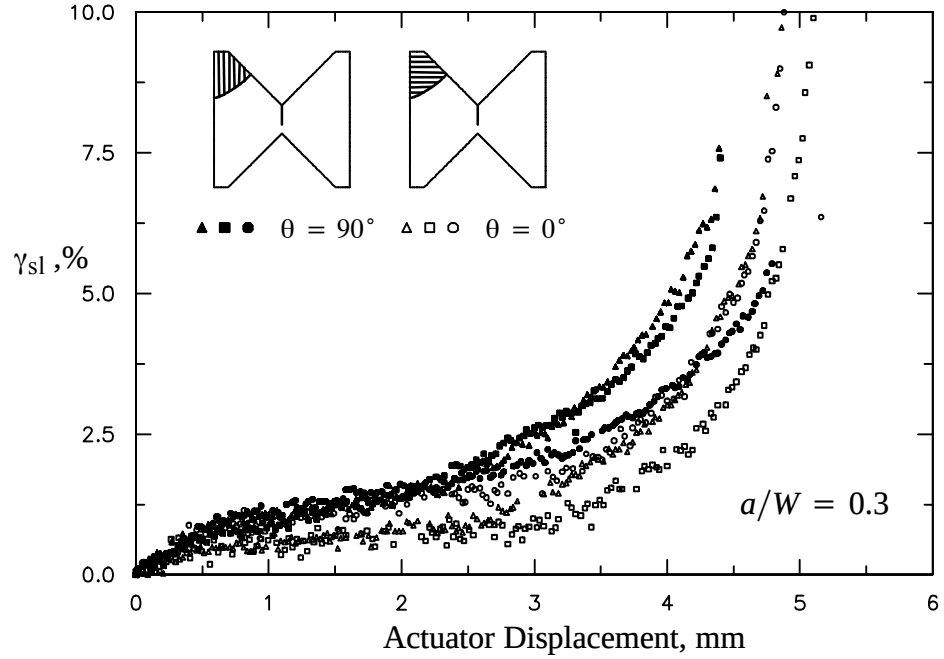

Figure 6.28 Apparent sliding strain versus actuator displacement for transverse and axial mode–II fracture specimens with a/W=0.3

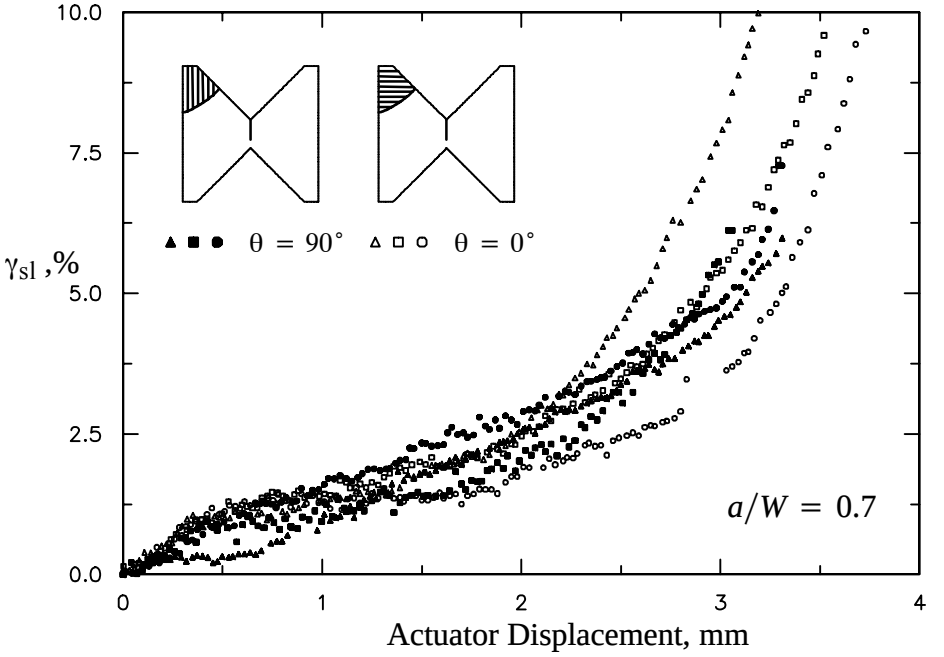

Figure 6.29 Apparent sliding strain versus actuator displacement for transverse and axial mode–II fracture specimens with a/W=0.7

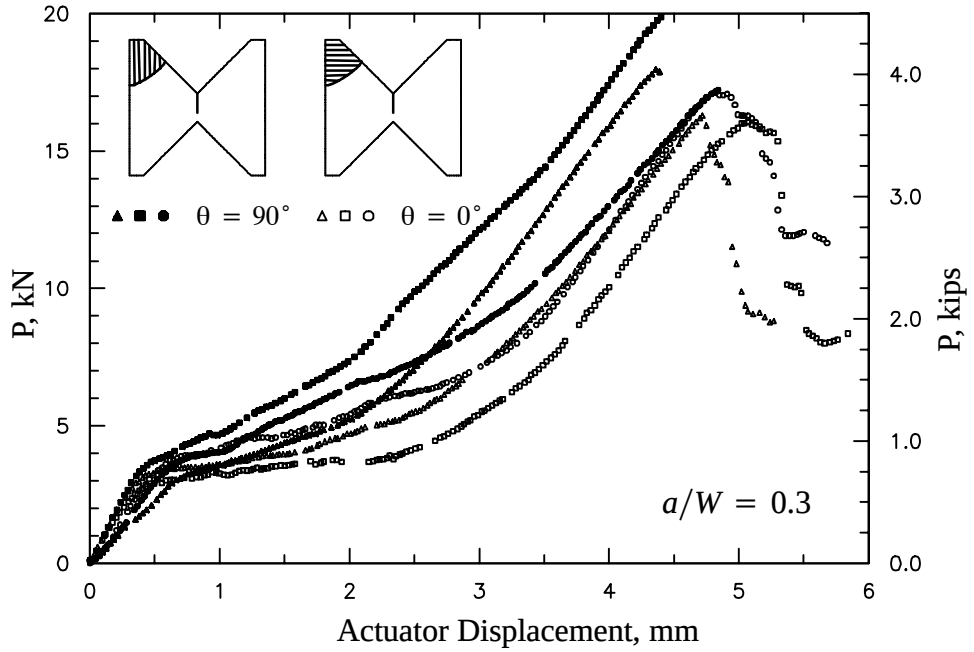

Figure 6.30 Load versus actuator displacement for transverse and axial mode-II fracture specimens with a/W=0.3

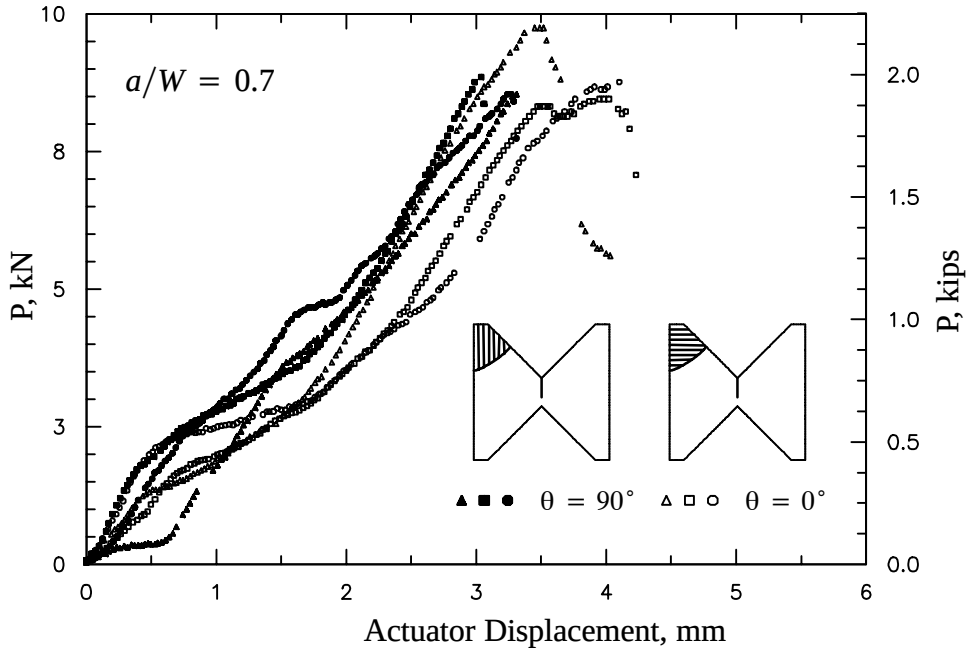

Figure 6.31 Load versus actuator displacement for transverse and axial mode-II fracture specimens with a/W=0.7

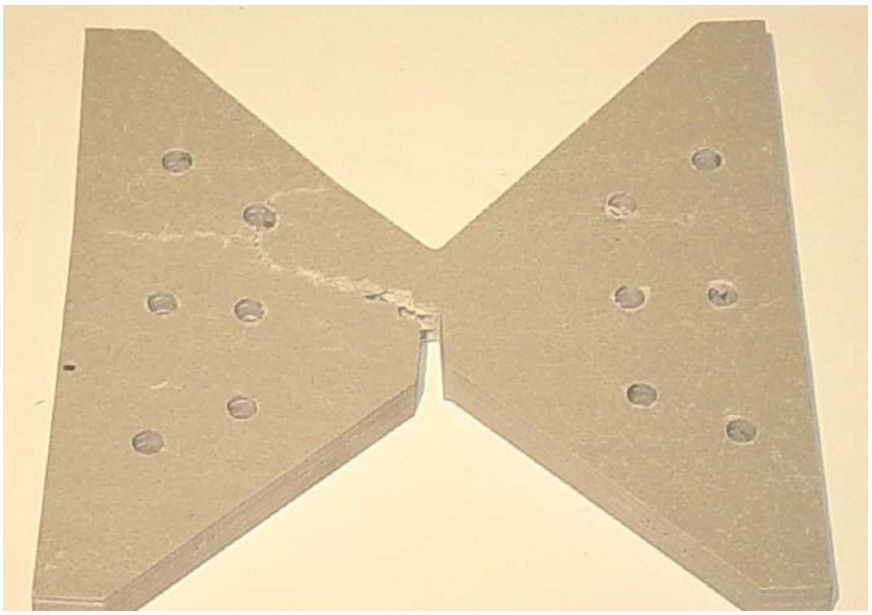

Figure 6.32 Fractured butterfly specimen with transverse orientation after mode-II test

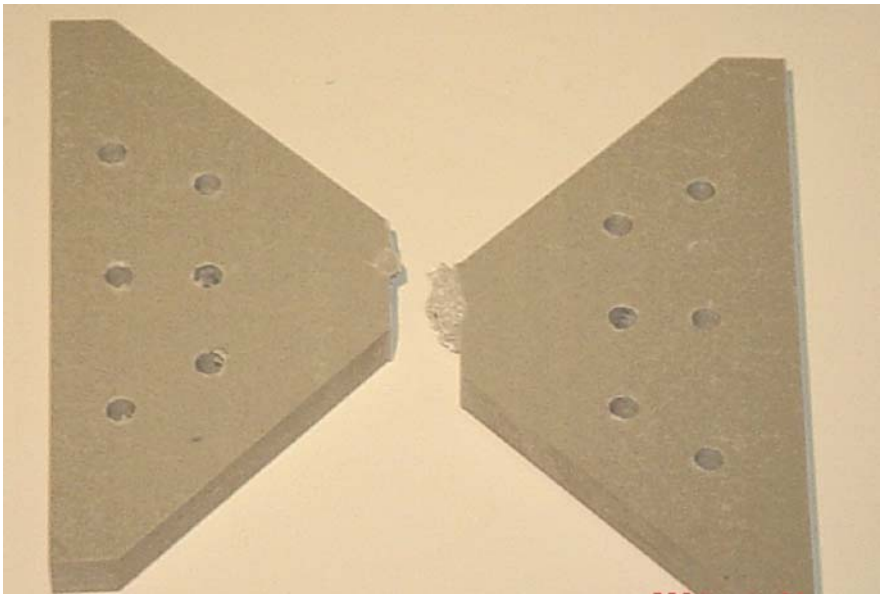

Figure 6.33 Fractured butterfly specimen with axial orientation after mode-II test

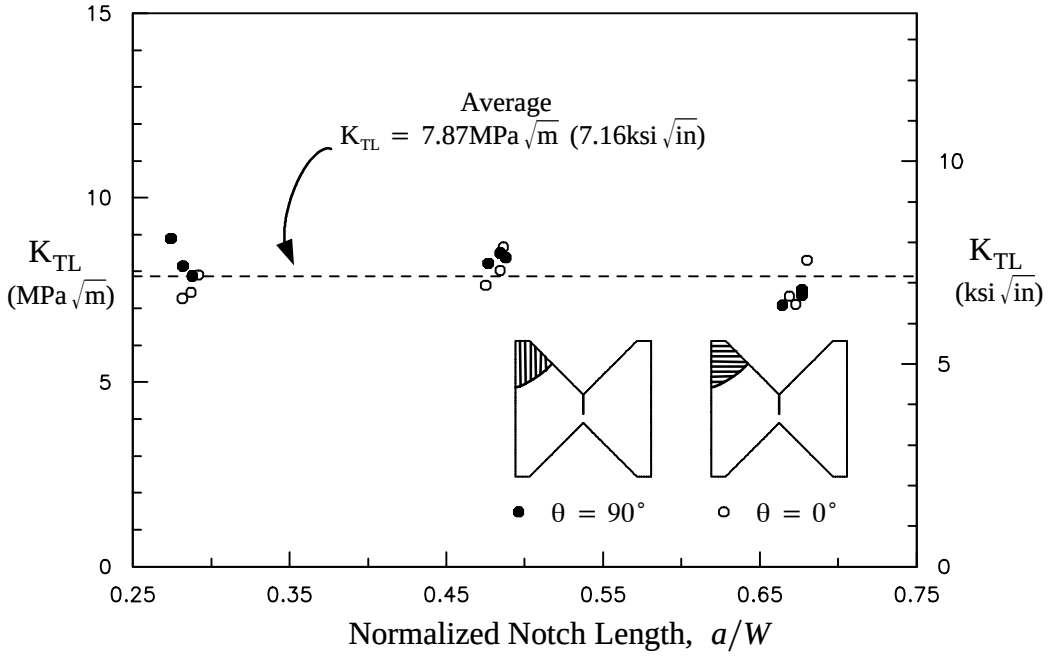

Figure 6.34 Mode-II fracture toughness from axial and transverse specimens

6.6 Integrated Cohesive and Micromechanical Models for Mode-II Crack Growth

Nonlinear constitutive micromechanical models were presented in Chapter 2. Calibration and verification of these micromodels for the E-glass/polyester composite were also presented. The CFM and roving micromodels were calibrated by assuming the same linear and nonlinear in-situ properties for their fiber and matrix subcells. Coupon tests were performed to calibrate and correlate the off-axis stiffness and the nonlinear stress-strain response in tension and compression. In this chapter, the experimental load versus γ_{SL} from the transverse specimens with a/W=0.3 was used to calibrate the mode-II parameters of the cohesive model. The cohesive shear failure stress, τ_n^f was set to 82.7 MPa (12.0 ksi) for both the axial and transverse fracture specimens. This value is the same as the unnotched shear strength. The release-time taken for the interface tractions to be ramped to zero was t_f = 0.003. The analysis was complete when the pseudo time reached t = 1.0. In comparison

to the mode-I fracture, the release time is ten times smaller and corresponds to the more brittle nature of crack propagation in this mode. As previoulsy for the mode-I case, the distance from the crack tip at which the failure criterion was evaluated was taken as L_c = 2.54 mm (0.1 in). Figure 6.35 shows the calibration for the mode-II fracture response from the tests on the transverse specimens. These test results were used for the calibration of the above cohesive parameters such that the FE response (solid line) correlates with the tests. The range of tested specimens included targeted a/W ratios of 0.3 and 0.7 with both axial and transverse roving orientations. More variability in the load-γ_{SL} response was observed in the axial orientations. Self-similar crack growth was evident in all axial specimen, probably due to the relatively low fiber volume fraction and the relatively smaller thickness of the roving layers. Self-similar crack growth was evident by examining the specimen after complete fracture occurred in all the axial specimens. Limited deviations from a straight (flat) crack were also observed, while the overall growth was self-similar in nature. The failure initiated at approximately the same load for the transverse specimens with the initiation starting at the notch root. After primary fracture the roving fibers play a role in bridging the propagating crack. For this mode, the use of mode-II crack models is justified until the maximum load.

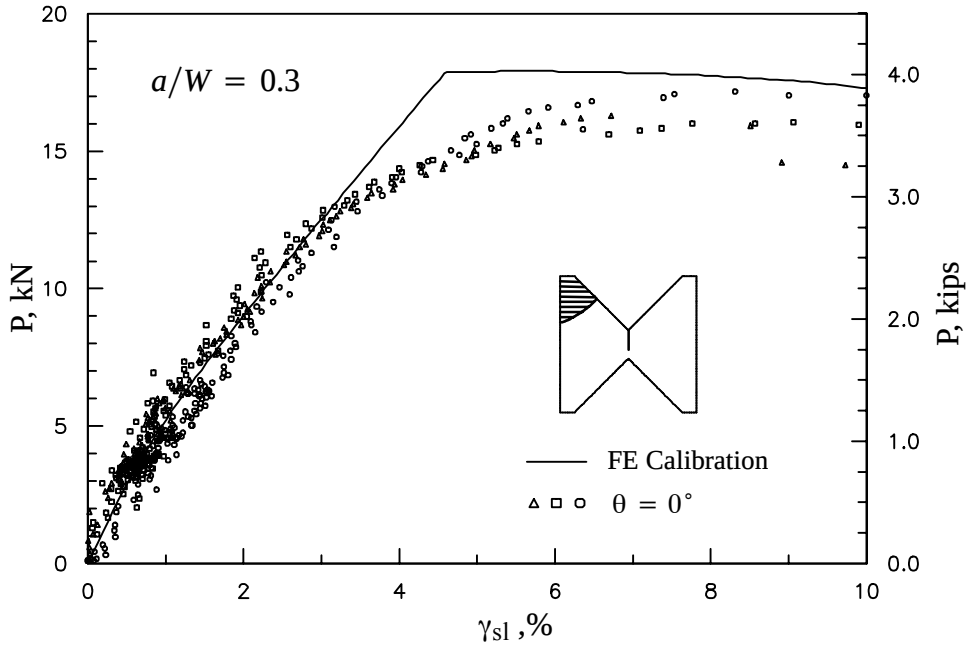

Figure 6.35 Calibration of the integrated models using the load versus apparent sliding strain from transverse mode-II fracture specimens with a/W=0.3

Figures 6.36 to 6.38 show the prediction of the load-γ_{SL} response for the axial and transverse mode-II fracture specimens with the targeted a/W of 0.3 and 0.7. The use of γ_{SL} was able to reduce the variability in the measurement of the test parameters caused by the boundary loading conditions (e.g. the bolts bearing on the specimen). This can be seen in the different regions on the response when using the actuator displacemnt as seen in Figures 6.28-6.31. There is an inherit rigid body motion in the displacment of the actuator which is reflected in the previous figures and probably adds to the scatter. The use of the γ_{SL} quantity enables the comparison of the results between the FE models and the experiments. The FE models were able to predict the softer response in the transverse specimens and all the failure loads for both the transverse and axial roving orientations. Overall, good predicions are demonstrated by the proposed combined crack growth modeling approach.

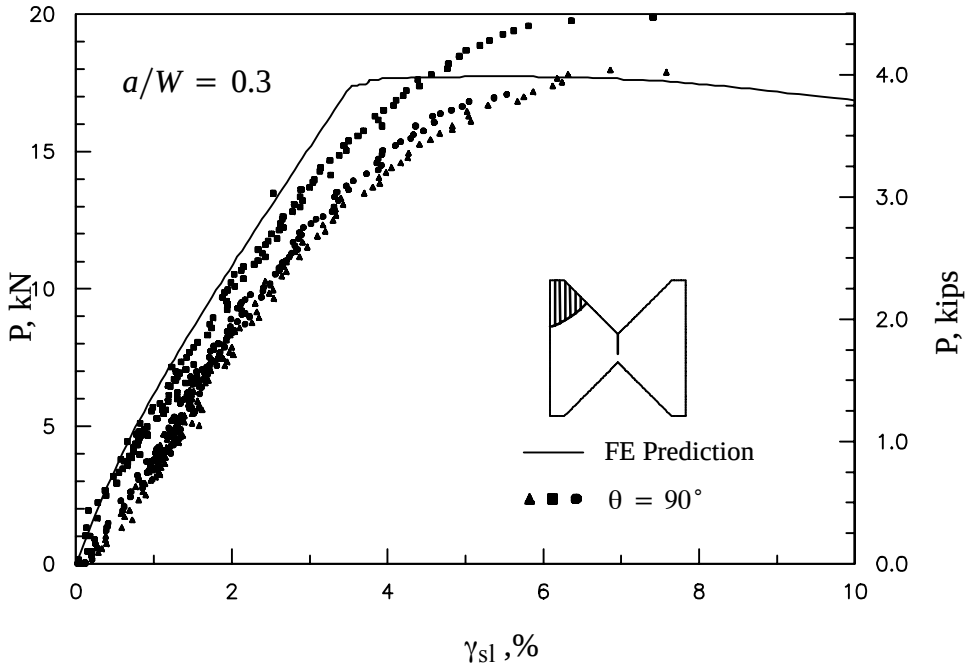

Figure 6.36 Prediction of the load versus apparent sliding strain response for axial mode-II fracture specimens with a/W=0.3

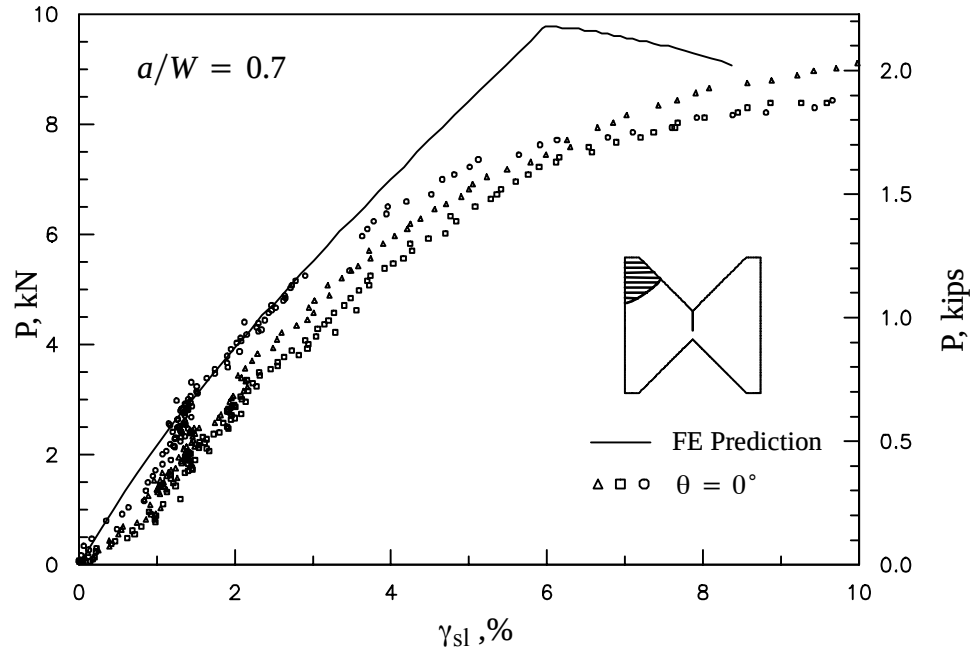

Figure 6.37 Prediction of the load versus apparent sliding strain response for transverse mode-II fracture specimens with a/W=0.7

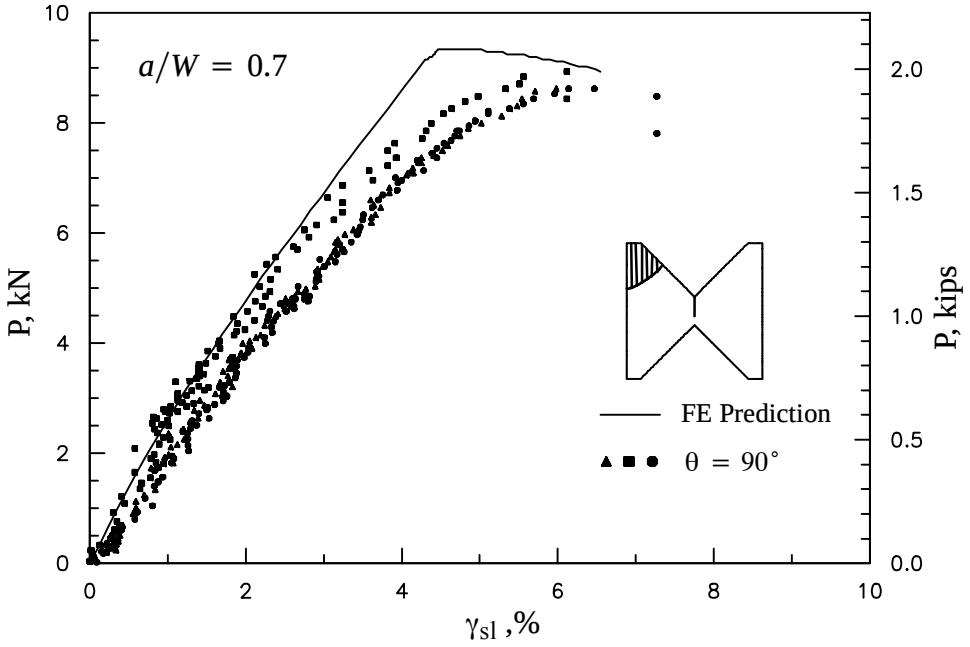

Figure 6.38 Prediction of the load versus apparent sliding strain response for axial mode-II fracture specimens with a/W=0.7

CHAPTER 7

APPLICATION OF MIXED MODE FRACTURE CRITERION IN STRUCTURAL ANALYSIS AND DESIGN

In this chapter a mixed mode fracture criterion is presented for thick-section pultruded composites. Experiments on the mixed-mode fracture behavior of pultruded butterfly specimen are performed by varying the angle of the load using the modified 'Arcan' fixture described in the previous chapter. The parameters for the proposed fracture criterion are evaluated from experimental results. Using a fracture assessment diagram, the mixed mode test results are found to be bound between linear and quadratic forms of the mixed mode criterion. In addition, example design applications are presented that utilize some of the principles presented in this study. The examples presented include application of linear fracture mechanics to crack systems that may occur in different pultruded structures. In addition, an example is presented that uses the virtual crack closure technique (VCCT) within a global finite element (FE) structural analysis for investigating the failure of a coped beam.

7.1 Mixed Mode Failure in FRP Composites

Various methods have been proposed in the literature for mixed mode fracture of FRP composite materials. One of the common methods of determining the mixed mode fracture is using a failure criterion in the form of:

$$\left\{\frac{K_I}{K_{IC}}\right\}^m + \left\{\frac{K_{II}}{K_{IIc}}\right\}^n = 1 \qquad (7.1)$$

where m and n are empirically obtained parameters. It should be noted that the above criterion is not based on physical interactions between the two modes, but is simply a method to fit the data. Jurf and Pipes (1982) used a quadratic form of this equation to evaluate the interlaminar fracture of a graphite/epoxy composite system. Donaldson (1985) performed

mixed-mode fracture experiments using off-axis coupons on graphite/epoxy and graphite/thermoplastic composites. A linear form of the above equation was found to be a lower bound for the experiments conducted. Whitney (1989) reported that the best fit for graphite/thermoplastic materials was obtained when m = 1 and n = 3/2 in Equation (7.1). Whereas for graphite/epoxy materials a linear criterion with m=1 and n=1 was found to be the most appropriate. Pang and Seetoh (1997) used the specimen proposed by Banks-Sills et al. (1984b) for mixed mode testing to study the mixed mode fracture of adhesive joints. Their study investigated the effect of the adhesive thickness and the mode-mixity on the fracture behavior. For the fracture criterion, their experimental results were found to be bound between a linear and elliptical fracture criterion rule. Rikards et al. (1998) used a compact tension shear specimen to study the mixed mode fracture behavior of glass/epoxy produced using a filament wounding technique. They found that the least error is found when m=1 and n=2.

7.2 Mixed Mode Fracture Tests

In this study, the fracture criterion parameters (Equation 7.1) for the E-glass/polyester pultruded composite were determined by testing 9 specimens in mode-I and mixed mode loading conditions. The tested specimens all had a transverse roving orientation (to the y-axis of fixture) and were tested by applying the load at various angles, α=0, 22.5 and 67.5 degrees. A normalized crack ratio of 0.5 was used for all the tests conducted. Figure 7.1 shows the off-axis load applied to the butterfly specimen. An analysis of the results shows that the mode-I response plays a larger role in the fracture response for the butterfly specimen than the mode-II response. This means that small variations from mode-II loading (α=90 degrees), will result in significant mode-I contributions. More variability is seen in the mode-I fracture toughness when compared to the mode-II values obtained. The average mode-I fracture toughness measured using the butterfly specimen was 7.19 MPa $\sqrt{m}$

(6.54 ksi$\sqrt{in}$) compared to the value from the ESE(T) tests which was 9.40 MPa $\sqrt{m}$ (8.56 ksi$\sqrt{in}$). This difference can be explained by the limited amount of stable crack growth that occurs in the ESE(T) specimen and is not seen in the butterfly specimen.

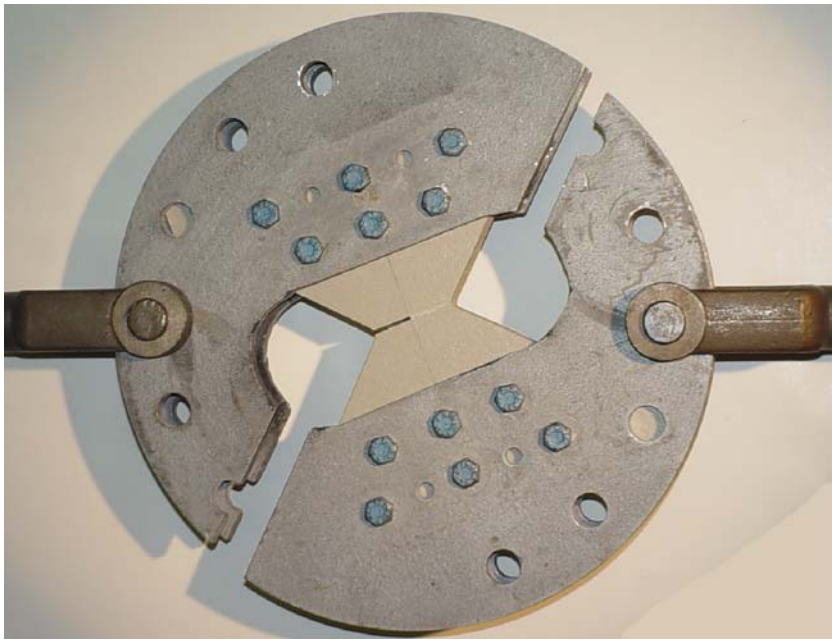

Figure 7.1 Mixed mode loading of a notched butterfly specimen

7.3 Mixed Mode Fracture Failure Criterion for Pultruded Composites

The proposed Equations (6.6) and (6.8) were used to determine the mode-I and II components of the applied load during mixed mode testing. A fracture criterion based on Equation (7.1) with m=1 and n=2 yields a suitable representation of the mixed mode fracture behavior than a purely quadratic form. Based on the mixed mode test results conducted, the fracture criterion in Equation (7.1) can then be written as:

$$\left\{\frac{K_I}{K_{IC}}\right\} + \left\{\frac{K_{II}}{K_{IIc}}\right\}^2 = 1 \qquad (7.2)$$

This criterion in graphical form can be seen in the fracture assessment diagram shown in Figure 7.2. Similarly it is assumed that when the rovings are oriented in the transverse direction a similar diagram can be constructed as shown in Figure 7.3. The criterion can also be expressed in terms of the critical strain energy release rates, G_{IC} and G_{IIC}. For the E-glass/polyester butterfly geometry tests, $G_{IC} = 4.30\ kJ/m^2$ (2.465×10^{-2} kip-in/in^2) with a coefficient of variation of 4.6 % and $G_{IIC} = 4.62\ kJ/m^2$ (2.636×10^{-2} kip-in/in^2) with a coefficient of variation of 1.7 % respectively. Equation (7.2) can alternatively be written as:

$$\left\{\frac{G_I}{G_{IC}}\right\} + \left\{\frac{G_{II}}{G_{IIc}}\right\}^2 = 1 \tag{7.3}$$

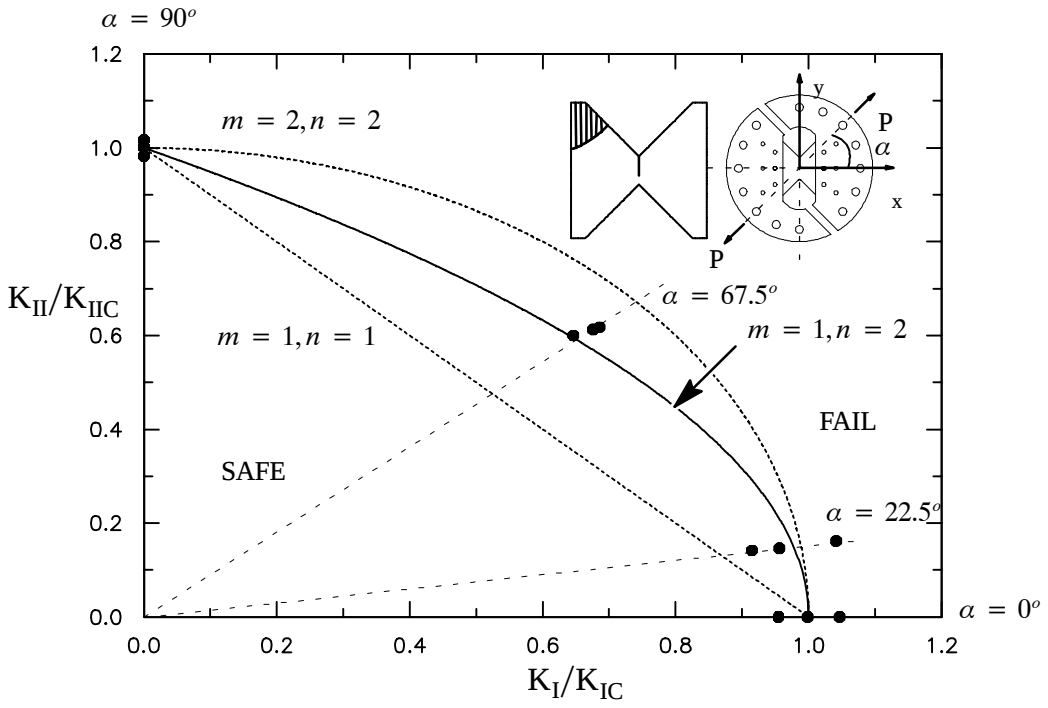

Figure 7.2 Mixed-mode fracture assessment diagram for axial specimen tests

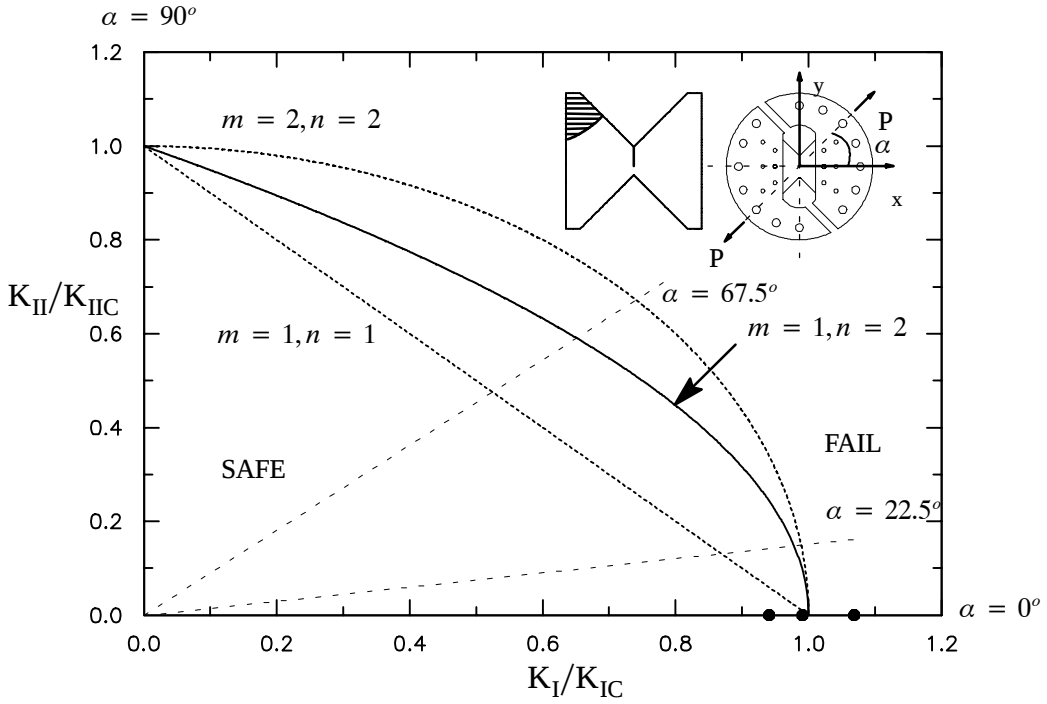

Figure 7.3 Mixed-mode fracture assessment diagram when fibers are transverse specimen tests

7.4 Example Design Problem: Mode-II Failure of Coped Beam

This example illustrates the advantages of using FE based fracture mechanics analyses in the structural design of pultruded FRP members and connections. In standard design practice, where one beam is to frame into another, sections of one beam are cut in order to achieve a flat surface along the flanges. In addition to the cut-out, the pultruded beam is usually connected to another section using a bolted connection. For this design problem, determine the failure load and location of fracture in the coped beam shown in Figure 7.4. The beam is simply supported and is 20 ft long. 9/16 in diameter holes are used to accommodate 1/2 in diameter bolts required for the connection.

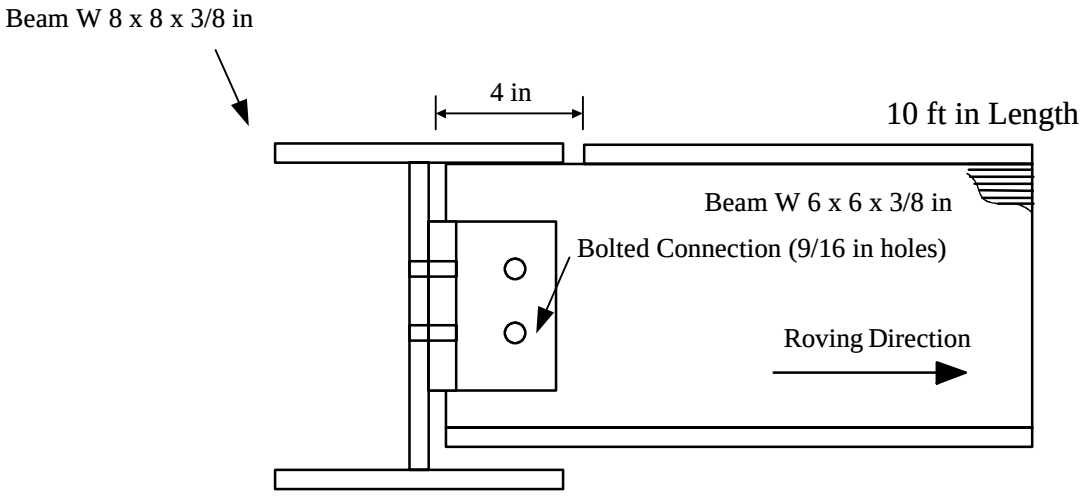

Figure 7.4 Side view showing the coped beam connection

The connection region is an area of high shear stresses. These stresses are capable of propagate a crack along the direction of the flange/web interface or at one of the holes. A simple connection is assumed between the 6 in x 6 in x 3/8 in Wide Flange Section which is coped into the 8 in x 8 in x 3/8 in beam. In the fracture analysis, a hypothetical crack system is imposed on the coped beam. Cracks of 0.2 in length are modeled at all the locations where a crack is suspected of propagation. A FE based analysis is used to determine the strain energy release rate for all the cracks analyzed. Figure 7.5 shows the system of cracks investigated. The possibility of mode-II failure at these locations was considered in this analysis. The VCCT method for mode-II cracks discussed in Chapter 6 is used to determine the strain energy release rate at the locations specified by using a series of soft and stiff springs. Plane strain reduced integration 8-node (CPE8R) elements using ABAQUS (2002) were used to generate the FE model. The mesh used had a refined area around the end and in total consisted of approximately 28,000 nodes and 8,900 elements. Figure 7.6 shows the FE mesh around the coped section on the half model of the simply supported beam analyzed.

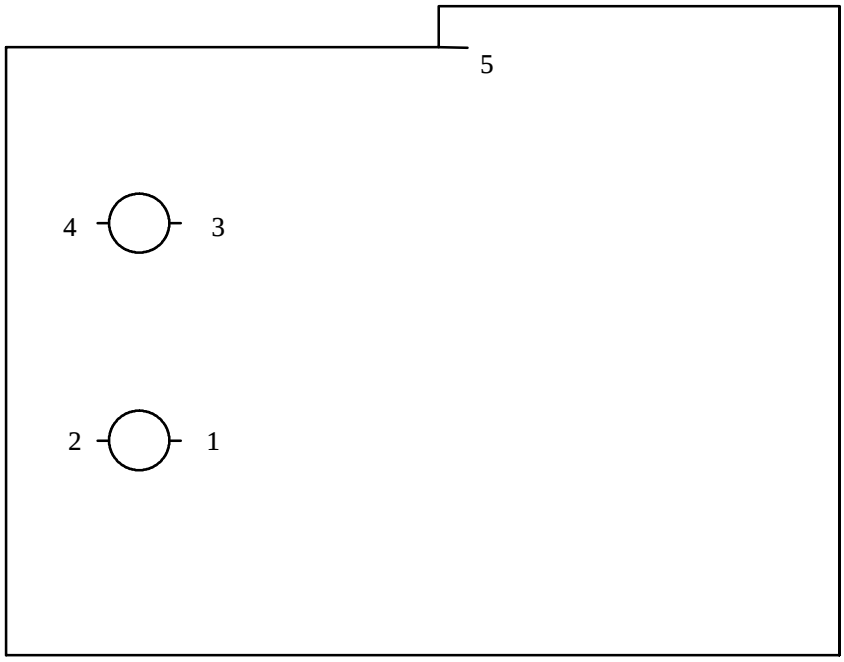

Figure 7.5 Postulated crack locations where the VCCT technique is used to determine the failure load and crack growth location

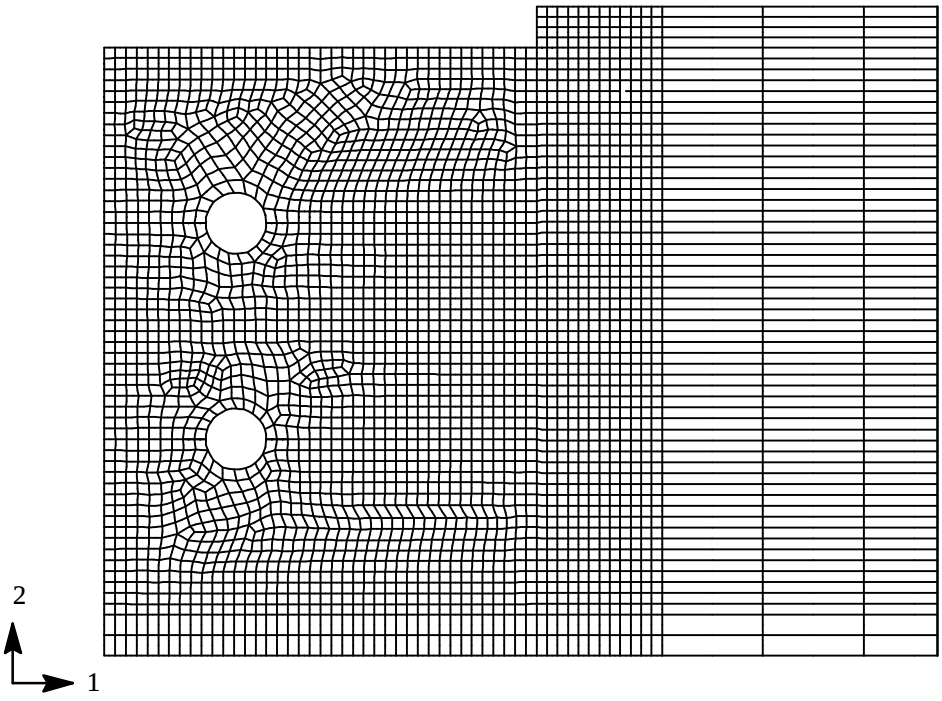

Figure 7.6 FE mesh near coped end

Linear elastic analysis was performed using the orthotropic properties of the E-glass/polyester pultruded composite (Chapter 2). Figure 7.7 shows the shear strains near the end of the beam. Note the areas of high shear stresses near the top flange and around cracks 1 and 3. Table 7.1 shows a summary of the G_{II} values for the five crack locations analyzed. The relation between the shear load at the support and the mode-II strain energy release rate, G_{II} is:

$$G_{II} = G_{II\_(V=1)} \; V^2 \tag{7.4}$$

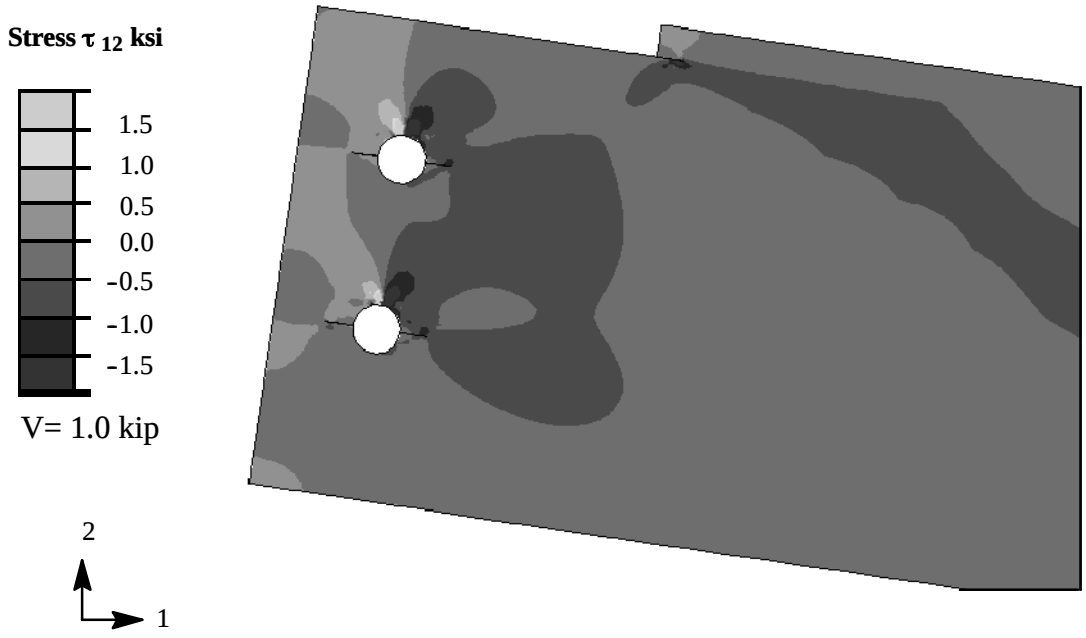

Figure 7.7 FE analysis shear strain distribution for deformed shape at coped end

Table 7.1 Mode-II strain energy release rate values of postulated cracks (V = 1.0)

Crack #	G_{II} (kip-in/in^2)
1	1.15×10^{-4}
2	2.77×10^{-6}
3	$\mathbf{1.29 \times 10^{-4}}$
4	2.22×10^{-6}
5	$\mathbf{5.48 \times 10^{-4}}$

The G_{II} values at cracks 2 and 4 are orders of magnitude lower than cracks 1 and 3 and it is unlikely that the crack will initially propagate at these locations. Using the equation above and the failure criterion in Equation (7.3) with the assumptions that $G_{IIC} = 2.636 \times 10^{-2}$ kip-in/in^2 and $G_I = 0$, the shear load that will cause a crack to propagate from the top hole (Crack 3) is calculated as:

$$V_3 = \sqrt{\frac{2.636 \times 10^{-2}}{1.29 \times 10^{-4}}} = 14.3 \text{ kips} \tag{7.5}$$

Similarly the failure load that will cause the crack to propagate across the web/flange interface (Crack 5) is:

$$V_5 = \sqrt{\frac{2.636 \times 10^{-2}}{5.48 \times 10^{-4}}} = 6.9 \text{ kips} \tag{7.6}$$

Since $V_3 < V_5$, the crack is likely to propagate at the web/flange interface (Crack 5) instead of the right crack on the top hole (Crack 3).

7.5 Example Design Problem: Leak Before Brake in a Pultruded Pipe

In this example, determine whether a crack developing in a pultruded composite pipe will propagate in such a way that it will reach the surface and cause a leak before catastrophic failure can occur. A crack on the inside surface of the pipe can grow and can be driven by localized stresses. However, once the crack breaks into the surface, it is desired that it is arrested so that a leak can occur before it continues to grow and cause catastrophic failure. In other words, the critical size of the crack at the design stress level would have to be larger than the wall thickness. Assuming an initial defect, the stress intensity factor (SIF) will increase as the crack is growing and will not cause failure as long as it does not exceed the material's resistance to fracture. If this condition prevails, then a leak situation will occur. Note that because of the manufacturing process of pultruded pipes, the roving fibers are not oriented in the optimum direction to resist the hoop stresses and translaminar propagating cracks parallel to the rovings. In this example it is required to make a leak before fracture assessment. The pultruded composite pipe has a radius (R) of 5 in and thickness (t) of 0.5 in. Since R/t = 10, membrane theory can be used. Figure 7.8 shows a schematic of this pipe under internal pressure. The fracture toughness of the FRP composite is given as 9.0 ksi$\sqrt{\text{in}}$ and the transverse failure stress is given as 12.0 ksi. In this assessment it is customary to assume that the through crack that will break through the pipe will have a length of 2t (Broek, 1997). This crack can be modeled as a through crack in an infinite plate (Figure 7.9). The stress at which this crack can cause failure of this pipe and leak can then be determined from:

$$K_I = \sigma\sqrt{\pi a}\ F(a) \tag{7.7}$$

Where F(a) is related to the geometry and is assumed to be 1.0.

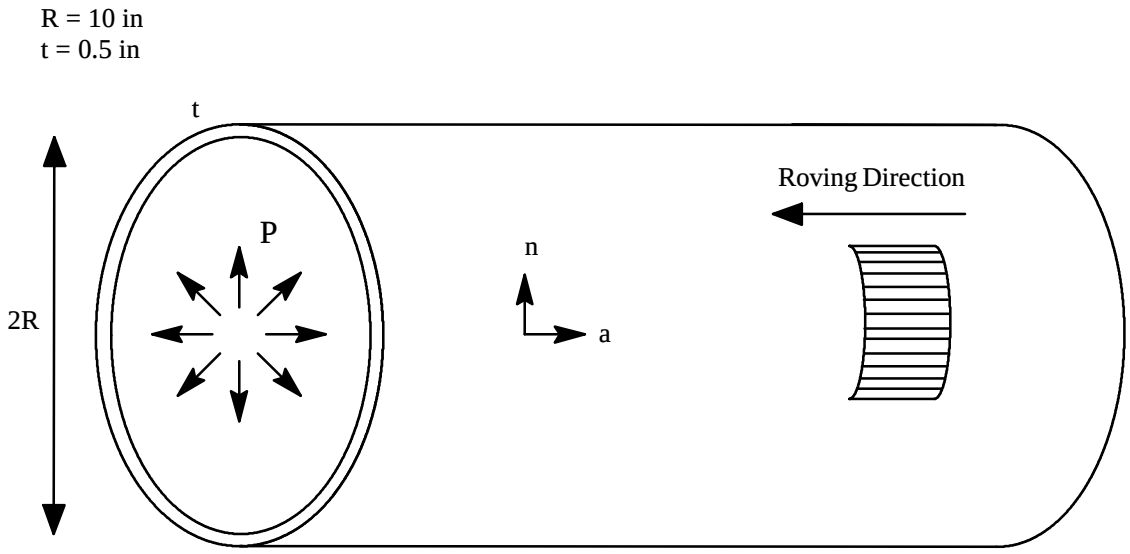

Figure 7.8 Pultruded pipe carrying liquid under pressure

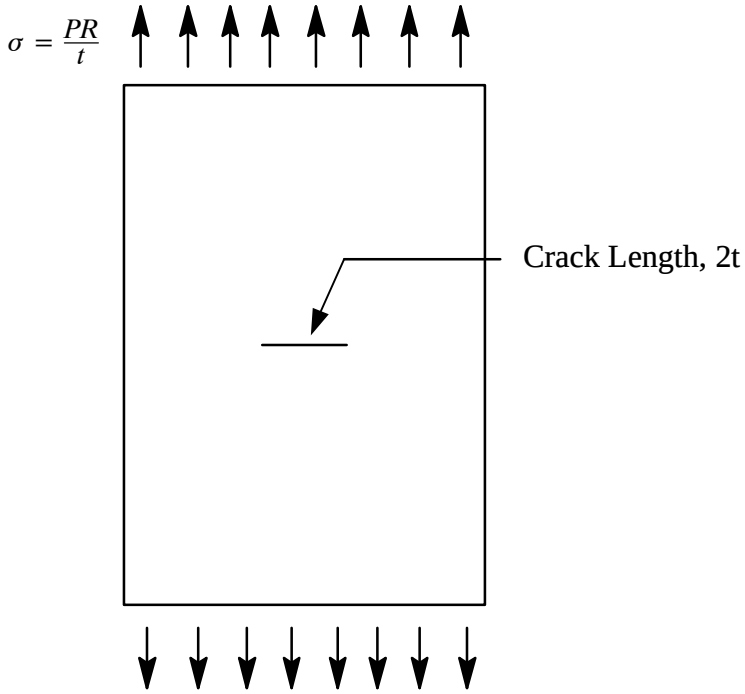

Figure 7.9 Through thickness crack in pultruded pipe

Since the axial stresses are smaller than the hoop stresses and are acting in the roving or strong orientation of this material, the analysis in that direction is not considered critical. Using membrane theory the maximum pressure that the pipe can hold assuming a factor of safety of 2, is:

$$P = \frac{\sigma_{tf}\, t}{R\, S_f} = \frac{12.0 \times 0.5}{5 \times 2} = 0.6 \text{ ksi} \tag{7.8}$$

An estimate of the critical crack size that will cause fracture at the pressure calculated above is determined from Equation (7.7):

$$a_{cr} = \frac{1}{\pi}\left\{\frac{S_f\, K_{IC}}{\sigma_{tf}}\right\}^2 = \frac{1}{\pi}\left\{\frac{2 \times 9.0}{12.0}\right\}^2 = 0.72 \text{ in} \tag{7.9}$$

Since $t < a_{cr}$, the leak-before-break conditions are met. A 0.5 in through crack can be tolerated at the service loading conditions.

7.6 Example Design Problem: Bolted Connection in Tension

One of the problems that arises in the design of pultruded composite connections are cracks that may emanate from loaded bolt holes. Determine the fracture stress for the bolted connection shown in Figure 7.10. Figure 7.11 shows a TSA image showing how cracks can initiate in pultruded composites near high stress regions. The mode-I fracture toughness of the FRP composite is given as 17.0 ksi$\sqrt{\text{in}}$ and the uniaxial failure stress in tension, σ_{tf} is 26.0 ksi. The hole diameter is 0.5 in and the crack size a, on either side of the hole is 0.4 in. The width is taken as 3 in.

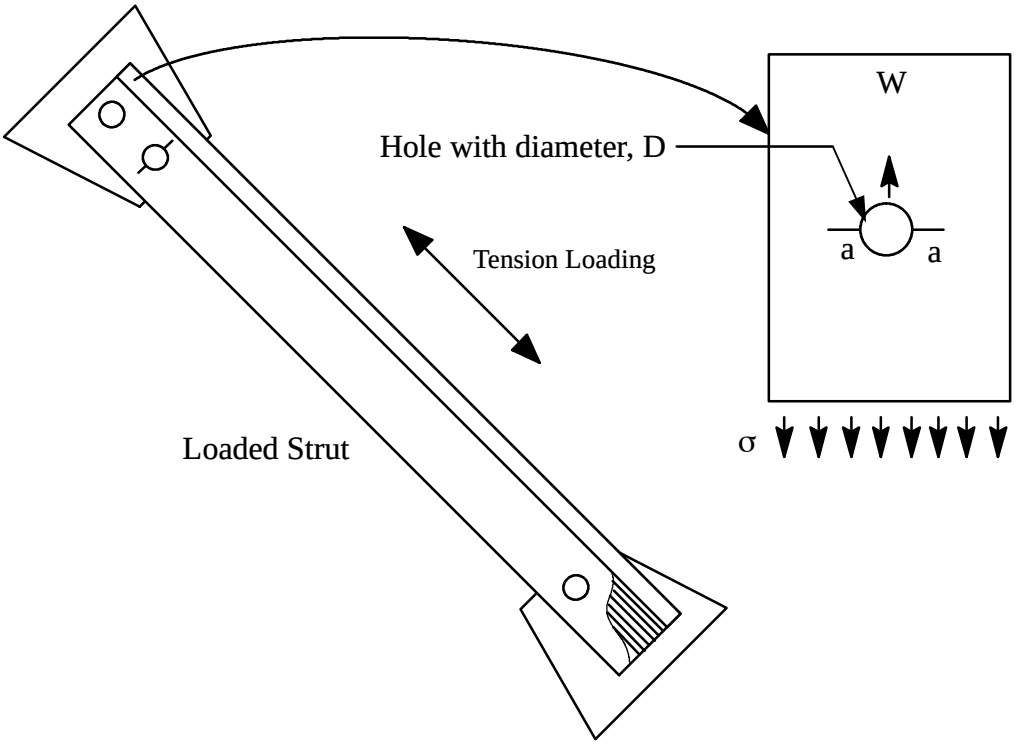

Figure 7.10 Angle–gusset plate bolted connection

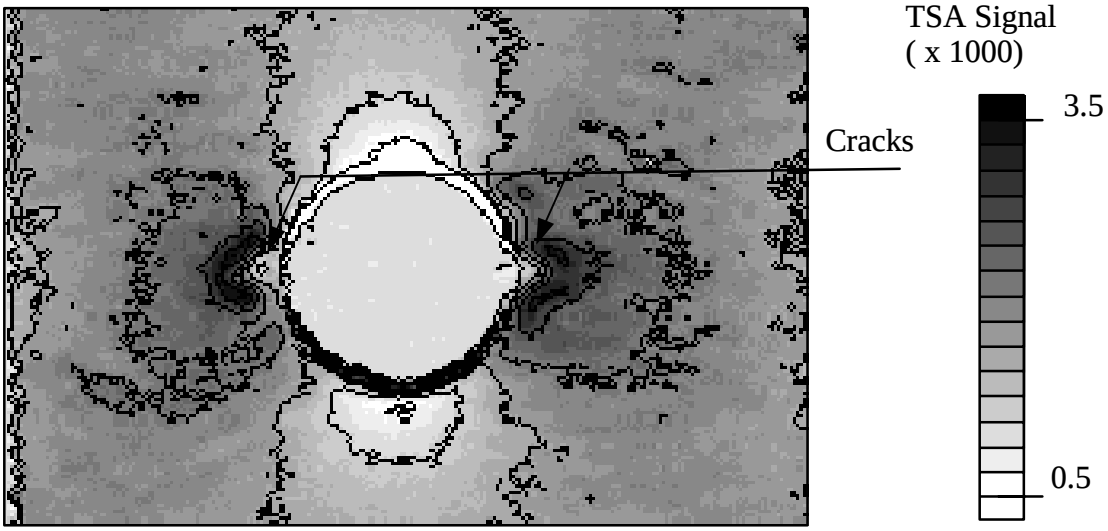

Figure 7.11 TSA image showing cracks that have initiated under high stresses in a notched pultruded plate loaded in tension

To analyze this problem, the stress intensity factor for this situation is obtained by idealizing the connection using the superposition of the SIF solutions of a strip in tension with cracks emanating from the hole and that of a crack centrally loaded with a wedge force. This idealization simulates the action of the bolt against the composite. For a strip in tension with a crack emanating from the hole, the mode-I SIF is (Broek, 1997):

$$K_{IA} = \sigma\sqrt{\pi a}\ \sqrt{\frac{D}{2a} + 1} \tag{7.10}$$

where σ is the applied stress, D is the diameter of the hole and, a is the crack size on each side. Similarly, for the cracked plate with a centrally loaded wedge force, the mode I SIF is:

$$K_{IB} = \frac{P}{\sqrt{\pi a}} \tag{7.11}$$

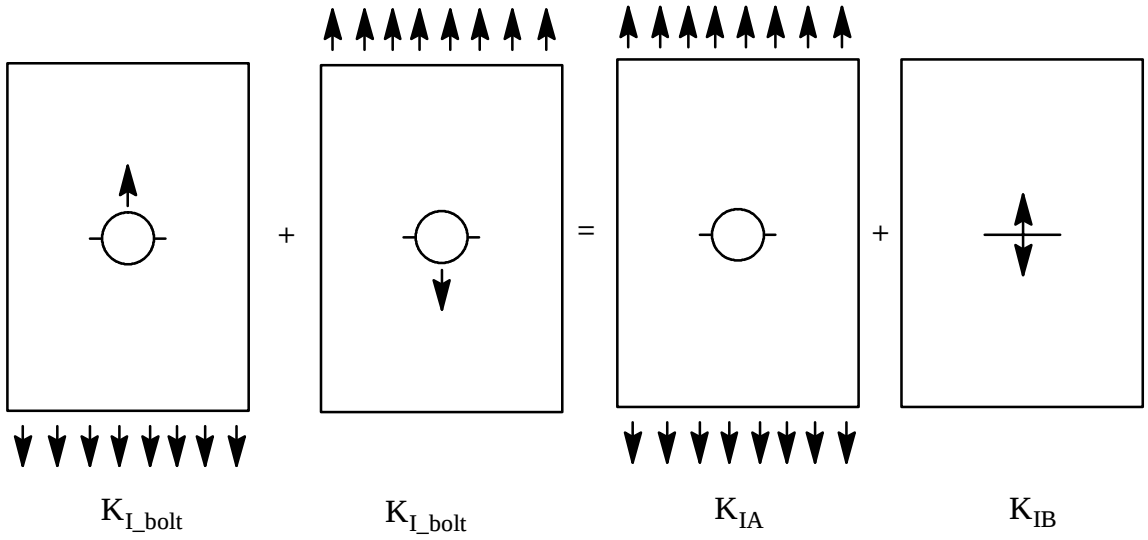

Figure 7.12 Bolted connection SIF using superposition

where P is the load per unit thickness and a is the crack size. It is interesting to note that the SIF for the centrally loaded wedge decreases as the crack increases. This could result in a crack being arrested after it propagates away from the bolt. Figure 7.12 illustrates how using superposition, the mode-I SIF for the loaded bolt connection can be obtained using the following relationship:

$$2\,K_{I\_bolt} = K_{IA} + K_{IB} \tag{7.12}$$

$$K_{I\_bolt} = \frac{1}{2}\left\{\sigma\sqrt{\pi a}\,\sqrt{\frac{D}{2a}+1} + \frac{\sigma W}{\sqrt{\pi a}}\right\} \tag{7.13}$$

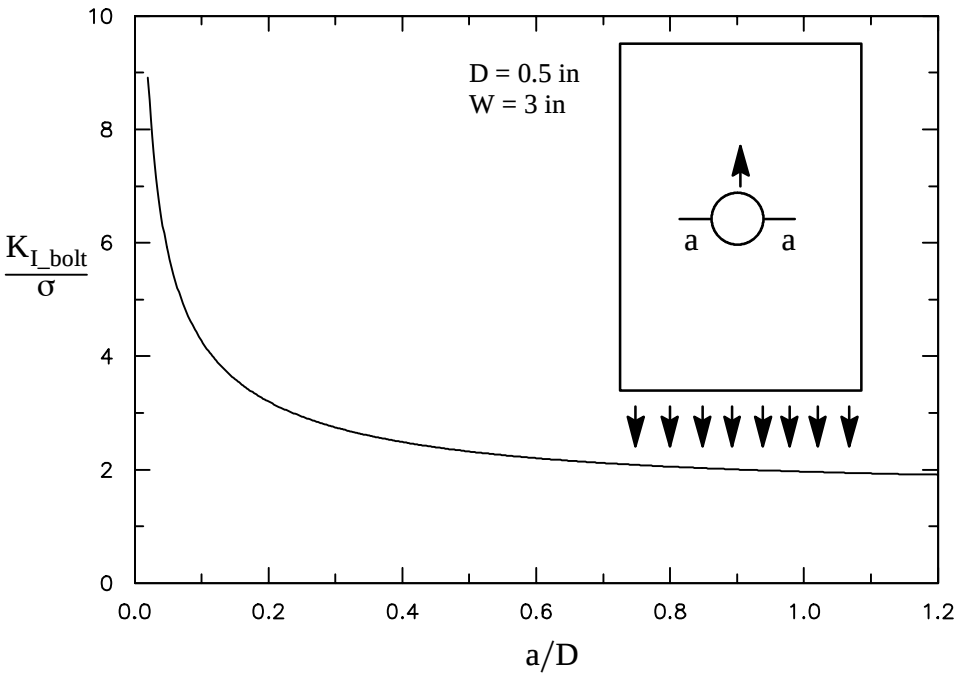

Figure 7.13 Normalized Mode-I in bolted connection as a function of crack size

Using Equation (7.13), we can solve for the fracture stress, $\sigma_{fracture}$

$$\sigma_{fracture} = \frac{2\,K_{I\_bolt}}{\left\{\sqrt{\pi a}\,\sqrt{\frac{D}{2a}+1}+\frac{W}{\sqrt{\pi a}}\right\}} = \frac{2\times 17.0}{\left\{\sqrt{0.5\pi}\,\sqrt{\frac{0.5}{2(0.5)}+1}+\frac{3}{\sqrt{\pi 0.5}}\right\}} = 5.31 \text{ ksi} \qquad (7.14)$$

Based on the net section failure of this composite and a factor of safety of 3 corresponding to a stress concentration near the edge of the hole, the failure stress can be estimated:

$$\sigma_{strength} = \frac{\sigma_{tf}}{S_f}\left\{\frac{W-2a-D}{W}\right\} = \frac{26}{3}\left\{\frac{3-2(0.5)-0.5}{3}\right\} = 6.64 \text{ ksi} \qquad (7.15)$$

Since $\sigma_{fracture} < \sigma_{strength}$, the crack is likely to propagate at a lower stress than that estimated using the strength approach.

7.7 Example Design Problem: Crack in Flange Section

Pultruded structural profiles may sometimes become damaged due to impact. This may occur during shipment or when the structure is in service. The structural integrity of a damaged profile needs to be assessed when determining whether a replacement is necessary or a reduction of the allowable loads needs to be made. Some fabricators of pultruded profiles recommend that an entire section be replaced if a fracture in excess of a certain size occurs. If the section is not replaced then a fracture may propagate along the entire length of the structure (Strongwell ,2003). In this example, it is required to assess, the structural integrity of a 10 ft simply-supported beam section, W10 x 10 x 1/2 in, that has a 5 in crack in the flange at the flange/web junction, in a zone near the supports where the shear stress are particularly high (Figure 7.14). Determine whether crack propagation would dominate the failure of this section. The principal design controlling parameter is given for the local compression buckling for a distributed load of 4.97 kip/in (Creative, 2000).

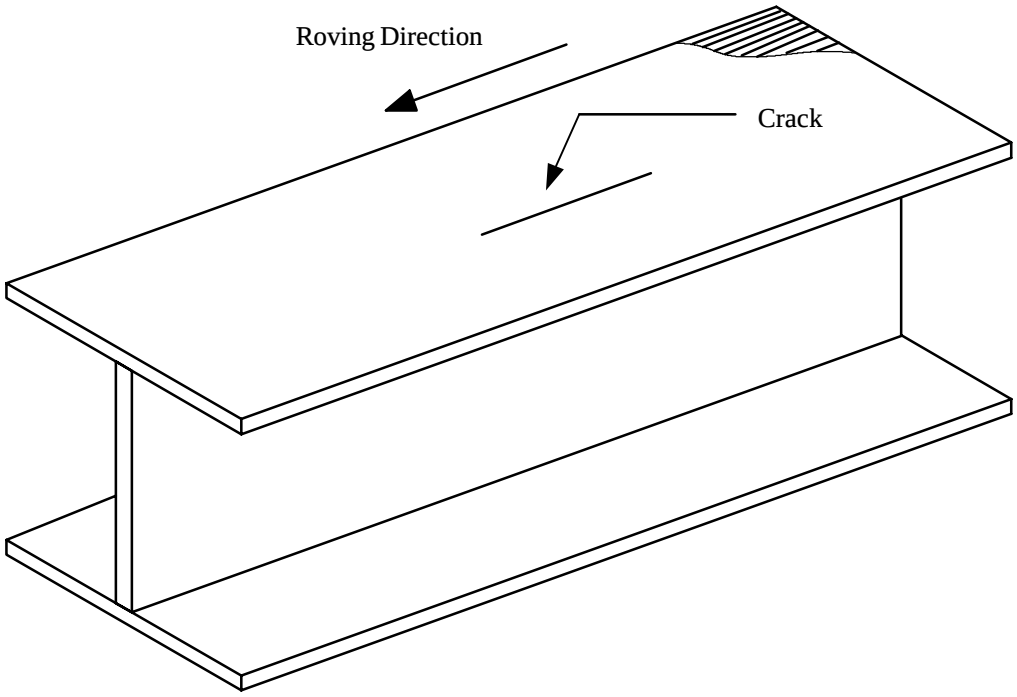

Figure 7.14 Pultruded wide flange section with a crack along the upper flange

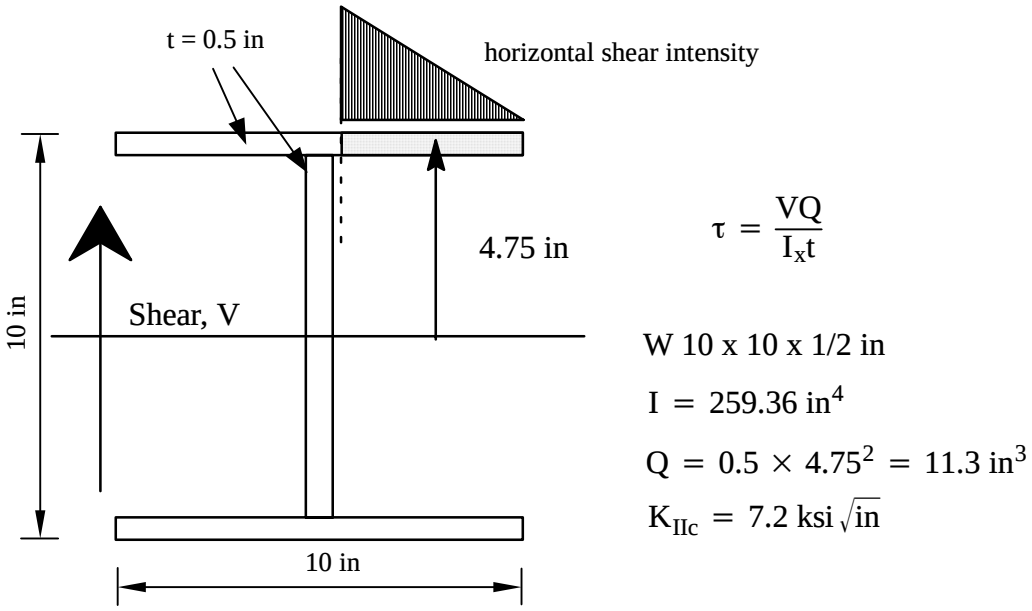

Figure 7.15 Cross-section showing horizontal shear in the flange of I section

Figure 7.15 shows the cross-section of the beam with the material and section properties considered. Equation (7.16) is used to determine the horizontal shear τ in the wide flange section:

$$\tau = \frac{VQ}{I\,t} \tag{7.16}$$

where V is the applied shear, Q is the first moment of area at the location considered, I is the moment of inertia and t is the thickness of the flange. The mode-II SIF solution used for this problem is given by Equation (7.17).

$$K_{II} = \tau\sqrt{\pi a}\ F(a) \tag{7.17}$$

Where F(a) is related to the geometry and is assumed to be 1.0. To complete the fracture analysis, the only material property required would be the mode-II fracture toughness. By substituting Equation (7.16) into (7.17), a relation between the shear load that causes fracture and the crack size can be determined:

$$V_{fracture} = \frac{K_{IIc}\,I\,t}{Q\ \sqrt{\pi a}} \tag{7.18}$$

Figure 7.16 shows the normalized shear load as a function of the crack size for some standard wide flange I-sections. The flaw is assumed at the most critical location of the web flange junction. The horizontal shear at other locations of the crack can also be calculated from the Equation (7.18). For the W10 section considered, the shear load that will cause the 5 in crack in the flange to propagate is:

$$V_{fracture} = \frac{K_{IIc}\,I\,t}{Q\ \sqrt{\pi a}} = \frac{7.2 \times 259.36 \times 0.5}{11.3\sqrt{5\,\pi}} = 20.8 \text{ kips} \tag{7.19}$$

Using the allowable distributed load, the maximum shear force near the supports can be calculated from:

$$V_{buckling} = \frac{wL}{2} = \frac{4.96 \times 10}{2} = 24.8 \text{ kips} \qquad (7.20)$$

Since $V_{fracture} < V_{buckling}$, the crack is likely to propagate before reaching the load that will cause the compression buckling of the beam section.

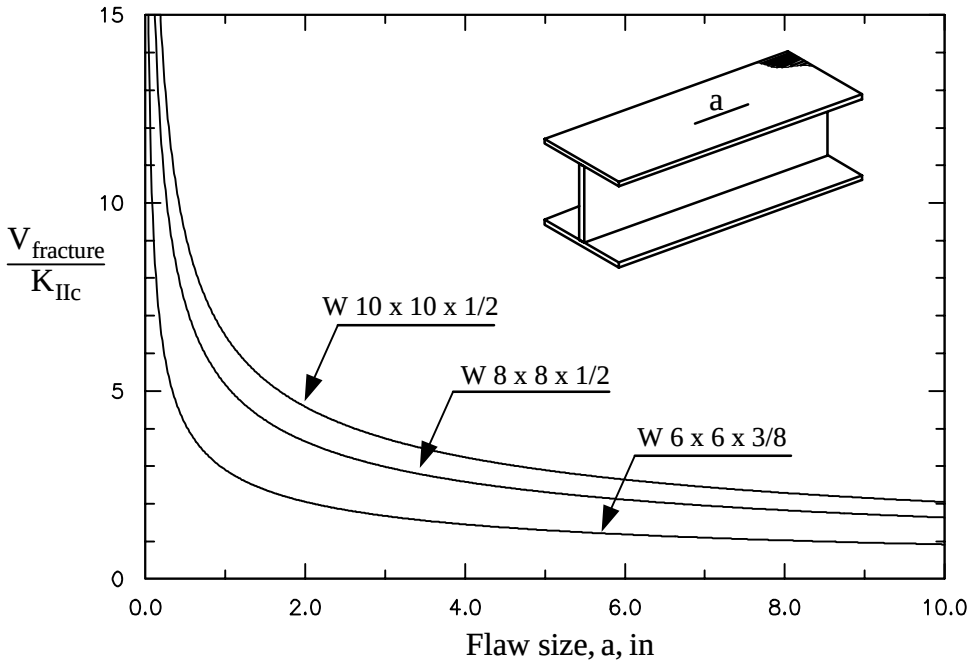

Figure 7.16 Normalized failure shear load as a function of crack size for various wide flange I-sections

CHAPTER 8

CONCLUSIONS AND FURTHER RESEARCH

An analytical and experimental study is presented for the analysis of the mode-I and II translayer fracture behavior in thick-section pultruded FRP composites. Micromechanical material models were applied and coupled with cohesive finite element (FE) analyses to predict the crack growth in these modes of fracture. Commercially available thick-section FRP composite materials were tested to demonstrate the proposed fracture approach along with the nonlinear constitutive modeling. The calibrated cohesive models are able to predict the measured crack growth in both modes I and II for various crack geometries. A new IR technique capable of measuring the strain fields around the crack geometries, was introduced and verified. Based on the experimental and analytical results, the proposed ESE(T) geometry can be used for measuring mode-I fracture toughness in the tested class of thick composites. Similarly, a butterfly shaped specimen was introduced to measure mode-II toughness and to assess the mixed-mode fracture response. A polynomial mixed mode failure criterion was verified with test results. Examples were presented for using this criterion and the crack growth analyses technique. These results can form a foundation for using a fracture-based method for the design of pultruded structures. This chapter presents a summary of major conclusions followed by further research recommendations.

8.1 Conclusions

The combined micromechanical and cohesive finite element (FE) modeling approach was successfully applied to predict the failure of a pultruded FRP composite under mode-I and II loading conditions. This is performed by using micromechanical constitutive models to capture the nonlinear material response and cohesive elements to capture crack growth. The applied micromechanical models used for the roving and CFM layers recognize the material

response at the fiber and matrix constituents. The combined models were successful in predicting the crack growth response in various specimen configurations for both the transverse and axial roving orientations. Calibration was achieved based on one specific geometry while verification of crack growth was done for a range of crack geometries. Stable crack growth before failure was also predicted using the proposed method.

A new quantitative thermoelastic stress/strain analysis (TSA) method, based on IR thermography, was derived and applied in the fracture studies. The proposed method measures the sum of the direct surface strains in FRP pultruded and other thick-section composites. It was used successfully to verify the validity of the combined FE modeling approach before the onset of crack growth. For the tested mode-I fracture specimens, the integrity of the test fixtures and setup was assessed by qualitatively examining the stresses around the loading pins and the notch tip. In designing the mode-II test specimen, IR thermography was also used to assess the uniformity of the stress field for 'pure shear' conditions at the center (gage section).

The ESE(T) specimen was successfully used to measure the pultruded material's mode-I translayer fracture toughness. This toughness was not dependent on the initial crack size for the range of tested a/W ratios (0.3 to 0.7). A limited amount of stable crack growth was found to occur before the ultimate load. To account for the material orthotropy, FE analysis using the virtual crack closure technique produced corrections to the 'isotropic' stress intensity factors (SIF). Therefore, the available isotropic solutions for the SIF can be used in testing and failure analysis.

A butterfly specimen geometry was developed and successfully used to determine the mode-II translayer fracture toughness. This toughness was not dependent on the initial crack size for the range of tested a/W ratios (0.3 to 0.7). Finite element analyses were used

to design the butterfly specimen and minimize the stress concentration at the notches to approach the nominal shear stress at the center of the gage section. It was found that using a radius of 2.54 mm (0.1 in) and aligning the fibers in the load direction during a 'pure shear' test results in a uniform shear stress distribution along the gage section. Low levels of normal strain were shown from the strain gages rosettes. The mode-I and II SIF solutions for the butterfly specimen were determined using the virtual crack closure technique and compared to results of similar geometries from the literature.

A mixed-mode fracture failure criterion was proposed for thick-section pultruded composites. This criterion was verified from mixed-mode tests using the modified 'Arcan' fixture and the butterfly specimen. Using a fracture assessment diagram, all the test data were bounded between the linear and quadratic fracture criteria. Combined linear and nonlinear terms were suggested for the proposed mixed-mode fracture criterion of the E-glass/polyester pultruded composite.

The proposed fracture toughness tests can provide valuable design information. In addition, these toughness tests can be used in acceptance criteria of manufactured composite materials.

8.2 Further Research

Thick-section FRP composites are used in lieu of other traditional materials because of their superior properties under corrosive or harsh environmental conditions. There are no studies on how environmental effects can influence the fracture behavior in these materials. Temperature or loading rate effects can also influence the measured or predicted fracture responses under creep conditions and are thus recommended areas for further research.

Analysis of microstructural effects on the global fracture response using parametric studies with parameters such as the fiber volume fractions and in-situ material properties. The modeling framework presented can be modified to include different microstructural effects on the global fracture response. Tradeoffs between material constituent properties and various design requirements can also be assessed. The proposed micromodels can also be extended to include different forms of matrix nonlinear behavior that incorporates environmental effects, such as moisture and temperature. A crack mouth opening displacement criterion can be applied in the cohesive layer to simulate the crack growth under creep conditions.

The proposed micromechanical framework can be modified to include different composite systems, such as woven or braided layers within the cross-section of the composite. This can be accomplished by using new and existing micromechanical formulations.

Further refinement of the micromechanical models to include fracture at the microstructural level is another area of research. Instead of using a homogenized crack growth, a local energy based crack-trapping and bridging model such as that proposed by Bower and Ortiz (1991) can be incorporated with the global structural analysis to model the fracture behavior in the individual layers of the pultruded composite.

The proposed IR thermography technique can be easily extended and applied in composite structures for nondestructive evaluation. This method can be used in various processes of design, manufacturing or in-service monitoring for higher structural reliability. In addition, mixed-mode fracture SIFs may be determined for thick-section composite materials by modifying the proposed TSA technique.

The procedures presented in this work are considered general enough to merit their application to other thick-section composite systems. Thick-section composites with various lay-ups and constituent materials can be tested using these methods. The use of other fixtures and setups on the same materials are also needed to ensure consistency of the measured material properties across the various test methods.

The mode I and II toughness test geometries assume the tested properties as material constants. The geometry limits of the material and the tested specimens can be further investigated to examine the limits of the above assumption (material invariant). Different parameters can then be varied, such as the thickness, number of layers or the geometry of the ESE(T) and butterfly specimens.

REFERENCES

ABAQUS, (2002), Hibbitt, Karlsson and Sorensen, Inc.,"User's manual", Version, 6.3.

Aboudi, J. (1991), "Mechanics of composite materials: a unified micromechanical approach", Elsevier.

Aboudi, J. (1990), "Micromechanical characterization of the non-linear viscoelastic behavior of resin matrix composites", Composites Science and Technology, vol. 38, pp. 371-386.

Aboudi, J. and Cederbaum, G. (1989), "Analysis of viscoelastic laminated composite plates", composite structures," vol. 12, pp. 243-256.

Adams, R. D., and Short, D., (1973), "The effect of fibre diameter on the dynamic properties of glass-fibre-reinforced polyester resin," J. Phys. D: Appl. Phys., vol. 6, pp. 1032-1039.

Arcan, M., Hashin, Z., Voloshin, A, (1978), "Method to produce uniform plane-stress states with applications to fiber-reinforced materials," Experimental Mechanics, vol. 18, no. 4, p 141-146.

Armanios, E.A, (1989), "Interlaminar fracture in graphite/epoxy composites," Key Engineering Materials, vol. 37, pp. 85-102.

ASTM D 3039/D 3039M, (2000), "Standard test method for tensile properties of polymer matrix composite materials.", Annual Book of ASTM standards.

ASTM E 1922, (1997), "Standard test method for translaminar fracture toughness of laminated polymer matrix composites.", Annual Book of ASTM standards.

ASTM E 399, (1997), "Standard test method for plane-strain fracture toughness of metallic materials", Annual Book of ASTM standards.

ASTM D3410/D3410M (1995), "Standard test method for compressive properties of polymer matrix composite materials with unsupported gauge section by shear loading", Annual Book of ASTM standards.

Bakis , C. E., and Reifsnider, K. L., (1991), "The adiabatic thermoelastic effect in laminated fiber composites," Journal of composite materials, vol. 25, pp. 809-830.

Bank, L. C., and Yin, J., (1999), "Failure of web-flange junction in postbuckled pultruded I-beams," Journal of Composites for Construction, vol. 3, p 177-184.

Bank, L. C., (1990), "Shear properties of pultruded glass FRP materials," Journal of Materials in Civil Engineering, vol. 2, no. 2, pp. 118-122.

Banks-Sills, L., and Arcan, M., (1986), "A compact ode-II fracture specimen," Fracture Mechanics, Seventeenth Volume, ASTM STP 905, J. H. Underwood, R. Chait, C. W. Smith, D. P. Wilhem, W. A. Andrews, and J. C. Newman, Eds., American Society for Testing and Materials, Philadelphia, pp. 347-363.

Banks-Sills, L., Arcan, M., and Gabay, H., (1984a), "A mode-II fracture specimen - finite element analysis," Engineering Fracture Mechanics, vol. 19, no. 4, pp. 739-750.

Banks-Sills, L., Arcan, M., and Bortman, Y., (1984b), "A mixed mode fracture specimen for mode-II dominant deformation," Engineering Fracture Mechanics, vol. 20, no. 1, pp. 145-157.

Barbero, E. J., Makkapati, S., and Tomblin, J. S., (1999), "Experimental determination of the compressive strength of pultruded structural shapes," Composites Science and Technology, vol. 59, pp. 2047-2054.

Barone, S., and Patterson, E. A., (1998), "Polymer coatings as strain witness in thermoelasticity," Journal of strain analysis, vol. 33, No 3, pp. 223-232.

Binshan, S. Y., Svenson, A. L., and Bank, L. C., (1995), "Mass and volume fraction properties of pultruded glass fibre-reinforced composites," Composites, vol. 26, pp. 725-731.

Biot, M. A., (1956), "Thermoelasticity and irreversible thermodynamics," Journal Applied Physics, vol. 27, no. 3, pp. 240-253.

Boa, G., Ho, S., Suo, Z., and Fan, B., (1992a), "The role of material orthotropy in fracture specimens for composites," International Journal of Solids and Structures, vol. 29, no. 9, pp. 1105-1116.

Boa, G., Ho, S., Suo, Z., and Fan, B., (1992b), Corriegnda, International Journal of Solids and Structures, vol. 29, no. 16, pp. 2115.

Bower, A. F., and Ortiz, M., (1991), "A three-dimensional analysis of crack trapping and bridging by tough particles," Journal of the Mechanics and Physics of Solids, vol. 39, no. 6, pp. 815-858.

Broek, D., (1997), Elementary Engineering Fracture Mechanics, Fourth Revised Edition, Kluwer Academic Publishers, Dordrecht, The Netherlands.

Brunner, A. J., (2000), "Experimental aspects of mode I and mode II fracture toughness testing of fibre-reinforced polymer-matrix composites," Computer Methods in Applied Mechanics and Engineering, vol. 185, pp. 161-172.

Chamis, C. C., and Sinclair, J. H., (1977),"Ten-deg-off-axis test for shear properties in fiber composites," Experimental Mechanics, vol. 17, no. 9, pp. 339-346.

Chandra, R., Singh, S.P., and Gupta, K., (1999), "Damping studies in fiber-reinforced composites - a review," Composite Structures, vol. 46, pp. 41-51.

Christensen, R. M., and Waals, F. M., (1972), ‘‘Effective stiffness of randomly oriented fibre composites,” Journal of Composite Materials, vol. 6, pp. 518–532.

Chu, T. C., Ranson, W. F., Sutton, M. A., and Peters, W. H., (1985), “Applications of digital–image correlation techniques to experimental mechanics,” Experimental Mechanics, vol. 25, no. 3, pp. 232–244.

Cowley, K. D., and Beaumont, P. W. R., (1997), ”The interlaminar and intralaminar fracture toughness of carbon–fibre/polymer composites: the effect of temperature,” Composites Science and Technology, vol. 57, pp. 1433–1444.

Creative Pultrusions Inc., (2000), ”Pultex pultrusion global design manual of standard and custom fiber reinforced polymer structural profiles,” vol. 3 – Revision 1, Creative Pultrusions Inc., Alum Bank, PA.

Cunningham, P. R., Dulieu–Barton, J. M., Dutton, A. G., and Shenoi, R. A., (2001), ”Thermoelastic characterisation of damage around a circular hole in a GRP component,” Key Engineering Materials, vol. 204–205, pp. 453–463.

Davalos, J. F., Qiao, P., Wang, J., Salim, H., Schlussel, J., (2002), ”Shear moduli of structural composites from torsion tests,” Journal of Composite Materials, vol. 36, no. 10, pp. 1151–1173.

DeltaTherm Operation Manual, (2001), Stress Photonics Inc. Madison, WI.

Donaldson, S. L., (1985), “Fracture toughness testing of graphite/epoxy and graphite/PEEK composites,” Composites, vol. 16, pp. 103–112.

Dulieu–Smith, J. M., Quinn, S., Shenoi, R. A., Read, P. J. C. L., and Moy, S. S. J., (1997), ”Thermoelastic stress analysis of a GRP tee joint,” Applied Composite Materials, vol. 4, pp. 283–303.

Dunn, S. A., (1993), ”On the effects of through–thickness thermal conduction on stress measurement by thermoelastic techniques,” Experimental Mechanics, vol. 33 pp. 32–36.

Dunn, S. A., (1992),”Analysis of thermal conduction effects on thermoelastic temperature for composite materials,” Journal of Applied Mechanics, vol. 59, pp. 552–558.

El–Hajjar, R. F., and Haj–Ali, R. M., (2003), ”A quantitative thermoelastic stress analysis method for pultruded composites,” Composites Science and Technology, vol. 63, no. 7, pp. 967–978.

Haj–Ali, R. M. and El–Hajjar, R. F., (2003),”Crack propagation analysis of Mode–I fracture in pultruded composites using micromechanical constitutive models,” Mechanics of Materials, vol. 35, no. 9, pp. 885–902.

Haj–Ali, R., M. and, Kilic, H., (2003) ”Nonlinear constitutive models for pultruded frp composites,” Mechanics of Materials, vol. 35, no. 8, pp. 791–801.

Haj-Ali, R. and Muliana, A. H. (2003), "Micromechanical models for the nonlinear viscoelastic behavior of pultruded composite materials," International Journal of Solids and Structures, 40, pp. 1037-1057.

Haj-Ali, R., M. and, Kilic, H., (2002), "Nonlinear behavior of pultruded FRP composites," Composites Journal Part B: Engineering. vol. 33, no. 3, pp. 173-191.

Haj-Ali, R. M., Kilic, M., and Zureick, A-H, (2001),"Three-dimensional micromechanics -based constitutive framework for analysis of pultruded composite structures," ASCE Journal of Engineering Mechanics , vol. 127, no. 7, pp. 653-660.

Haj-Ali, R. M., and Pecknold, D.A., (1996), ''Hierarchical material models with microstructure for nonlinear analysis of progressive damage in laminated composite structures", Structural Research Series no. 611, UILU-ENG-96-2007, Department of Civil Engineering, University of Illinois at Urbana-Champaign.

Hartmann, H. R., and Churchill, R. W., (1981), "Krak-Gage, a new transducer for crack growth measurement," SESA Fall Meeting, Keystone, CO October, 1981.

Harwood, N., and Cummings, W. M., (1991), Thermoelastic Stress Analysis, Adam Hilger Pub., New York, NY.

Helm, J. D., Sutton, M.A., Boone, M.L., (2001), "Characterizing crack growth in thin aluminum panels under tension-torsion loading using three-dimensional digital image correlation," Nontraditional Methods of Sensing Stress, Strain, and Damage in Materials and Structures: Second Volume, ASTM STP 1323, G. F. Lucas, P. C. McKeighan, and J. S. Ransom, Eds., American Society for Testing and Materials, West Conshohocken, PA.

Herakovich, C. T., and Mirzadeh, F., (1991), "Properties of pultruded glass/epoxy," Journal of Reinforced Plastics and Composites, vol. 10, pp. 2-28.

Holdsworth, A. W., Owen, M. J., Morris, S., (1974), "Macroscopic fracture of glass reinforced polyester resin laminates", Journal of Composite Materials, vol. 8, p. 177.

Hung, S.-C., and Liechti, K. M., (1999), "Finite element analysis of the arcan specimen for fiber reinforced composites under pure shear and biaxial loading," Journal of Composite Materials, vol. 33, no. 14, pp. 1288-1317.

Hung, S.-C., and Liechti, K. M., (1997), "An evaluation of the arcan specimen for determining the shear moduli of fiber-reinforced composites," Experimental Mechanics, vol. 37, no. 4.

John, R. , (1997), "Stress intensity factor and compliance solutions for an eccentrically loaded single edge notch geometry", Engineering Fracture Mechanics, vol. 58, pp. 87-96.

Jurf, R. A., and Pipes, B., (1982), "Interlaminar fracture of composite materials," J. of Composite Materials, vol. 16, pp. 386-394.

Kanninen, M. F., Rybicki, E. F., and Brinson, H. F., (1977a), ”A critical look at current applications of fracture mechanics to the failure of fiber-reinforced composites,” Composites, vol. 8, pp. 17-22.

Kanninen, M. F., Rybicki, E. F., and Griffith, W. I., (1977b), ”Preliminary development of a fundamental analysis model for crack growth in a fiber reinforced composite material,” Composite Materials: Testing and Design, ASTM STP 617, American Society for Testing and Materials., pp. 53-69.

Kelvin, (1878), (Thomson, W.), ”On the thermoelastic, thermomagnetic and pyro-electric properties of matter”, Phil. Mag., vol. 5, pp. 4-27.

Kilic, H. and Haj-Ali, R. (2003a), ”Elastic-degrading analysis of pultruded composite structures,” Composites Structures, vol. 60, no. 1, pp. 43-55.

Kilic, H. and Haj-Ali, R. (2003b), ”Progressive damage and nonlinear analysis of pultruded composite structures,” Composites part B: Engineering, vol. 34, no. 3, pp. 235-250.

Konish Jr., H. J., Swedlow, J. L., Cruse, T. A.,(1973), ”Fracture phenomena in advanced fiber composite materials”, AIAA Journal, vol. 11, no. 3, pp.40-43.

Konish, H. J., Swedlow, J. L., and Cruse, T. A., (1972), ”Experimental investigation of fracture in an advanced fiber composite,” Journal of Composite Mat., vol. 6, pp. 114-124.

Krueger, R., (2002), ”The virtual crack closure technique: history, approach and applications,” NASA/CR-2002-211628, ICASE Report no. 2002-10. April.

Kyriakopoulos, M. K., De Wilde, W. P., Van Hemelrijck, D., and Schillemans, L., (1992), ”A finite element approach for thermal-structural response in fibre reinforced composite systems,” 3rd International Conference on Computer Aided Design in Composite Material Technology - CADCOMP 92, pp. 599-614.

Lin, S. T., and Rowlands, R. E., (1995), ”Thermoelastic stress analysis of orthotropic composites”, Experimental Mechanics , vol. 35 , no. 3, pp. 257-265.

Luciano, R., and Barbero, E. J., (1994), “Formulae for the stiffness of composites with periodic microstructures,” International Journal of Solids and Structures, vol. 31., no. 21., pp. 2933-2944.

Mackenzie, A. K., (1989), ”Effects of surface coatings on infrared measurements of Thermoelastic Responses,” SPIE, vol. 1084, pp. 59-71.

Mackin, T. J., and Vernon, P. J., (2001), ”Detecting sub-surface cracking in laminated membranes using infrared imaging,” Polymer Composites, vol. 22, no.6, pp. 752-761.

Mandell, J. F., McGarry, F. J., Wang, S. S., and Im, J., (1974), ”Stress intensity factors for anisotropic fracture test specimens of several geometries,” Journal of Composite Materials, vol. 8, pp. 106-116.

Matlab, (2001), Version 6.1, The MathWorks, Inc, Natick, MA.

Oliver, D. E., (1988), "Stress pattern analysis by thermal emission (SPATE)," Experimental Techniques, 3-6, March.

Pagano, N. J., (1974), "Exact moduli of anisotropic laminates," Mechanics of Composite Materials, Sendeckyj, G. P., (Ed.), Academic Press, pp. 23-44.

Pang, H. L., and Seetoh, C. W., (1997), "A compact mixed mode (CMM) fracture specimen for adhesive bonded joints," Engineering Fracture Mechanics, vol. 57, no. 1., pp. 57-65.

Parhizgar, S., Zachary, L. W., and Sun, C. T., (1982), "Application of the principles of linear fracture mechanics to the composite materials," International Journal of Fracture, vol. 20, pp. 3-15.

Parks V. J., (1982), "Strain measurement using grids," Optical Engineering, vol. 21, pp. 633-639.

Piascik, R. S., Newman, J. C., Jr., and Underwood, J. H., (1997), "The extended compact tension specimen", Fatigue and Fracture of Engineering Materials and Structures, vol. 20, n. 20, pp. 559-563.

Piascik, R. S., and Willard, S. A., (1994), "The growth of small corrosion fatigue cracks in alloy 2024", Fatigue and Fracture of Engineering Materials and Structures, vol. 17, n. 11, pp. 1247-1259.

Potter, R.T., and Greaves, L.J., (1987), "The application of thermoelastic stress analysis technique to fibre composites", Optomechanical Systems Engineering, Daniel Vukobratovich, Editor, Proc. SPIE 817, pp. 134-146.

Raju, I. S., (1987), "Calculation of strain-energy release rates with higher order and singular finite elements," Engineering Fracture Mechanics, vol. 28, pp. 251-274

Rand, J. L., Henderson, J. K., and Grant, D. A., (1996), "Nonlinear behavior of linear low-density polyethylene," Polymer Engineering and Science, vol. 36, no. 8, p 1058-1064

Reber, R., De Haan, J., Mayer, J., Petitmermet, M., Wintermatnel, E., (2000), "Intralaminar fracture of weft-knitted carbon fiber reinforced PEEK", ESIS Publication 27, Elsevier. pp. 123-133.

Richardson, D. E., and Goree, J. G., (1993), "Experimental verification of a new two-parameter fracture model," ASTM STP 1189 (Edited by T. Chona). pp. 738-750.

Rikards, R., (2000), "Interlaminar fracture behaviour of laminated composites," Computers and Structures, vol. 76, pp. 11-18.

Rikards, R., Buchholzb, F. -G., Wangb, H., Bledzkic, A. K., Korjakina, A., and Richard, H. -A., (1998), "Investigation of mixed mode I/II interlaminar fracture toughness of laminated composites by using a CTS type specimen," Engineering Fracture Mechanics, vol. 61, pp. 325-342.

Saxena, Ashok, (1979), "Application of linear elastic fracture mechanics to the evaluation of aluminum-epoxy bonds," Fibre Science and Technology, vol. 12, no. 2, pp. 111-128.

Sih. G. C., Chen, E. P., Huang, S. L., and, McQuillen, E. J., (1975), "Material characterization on the fracture of filament reinforced composites," Journal of Composite Materials, vol. 9, pp. 167-186.

Sih, G. C., Paris, P. C., Irwin, G. R., (1965), "On cracks in rectilinearly anisotropic bodies", International Journal of Fracture Mechanics, vol. 1, no. 3, pp. 189-203.

Smith, S. J., Parsons, I. D., and Hjelmstad, K. D. (1998), "An experimental study of the behavior of connections for pultruded GFRP I-beams and rectangular tubes," Composite Structures, vol. 42, pp. 281-290.

Sonti, S. S., and Barbero, E., (1996), "Material characterization of pultruded laminates and shapes," Journal of Reinforced Plastics and Composites, vol. 15, pp. 701-717.

Strongwell Corporation, (2003), "Fabrication and repair manual for EXTREN fiberglass structural shapes," accessed online, www.strongwell.com, November 15. Bristol, VA.

Suo, Z., Boa, G., Fan, B., Wang, T-C., (1991), "Orthotropy rescaling and implications for fracture in composites," International Journal of Solids and Structures, vol. 28, no. 2, pp. 235-248.

Sutton, M. A., Turner, J. L., Bruck, H. A. and Chae, T. A., (1991), "Full-field representation of discretely sampled surface deformation for displacement and strain analysis," Experimental Mechanics, vol. 31, pp. 168-177.

Thomson, W., (Kelvin), (1878), "On the thermoelastic, thermomagnetic, and pyro-electric properties of matter," Phil. Mag., vol. 5, pp. 4-27.

Toll, S., and Aronsson, C., (1992), "Notched strength of long- and short-fibre reinforced polyamide," Composites Science and Technology, vol 45, pp 43-54.

Towse, A., Setchell, C. J., Potter, K. D., Clarke, A. B., Macdonald, J. H. G., Wisnom, M. R., and Adams, R. D., (2001), "Use experience with a developmental general purpose non-contacting extensometer with high resolution," American Society for Testing and Materials, Nontraditional Methods of Sensing Stress, Strain and Damage in Materials and Structures, ASTM STP 1323

Tsai, S., W., Pagano, N. J., (1968), "Invariant properties of composite materials," Composite Materials Workshop, Technomic Publishing Co.

Turvey, G. J., (1998), "Torsion tests on pultruded GRP sheet," Composites Science and Technology, vol. 58, pp. 1343–1351.

Underwood, J. H., Kortschot, M. T., Lloyd, W. R., Eidenoff, H. L., Wilson, D. A., Ashbaugh, N, (1995), "Translaminar fracture toughness test methods and results from interlaboratory tests of carbon/epoxy laminates," Fracture Mechanics: 26th Volume, Walter G. Reuter, John H. Underwood and James C. Newman, Jr. Eds., American Society for Testing and Materials, Philadelphia.

Van Hemelrijck, D., Schillemans, L., De Roey, F., Daerden, I., Boulpaep, F., De Wilde, P., and Cardon, A., (1992), "Thermoelastic stress analysis of fibre reinforced composite systems", 3rd International Conference on Computer Aided Design in Composite Material Technology - CADCOMP 92, pp. 626–633.

Vishay (2003, August 1st), Bulletin S–116, "Materials for photoelastic coatings", Raleigh, NC, from: http://www.vishay.com/

Voloshin, A., and Arcan, M., (1980), "Pure–shear moduli of unidirectional fibre–reinforced materials (FRM)," Fibre Science and Technology, vol. 13, pp. 125–134.

Waddoups, E. M., Eisenmann, J. R., and Kaminiski, B. E., (1971), "Macroscopic fracture mecchanics of advanced composite materials." Journal of Composite Materials, vol. 5, p. 446.

Wang, Y., and Zureick, A., (1994), "Characterization of longitudinal tensile behavior of pultruded I–shaped structural members using coupon specimens," Composite Structures, vol. 29, pp. 463–472.

Welch, C. S., and Zickel, M. J., (1993), "Thermal coating characterization using thermoelasticity," Review of Progress in Quantitative Nondestructive Evaluation, vol. 12, Thomson, D. O., and Chimenti, D. E., Eds., Planum Press, NY, NY.

Whitney, J. M., (1989), "Experimental characterization of delamination fracture," Pagano, NJ editors. Interlaminar response of composite materials. Amsterdam, Elsevier, pp. 161–250.

Whitney, J. M., and Nusimer, R. J., (1974), "Stress fracture criteria for laminated composites containing stress concentrations." Journal of Composite Materials, vol. 8, p. 253–265.

Wong, A. K., Jones, R., and Sparrow, J. G., (1987), "Thermoelastic constant or thermoelastic parameter?" Journal of Phys. Chem. Solids, vol. 48, no. 8., pp. 749–753.

Yen, S. –C, Craddock, J. N., and Teh, K. T., (1998) "Evaluation of a modified arcan fixture for the in–plane shear test of materials," Experimental Techniques, vol. 12, no. 12, p 22–25.

Yuan, W. G., Lai, M. O., and Lee, K. H., (1994), "Evaluation of test specimens using J–integral," Finite Elements in Analysis and Design, vol. 18, pp. 221–224.

Zhang, D., Enke, N. F., and Sandor, B. I., (1990), ”Thermographic stress analysis of composite materials,” Experimental Mechanics, vol. 30, 1, pp. 68–73.

Zureick, A. H., Berghaus, D. G., Cho, B. K. and Park, J. Y., (1999), ”The in–plane shear properties of pultruded materials,” FHWA–Report, Georgia Institute of Technology, Atlanta, Georgia.

VITA

Rani Fayez El-Hajjar, Palestinian, was born in Muharraq, Bahrain on May 4, 1977. After completing his secondary education at the Sacred Heart School in Bahrain, he entered the University of Nebraska. In 1998, he graduated a summa cum laude, with a BS in Civil Engineering and was also selected amongst his graduating class as the most outstanding student in Civil Engineering. In 2000, Rani El-Hajjar was awarded a MS degree in Civil Engineering from the University of Texas at Austin. His master's thesis was on his development of an Acoustic Emission test technique for the structural integrity assessment of Railroad Tank Cars. In fall 2000, Rani El-Hajjar started his doctoral studies at the Georgia Institute of Technology in Atlanta to research in the area of fracture mecahnics of fiber reinforced composite materials. A selection of his publications while at the Georgia Institute of Technology follows:

El-Hajjar, R. F. and Haj-Ali, R. M., (2004), "Mode-I fracture toughness testing of thick section FRP composites using the ESE(T) specimen", Engineering Fracture Mechanics, Accepted for publication, In press.

El-Hajjar, R. F., and Haj-Ali, R. M., (2004), "Infrared (IR) thermography for strain analysis in pultruded fiber reinforced plastics," 2nd Place entry at the 2003 Society for Experimental Mechanics (SEM) International Student Paper Competition, Experimental Techniques, March/April 2004 Issue.

El-Hajjar, R. F., and Haj-Ali, R. M., (2003), "In-plane shear testing of thick-section pultruded FRP composites using a modified Arcan fixture," Composites Part B: Engineering, Accepted for publication, In press.

Haj-Ali, R. M. and El-Hajjar, R. F., (2003), "Crack propagation analysis of mode-I fracture in pultruded composites using micromechanical constitutive models," Mechanics of Materials International Journal, vol. 35, no. 9, pp. 885-902.

El-Hajjar, R., and Haj-Ali, R., (2003), "A quantitative thermoelastic stress analysis method for pultruded composites," Composites Science and Technology, vol. 63, no. 7, pp. 967-978.

El-Hajjar, R. F., and Haj-Ali, R. M., (2003), "Fracture toughness and crack growth in FRP pultruded composites," 16th ASCE Engineering Mechanics Conference, 16th ASCE Engineering Mechanics Conference, University of Washington, Seattle, WA, July 16-18.